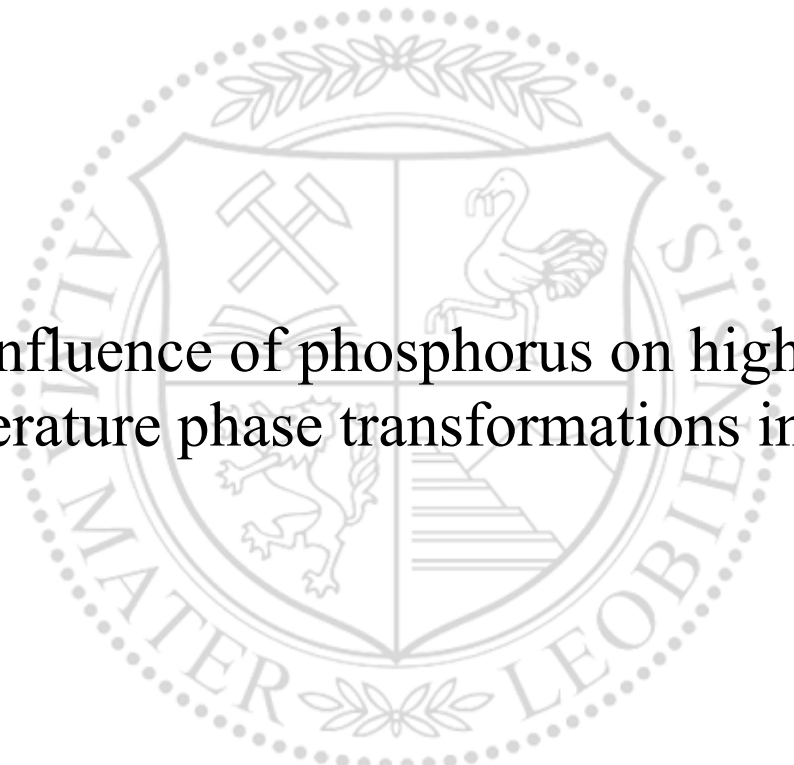




Chair of Ferrous Metallurgy

Doctoral Thesis



Influence of phosphorus on high-
temperature phase transformations in steel

Dipl.-Ing. Michael Christian Bernhard, BSc

July 2021



EIDESSTÄTTLICHE ERKLÄRUNG

Ich erkläre an Eides statt, dass ich diese Arbeit selbständig verfasst, andere als die angegebenen Quellen und Hilfsmittel nicht benutzt, und mich auch sonst keiner unerlaubten Hilfsmittel bedient habe.

Ich erkläre, dass ich die Richtlinien des Senats der Montanuniversität Leoben zu "Gute wissenschaftliche Praxis" gelesen, verstanden und befolgt habe.

Weiters erkläre ich, dass die elektronische und gedruckte Version der eingereichten wissenschaftlichen Abschlussarbeit formal und inhaltlich identisch sind.

Datum 09.07.2021

Unterschrift Verfasser/in
Michael Christian Bernhard

Expression of thanks

First of all, I would like to thank Univ.-Prof. Dipl.Ing. Dr.techn. Johannes Schenk for providing the possibility to write my PhD thesis at the Chair of Ferrous Metallurgy.

The supervision of my PhD thesis and the valuable feedback of Assoc.Prof. Dipl.Ing. Dr.mont. Susanne Michelic and Univ.-Prof. Dipl.Ing. Dr.mont Helmut Clemens during my research work is greatly acknowledged.

A special thanks goes to my colleague and friend Dipl.Ing. Dr.mont. Peter Presoly who introduced me to the wide field of thermal analysis techniques and showed me what the term “careful” means with respect to experiments in the laboratory. Beside our intensive technical discussions, I enjoyed our talks on daily news and the valuable time we spent outside of work.

Further, I would like to thank my project partners Dr. Susanne Hahn from primetals technologies Austria GmbH and Dr. Sergiu Ilie from voestalpine Stahl GmbH for the trust in my research and showing me the industrial relevance of my project work. I’m looking forward to further collaborations with you.

Prof. Youn-Bae Kang from Graduate Institute of Ferrous Metallurgy at Pohang University of Science and Technology (South Korea) introduced me to computational thermochemistry and the CALPHAD approach. Thank you for the extensive supervision of the modelling work, I really enjoyed the time of my research stay at École polytechnique de Montréal (Canada)!

I would like to thank our engaged crew in the melting shop: Michael Jäger, Anton Reitbauer, Ewald Suchadolnik and Gerhard Winkler. It is not self-evident to perform complex solidification experiments and having a good time at once.

Without the extensive metallographic work of Bernhard Gerstl, Bernd Lederhaas, Tobias Rieger and Nadine Tatzreiter, only a small fraction of the present results would be created.

Franz Prucha from voestalpine Stahl Linz GmbH performed the chemical analysis of all samples in an outstanding manner. Thank you for sharing your expertise on analytics with me!

My colleagues and friends Michael Lammer, Dipl.Ing. Dr.mont. Lukas Preuler and Paul Reisinger not only helped me in my working life but also we pushed our fitness to the physical limit. I really don't want to miss our hiking trips and joint mountain runs!

Last but not least I gratefully thank my family - my parents, my grandparents and my girlfriend - for all the support I got through my whole life and during my study time. The good mood of my mother always put a smile on my face, even in the worst moments of preparing myself for a tough examination. My father is not only the person who inspired me as a role model with the passion he has for solving scientific problems but is also the friend I can talk to in any - private or profession - situation of my life.

Kurzfassung

Im Allgemeinen wird Phosphor als unerwünschtes Begleitelement und als Schädling bei der Stahlherstellung betrachtet. Während der Erstarrung führt die starke Anreicherung von Phosphor in der interdendritischen Schmelze zu einer deutlichen Absenkung der Solidustemperatur. Die auftretende Seigerungstendenz ist dabei von der Erstarrungsabfolge im Peritektikum des Fe-C Diagramms abhängig und nimmt mit steigendem Kohlenstoffgehalt zu. Die signifikante Aufweitung des Erstarrungsintervalls führt in weiterer Folge zu einer erhöhten Heißrissempfindlichkeit des Stahls.

Heutzutage wird Phosphor trotz seiner negativen Auswirkungen auf die Produktqualität spezifisch als kostengünstiges Legierungselement im Stahl verwendet. Beispielsweise wirkt Phosphor als effektiver Mischkristallverfestiger und verbessert die elektrischen Eigenschaften von siliziumhaltigen Elektroblechen. In phosphorlegierten Stahlgütern liegt der Leigerungsgehalt bei 0.10 % und ist damit deutlich höher als in der Stahlherstellung üblicherweise angestrebt: Hochreine Stähle enthalten weniger als 0.01 %P während die Toleranz bei Baustählen mit einem Maximalwert von 0.05 % etwas großzügiger ausgelegt wird.

Im Stranggießprozess wird der erstarrende Strang hohen mechanischen Belastungen ausgesetzt, welche durch Ausbauchung, Biegen und Richten des Strangs sowie durch thermische Gradienten innerhalb der Strangschale entstehen. Zugspannungen an der Erstarrungsfront können in Kombination mit der erhöhten Heißrissempfindlichkeit von phosphorlegierten Stählen zu einer deutlichen Beeinträchtigung der Produktqualität führen. Die Anpassung der Prozessparameter für das Vergießen von phosphorlegierten Stählen ist daher von größter Bedeutung. Für die erfolgreiche Optimierung der Gießparameter ist dabei

die exakte Kenntnis von Phasenumwandlungstemperaturen und thermodynamischen Daten des Stahls unumgänglich.

In der vorliegenden Arbeit wurde daher der Einfluss von Phosphor auf die Hochtemperaturphasenumwandlungen von Stahl anhand des Fe-P Phasendiagramms sowie mehrerer vertikaler Schnitte im ternären Fe-C-P System untersucht. Fokus lag hierbei auf der Bedeutung für den Stranggießprozess. Im experimentellen Teil wurden die *in-situ* Techniken der Dynamischen Differenzkalorimetrie (DSC), der Hochtemperatur-Laserscanning-Konfokalmikroskopie (HT-LSCM), der Hochtemperatur-Röntgenbeugung (HT-XRD) und der Dilatometrie zur Bestimmung der Umwandlungstemperaturen eingesetzt. Neben der klassischen DSC-Analyse wurde ein neuartiger Ansatz zur Kopplung von DSC und HT-LSCM Beobachtungen entwickelt, um die Phasengrenzlinien des geschlossenen „*γ-loops*“ im binären Fe-P System zu rekonstruieren. Unter Berücksichtigung der neu gewonnenen experimentellen Erkenntnisse wurde eine CALPHAD-basierende (Calculation of Phase Diagrams), thermodynamische Optimierung des Fe-P und Fe-C-P durchgeführt. Erstmals erfolgte die Beschreibung der Flüssigphase in diesem Legierungssystem mit dem modifizierten quasichemischen Modell (MQM). Die experimentellen Daten sowie die thermodynamischen Berechnungen konnten genutzt werden, um ein Mikrosegierungsmodell zur Beschreibung der Erstarrung von Stahl unter stranggießähnlichen Bedingungen zu verbessern. Spezieller Fokus lag hierbei auf phosphorlegierten Stählen.

Abstract

Phosphorus is generally known as harmful element in steel. During the solidification, P strongly segregates in the interdendritic liquid leading to a significant drop of the solidus temperature. Depending on the solidification sequence in the peritectic range of the Fe-C based, multicomponent phase diagram the segregation tendency increases with higher amount of carbon. As a consequence, even small amounts of P favour the hot tear formation in technological solidification processes. However, in recent steel design, P is added as alloying element to improve the physico-mechanical properties of advanced steel grades. In so called "*rephosphorized*" steels, the maximum P content exceeds 0.10 mass percent and is far higher than the typical concentration of $P < 0.010\%$ in high-quality steels or $P < 0.05\%$ in construction steels.

In the continuous casting process, mechanical stresses are exerted on the solidifying shell due to bulging, bending/straightening and thermal gradients. In combination with the increased hot tear sensitivity of highly P-alloyed steels, the tensile stresses along the solidification front may cause serious internal defects and special care has to be taken in optimizing the process parameters for casting rephosphorized steels. However, beside the precise knowledge of the actual process conditions, accurate phase diagram data and thermodynamic properties of the steel are required for a successful process control during casting.

In the present PhD thesis, the effect of phosphorus on high-temperatures phase transformations with respect to the continuous casting process was therefore studied by investigating the binary Fe-P and ternary Fe-C-P key-systems. In the experimental part various *in-situ* techniques of differential scanning calorimetry (DSC), high-temperature laser scanning confocal microscopy (HT-LSCM), high-temperature X-ray diffraction (HT-XRD) and dilatometry were applied to characterize the phase transformation temperatures and phase stabilities. In

addition to classical DSC analysis of high-temperature phase equilibria, a novel approach of coupling DSC analysis and HT-LSCM observations was developed to characterize the “ γ -loop” in the Fe-P system. CALPHAD-type (Calculation of Phase Diagrams) thermodynamic optimizations of the Fe-P and Fe-C-P systems were carried out considering the newly gained phase diagram data. For the first time, the modified quasichemical model (MQM) was applied for the liquid phase in this alloying system. Finally, the experimental data and the improved thermodynamic assessment were used to further develop a microsegregation model for calculation of solidification close to continuous casting conditions with particular focus on rephosphorized steels.

Table of contents

Expression of thanks	I
Kurzfassung	III
Abstract	V
Table of contents	VII
1 Introduction	1
2 State of the art	3
2.1 Phosphorus in steel.....	3
2.1.1 Relevance of phosphorus in recent design of advanced steel grades.....	4
2.1.2 Phase stabilities in the Fe-P and Fe-C-P systems.....	5
2.1.2.1 The binary Fe-P phase diagram.....	6
2.1.2.2 Phase equilibria in the ternary Fe-C-P system.....	9
2.1.3 Aspects of continuously casting rephosphorized steel grades.....	13
2.1.3.1 Continuous casting and product quality: A brief introduction.....	13
2.1.3.2 Segregation of phosphorus on microscopic scale.....	15
2.1.3.3 Influence of phosphorus on hot tear formation.....	23
2.2 Computer coupling of phase diagrams and thermochemistry.....	25
2.2.1 Computational thermodynamics: The CALPHAD approach.....	26
2.2.2 Thermodynamic modelling of solutions.....	29
2.2.2.1 Gibbs-energy of pure elements and stoichiometric compounds.....	30
2.2.2.2 Bragg-Williams (BW) model and compound-energy formalism (CEF).....	30
2.2.2.3 Modified quasicheical model (MQM) for short-range ordering (SRO).....	32

2.2.2.4	Thermodynamic assessments of the Fe-P and Fe-C-P systems	35
2.2.3	Application of a CALPHAD-based tool to the continuous casting process.....	37
3	List of publications.....	41
4	Novel research findings and discussion	44
4.1	Experimental reassessment of the binary Fe-P phase diagram and Fe-C-P key systems using DSC (Paper I).....	45
4.2	Thermodynamic modelling of the Fe-P and Fe-C-P system using the MQM for the liquid phase (Paper II)	48
4.3	A novel approach for <i>in-situ</i> characterization of γ -loops by coupling DSC and HT-LSCM: Application to the binary Fe-P system (Publication III).....	51
4.4	Development of a microsegregation model for the continuous casting process with special focus on rephosphorized steels (Paper IV-V).....	55
4.4.1	General model description	56
4.4.2	Determination of the partition coefficients $k_P^{\delta,\gamma}$ from Paper I and II	59
4.4.3	Assessment of analytical liquidus equations for steel and incorporating the start of the peritectic reaction into the model.....	61
5	Summary and conclusion	64
	Bibliography	66
	Appendix: Publications	83

1 Introduction

Today, continuous casting is the most dominating casting process in the steelmaking industry. The process is characterized by its cost-efficiency and provides the possibility of manufacturing a wide range of steel grades. More than 96 % [1] of the annual steel production is continuously cast to billets, blooms or slabs. Billets and blooms are the starting materials for long products, e.g. wire rods and rails whereas slabs are typically further processed to heavy plates and steel sheets for the automotive sector.

In order to guarantee a successful process control, detailed information on the solidification behaviour of the steel grade is required. Many continuously casted steels contain less than 0.60 mass percent of carbon and solidify in the peritectic part of the Fe-C based, multicomponent phase diagram. Depending on the chemical composition, the different phase transformation paths are characterized by unique solidification phenomena occurring within the casting process. The pre-identification of the ferrite (δ -Fe) and austenite (γ -Fe) phase stabilities in the peritectic range as well as the precise knowledge of liquidus and solidus temperatures are therefore of great importance in order to adjust the practical operation parameters. For instance, increased trace levels of strongly segregating elements like phosphorus decrease the solidus temperature and favour hot tearing in the liquid + solid two-phase region. As a consequence, the secondary cooling strategy, the casting speed and position of the softreduction have to be modified avoiding the formation of defects in the solidifying strand.

Aim of the PhD work was therefore to experimentally and to thermodynamically investigate the influence of phosphorus on high-temperature phase transformations in steel with respect to the continuous casting process. For this purpose, various *in-situ* experimental techniques were applied including differential scanning calorimetry (DSC), high-temperature laser scanning

confocal microscopy (HT-LSCM), high-temperature X-ray diffraction (HT-XRD) and dilatometry. The newly gained phase diagram data were further processed in a CALPHAD-type (Calculation of Phase Diagrams) thermodynamic modelling of the binary Fe-P and ternary Fe-C-P systems. Finally, the results were implemented into an in-house microsegregation model for solidification calculation of steel under conditions close to continuous casting.

Though the influence of phosphorus on phase equilibria in steel was frequently studied in the past, this research field is “*again*” of great interest for the iron and steelmaking community. In recent steel design, P is added as alloying element in order to improve several physico-mechanical properties of advanced steel grades. In so called “*rephosphorized*” steels, the maximum P content partly exceeds 0.10 mass percent, which is far higher than the typical trace element level of $P < 0.01 \%$ in high-quality steels or $P < 0.05 \%$ in steels for structural applications.

The present cumulative-type PhD thesis is structured into two main parts. The first section summarizes the state of the art and deals with challenges in continuous casting of steels with high amount of phosphorus. Aspects of applying computational thermodynamics in process modelling are also discussed in this chapter. The second part highlights the novel research findings of the present work and contains the peer-reviewed papers published within the project of the PhD thesis.

2 State of the art

This chapter emphasises the need of ongoing research activities to characterize the influence of phosphorus on high-temperature phase transformations in steel with special focus on the continuous casting process. The first part deals with the general role of phosphorus as alloying element in advanced steels. Then, aspects of casting of rephosphorized steels are discussed based on the binary Fe-P and ternary Fe-C-P phase diagrams. Finally, potentials of computational thermodynamics in modelling the casting process are presented considering the CALPHAD approach and optimizations of the Fe-C-P system.

2.1 Phosphorus in steel

Phosphorus is generally known to be a harmful element in steel. During the solidification, P strongly segregates in the liquid phase and even low amounts (0.01 - 0.03 %) may seriously affect the product quality in the continuous casting process. Further, the phosphorus impurity level is relevant to consider in the heat treatment processing of low-alloyed Q(ueenched) & T(empered) steel grades. Particularly for Mn-, Mn-Cr and Cr-Ni steels, long holding times between 350 - 600 °C [2,3] or slow cooling through this critical temperature range favor the segregation of impurities (P, Sb, Sn and As) to (prior austenite) grain boundaries [3] during tempering. This effect is well-known as "*temper embrittlement*" and leads to a loss of ductility and an increase of the brittle-ductile transition temperature in the final product. It was shown by various researchers [2,4,5] that the grain boundary segregation of P raises the sensitivity of steel to temper embrittlement at already low impurity levels ($P \geq 0.02 \%$).

2.1.1 Relevance of phosphorus in recent design of advanced steel grades

Despite its negative effects on steel, phosphorus is specifically added in recent material design with concentrations up to 0.15 mass percent as P shows beneficial influence on selected material properties of advanced steel grades. Highly P-alloyed steels are known as “*rephosphorized grades*”, their applications and typical P contents are briefly summarized as follows, see also attached **Papers I-III**:

- High-strength interstitial-free (HSIF) and Ultra-Low-Carbon (ULC) steels are widely used in the automotive sector. The low carbon and nitrogen contents (< 0.003 %) guarantee superior deep drawability required for a high surface quality of exterior skin parts. Typically, solution hardening elements such as Mn, Si and P are added to IF steels contributing to increased strength values. [6] Among these elements, phosphorus has been proven as most effective in the steel matrix. [7] Alloying of 0.085 mass pct. increase the yield strength by 60 MPa and the tensile strength by 80 MPa [8]. Further, it was reported [9] that phosphorus can contribute to the bake hardening (BH) effect in ULC-BH steel grades.
- Transformation-Induced-Plasticity (TRIP) steel grades belong to the group of advanced high strength steels (AHSS) being applied for crash-relevant components in automotive engineering. The microstructure consists of about 60 vol. % ferrite, 25 vol. % bainite balanced with ~ 15 vol. % retained austenite. [10] Alloying elements such as Si, Al and P suppress the precipitation of carbides (Fe_3C) and stabilize the retained austenite at room temperature. During final forming, the metastable austenite transforms into martensite leading to an excellent combination of strength and ductility. [10] In TRIP steels, phosphorus partly substitutes silicon and aluminum. Amounts of about 0.10 mass pct. are considered to show beneficial influence on the TRIP effect. [11,12]
- Instead of plain carbon steels, weathering steels with improved atmospheric resistance are often used in structural application. Alloying of minor amounts of Cr, Ni, Si, P and Cu promote the formation of a stable rust layer under long-term use in corrosive atmospheric environment. Therefore, coating or painting of the components is not required. [13,14] The maximum P content of weathering steels is defined by 0.15 %. [13–15]
- In silicon steel sheets for electrical applications (Si-steel) it was shown that alloying of phosphorus with amounts up to 0.10 mass pct. improve the crystallographic texture and reduce the core loss [16,17]. Within the current energy evolution, these steel grades attract much attention due to their application in transformer technology and electrical motors.

2.1.2 Phase stabilities in the Fe-P and Fe-C-P systems

Phase diagrams can be seen as a roadmap for developing new materials. Many product properties and process relevant issues are closely related to the corresponding phase diagrams. In order to describe the physical-chemical influence of phosphorus in the steel matrix, the precise knowledge of the binary Fe-P and ternary Fe-C-P key systems are of great importance. Hence, this chapter provides an overview of available experimental data based on the work of Okamoto [18] and Perrot [19] and introduces the general constitution of the Fe-P and Fe-C-P systems.

According to Okamoto [18], nine phases are stable in the binary Fe-P system: The stability of three solution phases - liquid, body centered cubic ferrite (bcc or α/δ -Fe) and face centered cubic austenite (fcc or γ -Fe) - as well as the existence of three stoichiometric compounds - Fe_3P , Fe_2P and FeP - was confirmed in previous work. Though the existence of higher order phosphides (FeP_2 and FeP_4) was reported in references [20–23], the exact phase boundaries in the P-rich part are still unknown [18] as no reliable experimental data are available at compositions higher than that of the FeP compound (P ~ 35 mass pct.). The high volatilization of P makes experimental investigations in the P-rich region quite challenging. [24] For pure phosphorus the most common form is white P (or α -P). [18] The ternary Fe-C-P system comprises 11 phases including the nine phases from the Fe-P phase diagram as well as the metastable cementite (Fe_3C) and stable C (graphite) from the Fe-C system. No ternary phases were reported in the Fe-C-P system. All phases found under atmospheric pressure conditions are summarized in **Table 1** along with crystallographic data (Pearson symbol, space group, Strukturbericht designation and the corresponding prototype).

Numerous experimental techniques were applied to characterize the Fe-P and Fe-C-P phase diagrams (see **Table 2** and **Table 3**): (i) “*Thermal analysis*” is based on the enthalpy change during the investigated phase transformation and was frequently used to study melting equilibria, (ii) “*thermo-magnetic analysis*” is of particular relevance for determining solid-state phase equilibria between austenite and ferrite taking into account the different magnetic susceptibility of bcc and fcc above the Curie temperature and (iii) “*equilibration methods*” are performed by heat-treating the samples at elevated temperatures. After chemical and thermal equilibration the specimen is quenched in ice-water to stabilize the high-temperature microstructure down to room temperature. The final phase analysis is done either by optical microscopy or electron probe microanalysis (EPMA). Extensive discussion on the reliability of the phase diagram data with particular focus on liquid/solid equilibria can be found in **Paper I**; **Paper III** deals in detail with the analysis of the solid state ferrite/austenite phase equilibrium

data. Beside the phase diagram data, measurements of the thermodynamic properties (activities, enthalpies, etc.) and previous thermodynamic descriptions were critically evaluated within the CALPHAD-type optimization in **Paper II**.

For graphical representations of phase diagrams in this section, the thermodynamic descriptions of the Fe-P system according to Shim et al. [25], Miettinen and Vassilev [26] and You and Jung [27] were implemented into the FactSage 8.0 thermochemical software [28]. From literature, two parameter sets for the Fe-C-P system are available from Gustafson [29] and Shim et al. [30]; the more recent work of Shim et al. [30] was used in the present chapter.

Table 1: Stable phases in the ternary Fe-C-P system along with crystallographic data [18,19,31]

Phase	Pearson symbol	Space group	Strukturbericht	Prototype
Liquid	-	-	-	-
(γ Fe)	cF4	Fm $\bar{3}$ m	A1	Cu
(α Fe), (δ Fe)	cI2	Im $\bar{3}$ m	A2	W
Fe ₃ P	tI32	I $\bar{4}$	D0 _e	Ni ₃ P
Fe ₂ P	hP9	P $\bar{6}$ 2m	C22	Fe ₂ P
FeP	oP8	Pna2 ₁	-	MnP
FeP ₂	oP6	Pnm	C18	FeS ₂ (marcasite)
FeP ₄	mP30	P2 ₁ /c	-	FeP ₄
(P) white	c**	-	-	(P) white
Fe ₃ C	oP16	Pnma	D0 ₁₁	Fe ₃ C
C (gr.)	hP4	P6 ₃ /mmc	A9	C (gr.)

2.1.2.1 The binary Fe-P phase diagram

First experimental investigations of the Fe-P phase diagram started already at the beginning of the 20th century by Stead [32] and Gercke [33]. Saklatwalla [34] and later, Konstantinow [35] reconstructed the phase diagram up to ~ 25 mass pct. by evaluating cooling curves of thermal analysis. Haughton [36] combined thermal analysis, magnetic measurements and metallographic examination to identify phase transformation temperatures and magnetic transitions between 0.089 - 30 mass pct. P. Solid state phase stabilities of austenite and ferrite were studied by Roquet and Jegaden [37] using dilatometry and equilibration experiments with subsequent quenching, including metallographic examination. Lorenz and Fabritius [38] and Fischer et al. [39] used the concept of the magnetic balance to completely reconstruct the austenite/ferrite phase boundaries. Wachtel et al. [40] characterized the solid/liquid phase

boundaries up to 13 mass pct. P. The solubility of P in ferrite was reported in the temperature range of 550 - 1200 °C in the studies of Kaneko et al. [41], Doan and Goldstein [42] and Ko and Nishizawa [43]. The most recently published data of Schürmann and Kaiser [44] in the year 1980 and Morita and Tanaka [45] in 1986 focused on the solid/liquid phase boundaries. In both studies equilibration experiments with subsequent EPMA were intensively used. However, further experimental research on the phase diagram constitution stopped after the year 1986. Since then, first activities were reuptaken within the present thesis for the Fe-rich part in **Paper I** and **III**. All available data from literature and the used experimental techniques are summarized in **Table 2**.

Table 2: Experimental phase diagram data of the Fe-P system from literature [34–45]. Note, that in case of equilibration experiments the given composition is not the initial sample analysis but corresponds to the directly measured value of the respective phases.

Authors (year)	Experimental technique	Temperature [°C]	Composition [mass pct.]	Ref.
Saklatwalla (1908)	Thermal analysis	885 - 1510	0 - 24.5	[34]
Konstantinow (1910)	Thermal analysis	925 - 1505	0.50 - 21	[35]
Haughton (1927)	Thermal analysis, magnetic tests	731 - 1440	0.089 - 30	[36]
Roquet and Jegaden (1951)	Equilibration, dilatometry	860 - 1425	0.075 - 0.35	[37]
Lorenz and Fabritius (1962)	Magnetic balance	940 - 1330	0.25 - 0.62	[38]
Fischer et al. (1966)	Magnetic balance	920 - 1370	0 - 0.60	[39]
Wachtel (1963)	Thermal analysis, magnetic tests	1048 - 1534	0 - 13.13	[40]
Kaneko et al. (1965)	Equilibration	700 - 1000	~ 0.8 - 2.5	[41]
Doan and Goldstein(1970)	Equilibration	550 - 1100	0.0025 - 16.50	[42]
Ko and Nishizawa (1979)	Equilibration	600 - 1200	~ 0.30 - 2.50	[43]
Schürmann and Kaiser (1980)	Thermal analysis, equilibration	950 - 1520	~ 0.75 - 22	[44]
Morita and Tanaka (1986)	Equilibration	1132 - 1460	~ 0.35 - 10	[45]

The binary Fe-P phase diagram [25–27] calculated up to 35 mass pct. P (composition of FeP), is plotted in **Figure 1**; along with experimental data from literature [34–46]. In the Fe-rich part, the liquid phase, ferrite (bcc) and the Fe₃P compound form an eutectic type phase equilibrium at the temperature of 1048 °C [18], where the maximum solubility of P is given with 2.8 % and the eutectic composition is 10 mass pct. P. [18] Between 0 - 0.7 mass pct. P and temperatures of 900 - 1400 °C, the phase boundaries of austenite and ferrite are characterized by a completely closed fcc field, well known as “*γ-loop*”, where ferrite is stable over a wide region in the phase diagram. In the P-rich part of the phase diagram, various authors [35,36,44] reported incongruent melting of the Fe₃P compound in the temperature range of 1155 - 1173 °C, the peritectic phase equilibria liquid + Fe₂P ↔ Fe₃P is accepted at 1166 °C [18]. The Fe₂P phosphide melts congruently at a temperature of 1370 °C [18], the measured melting point in this case varies between 1270 °C [34], 1350 °C [35] and 1370 °C [36]. The eutectic temperature of the reaction liquid ↔ Fe₂P + FeP is consistent in the studies of Haughton [36] (1262 °C) and Schürmann and Kaiser [44] (1265 °C) with the eutectic composition of 27 mass pct. P [36].

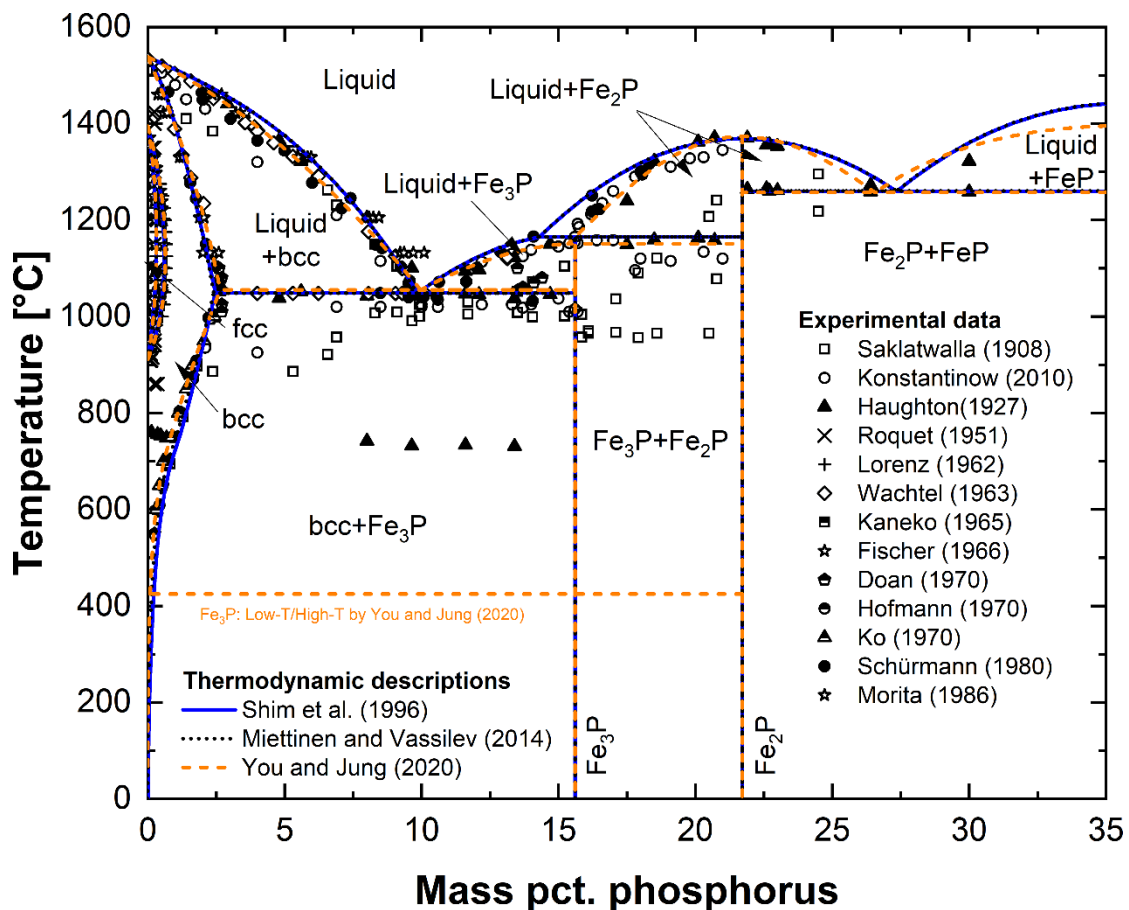


Figure 1: Binary phase diagram calculated with the thermodynamic descriptions of Shim et al. [25], Miettinen and Vassilev [26] and You and Jung [27] up to the FeP composition. Experimental data were taken from references [34–46].

The enlarged parts of the liquid/solid equilibria in the Fe-rich part of the Fe-P phase diagram is shown in **Figure 2 (a)**. P strongly lowers both, the liquidus (T_L) and solidus (T_S) temperature of Fe. Starting from the melting point of pure iron (1538 °C), and considering a theoretical linear shape of the phase boundaries, T_L is decreased by - 50 [°C/%P]. The drop of T_S is even larger with - 200 °C/%P. Further, the diverging phase boundary lines of T_L and T_S result in a pronounced segregation tendency of P during solidification of steel.

A detailed view on the calculated solid-state γ -loop [25–27] is provided in **Figure 2 (b)** with the experimental data of references [36–39]. The maximum solubility of P in austenite is generally defined by 0.31 mass pct. [18,38] whereas larger differences can be obtained for the fcc+bcc/bcc phase boundary. Lorenz and Fabritius [38] proposed that austenite is stable until 0.66 mass pct. P, the given value of Fischer et al. [39] is around 0.60 mass pct. and indicates a stronger ferrite stabilizing effect of P. In addition, the dependence of the Curie temperature on the P content is shown in **Figure 2 (b)**. The magnetic transition is shifted to lower temperatures with increasing amount of P.

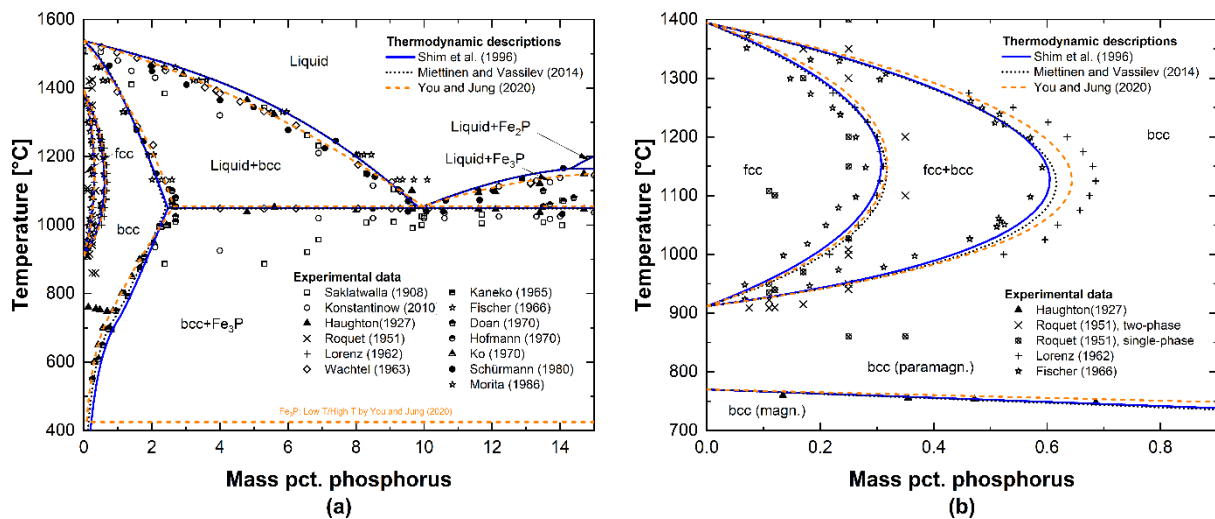


Figure 2: Enlarged Fe-P phase diagram in the Fe-rich part [25–27] along with experimental data of [34–46] (a) and “ γ -loop” in the Fe-P diagram [25–27] compared with data of references [36–39] (b).

2.1.2.2 Phase equilibria in the ternary Fe-C-P system

A lot of attention has been paid to phase equilibria in the ternary Fe-C-P system in foundry research work: The strong segregation tendency of P favors the formation of a low melting eutectic during solidification of cast iron at 955 °C [47], known as “*Steadit*”. The ternary eutectic (Liquid \leftrightarrow fcc + Fe₃C + Fe₃P), if not specifically intended to increase the wear-resistance, is often considered as harmful microstructure constituent in cast iron. [48]

First investigations on the Fe-C-P phase diagram have been carried out by Görens and Döbelstein [49], Wüst [50] and Stead [51]. In 1929, Vogel [52] published various isopleths of the Fe-C-P system obtained from thermal analysis and metallographic examinations. A vertical section with constant carbon content (2.4 mass pct. C) was reported by Ohide and Ohira [53]. Isothermal sections between 800 - 1100 °C and in the composition range of 0 - 3 mass pct. C and 0 - 6 mass pct. P were reconstructed in references [41,46,54,55]. The liquidus projection of the Fe-C-P system is accepted from the experimental investigation of Schürmann et al. [47]. The available experimental data are summarized in **Table 3**. For detailed information on the the composition range investigated by Vogel please see reference [52]. However, similar to the binary Fe-P system the experimental research stopped nearly 30 years ago. It can be seen in **Table 3** that a lack of data exists in the literature for melting equilibria at low phosphorus (P < 0.20%) and carbon content (C < 0.60%). This composition range is of particular relevance for the continuous casting of typical advanced steel grades.

Table 3: Experimental phase diagram data of the Fe-C-P system. Note that for equilibration experiments in references [41,46] the given composition range corresponds to the directly measured analysis of each phase; for reference [54] the initial chemical analysis of the samples is given.

Authors (year)	Experimental technique	Temperature [°C]	Composition [mass pct.]	Ref.
Vogel (1929)	Thermal analysis	700 - 1500	see reference	[52]
Kaneko (1965)	Equilibration	800 - 1000	0.58 - 1 %C, 0.2 - 0.8 %P	[41]
Langenscheid (1970)	Equilibration	900 - 1000	0.09 - 3.52 %C, 0.05 - 5.2 %P	[54]
Hofmann et al. (1970)	Equilibration (Diffusion couples)	600 - 900	0 - 0.60 %C, 0.15 - 1.9 %P	[46]
Ohide and Ohira (1975)	Unidirectional solidification	950 - 1350	2.4 %C, 0.43 - 8 %P	[53]
Schürmann et al. (1984)	Thermal analysis	1100 - 1450	0.10 - 3.45%C, 0.66 - 7.81	[47]

The calculated metastable liquidus projection of the Fe-rich part in the ternary Fe-C-P system [30] is presented in **Figure 3 (a)**; along with the data of Schürmann et al. [47]. At a carbon content lower than 0.6 mass pct., the primary solidifying phase is typically ferrite (bcc); with

increasing amount of C the solidification changes from ferrite type to austenite (fcc) type. Phosphorus slightly influences the primary solidification mode according to the peritectic line [30]: At $P < 6$ mass pct. the univariate line is independent of the P content, only if P exceeds ~ 7 % ferrite is stabilized as the primary phase. The peritectic line ends in the invariant point (IP) U_1 (0.80 %C and 8.55 %P), where Liquid + bcc are in equilibrium with fcc + Fe_3P at a temperature of 1004 °C [47]. The invariant point E_1 at 1.9 %C and 6.75 %P corresponds to the Steadit ternary eutectic equilibrium Liquid \leftrightarrow fcc + Fe_3C + Fe_3P at 955 °C [47].

Section A in **Figure 3 (b)** shows the influence of 0.075 and 0.15 mass pct. P on the peritectic range in the binary Fe-C phase diagram. The three characteristic points c_A , c_B and c_C indicate the change of the phase transformation paths in the peritectic system depending on the C content [56,57]. Left to c_A (0.09 %C) melting/solidification is observed in ferrite structure. Within the “*hypo-peritectic*”, region between the points c_A and c_B (0.17 %C), the final solidification/first melting, coincides with the peritectic phase transformation (Liquid + bcc \leftrightarrow bcc + fcc) and is of special interest for continuous casting of steel: The strong contraction at the final stage of solidification resulting from the transformation of bcc-Fe to fcc-Fe may cause serious problems in the casting process, e.g. breakout and affects the product quality, e.g. crack formation and poor surface quality. [58] In the “*hyper-peritectic*” range of c_B - c_C (0.53 %C) the peritectic transformation is completed during solidification, the further solidification progress takes place in austenite structure. At C contents higher than c_C pure solidification/melting of austenite is observed from the phase diagram. Alloying elements may significantly influence the position of the characteristic points depending on whether they stabilize the ferrite phase (Si, Al, Cr, ...) or austenite (Mn, Ni, ...). However, according to the work of Shim et al. [30] even higher amounts of P (0.15 mass pct.) only slightly shift the hypo-peritectic range of the binary Fe-C system to 0.087 - 0.178 %C. Nevertheless, phosphorus strongly decreases the solidus temperature of ferrite and austenite in the Fe-C diagram. Further, P lowers the peritectic start temperature, decreases the solid state δ/γ -transformation (bcc \leftrightarrow bcc + fcc; bcc + fcc \leftrightarrow fcc) and forms an extended three-phase equilibrium (bcc + fcc + Liquid). All described effects of P on the Fe-C diagram are consistent with the characteristics of the binary Fe-P system in **Chapter 2.1.2.1**.

Section B in **Figure 3 (c)** corresponds to a constant mass pct. ratio of P to C is equal to one and represents a high phosphorus - high carbon section with selected experimental data of references [52,54,55]. Most of the changes in the Fe-C phase diagram are in agreement with section A. It can be seen, that at increased contents of C and P (> 0.75 mass pct.), the Fe_3P and Fe_3C compounds form already during final stage of solidification.

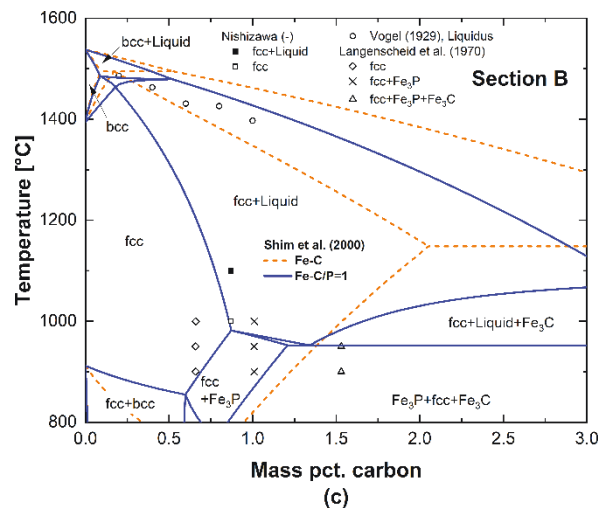
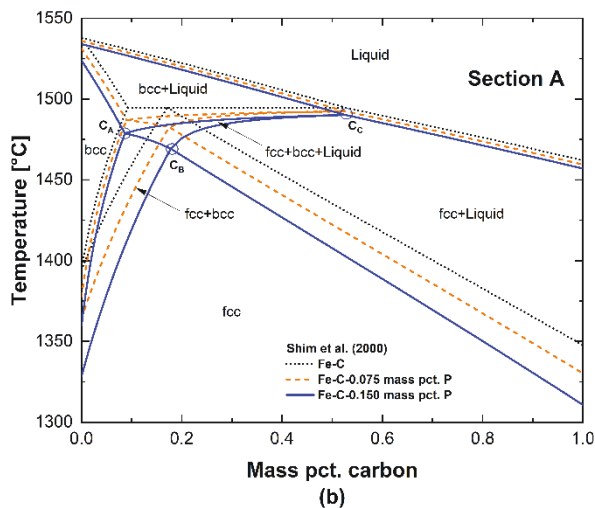
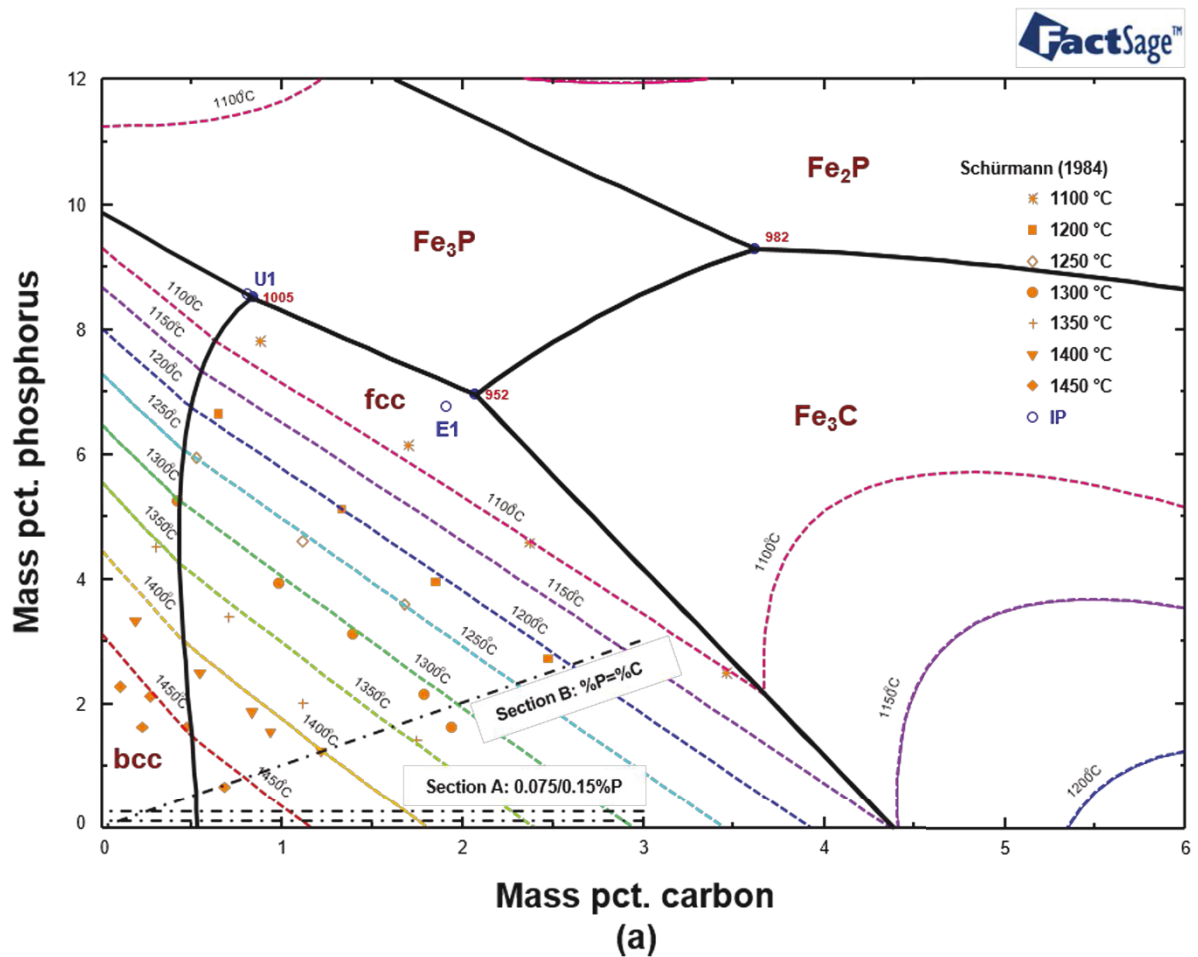


Figure 3: Metastable liquidus projection of the Fe-C-P system in the Fe-rich part [30] along with experimental data of Schürmann et al. [47] (a), calculated vertical section [30] with constant mass pct. ratio of P/C = 1 and experimental data from references [52,54,55] (b) and influence of phosphorus (0.075/0.15 mass pct.) on the peritectic range of the Fe-C diagram [30] (c).

2.1.3 Aspects of continuously casting rephosphorized steel grades

2.1.3.1 Continuous casting and product quality: A brief introduction

In general, continuous casting machines are divided into billet, bloom and slab casters. Billets and blooms are mainly used for long products (e.g. bars/rods and rails/structural shapes) whereas slabs are further processed into flat products (e.g. heavy plates/coils). However, the general process is similar for all caster layouts and is schematically shown for slabs in **Figure 4** [59]. Liquid steel is transported with a defined superheat from secondary metallurgy via ladles to the caster. From the ladle, the liquid steel flows through the ladle shroud into the tundish. The tundish represents an intermediate vessel which guarantees the actual continuity of the process without interrupting the casting sequence. Tundish and mold are interconnected via the submerged entry nozzle (SEN) where the inlet quantity is controlled by a stopper rod. The stopper ensures proper feeding according to the current casting format and casting speed. At the meniscus, close to the top of the water-cooled copper mold, the initial solidification starts. Mold oscillation and the utilization of casting powders ensure sufficient lubrication and control the heat flux in the mold.

When the solidifying shell exits the mold, supporting rolls are required to minimize bulging of the strand due to the ferrostatic pressure caused by the liquid pool inside the solidified shell. The zone ranging from the exit of the mold until the cutting-off point is called secondary cooling zone (SCZ), where the strand surface is intensively cooled by water(-air) spray-nozzles. The SCZ is subcategorized into the bending zone, the curved section and the straightening zone. Bending and straightening transfer the strand from the vertical direction at the exit of the mold to the horizontal direction at the end of the continuous casting machine. Bending and straightening are continuously performed in various points of the caster in order to reduce the occurring strain and strain rates. When the center of the strand is completely solidified the billet/bloom/slab is cut off, according to the desired length for further processing. The distance between the meniscus and the final solidification point is called "*metallurgical length*". The precise knowledge of the metallurgical length is of major importance for the position of a softreduction or final electromagnetic stirrer in order to improve the internal soundness.

During the casting process, significant mechanical stresses are exerted on the solidifying strand resulting from bulging, bending/straightening, thermal gradients, as well as from possible misalignment of the supporting rolls. In combination with the decreased ductility of steel in specific high-temperature regions, the mechanical loads may seriously affect the final product quality with respect to crack formation. Depending on the position, internal and surface cracks are distinguished as shown in **Figure 4**.

The ductility of steel as a function of temperature is plotted in **Figure 5** according to Thomas et al. [60] and Brimacombe [61]. Internal cracks are mainly hot tears and hot tear segregations formed during solidification close to T_s (Region I), see also **Chapter 2.1.3.3**. Surface cracks occur at temperatures within secondary ductility trough (600 °C to 1200 °C [60,62]) and are associated with (i) pinning effects and actions of precipitates at the austenite grain boundaries (Region II and III,) or solid state phase transformations (Region IV and V) in the austenite/ferrite two-phase region. [60] Recently, Krobath et al. [63] emphasized (iii) the relevance of selective grain boundary oxidation on the surface crack formation in the casting process.

In the continuous casting process, higher amounts of phosphorus mainly affect the internal quality due to the strong segregation tendency during solidification. The segregations on microscopic scale may lead to inhomogeneities on macroscopic scale (centerline segregations) and generally increase the hot tearing sensitivity of a steel. Quality relevant issues, with respect to segregations and hot tearing induced by phosphorus, will be now discussed in the following sections.

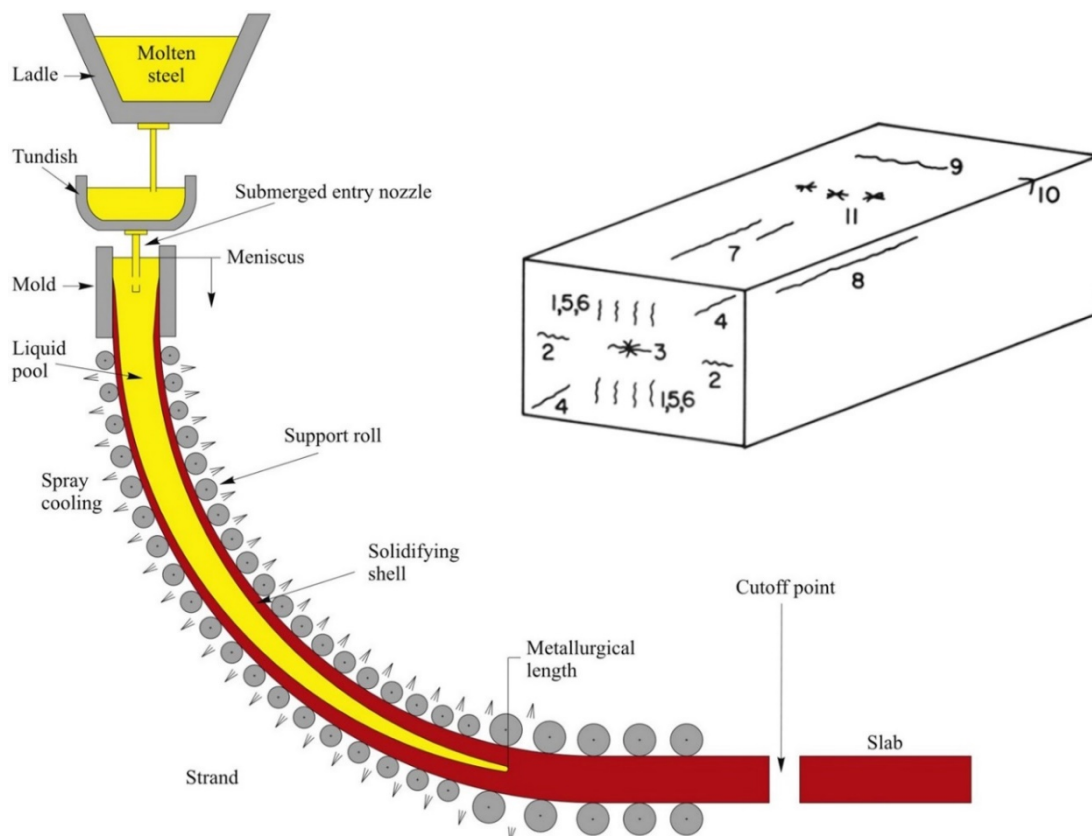


Figure 4: Schematic layout of a continuous slab caster for steel (reprinted by permission from Elsevier [59]) and cracks found in continuously cast steel according to Brimacombe [62]: Internal cracks (1 midway, 2 triple-point, 3 centreline, 4 diagonal, 5 bending/straightening, 6 pinch roll) and surface cracks (7 longitudinal mid-face, 8 longitudinal corner, 9, transverse mid-face, 10 transverse corner, 11 star).

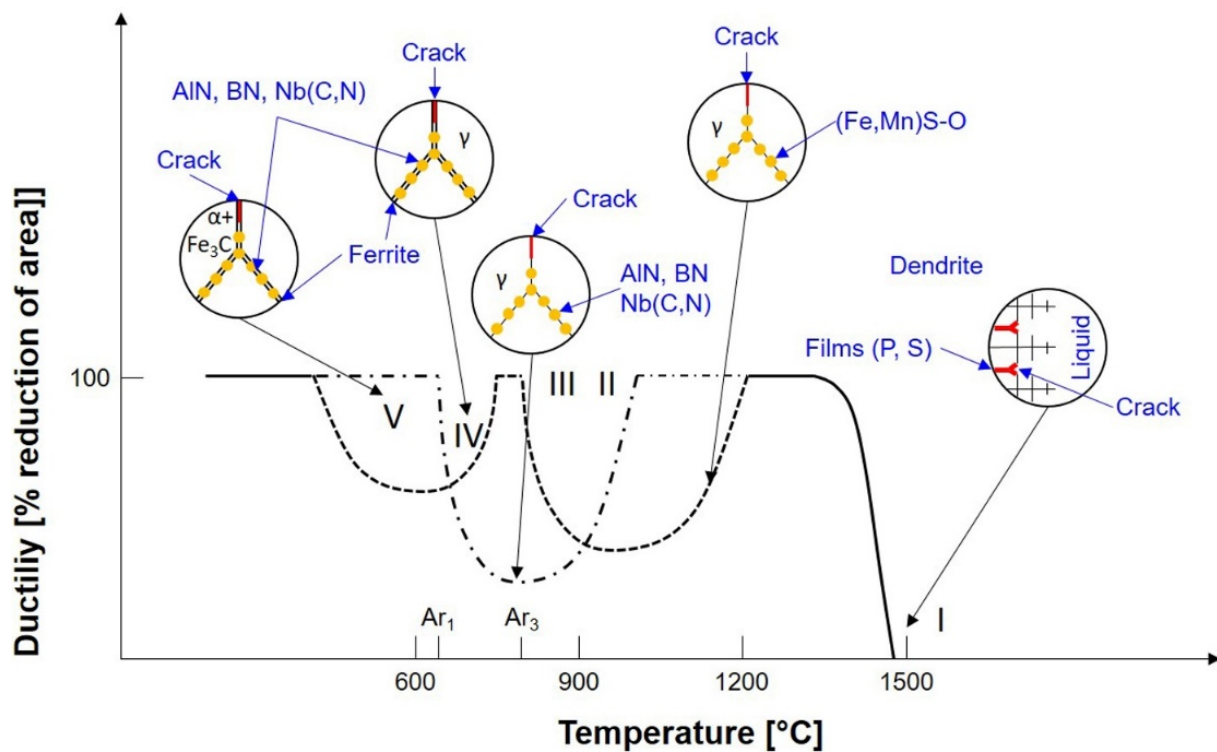


Figure 5: Ductility of steel as a function of temperature, redrawn from the work of Thomas et al. [60] and Brimacombe [61] (adapted by permission from Springer Nature [61]).

2.1.3.2 Segregation of phosphorus on microscopic scale

During solidification of steel, alloying elements show a different solubility in the liquid and the solid phase. In general, the solubility of an element is lower in the solid, leading to an enrichment of the component in the melt. Under equilibrium conditions, the solute redistribution is given by the equilibrium partition coefficient $k = C_S/C_L$, where C_S is the concentration of the component in the solid phase and C_L defines the amount in the liquid phase, respectively. The smaller the ratio of C_S to C_L , the higher is the tendency of the element to segregate in the liquid. The value of k for an element X is closely related to the Fe- X binary phase diagram; its calculation is schematically illustrated in **Figure 6**. The initial concentration C_0 is considered to be 0.30 mass percent. By reaching the liquidus temperature T_L , the first fraction of the solid phase forms. During further cooling, C_S and C_L follow the course of the solidus and liquidus line. Hence, k can be calculated at each temperature from T_L to T_S in the liquid/solid two-phase region. In the present example, k is calculated at $T_1 - T_3$ by 0.34. If both phase boundaries are linear, the value of k is more or less constant over the whole solidification interval. However, in reality k is slightly depending on temperature as all phase diagrams show a certain curvature of the liquidus or solidus line.

In case of solidification in the Fe-C diagram, two separated partition coefficients of an element have to be defined between ferrite/liquid and austenite/liquid. In general, the relation $k^\delta > k^\gamma$ is valid for ferrite stabilizing element and vice versa. [45] Strongly segregating elements in steel are sulphur, boron and also phosphorus. For example, the partition coefficient of S between ferrite/liquid is 0.02 [64] and between austenite/liquid 0.05 [64]. On the other hand, Cr and Ni show a high solubility in Fe and their partition coefficients (k^δ , k^γ) are close to 1 [64].

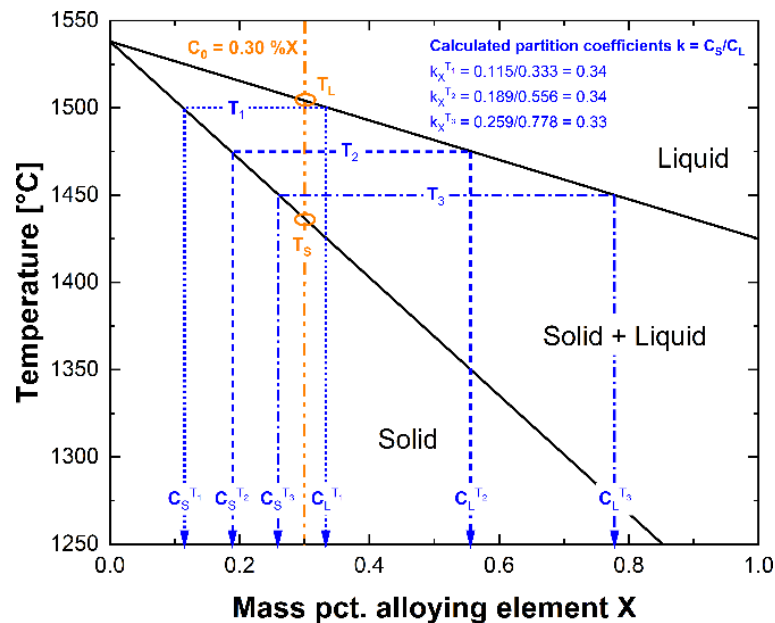


Figure 6: Schematic calculation of the partition coefficient $k = C_S/C_L$ from the phase diagram depending on temperature.

Detailed discussion on the partition coefficient of P was reported in experimental work [45,65–67] and theoretical analysis [68,69]. The topic on partition coefficients was frequently studied using zone melting [70] related techniques. Smith and Rutherford [65] applied floating zone experiments using pre-purified Fe. The suggested value of k_P is in the range 0.20 - 0.50; a further phase diagram analysis resulted in $k_P = 0.27$. Classical zone melting trials were conducted by Fischer et al. [66] and later, by Fischer and Frye [67]. It is evident from the Fe-P phase diagram in **Figure 1**, that during melting/solidification of Fe-P alloys, the liquid phase is in equilibrium with ferrite. Hence, their determined values of $k_P^\delta = 0.18$ [66] and $k_P^\delta = 0.16 \pm 0.04$ [67] are only valid for ferrite/liquid equilibrium and a value for k_P^γ could not be proposed.

Nakamura and Esaka [71] as well as Morita and Tanaka [45] used the equilibration concept in which the coexistence of liquid and solid, a selected experimental temperature results in a separation of P, according to the Fe-P phase diagram. After isothermal holding, the sample was rapidly cooled in a quenching medium to freeze the high-temperature phases. Finally, the chemical composition along the microstructure was determined by analytical methods. In order

to characterize the partition coefficient of P for both phases, ferrite and austenite, the experiments were carried out for Fe-P and Fe-C-P alloys. The addition of carbon leads to the stabilization of γ -Fe in the peritectic range of the Fe-C-P ternary system (**Chapter 2.1.2.2**) and enables the analysis of the P distribution in the γ -Fe/liquid phase equilibrium. Nakamura and Esaka [71] proposed values for $k_{P^\delta} = 0.23$ and $k_{P^\gamma} = 0.13$; the influence of C on the individual values of $k_{P^{\delta,\gamma}}$ was reported to be very small. Morita and Tanaka [45] obtained a constant partition of $k_{P^\delta} = 0.136$ at infinite dilution, but suggested the temperature relation $k_{P^\delta} = 0.643 - 2.80 \times 10^{-4}T$ [K] between 1460 - 1132 °C as their determined value of k_{P^δ} indicated a non-linear decrease of the liquidus and solidus line. In highly C and P alloyed ternary samples with 2.08 - 3.93 mass pct. C and fixed P content of 0.50 mass pct. the partition coefficient k_{P^γ} was measured by 0.09. The value at infinite dilution was thermodynamically recalculated considering the experimental results and finally proposed as $k_{P^\gamma} = 0.06$. Similar to the work of Nakamura and Esaka [71] addition of C seems to have only a minor effect on k_{P^γ} .

In a theoretical work on the metallurgical fundamentals of solidification of steel, Oeters et al. [68] suggested a value of k_P in ferrite of 0.15 - 0.18. Battle and Pehlke [69] thermodynamically derived the partition coefficient of P between ferrite and liquid considering the first consistent description of the Fe-P system by Spencer and Kubaschewski [72]. The partition coefficient for ferrite, with respect to mole fraction, is given by $k_{P^\delta} = -24.90 + 4.808 \times 10^{-2} T$ [K] - $3.018 \times 10^{-5} T^2$ [K] + $0.62 \times 10^{-8} T^3$ [K] and is valid in the temperature range of 1132 - 1538 °C

The literature data are summarized in **Table 4**. The low partition coefficients of phosphorus for ferrite ($k_{P^\delta} = 0.136 - 0.27$) and austenite ($k_{P^\gamma} = 0.06 - 0.13$) indicate that P strongly segregates during solidification of steel. Though the absolute values for k_{P^δ} and k_{P^γ} are slightly different in all publications the ratio of $k_{P^\delta}/k_{P^\gamma} \sim 2$ is nearly constant. As k_{P^δ} is larger than k_{P^γ} , it can be concluded, that the enrichment of P in the melt is enhanced during freezing of austenite.

Table 4: Selected experimental data of the partition coefficient of P for δ -Fe and γ -Fe. [45,65–67,71]

	Smith/Rutherford [65]	Fischer et al. [66]	Fischer/ Frye [67]	Nakamura/Esaka [71]	Morita/Tanaka [45]
k_{P^δ}	0.2 - 0.5 ¹⁾ 0.27 ²⁾	0.18	0.16 ± 0.04	0.23	0.136 ³⁾ 0.153 - 0.242 ⁴⁾
k_{P^γ}	-	-	-	0.13	0.06 ³⁾

¹⁾ experiment; ²⁾ phase diagram analysis; ³⁾ infinite dilution; ⁴⁾ 2.31 - 8.99 mass pct. P

In equilibrium solidification, the concentration of an alloying element in the liquid phase (C_L) can be calculated from the initial concentration (C_0) by the Lever-Rule (**Equation 1**).

$$C_L = C_0 [1 - f_s(1 - k)]^{-1} \quad (1)$$

Here, f_s denotes the solid fraction which continuously increases from 0 at T_L to 1 at T_S . Using the partition coefficients in **Table 4**, the calculated enrichment of P in the liquid phase is plotted in **Figure 7** for $C_0 = 0.10$ %P. Depending on the used value for k_P , the concentration of phosphorus at the final stage of solidification varies between 0.37 - 0.73 %P for ferrite and may even exceed values of 1.6 %P in case of austenite. However, as infinite time for complete diffusion equalization is considered in the Lever-Rule, the concentration gradients will be reduced to C_0 again in the complete solid state.

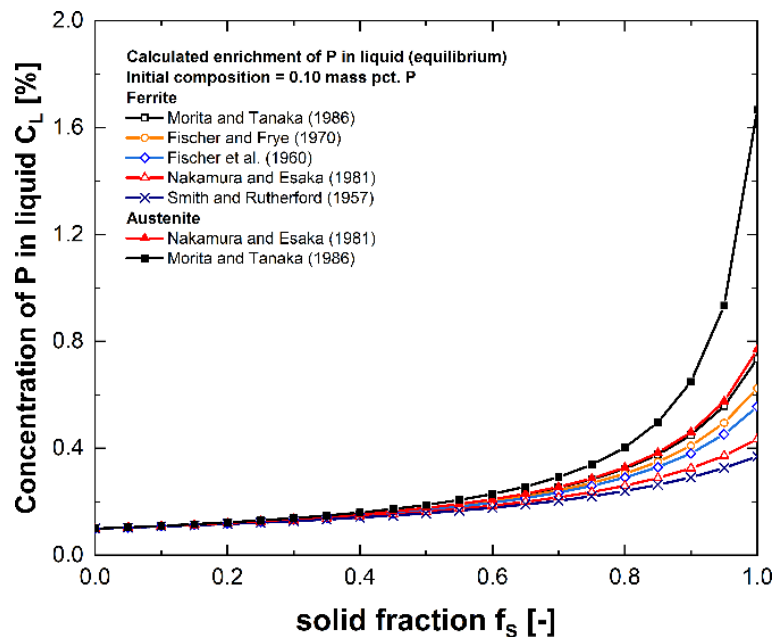


Figure 7: Calculated enrichment of P in the liquid phase during solidification in ferrite and austenite structure (equilibrium conditions).

In continuous casting of steel, the diffusion of alloying elements is limited due to the finite process time. As a consequence, solidification takes place under non-equilibrium conditions leading to an interdendritic accumulation of alloying elements higher than predicted by the Lever-Rule. This phenomenon is known as *microsegregation*, where chemical inhomogeneities still exist along the dendritic microstructure; even after the solidification is completed. The typical appearance of C, Mn and P microsegregation in a continuously cast slab (800 mm width x 100 mm thickness) is shown in **Figure 8** [73]. The concentration was measured by electron probe microanalysis (EPMA) and the addition of 0.01, 0.097 and 0.197 % P to the basic alloying concept of 0.10%C, 0.16 %Si, 0.60 %Mn and 0.003 %S was studied.

The samples were taken from the center of the wide face at a quarter thickness (25 mm). The enrichment of Mn and P optically visualizes the primary dendritic microstructure: The depleted zones correspond to the axis of the dendrites, the enriched parts with high concentrations of Mn and P to the interdendritic spaces last to solidify. The maximum content of phosphorus detected for the 0.097 %P steel grade is 0.50 %. The absolute segregation level raises with increasing amount of P (0.197 mass pct.) and favors the formation of phosphides (indicated by the small dots with very high P content). Further, the interaction between Mn and P segregation is clearly visible in **Figure 8**. At low P content (0.01 %), the Mn segregation line is strongly pronounced, whereas in case of 0.097 %P and 0.197 %P, manganese is finely dispersed and forms MnS inclusions. This effect may be assigned to (i) the MnS formation, which reduces the Mn concentration intensities in the interdendritic regions and (ii) the stabilization of ferrite by adding phosphorus results in a possible change in the phase transformation sequence and a different segregation behaviour. [73]

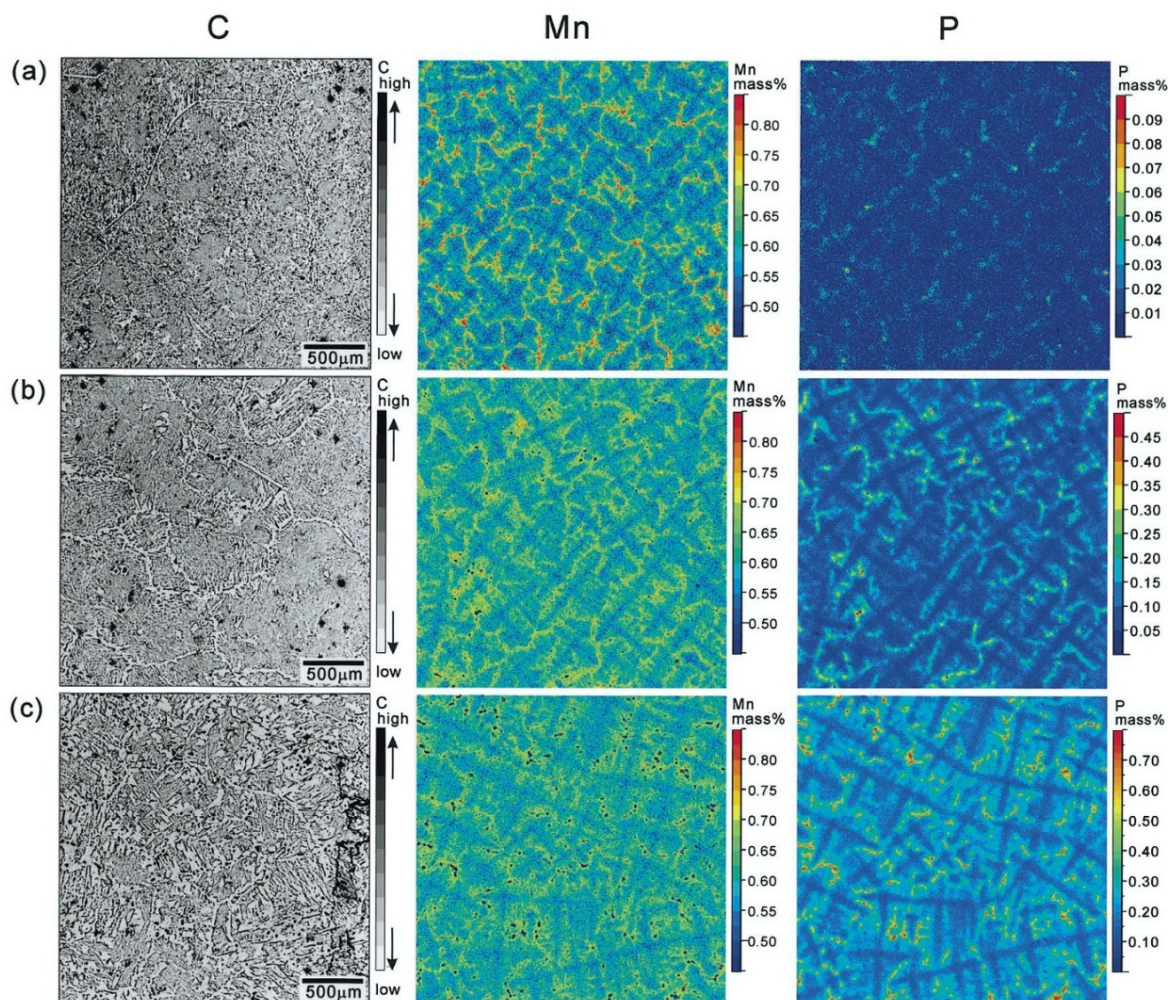


Figure 8: EPMA mapping of microsegregation of a continuously casted slab with basic composition of 0.10 %C, 0.16 %Si, 0.60 %Mn and 0.003 %S. The intensity of C is given in arbitrary unit, the concentrations of Mn and P in mass pct. (a) 0.01 %P, (b) 0.097 %P and (c) 0.197 %P. [73]

In the past, various mathematical approaches of microsegregation modelling have been postulated in the literature, e.g. [74–80]. The most popular analytical equation is the well known Gulliver-Scheil model [74,75]; given in the original form in **Equation 2**. This equation assumes infinite diffusion in the liquid phase, but negligible diffusion in the solid state. For steel, the application of the Gulliver-Scheil equation is limited, as interstitially dissolved carbon and nitrogen are fast diffusing elements in the solid. The model was therefore modified in several research work of Kozeschnik et al. [81,82] and Chen and Sundman [83] in terms of “*partial equilibrium*” considering thermodynamic equilibrium conditions for C and N, but no diffusion for substitutional elements, e.g. Si, Mn, P and S.

$$C_L = C_0[1 - f_S]^{(k-1)} \quad (2)$$

In other models, the general concept of “*back-diffusion*” was introduced [76–78] where the solute redistribution is described by (i) the local cooling conditions, or cooling rates T' , (ii) the morphology of the dendrites, (iii) the coarsening of dendrites during solidification, (iv) the diffusivity of the alloying elements and (v) thermodynamic equilibrium at the solid/liquid interface defined by the partition coefficient. The solidification parameters are connected in the dimensionless Fourier-Number α in **Equation 3**,

$$\alpha = \frac{D_S t_f}{L^2} = \frac{4D_S t_f}{\lambda_2^2} \quad (3)$$

where D_S is the diffusion coefficient of the alloying element and t_f is the local solidification time given by $(T_L - T_S)/T'$. The characteristic diffusion length is defined by the half of the secondary dendrite arm spacing (λ_2). According to Ohnaka [78], the concentration in the liquid phase can be calculated using **Equation 4**,

$$C_L = C_0[1 - \Gamma f_S]^{(k-1)/\Gamma} \quad (4)$$

where Γ is defined by **Equation 5** as

$$\Gamma = 1 - \beta k / (1 + \beta k) \quad (5)$$

The backdiffusion parameter $\beta = 2\alpha$ is valid for a plate-like shape of the dendrites whereas for columnar dendritic growth $\beta = 4\alpha$ is applied. The Ohnaka model reduces the Lever-Rule if $\alpha \rightarrow \infty$ and is equal to the Gulliver-Scheil equation if $\alpha \rightarrow 0$.

In the following sections, all illustrating microsegregation calculations were performed using the model published in **Paper V (Chapter 4.4)** taking the example of the 0.10%C-0.16%Si-0.60%-0.003%S alloying concept in **Figure 8** [73] as a reference.

In **Figure 9**, the calculated P-enrichments during solidification of the 0.10%C-0.16%Si-0.60%-0.003%S-P steels are graphically represented using the Lever-Rule and the modified Ohnaka equation [84]. In the microsegregation model, a cooling rate of 1 °C/s was assumed. Less difference between both equations is obtained for the low-P concept (0.01%P). The concentration of P at $f_s = 1$ in equilibrium solidification is 0.0623 % and slightly increases to 0.0912 % by defining a cooling rate of 1 °C/s. However, for the rephosphorized steel concepts with 0.097 %P and 0.197 %P, clear deviations are observed between both equations: Considering the solidification kinetics, the P content at the final stage of solidification is nearly doubled and exceeds 1 % for $C_0 = 0.097$ % and 2.5 % for initial P content of 0.197 %. Compared with the experimental data in **Figure 8**, the calculated values of the P enrichment are significantly higher. However, it is challenging to quantify the real microsegregation concentration in the solidifying shell due to the high diffusion rate in the solid during further cooling from solidus to ambient temperature. [85] Hence, the actual segregation of P may significantly exceed the measured value from the casting machine.

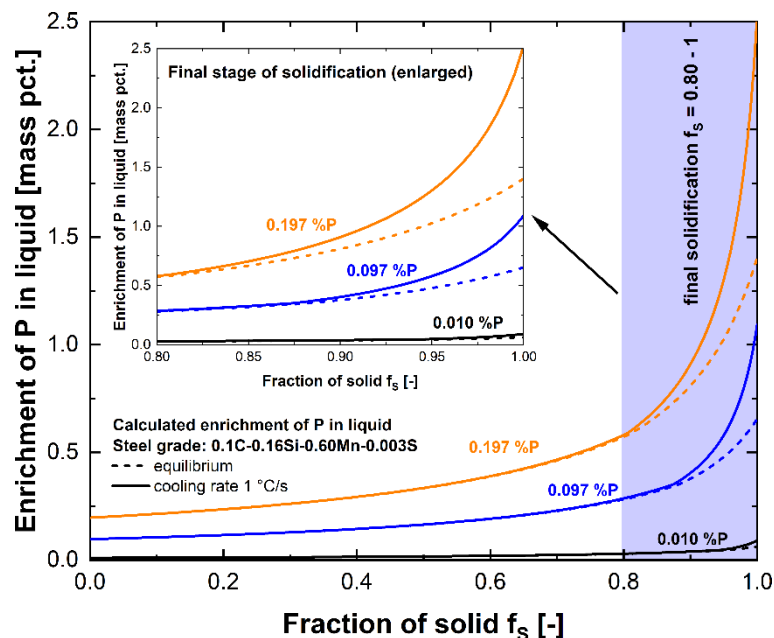


Figure 9: Enrichment of phosphorus in interdendritic liquid for a 0.10%C-0.16%Si-0.60%Mn-0.003%S steel with different initial P content (0.01, 0.097 and 0.197 %P).

The influence of the carbon content on the segregation tendency of phosphorus is shown in **Figure 10 (a)**. The calculations were performed for the three 0.16%Si-0.60%Mn-0.003%S-P steels [73] as well as for a Fe-C-0.04%P alloy for comparison with the work of Wolf and Kurz [85]. For all alloys, the plot in **Figure 10 (a)** indicates a similar trendline of the P-segregation: At higher amounts of C the enrichment of phosphorus at final stage of solidification is much more pronounced than in the low-C region. This fact may be explained by the reasons:

- **Solidification sequence:** Left to c_A , freezing of ferrite takes place; whereas right to c_A , the solidification during the peritectic reaction is controlled by austenite [84,86]. According to **Table 4**, the lower value of k_P^γ compared to k_P^δ leads to an abrupt increase of the P-enrichment close to c_A . Further increase of carbon favors the complete change to the γ -Fe type solidification.
- **Diffusion and solidification temperatures:** In contrast to interstitial elements, like carbon, P is a slowly diffusing element in steel, see **Figure 10 (b)**. In the body centered cubic crystal lattice of δ -Fe, phosphorus shows a significantly higher mobility than in the face centered cubic γ -Fe phase. Hence, the P-microsegregation is further intensified if γ -Fe is stable during solidification. At $C > 0.20$ mass pct. the enrichment of P continuously raises due to the lower solidification temperatures and the temperature dependence of the diffusion coefficient itself.

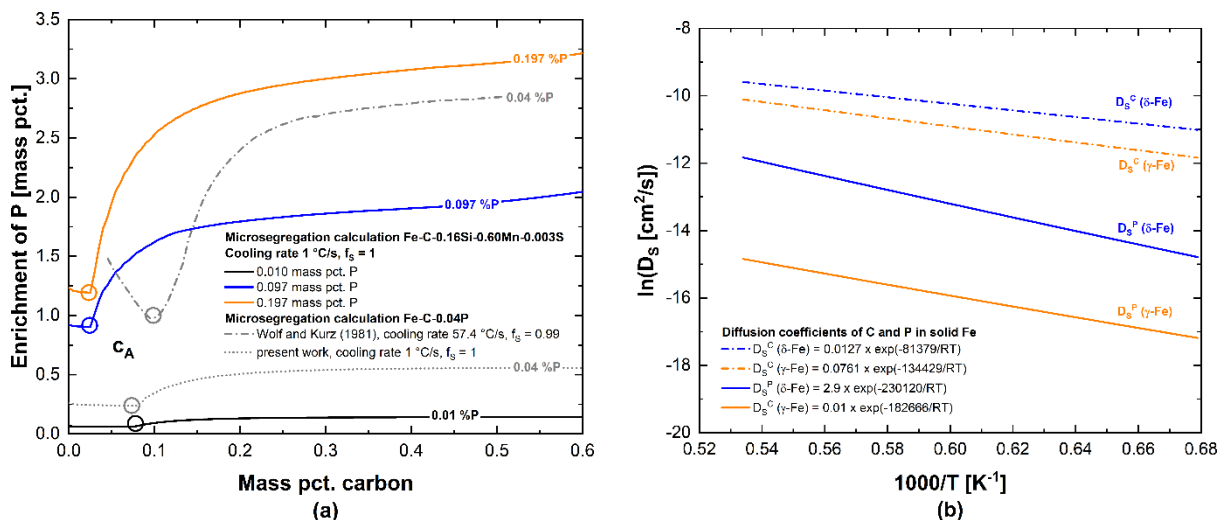


Figure 10: Influence of carbon content on the enrichment of phosphorus in a 0.16%Si-0.60%Mn-0.003%S steel with different initial content of P (0.01, 0.097 and 0.197 %P) and for a Fe-C-0.04%P alloy in comparison with calculation of Wolf and Kurz [85] (a). Diffusion coefficients of C and P in austenite and ferrite depending on temperature taken from the work of Ueshima et al. [79] (b).

Until this point, microsegregation was discussed only from a viewpoint of the interdendritic enrichment itself and the change of the chemical concentration during solidification. However, the enhanced segregation tendency of phosphorus under non-equilibrium conditions leads also to a drop of the real solidus temperature, shown in **Figure 11 (a)**. Taking again the example of the 0.10%C-0.16%Si-0.60%Mn-0.003%S-P steels [73], the calculated values of T_S (Lever-Rule) and T_S (1 °C/s) are represented in **Figure 11 (b)**. In case of the low-P concept (0.01%P) both temperatures are nearly identical ($\Delta T_S = 3$ °C) but for the rephosphorized steels ΔT_S exceeds 30 °C (0.097%P) or even 40 °C for the 0.197%P steel. Hence, microsegregation

phenomena can not be ignored in accurate solidification modelling of highly P-alloyed steel grades and play an important role in the theory of hot tear formation as will be explained in the next chapter.

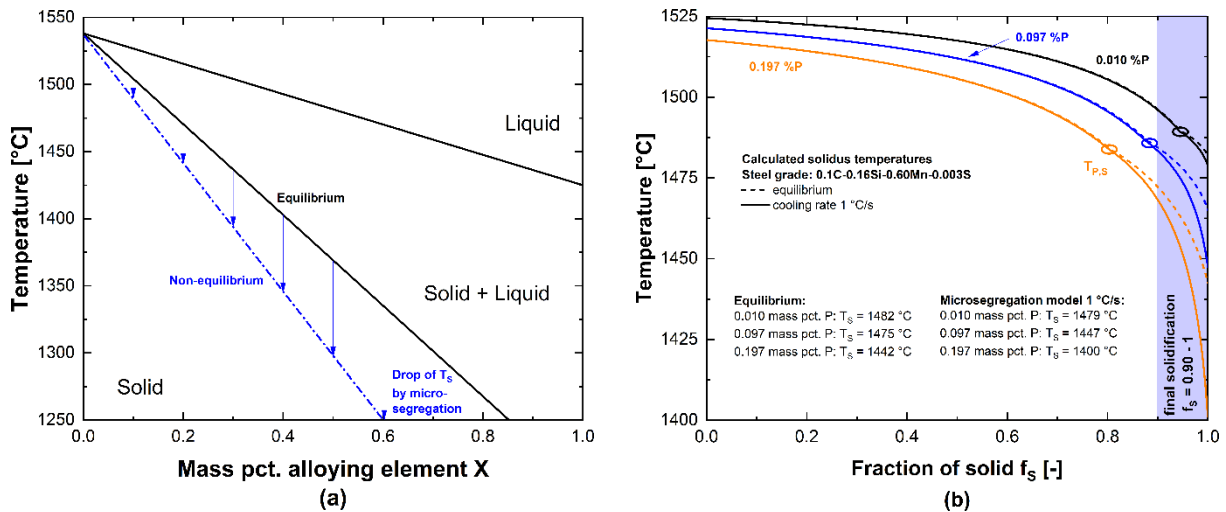


Figure 11: Schematic representation of the influence of microsegregation (non-equilibrium conditions) on the real solidus temperature of an alloy (a) and difference of T_s calculated with the Lever-Rule and the modified Ohnaka equation [84] for the 0.10%C-0.16%Si-0.60%Mn-0.003%S steel grade in reference [73] (b).

2.1.3.3 Influence of phosphorus on hot tear formation

The term “hot tear” (HT) summarizes cracks which are formed during solidification of steel along the interdendritic paths and the primary grain boundaries. According to C. Bernhard [87], hot tears in the continuous casting process occur due to an overcritical amount of tensile strain in perpendicular direction to the solidifying dendritic microstructure. A precondition for the HT initiation is a columnar dendritic morphology; whereas coarse equiaxed grains increase the resistance to further hot tear propagation. [88]

In the present work, the mechanism of hot tearing in steel is briefly explained based on Pellini’s popular “Strain theory of hot tearing” [89] in **Figure 12 (a)**. In general, this theory correlates the phenomenon of hot tearing with microsegregation processes close to the non-equilibrium solidus temperature. At very high solid fraction, the solidifying steel reaches the film stage, where small fractions of residual liquid are still present along the primary grain boundaries. The hot tear sensitivity is directly influenced by the amount of strain which is initiated at the film stage. This means that a high strain rate resulting from the mechanical stresses as well as a long life time of the films will increase the hot tear sensitivity. The strain rate depends on the casting process parameters (secondary cooling, casting speed, ...) whereas the existence of liquid films is strongly influenced by the chemical composition. As shown in the previous

Chapter 2.1.3.2, the presence of phosphorus leads to a drop of T_S and a stabilization of segregated films below the equilibrium solidus temperature. As a consequence, the life time of the films is largely increased. If the accumulated strain at the film stage is close to a critical value, pre-stages of hot tears, so called “*hot tear segregations*” (HTS) are formed. With increasing strain, the coalescence of pores may lead to open hot tears. **Figure 12 (b)** exemplarily shows concentration mappings of the defect pattern of HTS and HTS with initial pore formation. The micrographs were taken from internal research at the Chair of Ferrous Metallurgy (Montanuniversitaet Leoben) using an in-situ hot tensile test during solidification. The results were partly published by Reiter et al. [90,91] using EPMA.

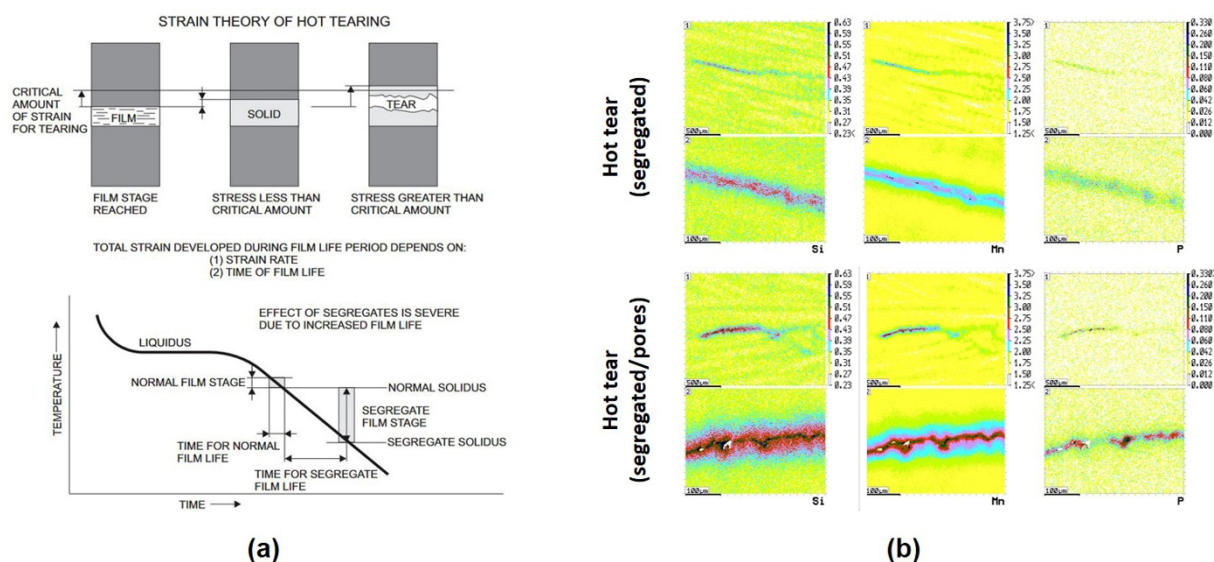


Figure 12: Strain theory of hot tearing according to Pellini [89] (a); the figure was taken from the work of Pierer [88]. Concentration mappings of Si, Mn and P close to/within hot tear segregations obtained in an in-situ hot tensile test at laboratory scale using EPMA (b) the figure was created from internal research at the Chair of Ferrous Metallurgy, Montanuniversitaet Leoben; partly published by Reiter et al. [90,91].

Pierer [88] defined the temperature range ΔT_{SA} , within which the liquid films are able to accumulate the tensile strain, between $f_S = 0.96$ and $f_S = 1$. The influence of phosphorus on ΔT_{SA} of the 0.10%C-0.16%Si-0.60%Mn-0.003%S-P steels [73] is plotted in **Figure 13** as a function of the C content. Again, additional calculations for a Fe-C-0.04%P alloy are qualitatively compared with the results of Wolf and Kurz [85]. The high value of ΔT_{SA} of P-containing high carbon steels represents a main aspect for the higher HT/HTS sensitivity compared to steels with low amount of C. [85,92,93] At a fixed carbon content of 0.10%C, ΔT_{SA} in **Figure 13** raises from 9 °C in the low P-concept (0.01 %P) to a maximum value of 45 °C in case of $C_0 = 0.197$ %P. Considering typical continuous slab casting conditions with a cooling rate of 1 °C/s and a casting speed of 1.2 m/min, the critical temperature range exists for 9 s

and 45 s, respectively, and may accumulate tensile strains over a distance of 0.18 m (0.01 %P) and 0.90 m (0.197 %P) in the casting machine. Hence, even at low amount of 0.10 %C, the distance of strain accumulation is more than five times higher in casting rephosphorized steel grades.

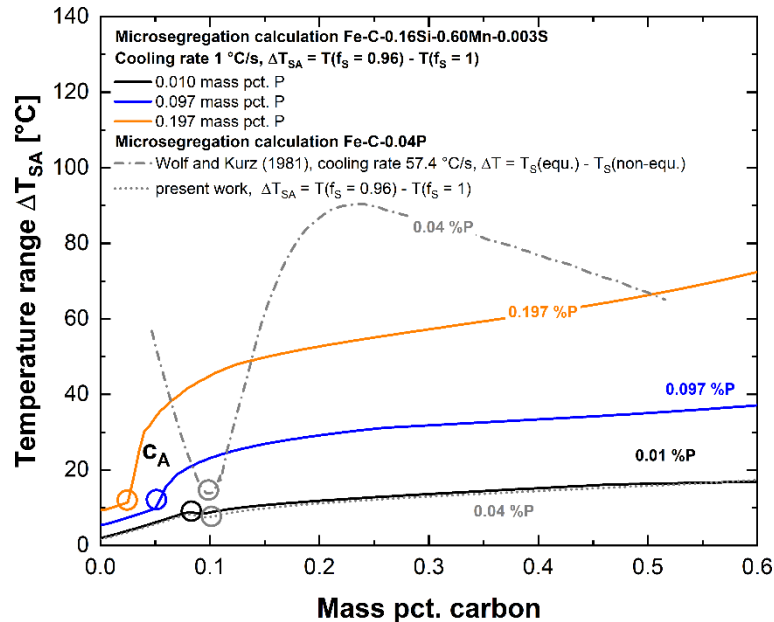


Figure 13: Influence of phosphorus on the critical temperature range of hot tearing depending on the carbon content. Case 1: 0.10%C-0.16%Si-0.60%Mn-0.003%S. Case 2: Fe-C-0.04%P along with calculations of Wolf and Kurz [85].

2.2 Computer coupling of phase diagrams and thermochemistry

The following sections deal with the fundamentals of computational thermodynamics. The first part demonstrates the CALPHAD-type optimization procedure of binary and ternary systems and highlights the key issues in developing thermodynamic databases for multicomponent alloys. The second part summarizes the mathematical formulations of the Gibbs-energy equations for solutions and compounds, which were used in the framework of developing databases for the Fe-P and Fe-C-P systems in previous work and the present study. Finally, selected applications of a CALPHAD-based software to the continuous casting process will be presented.

2.2.1 Computational thermodynamics: The CALPHAD approach

New innovations in recent steel design and the successful control of advanced steelmaking processes require accurate thermodynamic data: In the past decades, extensive experimental research of phase diagrams, phase transformations and thermodynamic properties in multicomponent steel alloys has been carried out. Experiments - on laboratory or industrial scale - are the key for developing a fundamental understanding of the material behavior under real process conditions. However, experiments are time consuming and cost-intensive and reliable data are often available only in limited alloying ranges. With the advances in the computer technology, the idea of computer aided thermodynamic calculations was therefore born. 50 years ago, Kaufmann and Bernstein [94] introduced the CALPHAD (CALculation of PHase Diagrams) approach; originally intended to perform phase diagram calculations. Nowadays, this concept is widely used in the field of Integrated Computational Materials Engineering (ICME) [95–97] enabling the calculation of a large variety of data, involving phase equilibria, chemical activities and calorimetric functions (H , C_P , ...), from a self-consistent set of Gibbs energy parameters of the alloying system. [98] These model parameters (see **Chapter 2.2.2**) are typically stored in thermodynamic database files. The great advantage of CALPHAD-type databases is their possible extrapolation to higher-order multicomponent systems as well as to provide detailed information on thermodynamic properties and phase equilibria over the whole composition range of steel. For that purpose, various commercial thermochemical software packages with comprehensive databases are available, e.g. FactSage [28], MatCalc [99], MTDATA [100], Pandat [101] and ThermoCalc [102]. Recently, OpenCalphad [103] and PyCalphad [104] were developed in the framework of open-source software projects. Due to the general nature of the CALPHAD method, the terms “*computational thermodynamics*” or “*computational thermochemistry*” were established. [98,105]

For schematic illustration, the development of a CALPHAD-type database for five components is graphically represented in **Figure 14**. [105–108]. Typically, one begins with the implementation of the Gibbs energy descriptions of the pure components which are listed as functions of temperature and pressure in the work of Dinsdale [109]. These data are universally accepted in the scientific community and considered as standard reference data for the unary phases. The actual database work starts by modelling binary, ternary and rarely, quaternary subsystems. This procedure is known as “*assessment*” or “*optimization*” of the phase diagram, meaning more or less, that the Gibbs energy model parameters of the stable phases are adjusted with respect to the available experimental data. The number of constituent subsystems which have to be considered in the optimization of an n-component system is

defined by the binomial coefficient $\binom{n}{k}$ where k is the number of components in the subsystems. [110] Hence, a database for five components consists of ten binary, ten ternary and five quaternary systems. It is evident that the number of subsystems rapidly increases with the amount of components in the system, e.g. 45 binaries, 120 ternaries and 210 quaternaries in the presence of ten components. However, alloying elements are often added in very small amounts or are present only as trace element. In this case, accurate thermodynamic description in the multicomponent system can be achieved by including only the contribution of the binary phase diagram. Further, the most dominating element in steel is Fe; in order to develop a database for steel, it is sufficient to only consider ternary systems with Fe as a component. As a consequence, the required thermodynamic assessments are significantly reduced, if the alloy is mainly based on one specific component. Quaternary terms are rarely included as (i) their effect on calculations in multicomponent systems is mostly small and (ii) a large number of higher-order parameters typically indicate that the thermodynamic model is not well suited for describing the phase.

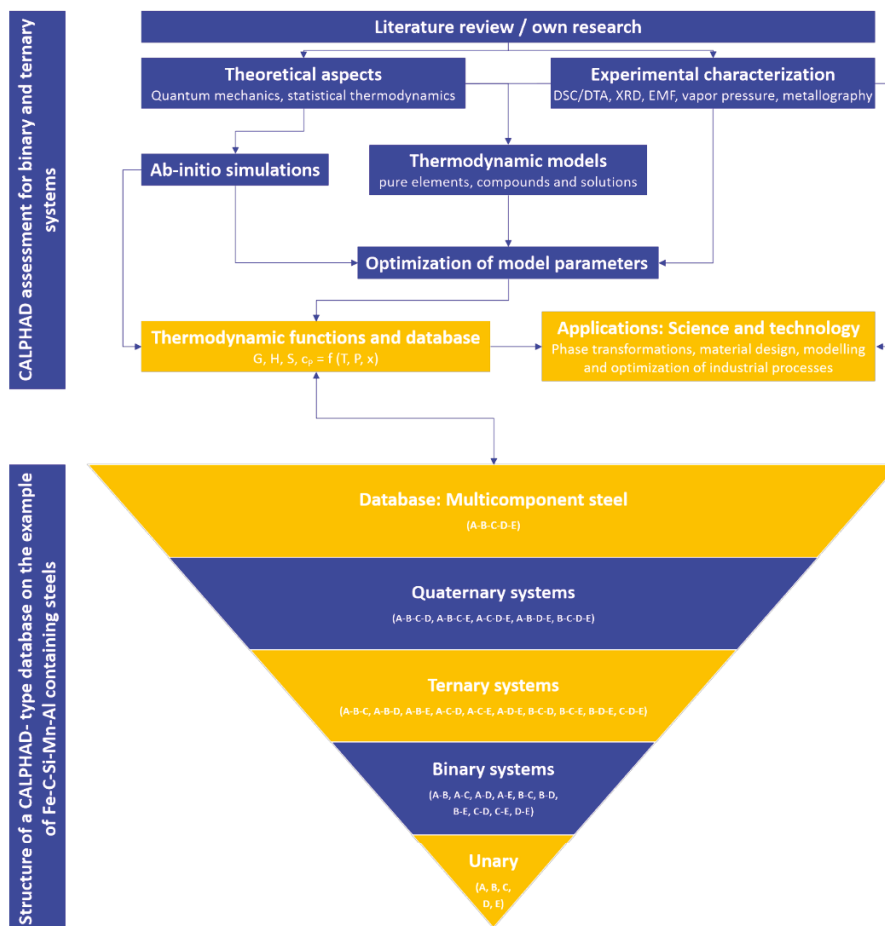


Figure 14: Schematic illustration of the CALPHAD approach to assess phase diagrams and the development of CALPHAD-type databases; according to National Institute of Standards and Technology (NIST) [106], Scientific Group Thermodata Europe (SGTE) [107] and references [105, 108].

The classical way of assessing a binary or ternary system can be summarized as follows [111].

Part I (Literature study): The optimization starts with the literature survey of all available crystallographic information and experimental data. There exist a large number of techniques to study phase diagrams and thermodynamic relations in alloys, e.g. thermal analysis and metallography to identify phase stabilities, or, on the other hand, galvanic cells and vapor pressure measurements to obtain chemical potential data. The first part builds the most crucial step in developing a high quality database as the final calculation results will strongly depend on the underlying experimental datasets. Hence, one has to critically evaluate the data concerning reliability. To this, Kattner [112] pointed out the following criteria:

- Purity of the starting materials and sample preparation,
- reactions of the sample with the environment (evaporation, reaction with the crucible),
- quality of the reference sample and the calibration of the instruments used,
- analysis of the results and accurate documentation (numerical values and error bars) and
- use of originally measured data only; derived data may include errors due to interpretation or conversion. [113]

Besides experiments, computational results obtained from first-principle quantum mechanics based on the density functional theory (DFT) have been frequently implemented in the CALPHAD approach [114–116]. DFT data are often used to describe enthalpies of formation of end-members in the compound energy formulation (CEF) model (**Chapter 2.2.2**). Such enthalpy values are generally hypothetical and cannot be validated experimentally.

Part II (Selection of thermodynamic models): Experimental information and crystal structure data enable a proper selection of the thermodynamic model for each phase. In general, the description should be kept as simple as possible but it has to be noted that the more suitable the model choice, the more accurate is the extrapolation to higher-order systems. [111]

Part III (Optimization of the model parameters): It is evident that for hundreds of experimental data, the manual optimization by trial-and-error procedure means often great work effort and requires high expertise in selecting the relevant parameter sets. For complex systems and a high number of experimental data various programs were developed in the scientific community based on least-square methods [117], Levenberg-Marquardt method [118] or Bayesian estimation approach [119]. [110] The most important software tools are BINGSS [105,120], ESPEI [121], OptiSage [28] and the PARROT module [105,122].

Part IV (Database management): By storing all Gibbs energy parameters in the database file, several thousands of lines are created. In order to guarantee a detailed overview of the used sources, a precise documentation has to be included in the data file. Within updating the

database with new thermodynamic information, one has to consider the influence of a selected subsystem on the thermodynamic description of the multicomponent system. For example, if a binary phase diagram A-B is updated, the adjustment will influence all other ternary systems containing the A-B system.

Part V (Applications in science and technology): A recent review on the way from database development to virtual steelmaking process simulations (e.g. dephosphorization of hot metal in the basic oxygen furnace, degassing processes and reoxidation in the continuous casting process) using the FactSage thermochemical software [28] was given by Jung and van Ende [123]. With respect to continuous casting, the MatCalc tool [99] provides a large variety of options to predict precipitation formation in the solid state in processing of micro-alloyed steels [124–126]. An application of a CALPHAD-based software to solidification simulation and quality prediction in the continuous casting process is also content of **Chapter 2.2.3**.

2.2.2 Thermodynamic modelling of solutions

The general form of the Gibbs energy G of a phase θ per mole of components (subscript m) is given by **Equation 6** [105,127],

$$G_m^\theta = G_m^{\theta,\text{srf}} + G_m^{\theta,\text{phys}} - TS_m^{\theta,\text{conf}} + G_m^{\theta,\text{E}} \quad (6)$$

where $G_m^{\theta,\text{srf}} = x_i G_i^\circ$ is the “*surface*” Gibbs energy representing the mechanical mixture of the pure components in the phase; $x_i = n_i/n$ is the mole fraction of the component i . $G_m^{\theta,\text{phys}}$ is the contribution to the Gibbs energy by other physical phenomena, e.g. the magnetic transition in Fe [105]. The configurational entropy $S_m^{\theta,\text{conf}}$ of a phase, results from statistical thermodynamics and defines the possible positions of the constituents in the phase according to the Boltzmann equation $S = R/N_A \ln(W)$. Using Stirling’s formula the configurational entropy is expressed as $S = -R \sum x_i \ln x_i$. [105] The term $G_m^{\theta,\text{E}}$ is the excess Gibbs energy and corresponds, more or less, to the difference between the real Gibbs energy and the summation of the first three parts. [105,128]

The excess term $G_m^{\theta,\text{E}}$ is the actual parameter optimized in the CALPHAD-type thermodynamic assessments of phase diagrams. In general, the more accurate the model selection for a phase, the less excess parameters will be required to guarantee accurate calculation results. The various thermodynamic models used in modelling work of the Fe-P and Fe-C-P systems will be explained in the following sections.

2.2.2.1 Gibbs-energy of pure elements and stoichiometric compounds

Pure elements and stoichiometric compounds (STCO) are phases with a fixed composition over their whole stability range. The Gibbs energy is therefore not depending on the composition, but on temperature and pressure. However, in thermodynamic modelling of steel alloys, the pressure is typically considered to be equal to the atmospheric pressure and is kept constant at 1 atm. The Gibbs energies of pure elements and STCO are of frequently formulated as a power series in temperature as given in **Equation 7** [105]

$$G_m - \sum_i b_i H_i^{\text{SER}} = a_0 + a_1 T + a_2 T \ln(T) + a_3 T^2 + a_4 T^{-2} + a_5 T^3 + \dots \quad (7)$$

Here, b_i is the stoichiometric coefficient of a component i in the phase θ . As the Gibbs energy is typically referenced to a standard state of 298.15 K (25 °C) and 1 bar, the sum $\sum_i b_i H_i^{\text{SER}}$ introduces the enthalpies in the “*standard element reference (SER) state*”. The Gibbs energies of pure elements as function of temperature (and pressure) and in various stable crystal structures are summarized in the classic work of Dinsdale [109].

A vast number of calorimetric studies on STCO is available from literature for Fe-based systems. The experimental data generally include (i) the enthalpy of formation of the compounds (ΔH_f) at selected temperatures, (ii) the heat capacities c_p depending on temperatures and (iii) the Gibbs energies of formation ΔG_f derived from measurements of chemical reactions, e.g. vapor pressure measurements by Knudsen effusion cells [129]. In modelling the Gibbs energy of STCO, the data can be directly used according to **Equation 8** considering the typical occurring experimental errors.

$$G_m = \Delta H_{298.15}^f + \int_{298.15}^T c_p dT - T \left[S_{298.15} + \int_{298.15}^T (c_p/T) dT \right] \quad (8)$$

$\Delta H_{298.15}^f$ is the standard enthalpy of formation at 298.15 K (25 °C), c_p the heat capacity over temperature and $S_{298.15}$ the standard entropy at 25 °C.

2.2.2.2 Bragg-Williams (BW) model and compound-energy formalism (CEF)

The single-lattice Bragg-Williams (BW) model assumes random mixing of the components in the unit cell and hence the probability of occupying the sites is identical for all components. The Gibbs energy for a multicomponent system is given by **Equation 9**

$$G_m = \sum_{i=1}^n x_i G_i^\circ + RT \sum_{i=1}^n x_i \ln(x_i) + G_m^E + G_m^{\text{phys}} \quad (9)$$

In the substitutional solution, the excess Gibbs energy is directly linked to the possible interaction of the components. Hence, in a binary solution, the G_m^E term is depending on the respective mole fractions, given by **Equation 10**

$$G_m^E = \sum_{i=1}^{n-1} \sum_{j=i+1}^n x_i x_j L_{ij} \quad (10)$$

L_{ij} are the binary Redlich-Kister polynomials [130], see following **Equation 11**:

$$L_{ij} = \sum_{v=0}^k (x_i - x_j)^v {}^vL_{ij} \quad (11)$$

where ${}^vL_{ij}$ is linearly depending on T (**Equation 12**):

$${}^vL_{ij} = {}^va_{ij} + {}^vb_{ij}T \quad (12)$$

Similar applies for the ternary interaction terms in **Equation 13** [105]

$$G_m^E = \sum_{i=1}^{n-2} \sum_{j=i+1}^{n-1} \sum_{k=j+1}^n x_i x_j x_k L_{ijk} \quad (13)$$

with the composition dependent ternary excess parameters, as for example suggested by Hillert [131] in **Equation 14 (a) - (b)**:

$$L_{ijk} = v_i {}^iL_{ijk} + v_j {}^jL_{ijk} + v_k {}^kL_{ijk} \quad (14a)$$

$$v_{i,j,k} = x_{i,j,k} + (1 - x_i - x_j - x_k)/3 \quad (14b)$$

For steel, the liquid phase is often modelled by the BW-model. However, the single-lattice BW-model is limited for the γ -Fe and α/δ -Fe solid solutions as small elements like C and N occupy the interstitial sites. Hence, the compound-energy formalism (CEF) [132] is typically used to describe the thermodynamic properties of austenite and ferrite. Considering a ternary solution, where A and B are located on the substitutional sublattice and C and Va (vacancies) occupy the interstitial sites, noted by $(A,B)_a(C,Va)_b$, the Gibbs energy is given by **Equation 15**. The stoichiometric coefficients are $a = b = 1$ for austenite and $a = 1$ and $b = 3$ for ferrite.

$$\begin{aligned} G_m = & y'_A y''_{Va} G_{A:Va} + y'_A y''_C G_{A:C} + y'_B y''_{Va} G_{B:Va} + y'_B y''_C G_{B:C} \\ & + aRT(y'_A \ln y'_A + y'_B \ln y'_B) + bRT(y''_C \ln y''_C + y''_{Va} \ln y''_{Va}) \\ & + \sum_{i,j,k} y'_i y'_j y''_k L_{i,j:k} + \sum_{i,j,k} y'_k y'_i y''_j L_{k,i,j} + \sum_{i,j,k,l} y'_i y'_j y''_k y''_l L_{i,j:k,l} + G_m^{\text{phys}} \end{aligned} \quad (15)$$

In **Equation 15**, y_i is the site fraction, defined by $y_i = n_i^{(s)}/n^{(s)}$ and gives the constituent fraction of i on the sublattice s . $L_{i,j:k}$ and $L_{k,i,j}$ are the interaction energies between i and j if the other sublattice is solely occupied by k , whereas $L_{i,j:k,l}$ is the reciprocal parameter describing the interaction among i , j , k , and l . The term G_{ij} is the Gibbs energy of an “*end-member*” (ij for ferrite and ij_3 for austenite): All elements are stable in a specific crystal structure, e.g. bcc and fcc in case of Fe, but show also a certain solubility in a different phases, e.g. P in fcc and bcc structure. The Gibbs energies of end-members of pure elements $G_{A:Va}$ or $G_{B:Va}$ in various crystal structures are called “*lattice stabilities*” and are summarized in the work of Dinsdale together. On the other hand, the end-members $G_{A:C}$ and $G_{B:C}$ in the CEF are often hypothetical

values, where the second sublattice is fully occupied by the component C. For these values, experimental data are rarely available and are often calculated by atomistic modelling approaches. The Gibbs-energy of an end-member is given similarly to **Equation 7**. If no measured heat capacity is found in literature, only two coefficients are considered according to **Equation 16**. In this case the heat capacity is taken from the values of pure elements. [105]

$$G_m - \sum_i b_i H_i^{\text{SER}} = a_0 + a_1 T \quad (16)$$

The CEF is the actual extension of the substitutional model to various sublattices and reduces to the BW-model if only one sublattice is occupied by constituents. [132] It represents a more general mathematic approach to include substitutional and interstitial solutions. [127]

2.2.2.3 Modified quasichemical model (MQM) for short-range ordering (SRO)

Short-range-ordering (SRO) describes a local ordering phenomenon on distances close to the atomic spacings due to energetically favorable configurations of specific atomic pairs. [133] According to Pelton and Kang [134], SRO in a solution is characterized by a negative “*V-shaped*” course in the enthalpy of mixing and a “*M-shaped*” entropy of mixing. The modified quasichemical model (MQM) in the pair-approximation [135,136] enables to take into account strong SRO effects exhibited in the liquid phase of Fe-based systems. Briefly summarized, the model considers the exchange reaction of pairs on the site of a quasi-lattice (**Equation 17**).



(*i-j*) corresponds to the first nearest neighbor pair and Δg_{AB} represents the non-configurational Gibbs free energy change forming two moles of (*i-j*) pairs. For a detailed mathematical description of the MQM [135,136], the author likes to refer to **Paper II**. Remarkable success was achieved using the MQM for liquid metallic solutions with respect to steel, e.g. Fe-Si [137], Fe-B [138], Fe-C-Mn and Fe-Mn-Al [139], Fe-C-Cu [140], Fe-C-Mn-S subsystems [141–143], Fe-Ni-S [144,145] or Mn-Si-C [146].

Maximum SRO composition and partial enthalpies of mixing: Based on outcomings from extensive modelling work of the FactSage group, this chapter emphasizes numerous advantages of the MQM compared to BW-models. Specific results for the Fe-P and Fe-C-P system will be discussed in **Chapter 4.2** and can be found in **Paper II**. Taking the example of the binary Fe-B [138,147] and Mn-C [146,148] systems, the calculated integral and partial enthalpies of the liquid phase are plotted in **Figure 15** and **Figure 16** along with calorimetric data from literature [149,150]. At low amounts of boron or carbon, respectively, the partial enthalpies of mixing are independent on x_B and x_C , but show a sharp increase at a specific chemical composition. This is an evidence of strong SRO between Fe and B, as well as

between Mn and C [134]. The SRO tendency is somewhat less pronounced in the Fe-B liquid. In the Fe-B liquid, the maximum SRO composition is close to the equimolar composition, whereas for the Mn-C system, the abrupt change of ΔH_{Mn} and ΔH_{C} occurs at $x_{\text{C}} \sim 0.33$. The advantage of the MQM for modelling the thermodynamic properties of the liquid phase is clearly visible: (i) the general course of the partial enthalpies is much better reproduced than using the BW-model and (ii) the MQM allows setting the maximum SRO to a specific composition, see **Figure 15 (a)** and **Figure 16 (a)**. In the BW-model, the reasonable modelling of SRO is only possible by introducing several higher-order ${}^{\vee}L_{ij}$ parameters. However, an accurate extrapolation to terminal compositions may still not be guaranteed by the BW-model and could result in large errors of other calculated thermodynamic properties. [134]

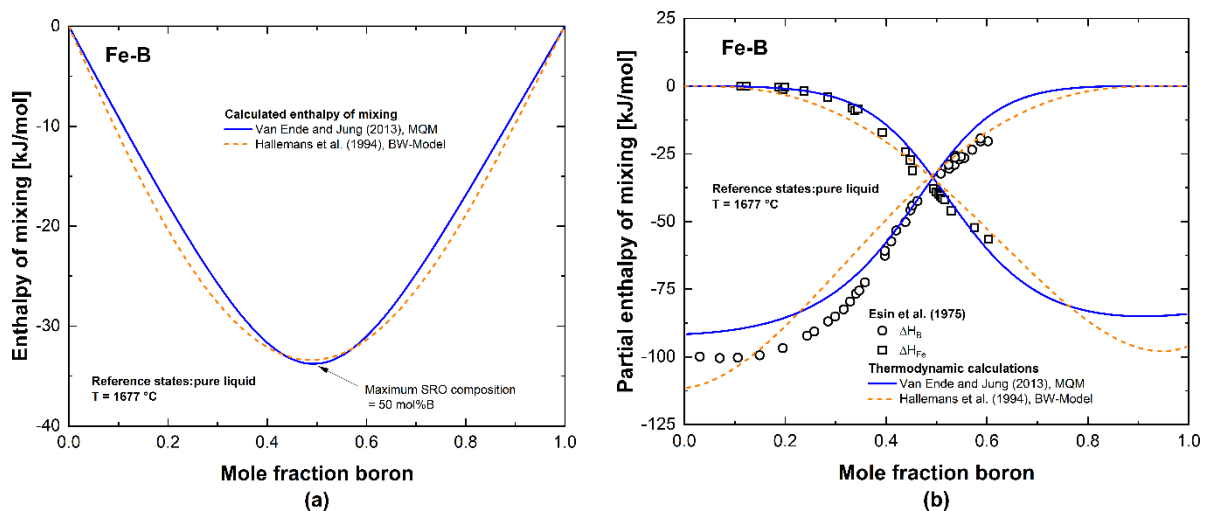


Figure 15: Calculated integral (a) and partial enthalpies (b) of mixing in the binary Fe-B system [138,147] along with experimental data from literature [149].

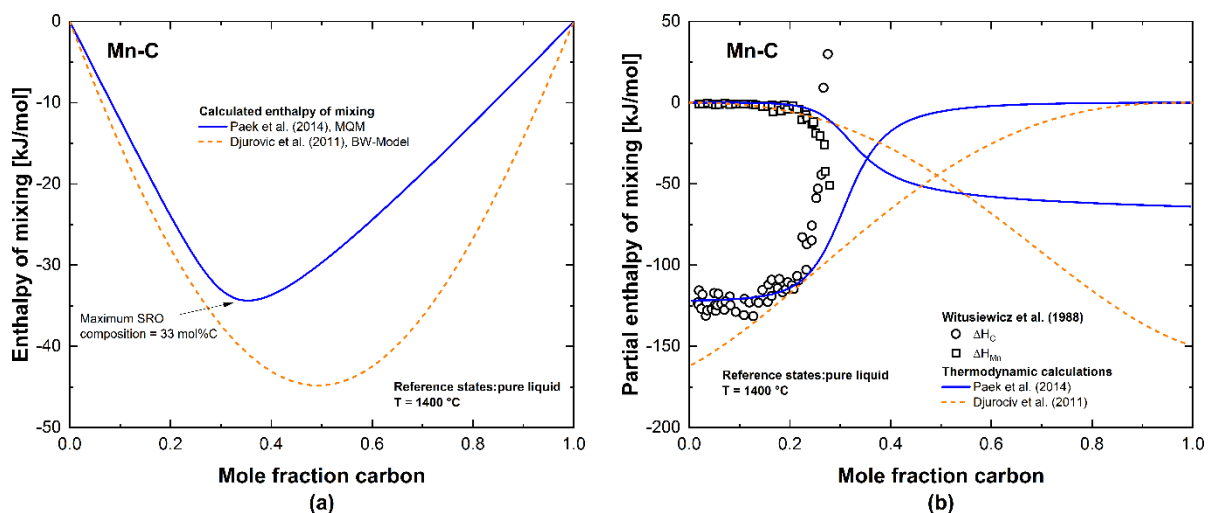


Figure 16: Calculated integral (a) and partial enthalpies (b) of mixing in the binary Mn-C system [146,148] along with experimental data from literature [150].

Binary phase diagrams and extrapolation to higher-order systems: As discussed in **Chapter 2.2.1**, a multicomponent database consists of unary data and thermodynamic assessments of the binary and ternary systems. Considering the ternary Fe-C-Mn system, schematically illustrated in **Figure 17**, the Fe-C and Mn-C liquid show strong SRO tendency. Less interaction in the liquid exists in the Fe-Mn system, as Fe and Mn have similar physico-chemical behaviour and can be found next to each other in the periodic table of elements. The more accurate the description of the binary systems (Fe-C, Mn-C and Fe-Mn) is, the less model parameters will be required to obtain reasonable thermodynamic properties in the ternary Fe-C-Mn system. By comparing two thermodynamic descriptions of the Fe-C-Mn system using (i) the MQM for the liquid phase as proposed by Kim and Kang [139] and (ii) the most recently published BW-model of Djurovic et al. [148], the following number of excess terms are obtained: Eleven binary and two ternary terms were required in the MQM [139] whereas eleven binary and four ternary terms were used in the BW-model [148]. Though the total number in the binaries is similar, the ternary terms are twice in the BW-model. Another important point is the possibility of a mixed implementation of the MQM and BW-model into a multicomponent database, as demonstrated by Pelton and Chartrand [136]. Extensive modelling of numerous binary subsystems has been performed in the past using the BW-model. Modelling work is time consuming and if the novel results do not significantly improve the calculations, it is often preferable to use the BW-model with well validated calculations. However, it is not only the model description itself but also the used extrapolation technique from a ternary composition to the binaries that will have significant influence on the binary contributions. Various geometric extrapolations are available from literature, e.g. Muggianu method [151], Kohler [152] or Toop [153] techniques. **Figure 17** shows the “Kohler”-model and “Kohler-Toop”-model in symmetric and asymmetric versions, respectively. In case of strong SRO, the two different options may result in very different results, if the ternary composition is extrapolated closely to the steep increase/decrease of the partial enthalpies in the binary systems. In such a case, the asymmetric “Kohler-Toop” method as suggested by Pelton and Chartrand [136] gives more appropriate results for SRO by setting C as asymmetric component.

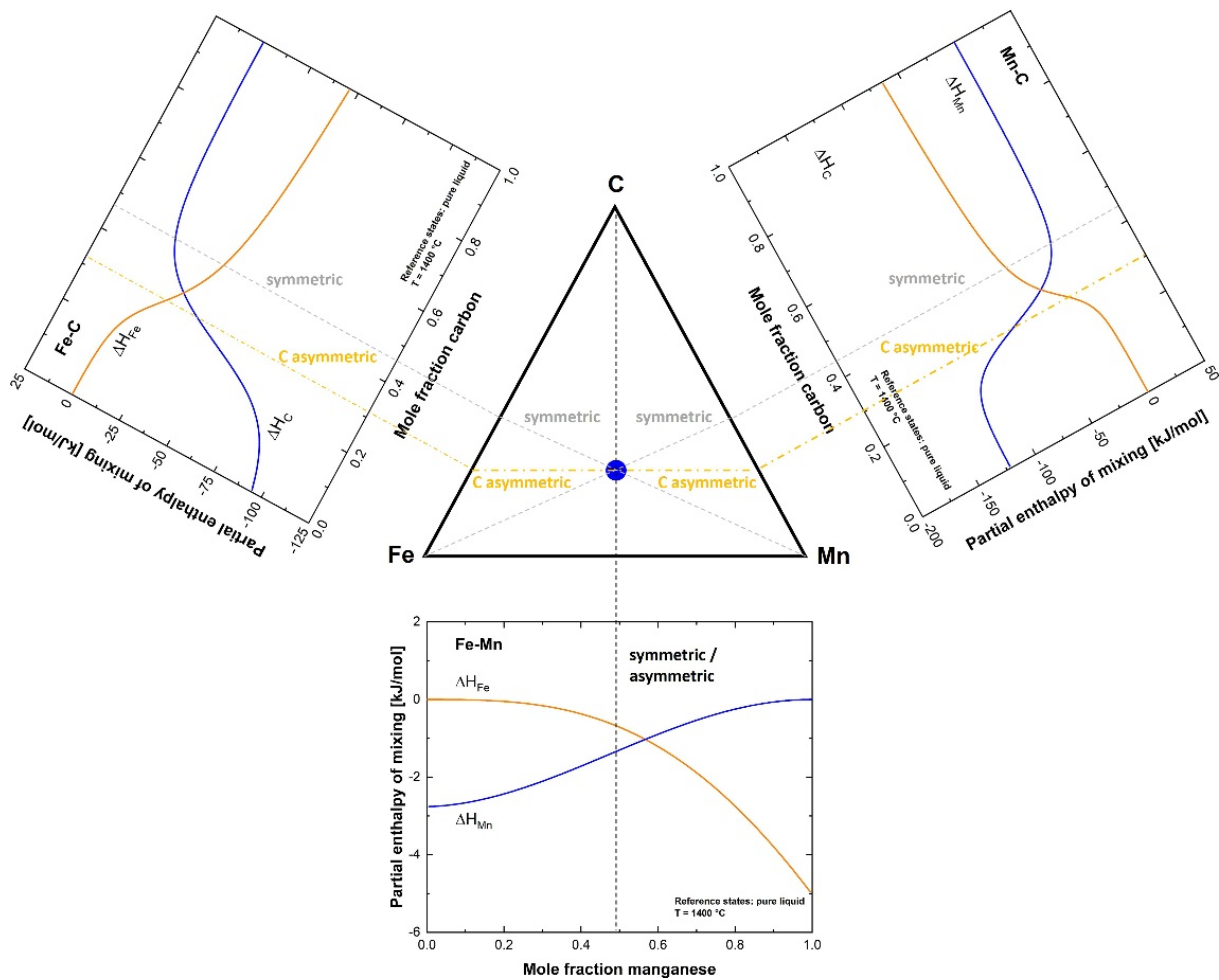


Figure 17: Illustration of the „Kohler“-type [152] extrapolation and comparison with “Kohler-Toop” [136] method, setting C in the ternary Fe-C-Mn as “asymmetric” component and influence on selected thermodynamic (partial enthalpies of mixing) properties obtained from the binaries.

2.2.2.4 Thermodynamic assessments of the Fe-P and Fe-C-P systems

Several thermodynamic descriptions and graphical phase diagram representations of the binary Fe-P system have been published in the past. The first self-consistent set of thermodynamic parameters was derived by Spencer and Kubaschewski [72] in 1978 considering all experimental data available at that time. Twelve years later, Gustafson [29] reassessed the phase diagram particularly in the Fe-rich part within a thermodynamic investigation on P-containing systems (C-Cu-Fe-P, Fe-Mo-P and Fe-Ni-P). In 1996, Shim et al. [25] established the “*standard reference work*” on the binary Fe-P system: (i) overall phase diagram data were used in the modelling procedure and (ii) most recently published experimental data on Fe and P activities in the liquid phase, as well as calorimetric functions of phosphides were taken into account and Until today, the Fe-P system of Shim et al. [25] is widely accepted in the scientific community. A first approach to provide a thermodynamic

description of the Fe-P system over the whole composition range (including FeP₂ and FeP₄) was attempted by Ohtani et al. [24] incorporating computer-aided atomistic modelling results into their thermodynamic analysis. Later, those data were also considered by Cao et al. [154]. Within the framework of developing a thermodynamic database for Fe-P-X multicomponent alloys, Miettinen and Vassilev [26] slightly modified the thermodynamic parameters of Shim et al. [25] with minor changes of the austenite and ferrite parameters, but kept the liquid phase unchanged. In all mentioned thermodynamic descriptions, the random mixing model was assumed for the liquid phase and the bcc and fcc solid solutions. In the attached **Paper II** and the optimization of You and Jung [27] the MQM was used in order to take into account the strong SRO tendency in the liquid Fe-P phase. The solid phases were modeled by the random mixing approach and the phosphides were treated as stoichiometric compounds. Both publications were independently published within a close time frame. In the work of You and Jung [27], the FeP₂ high-order phosphide was included which was not considered in the modelling work of **Paper II**. On the other hand, two different maximum SRO compositions were tested in **Paper II** and critically evaluated by extrapolating to the ternary Fe-C-P system. Selected thermodynamic assessments along with the used models for the stable phases are summarized in **Table 5**.

Table 5: Most recent thermodynamic optimizations of the Fe-P and Fe-C-P systems [24–27,30,154].

Phase	Shim [25,30]	Ohtani [24]	Cao [154]	Miettinen [26]	You [27]
Liquid	BW	BW	BW	BW	MQM
(γ Fe)	CEF	BW	BW	BW	CEF
(α/δ Fe)	CEF	BW	BW	BW	CEF
Fe ₃ P	STCO	CEF	STCO	CEF	STCO
Fe ₂ P	STCO	CEF	STCO	CEF	STCO
FeP	STCO	STCO	STCO	CEF	STCO
FeP ₂	-	STCO	STCO	-	STCO
FeP ₄	-	STCO	STCO	-	-
P	PURE	PURE	PURE	PURE	PURE
Fe ₃ C	STCO	-	-	-	-
C	GRAPH	-	-	-	-

2.2.3 Application of a CALPHAD-based tool to the continuous casting process

With particular respect to continuous casting, the “*Interdendritic Solidification*” (IDS) tool [155,156], developed at Aalto University (Helsinki, Finland), is one of the most comprehensive CALPHAD-based software packages. Briefly summarized, this thermodynamic-kinetic model includes [155] (i) an intern thermodynamic database, (ii) a sophisticated microsegregation model solving the thermodynamic equilibrium at the phase interface using chemical potential-equality equations for each component, (iii) a semi-empirical austenite decomposition (ADC) model to simulate the solid state phase transformations below 900 °C, (iv) a precipitation module for micro-alloyed steels and (v) the possibility of calculating thermo-physical properties (heat capacity, thermal conductivity, density, thermal expansion, ...) required for thermal modelling of the casting process, e.g. the steady-state three-dimensional heat transfer model TEMPSIMU3D [157]. The general structure of the IDS model with input and output data is shown in **Figure 18** [156]. Input parameters are the local cooling rates during solidification and in the solid state, the actual chemical composition and (optionally) process data (t-T profiles, deformations). As major output, the phase transformation temperatures, phase fractions, solute composition profiles and material properties are calculated.

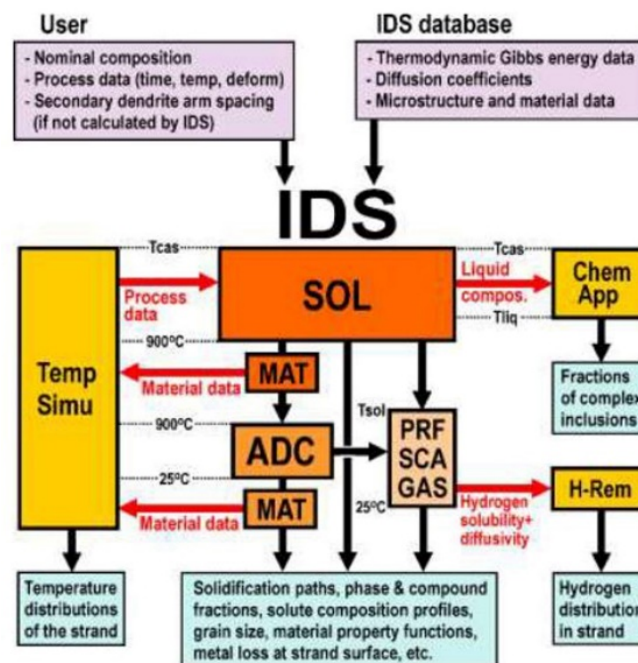


Figure 18: General structure (input/output data) of the IDS package [156].

Recently, the IDS model and the transient version of TEMPSIMU3D, called CastManager, were coupled to perform online predictions of temperatures, solidification progress and product quality on various slab casters in Finland [158]. Therefore, several quality indices (QI) were

implemented in IDS [159], which are closely related to the phase diagrams and kinetic phase transformations, e.g. peritectic reaction, microsegregation phenomena and austenite grain growth. Aim of the online QI strategy is the description of various types of surface cracks and internal defects by physically-based, computationally efficient criterions. Selected indices and the described defects according to the work of Louhenkilpi et al. [159] are listed in **Table 6**.

Table 6: Selected quality indices (QI) and described defects according to Louhenkilpi et al. [159].

Defect	QI _{SHE} ¹⁾	QI _{STR} ²⁾	QI _{SOL} ³⁾	QI _{DUC} ⁴⁾	QI _{GRA} ⁵⁾
Longitudinal surface cracking, facial and corner	x	x	x		
Transverse corner cracking	x	x		x	x
Star cracks	x			x	

¹⁾ SHE = Detachment of the solidifying shell from the mold surface, ²⁾ STR = Disturbed strengthening, ³⁾ SOL = Solute enrichment of strongly segregating elements (e.g. P, S and B), ⁴⁾ DUC = precipitations in micro-alloyed steels between below 1200 °C, ⁵⁾ GRA = coarse grain structure - austenite grain growth.

In **Table 6**, phosphorus influences the magnitude of QI_{SHE} and QI_{SOL}: The index QI_{SOL} describes the reduced ductility close to the solidus temperature and considers the interdendritic enrichment of strongly segregating elements (P, S and B). The value of QI_{SOL} raises, if the austenite fraction during solidification increases and as higher the enrichment of the elements takes place. [159] This fact is in agreement with the predicted hot tearing sensitivity due to microsegregation phenomena in **Chapter 2.1.3.3**, depending on the initial C content. In the intended concept, QI_{SOL} is calculated by IDS as a function of (i) the interdendritic composition of dissolved P, S and B at a solid fraction of 99.5 % and (ii) the amount of inclusions formed during solidification, e.g. (Fe,Mn)S and B₂O₃. Primary precipitations show a beneficial influence on QI_{SOL} as their precipitation reduces the amount of strongly segregating elements in the residual melt. In their work, Louhenkilpi et al. [159] proposed the general form $QI_{SOL} = f(x_i^L, f_{(Fe,Mn)S})$, but noted, that the exact function of QI_{SOL} itself is still open and topic of ongoing research.

In the present study, the calculation of QI_{SHE} is therefore schematically demonstrated based on **Figure 19**: The phenomenon in the continuous casting process described by QI_{SHE} is the detachment of the solidifying shell from the surface of the mold because of the contraction during the δ/γ -transformation in the peritectic reaction, see **Figure 19 (a)**. As a consequence, the non-uniform heat withdrawal in the mold leads to an uneven initial shell formation, coarse austenite grains and deep oscillation marks. Hence, hypo-peritectic steel grades with carbon content between c_A and c_B (see also **Chapter 2.1.2.2**) are prone to crack formation in the

casting process [58,62,160]. In $Q_{I_{SHE}}$ the contraction due to the δ/γ -transformation is considered by **Equation 18** [159];

$$Q_{I_{SHE}} = f_{SOL}^{\delta} - f_{MAX}^{\delta} \quad (18)$$

where f_{SOL}^{δ} is the δ -Fe fraction at the solidus temperature and f_{MAX}^{δ} is the maximum ferrite fraction between T_S and $T_S - 30$ °C. According to **Figure 19 (b)** the phase transformation temperature and respective fractions of ferrite are calculated with the IDS model. The maximum of $Q_{I_{SHE}}$ is indicated by the red area and is close to the point c_A . The values of $Q_{I_{SHE}}$ vary between 0 - 1 and higher values of $Q_{I_{SHE}}$ correspond to increased risk of crack formation. Within the online quality prediction procedure, the CastManager [158] calculates the temperature field where the obtained local cooling rates and actual steel composition are the input parameters for IDS. Based on the results, $Q_{I_{SHE}}$ can be efficiently calculated and give first information on the product quality and risk of crack formation during the process with respect to hypo-peritectic behaviour of the steel grade.

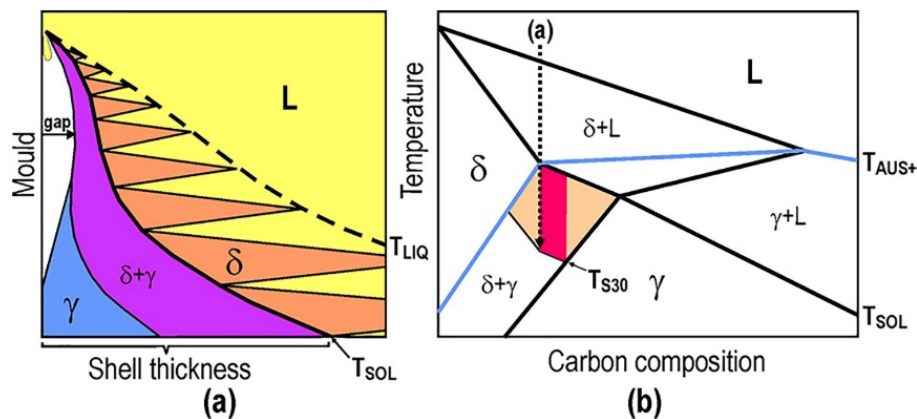


Figure 19: Detachment of the solidifying shell from the mold surface as a consequence of the contraction during δ -Fe/ γ -Fe transformation of the peritectic reaction (a) and link to the calculated phase diagram using IDS (b). Red indicates the maximum of the QI (worst case) and T_{S30} is the temperature 30 °C below the solidus temperature. [159].

The effect of phosphorus on $Q_{I_{SHE}}$ in the vertical section Fe-C-0.10%P is shown in **Figure 20**. The quality index was calculated for local cooling rates of 0.10 °C/s, 1 °C/s and 10 °C/s with IDS [155,156] and is compared with results of the microsegregation model, published in **Paper V** (see **Chapter 4.4**). The values are shown along with the experimental phase diagram in **Figure 20 (a)** and **Figure 20 (b)**, respectively. As expected, both models predict a maximum of $Q_{I_{SHE}}$ close to the characteristic point c_A . The magnitude of the maximum value of $Q_{I_{SHE}}$ is similar and varies from $Q_{I_{SHE}} \sim 0.70$ in IDS to $Q_{I_{SHE}} \sim 0.60$ in the present work. In IDS [155,156], the critical composition corresponds to 0.095 mass pct. P, which is in very good agreement with the experimental value for $c_A = 0.084$ %C. In **Figure 20 (a)**, only a minor influence of the

cooling rate on the calculation results is obtained. The function of QI_{SHE} implemented into the present microsegregation model of **Paper V** shows a higher sensitivity to the local cooling rate. At slow cooling with $0.01\text{ }^{\circ}\text{C/s}$, the maximum of QI_{SHE} can be found at $0.07\text{ }\%C$ and is shifted to lower carbon contents with increasing cooling rate. However, in both models, the influence of P on the peritectic range is well reproduced and the calculations indicate a good correlation with the experimental data. The QI strategy provides an efficient way to identify hypo-peritectic behaviour depending on the chemical composition and the local cooling rates.

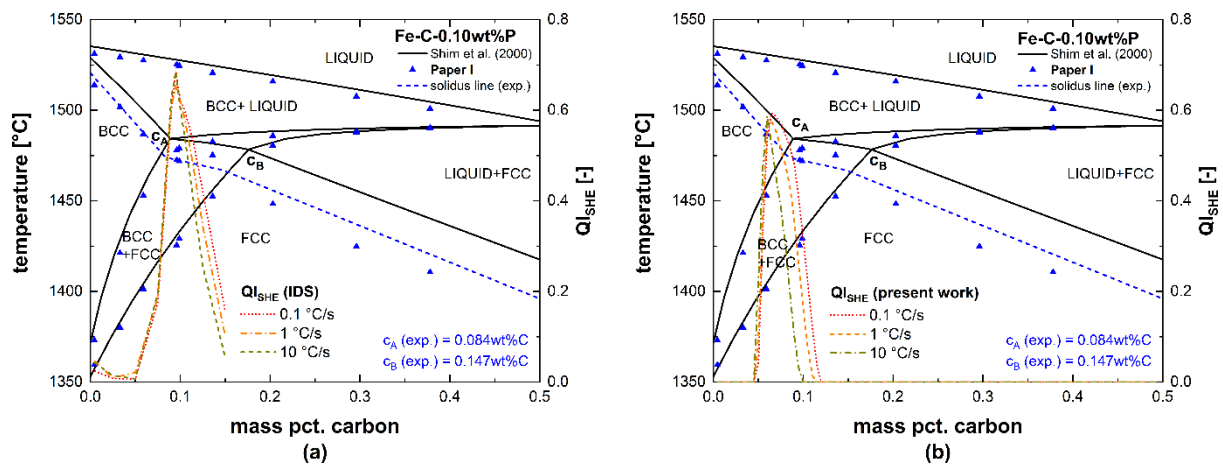


Figure 20: Influence of phosphorus on QI_{SHE} in the vertical Fe-C-0.10%P section calculated with cooling rates of $0.10\text{ }^{\circ}\text{C/s}$, $1\text{ }^{\circ}\text{C/s}$ and $10\text{ }^{\circ}\text{C/s}$ using the IDS software [155,156] (a) and the microsegregation model published in **Paper V** (see **Chapter 4.4**) (b) along with the experimental phase diagram determined in **Paper I**.

3 List of publications

Peer-reviewed publications included in the PhD thesis

- Paper I:** M. Bernhard, P. Presoly, N. Fuchs, C. Bernhard and Y.-B. Kang, Experimental Study of High Temperature Phase Equilibria in the Iron-Rich Part of the Fe-P and Fe-C-P Systems, Metallurgical and Materials Transactions A, 2020, vol. 51, pp. 5351-5364.
- Paper II:** M. Bernhard, Y.-B. Kang, P. Presoly, A.E. Gheribi and C. Bernhard, Critical evaluation and thermodynamic modeling of the Fe-P and Fe-C-P system, CALPHAD, 2020, vol. 70, art. no. 101795.
- Paper III:** M. Bernhard, N. Fuchs, P. Presoly, P. Angerer, B. Friessnegger and C. Bernhard, Characterization of the γ -loop in the Fe-P system by coupling DSC and HT-LSCM with complementary in-situ experimental techniques, Materials Characterization, 2021, vol. 174, art. no. 111030.
- Paper IV:** M. Bernhard, P. Presoly, C. Bernhard, S. Hahn and S. Ilie, An assessment of analytical liquidus equations for Fe-C-Si-Mn-Al-P alloyed steels using DSC/DTA techniques, Metallurgical and Materials Transactions B, 2021.
- Paper V:** M. Bernhard, P. Presoly, C. Bernhard, J. Six and S. Ilie, On the relevance of microsegregation models for process control in continuous casting of steel, Proceedings of the 26th International Conference on Metallurgy and Materials, 2017, Brno, Czech Republic.


All publications are attached in **Appendix A** and contributions of the present author are listed in detail in the following part.

Contributions of the author: All attached publications were planned, conceptualized and written by the author. All thermal analysis trials by differential scanning calorimetry (DSC) and their interpretation were carried out by the author. The thermodynamic modelling and processing of literature data within the CALPHAD-framework and all thermodynamic calculations were performed by the present author. A large part of the thermodynamic modelling work was performed within a research stay at École polytechnique de Montréal (Canada) under supervision of Prof. Youn-Bae Kang (Pohang University of Science and Technology, South Korea).

External contributions: In **Paper II**, the Density Function Theory (DFT) simulations were carried out by Dr. Aimen Gheribi (École polytechnique de Montréal, Canada) and were implemented into the thermodynamic model by the present author. In **Paper III**, the high-temperature X-ray diffraction (HT-XRD) and dilatometry experiments were performed at Materials Center Leoben Forschungs GmbH (MCL) by Bernhard Friessnegger and Dr. Paul Angerer. The results were interpreted in intensive joint discussion, the final results were graphically processed by the present author.

Acknowledgements to co-authors and co-workers: The author would like to gratefully thank Dr. Peter Presoly for supervising the thermal analysis experiments and sample production using high frequency remelting (HFR). Dr. Nora Fuchs performed the high-temperature laser scanning confocal microscope (HT-LSCM) experiments and supported the evaluation of the results with great expertise. Special thanks goes to Prof. Christian Bernhard for discussions on the topic of microsegregation modelling and valuable input for the conceptualizations of the publications. Dr. Susanne Hahn and Dr. Sergiu Ilie contributed as project partners to the technological relevance of the scientific work and improved the manuscript of **Paper IV** by reviewing and editing. Further, the author want to thank Bernhard Gerstl and Paul Reisinger for alloy melting using high frequency remelting (HFR) techniques; as well as for the extensive metallographic preparation of the DSC/HT-LSCM samples together with Tobias Rieger. The chemical analysis of the samples were provided by Franz Prucha from voestalpine Stahl Linz GmbH.

Publication No.	Conceptulation	Experiments/ modelling	Analysis/ interpretation	Manuscript preparation
1	100%	95%	100%	100%
2	100%	95%	100%	100%
3	100%	70%	90%	90%
4	100%	100%	100%	100%
5	100%	100%	100%	100%



(Dipl. Ing. Michael Bernhard)

Conference contributions not included in the PhD thesis:

M. Bernhard, C. Bernhard, P. Presoly and D. You, An alternative approach for the experimental verification of microsegregation models using an in-situ hot tensile test during solidification of steel, Proceedings of the 7th International Conference on Solidification and Gravity, 2018, Miskolc-Lillafüred, Hungary.

P. Presoly, M. Bernhard, D. You and C. Bernhard, High concentrations at the final solidification of advanced steels: Thermodynamic evaluation of replicated “segregation-samples” by means of DTA/DSC-measurements, Proceedings of the 7th International Conference on Solidification and Gravity, 2018, Miskolc-Lillafüred, Hungary.

P. Presoly, M. Bernhard and C. Bernhard, Investigation of the Fe-C-Si-Mn system with special focus on the Fe – 3 wt.-% Si – high Mn section, Proceedings of CALPHAD XLVII: International Conference on computer coupling of phase diagrams and thermochemistry, 2018, Queretaro, Mexico.

P. Presoly, M. Bernhard, C. Bernhard, S. Hahn, P. Pennerstorfer, S. Ilie and S. Six, High precious phase diagrams – a roadmap for a successful casting processing, Proceedings of the 4th European Steel Technology and Application Days, 2019, Düsseldorf, Germany.

G. Santos, C. Bernhard, M. Bernhard, M. Taferner, L. Preuler and S. Ilie, An Integrated Approach for Near Process Modelling of the Continuous Casting of Steel, 9th International Conference on Modeling and Simulation of Metallurgical Processes in Steelmaking, Vienna, Austria, 2021, accepted.

M. Bernhard, P. Presoly and C. Bernhard, Experimental investigations and computational thermodynamics of the Fe-C-P system, European Congress and Exhibition on Advanced Materials and Processes (Euromat), 2021, Graz, Austria, accepted.

M. Bernhard, G. Santos, S. Ilie, L. Preuler and C. Bernhard, Investigations on hot tearing in a continuous slab caster: Numerical modelling combined with analysis of plant results, 10th European Conference on Continuous Casting, Bari, Italy, 2021, abstract accepted.

Other publications not included in the PhD thesis:

L. Drozdova, B. Smetana, P. Presoly, V. Novak, M. Machu, M. Bernhard, H. Francova, S. Zla, L. Rehackova and C. Bernhard, Investigation of Fe–C–Cr and Fe–C–Cr–Ni-based systems with the use of DTA and HT-LSCM methods, Journal of Thermal Analysis and Calorimetry, 2020, vol. 142, pp. 535-546.

4 Novel research findings and discussion

The schematic workflow of the present PhD thesis and the link to the published **Papers I - V** is represented in **Figure 21**. The first workpackage (WP 1) dealt with the experimental reassessment of the binary Fe-P and Fe-C-P system using DSC, partly supported by high-temperature laser scanning microscopy (HT-LSCM). Based on the new phase diagram data, the Fe-P and Fe-C-P systems were reoptimized within the CALPHAD-framework (WP 2). However, as the DSC setup in WP 1 was specifically adjusted to characterize γ/δ -phase transformations and melting equilibria, a novel approach was proposed in WP 3 by coupling DSC data and HT-LSCM observations to determine the γ -loop in the Fe-P system. The results were evaluated with high-temperature X-ray diffraction (HT-XRD) and dilatometry. From the thermodynamics of WP 1 - 3, selected data and modelling results were used in WP 4 - 5 to improve a microsegregation model with focus on solidification of rephosphorized steels.

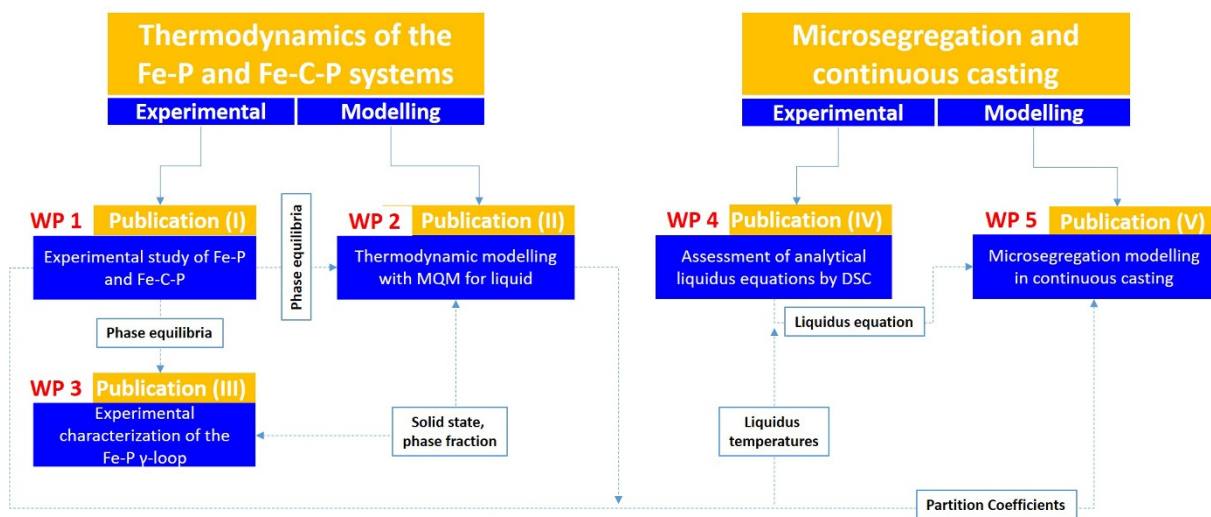


Figure 21: Schematic workflow of the present PhD thesis and the link to the attached **Papers I-V**.

4.1 Experimental reassessment of the binary Fe-P phase diagram and Fe-C-P key systems using DSC (Paper I)

The actual work in the PhD project started with the experimental investigations of the binary Fe-P phase diagram and selected vertical sections in the ternary Fe-C-P system using DSC. In total, 37 alloys with a mass of 50 g were produced by high-frequency remelting (HFR) technique. The subsequent chemical analysis by optical emission spectroscopy (OES) and X-ray fluorescence analysis (XRF), partly required a recalibration of the analytical instruments with results of inductively coupled plasma (ICP) - OES for samples with P > 0.10%. In the present study, a NETZSCH DSC 404F1 Pegasus was used for the determination of high-temperature phase equilibria. The DSC trials were carried out with 50 mg samples and a heating rate (HR) of 10 °C/min with an empty crucible chosen as the reference. An extensive section on the experimental details, as well as the list of chemical analysis of all samples can be found in **Paper I**.

One highlight of the DSC analysis represents the successful application of NETZSCH's Tau-R software [161,162]. The general procedure of incorporating the Tau-R method into standardized DSC analysis at the Chair of Ferrous Metallurgy (Montanuniversitaet Leoben) was firstly established by Presoly et al. [56] and is explained as follows: Melting of steel takes place under a large change of heat ($\Delta H > 200$ J/g) resulting in a shift of the measured "*peak temperatures*" to higher values with increasing heating rates. [163] However, "*onset temperatures*", defined as the first deviation of the baseline, are not affected by the HR. In general, peaks in the DSC signal indicate the end of a phase transformation during heating, e.g. liquidus, the end of the peritectic transformation and the end of the γ/δ -transformation; whereas onsets correspond to the respective beginning, e.g. solidus, start of the peritectic reaction or start of the γ/δ -transformation. The evolution of the DSC signal for a hypo-peritectic sample with Fe-0.136%C-0.105%P is shown in **Figure 22 (a)**, validating the explained effect of the HR on the DSC results. In order to obtain the equilibrium value, the phase transformation temperatures have to be extrapolated to a HR of 0 °C/min within a heating rate variation procedure [164], see **Figure 22 (b)**. In daily DSC practice the HR variation procedure is time consuming and cost intensive, as numerous samples have to be investigated. The Tau-R calculation [161,162] provides a more efficient way to obtain the equilibrium from a single DSC measurement by excluding all instrumental effects on the DSC signal. For this purpose the DSC has to be calibrated with several measurements of pure elements (NETZSCH's standards) under the pre-defined HR. In the PhD thesis a HR of 10 °C/min was selected as (i) linear behaviour of the HR variation extrapolation was obtained up to 10 °C/min, (ii) the time

for measurement, as well as the time spend in the high-temperature region is reduced and (iii) the HR is in reasonable agreement with values from literature [164]. It was demonstrated in **Paper I**, that the Tau-R calculations and the extrapolated equilibrium values of the HR variation method are in excellent agreement. The Tau-R calculation of the 10 °C/min DSC signal of sample Fe-0.136%-0.105%P is shown in **Figure 23**.

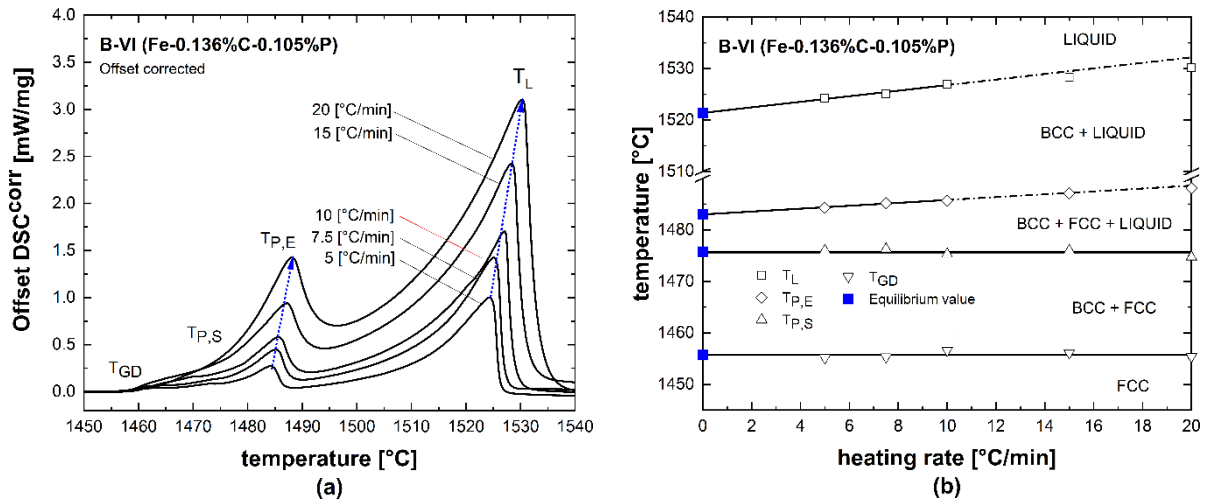


Figure 22: Evolution of the DSC signal for a Fe-0.136%C-0.105%P alloys with varying heating rates of 5 - 20 °C/Min (a) and determination of the equilibrium temperatures by a HR variation (b).

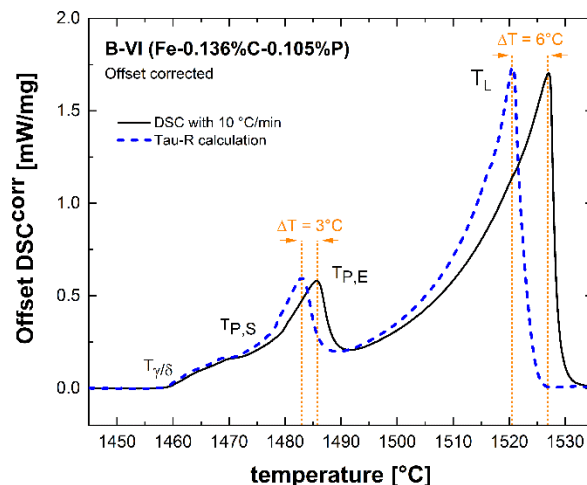


Figure 23: Graphical comparison between the original DSC signal and the Tau-R calculation. [165]

Within first experiments of studying the ternary vertical section Fe-C-0.10%P, a significant difference of the solidus temperature ($\Delta T_s \sim 20$ °C) was identified by comparing the measured values with calculations using the thermodynamic optimization of Gustafson [29]. The experimentally determined phase stabilities of δ -Fe and γ -Fe in the peritectic range indicated, that the liquid phase has to be considered as much more stable than assumed in the modelling work. In a first step, the author created therefore a ternary Fe-C-P database in the FactSage

[28] format implementing the more recent thermodynamic assessments of Shim et al. [25,30]. However, even the updated excess Gibbs energy parameters could not resolve the fact of predicting too high solidus temperatures within calculations, see **Figure 24**. Due to the low P content of 0.10 mass pct. in the vertical section, the ternary excess parameters in the BW-model do not contribute significantly to the excess Gibbs energy: In the Fe-rich corner of the Fe-C-P system, the accurate descriptions of the binary Fe-C and Fe-P systems play a keyrole to improve the phase diagram calculations. Hence, the starting point of the complete experimental reassessment of the binary Fe-P system in the PhD work was actually a non-acceptable error in predicting high-temperature phase equilibria in the ternary phase diagrams.

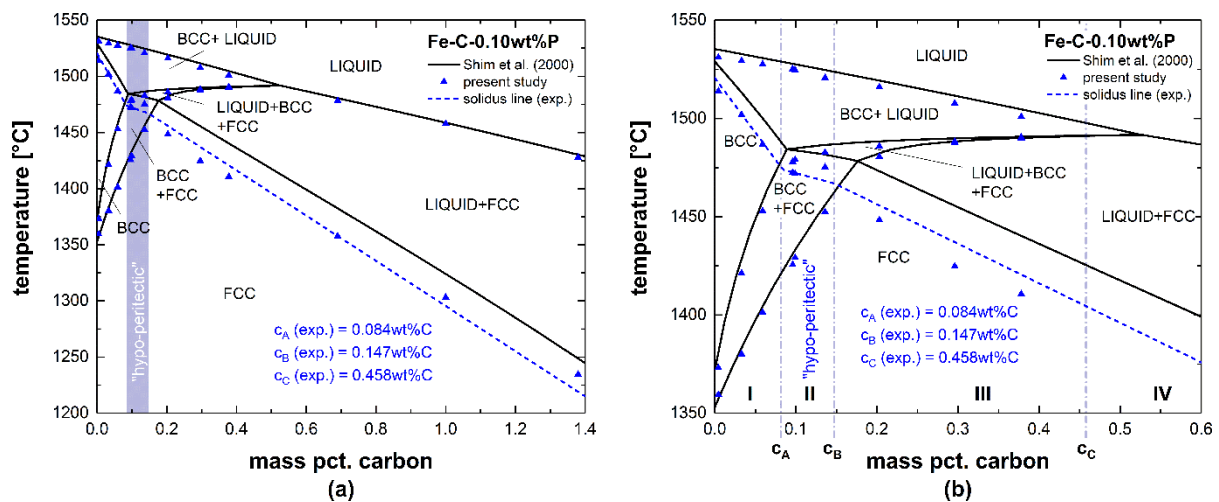


Figure 24: Comparison between DSC data of the present data and the thermodynamic calculations with the assessments of Shim et al. [25,30] for the vertical Fe-C-0.10%P section; 0 - 1.4 mass pct. C (a) and enlarged peritectic region (b). [165]

From literature survey, a lack of experimental data for melting equilibria in the Fe-P system was identified at $P < 1\%$. Reliable data in this composition range are of great importance to model the solidification of rephosphorized steels. Hence, particular focus was placed in the DSC trials on investigating samples with P content lower than 1%. Additional samples were produced to determine the phase boundaries up to the eutectic composition of ten mass percent. The newly assessed binary Fe-P system is represented in **Figure 25**. The solidus and liquidus temperatures are in best agreement with the most recently published data of Morita and Tanaka [45], but the present data are considered as superior due to the high deviation of the chemical composition analyzed by EPMA [45]. At $P < 1\%$, the results indicate a much stronger decrease of T_S than the calculations, but become more consistent with the assessment of Shim et al. [25] with increasing P contents. It can be concluded, that the error in the Fe-P system leads to significant deviations in the peritectic range of the ternary Fe-C-P system in **Figure 24**.

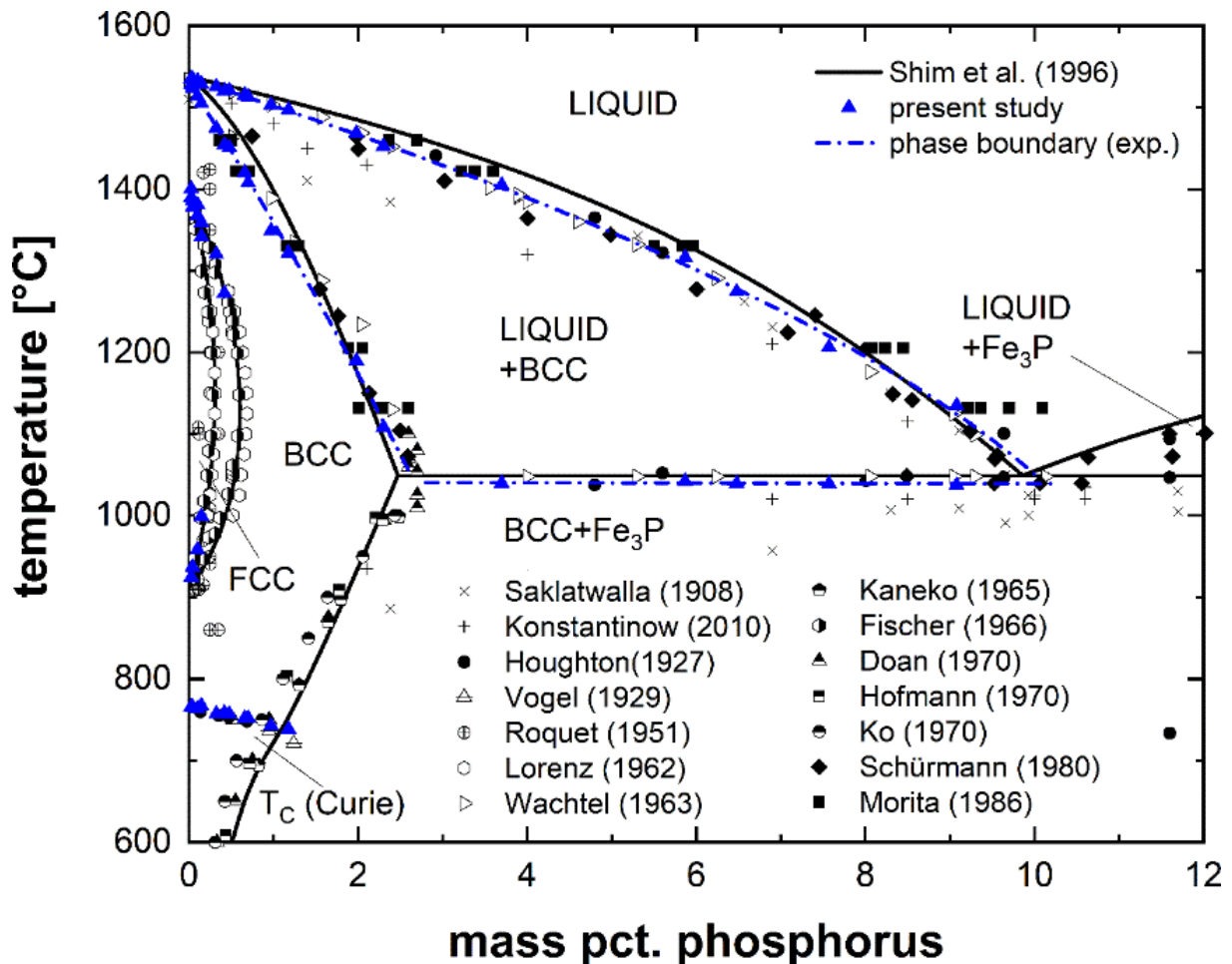


Figure 25: Newly assessed phase boundaries in the binary phase diagram with respect to melting equilibria and the high-temperature γ/δ -transformation. [165]

4.2 Thermodynamic modelling of the Fe-P and Fe-C-P system using the MQM for the liquid phase (Paper II)

Based on the gained data from DSC experiments in **Paper I** a complete thermodynamic reassessment of the binary Fe-P and Fe-C-P systems was performed. For the first time, the MQM was applied for the liquid phase in this alloying system. A summary of calculated thermodynamic properties (enthalpies, activities and calorimetric functions of phosphides) and various vertical and isothermal sections from literature is provided in **Paper II**. With respect to present work, the calculated Fe-rich part of the binary Fe-P system is shown in **Figure 26**. In **Paper II**, two sets of thermodynamic model parameters for the MQM were proposed as the maximum SRO composition was not evident from the literature data. “*Model I*” considers SRO at $x_P = 0.33$, “*Model II*” at the equimolar composition ($x_P = 0.50$). It is clearly visible in **Figure**

26, that both models could improve the phase diagram calculation compared to the work of Shim et al. [25] and perfectly agree with the DSC data of **Paper I**. However, although both MQM descriptions may be used in thermodynamic databases for highly P-alloyed steel grades, less excess parameters were needed in Model I and indicate a better suitability for the Fe-P phase diagram than Model II. Shortly after publication of **Paper II**, You and Jung [27] independently proposed a second description of the Fe-P phase diagram using the MQM for the liquid phase. Similar to Model I in **Paper II**, the authors [27] set the maximum SRO composition to $x_P = 0.33$ and achieved excellent results of describing the thermodynamic properties of the liquid phase.

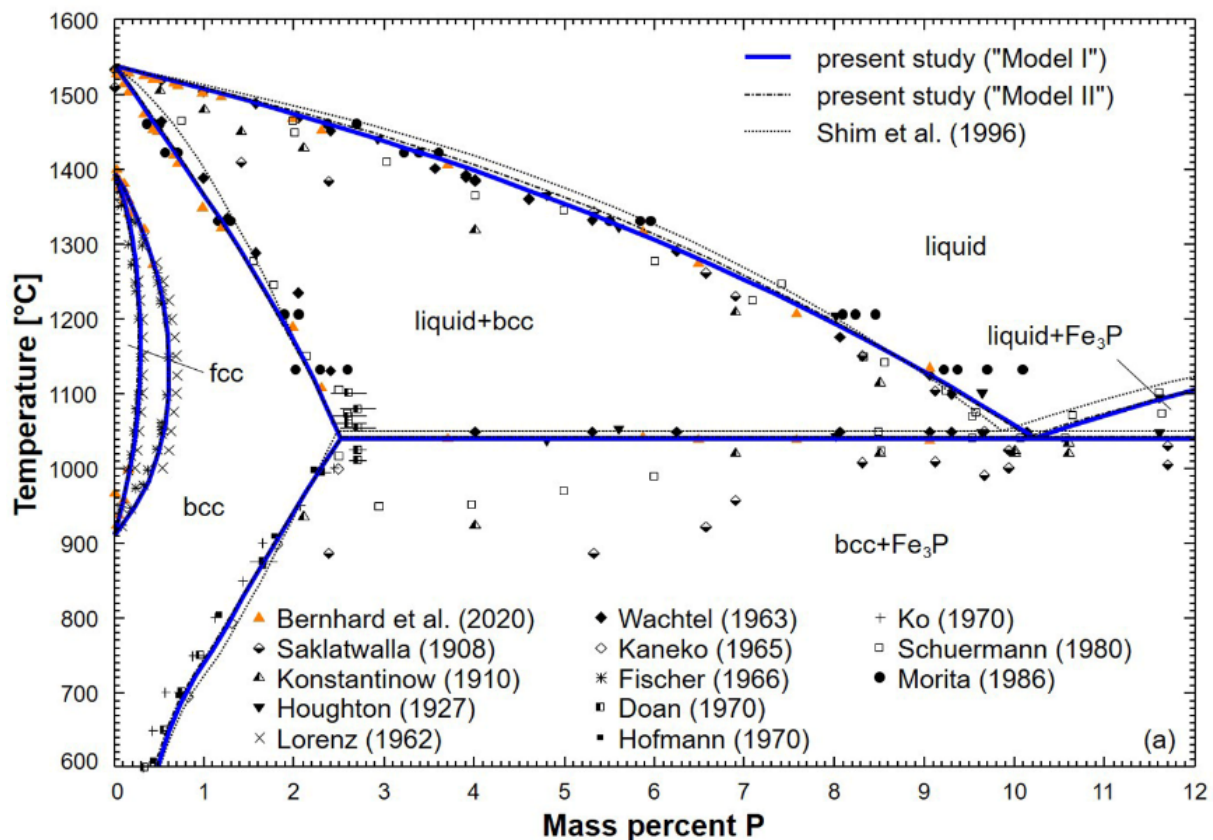


Figure 26: Calculated Fe-rich part of the binary Fe-P system using the novel set of thermodynamic parameters. The present DSC data are plotted by orange triangles and are labelled by Bernhard et al. (2020). The present assessment is compared with the work of Shim et al. [25] and experimental data from literature [34–36,38–42,44–46]. [166]

The last optimization of the ternary Fe-C-P system was published by Shim et al. [30] in the year 2000. In the modelling work of **Paper II**, the improved thermodynamic description of the binary Fe-P phase diagram was extrapolated to the ternary Fe-C-P system. Therefore, the assessment of the Fe-C system according to Shubhank and Kang [140] was considered, where the liquid phase was also modelled by the MQM. As no information on the C-P phase

diagram was available, its contribution to the ternary description was neglected. The Gibbs energy of the liquid phase was extrapolated by a “Kohler-Toop” method (**Chapter 2.2.2.3**), setting carbon as the asymmetric component. Without introducing a ternary excess Gibbs energy parameter, the thermodynamic properties of the liquid phase could be improved, compared to the BW-model of Shim et al. [30]. Particularly at higher amounts of P, the experimental data in **Figure 27** indicate a stronger decrease of the C solubility, depending on P; this tendency is reproduced much better using Model I of **Paper II** compared to previous work [30].

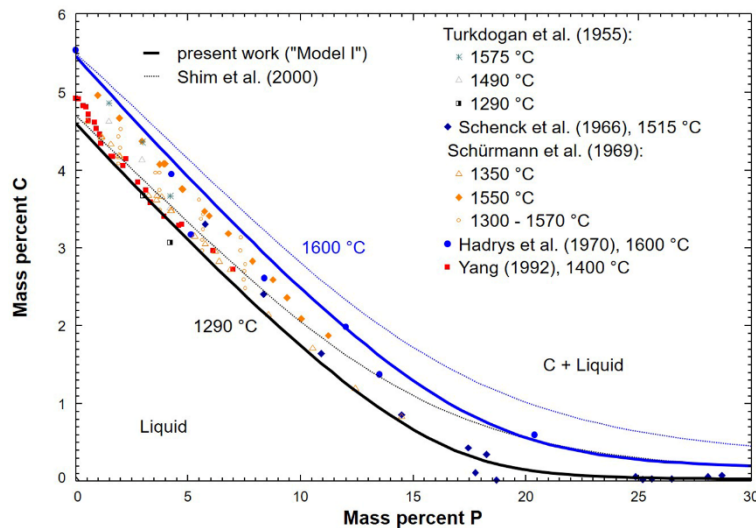


Figure 27: Calculated solubility of C in the ternary Fe-C-P liquid phase in the temperature range of 1290 - 1600 °C compared with the assessment of Shim et al. [30] and experimental data from literature [167–171]. [166]

In **Paper II**, the austenite and ferrite solutions were modelled with the Compound Energy Formalism, as C occupies the interstitial sites in the Fe-C-P system. According to **Chapter 2.2.2.2**, the CEF considers the Gibbs energies of end-members, in the Fe-C-P system described by $G_{\text{Fe:C}}$ and $G_{\text{P:C}}$. The terms of $G_{\text{Fe:C}}$ for ferrite and austenite were accepted from the work Shubhank and Kang [140], originally published by Gustafson [172]. However, as no experimental data were available for $G_{\text{P:C}}$, the enthalpies of formation were estimated *ab-initio* using Density Function Theory (DFT). According to **Equation 16**, the values of $G_{\text{P:C}}$ were implemented into the ternary Fe-C-P database. The magnitude of the *ab-initio* simulations is in reasonable agreement with the optimized data of Shim et al. [30], but the physical background of the DFT calculations makes the data more valuable. By introducing only one ternary excess parameter for the austenite phase, the prediction of various isothermal sections between 800 - 1100 °C was significantly improved, see **Paper II**. With respect to the presently measured vertical sections in **Paper I**, the divergence in the solidus temperature was resolved.

The thermodynamic calculations for the Fe-C-0.10%P and Fe-0.20%C-P sections are now within the experimental error of the DSC measurements and the phase stabilities in a isoplethal section with high amount of P and C are much better reproduced, than in the work of Shim et al. [30]; demonstrated in **Figure 28**.

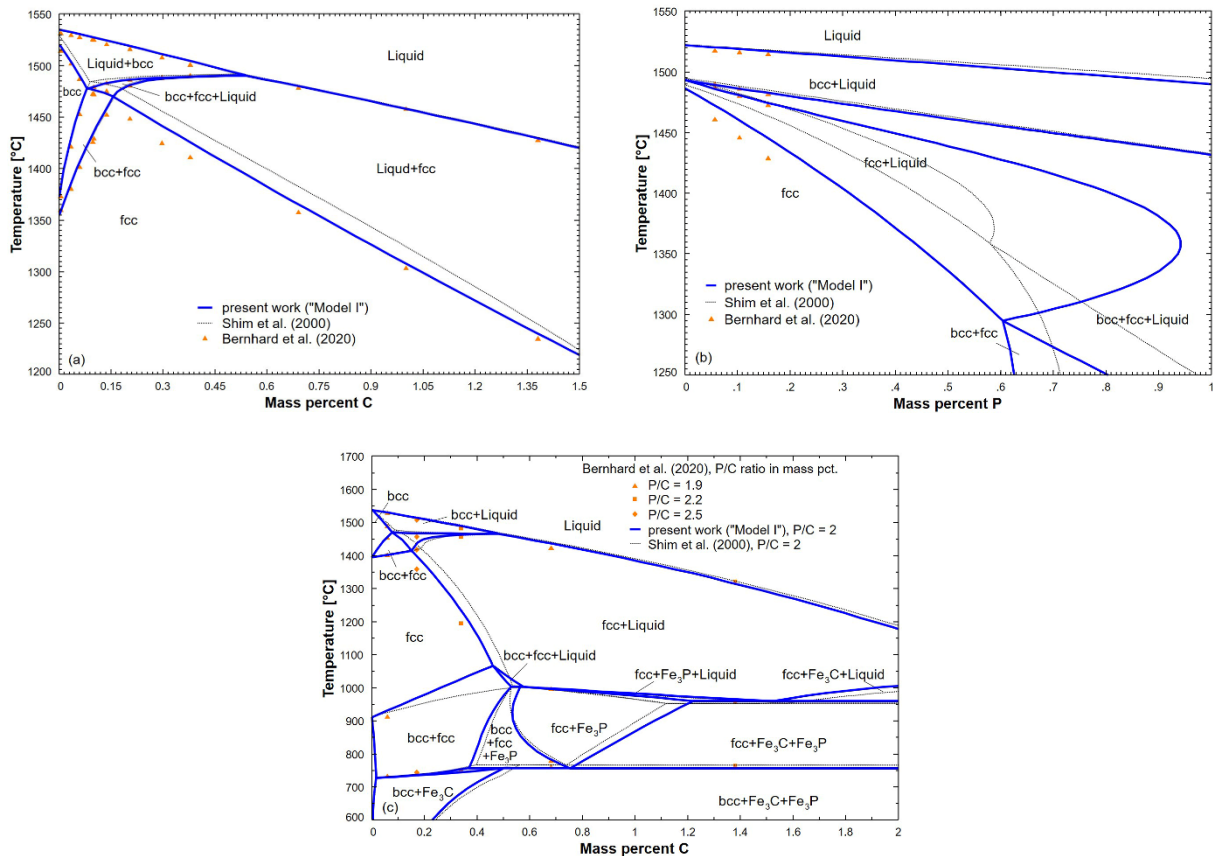


Figure 28: Comparison between calculated vertical sections and experimentally obtained phase boundaries from **Paper I** along with the thermodynamic assessment of Shim et al. [30]: Fe-C-0.10%P (a), Fe-0.20%C-P (b) and Fe with %P/%C ratio of 2 (c). [166]

4.3 A novel approach for *in-situ* characterization of γ -loops by coupling DSC and HT-LSCM: Application to the binary Fe-P system (Publication III)

In **Paper I**, special care was taken within the DSC trials on determining the melting equilibria and the γ/δ -transformation temperatures in the Fe-P and Fe-C-P systems. Therefore, the DSC setup was specifically adjusted to analyze the high-temperature (HT) region at $T > 1250$ °C. In the binary γ -loop, several parts of the phase boundaries could be precisely determined with the HT-setup. However, compared to the enthalpy change during melting, the measurable

effect in case of solid state transformations is limited, using the HT-setup. The start of the α/γ -transformation at temperatures between 900 - 1100 °C was not detectable in **Paper I**, see the lower phase boundary in **Figure 29 (a)**. Further difficulties arised in characterizing the end of the ferrite + austenite \leftrightarrow ferrite transformation at $P > 0.30$ %; corresponding to the upper phase boundary of samples B-I to B-III and C-I in **Figure 29 (a)** at $T > 1200$ °C. In a first step, see **Figure 29 (b)**, two samples with 0.147 %P and 0.419 %P were selected and the experimental parameters (sample mass, heating rate and crucible material) were modified to a DSC setup, typically used in classical heat capacity measurements up to $T \leq 1250$ °C (LT-DSC). The resolution of the DSC signal for both, the start of austenite formation and the end of the phase transformation, was sharply pronounced in case of the 0.147 %P sample. But while investigating the sample containing 0.419 %P, the onset in the DSC signal was still not detectable. Therefore, a novel approach was developed for coupling the DSC method and HT-LSCM for a complete reconstruction of the Fe-P γ -loop phase boundaries with the possibility to apply this approach for future work on the research field of Fe-based γ -loops in binary and ternary phase diagrams.

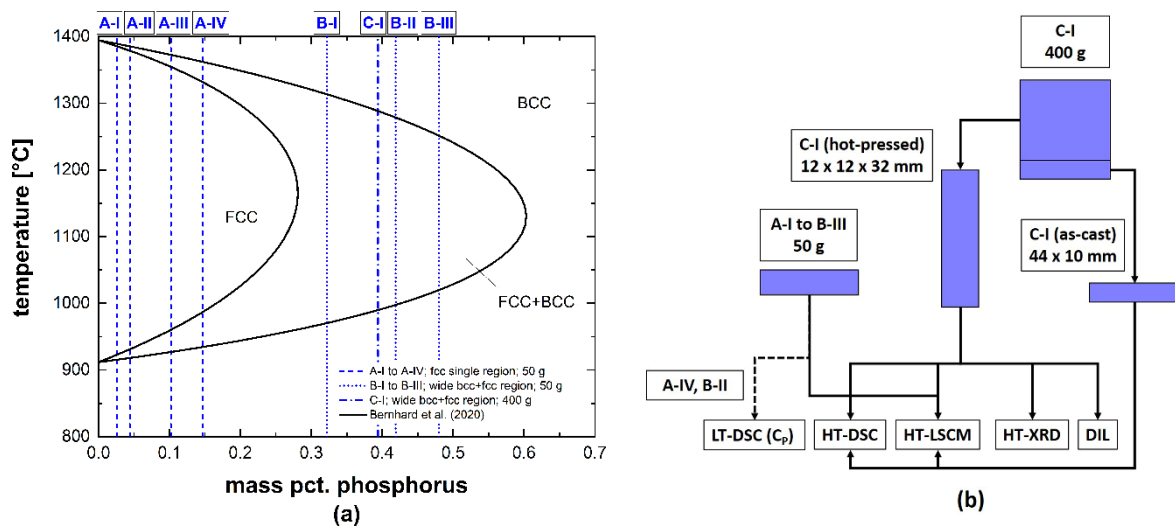


Figure 29: Investigated samples and their compositions in the binary Fe-P γ -loop (a) and “sample flow” in **Paper II** along with used experimental techniques. [173]

At the Chair of Ferrous Metallurgy (Montanuniversitaet Leoben), HT-LSCM represents a valuable tool for *in-situ* characterization of phase transformations at elevated temperatures. A description of the used microscope can be found in **Paper I** and **III**. In general, HT-LSCM enables the optical visualization of the phase transformation in a restricted field of observation. Recording with a selected frame rate provides the possibility for extensive post-processing and detailed analysis of the results. The HT-LSCM method was already applied in **Paper I** to support the evaluation of the DSC signal in the high-C and high-P region. In **Paper III**, a

standardized method was proposed to determine the phase boundaries of γ -loops in Fe-based systems. The procedure is based on image processing of coloured austenite and ferrite fractions, present at the surface of sample, and is explained in detail in **Paper III**. In order to critically evaluate the results of the coupled DSC/HT-LSCM approach, the utilization of other *in-situ* experimental methods were taken into account. Within extensive literature review provided in **Paper III**, the experimental techniques of equilibration, dilatometry, thermo-magnetic balance and X-ray diffraction were identified as standard methods, used to characterize phase stabilities in Fe-based γ -loops.

In a joint project together with Materials Center Leoben Forschungs GmbH, a general procedure was therefore established to perform *in-situ* HT-XRD experiments. The analysis was supported by additional standard dilatometry experiments. All four *in-situ* techniques (DSC, HT-LSCM, HT-XRD and dilatometry), were used to investigate a selected sample with 0.394 %P, see sample C-I in **Figure 29 (a)**. The phase transformation temperatures obtained from all experiments are summarized in **Table 7** and show reasonable agreement for both, the austenite formation ($bcc \leftrightarrow bcc + fcc$), as well as the austenite decomposition ($fcc + bcc \leftrightarrow bcc$). In the HT-XRD and dilatometry trials, the phase transformation temperatures were obtained at lower temperatures. However, similar to the DSC and HT-LSCM experiments, the analysis of the measured signals was quite challenging, see **Paper III**. Considering the observed errors, the temperatures are actually overlapping and the results confirmed the approach of coupling DSC and HT-LSCM for a full reconstruction of the γ -loop.

Table 7: Measured phase transformation temperatures of a sample containing 0.394 %P using various *in-situ* experimental techniques. [173]

Phase boundary	DSC	HT-LSCM	HT-XRD	Dilatometry
$bcc \leftrightarrow bcc + fcc$	-	$1000 \pm 10 \text{ }^\circ\text{C}$	$976.5 \pm 10 \text{ }^\circ\text{C}$	$976 \pm 20 \text{ }^\circ\text{C}$
$fcc + bcc \leftrightarrow bcc$	$1292.6 \pm 5 \text{ }^\circ\text{C}$	$1285 \pm 5 \text{ }^\circ\text{C}$	$1260 \pm 10 \text{ }^\circ\text{C}$	$1260 \pm 20 \text{ }^\circ\text{C}$

The γ -loop reconstructed by HT-LSCM observations and the data of the DSC analysis from **Paper I** and **III** are represented in **Figure 30**, along with data from literature [37–39]. In general, the present results are in best agreement with the most recently proposed temperatures of Fischer et al. [39]. In this work [39], high quality samples with low amounts of trace elements (C, Mn, N) were investigated by the thermo-magnetic balance. The good correlation with the work of Fischer et al. [39] indicates, that the developed approach leads to very reasonable results over the whole composition range. Higher deviations of the HT-LSCM observations from the available data have to be accepted only in the low P region ($P < 0.10$ mass pct.) at

decreased temperatures (900 - 1000 °C). However, in this range, the DSC analysis provides complementary, accurate temperatures for the fcc+bcc \leftrightarrow fcc transformation. By comparing the experimental data with thermodynamic optimizations from literature [25–27], best agreement was obtained with the work in **Paper II**.

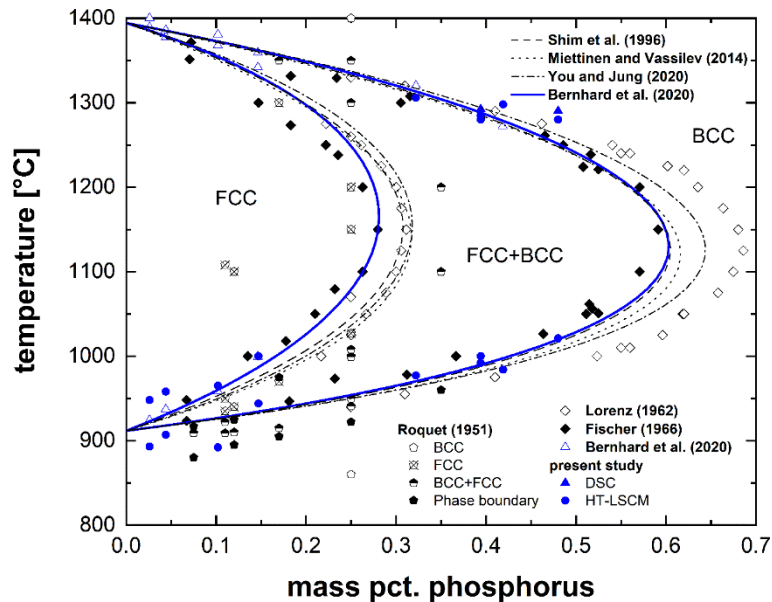


Figure 30: Experimentally characterized phase boundaries in the Fe-P γ -loop coupling DSC and HT-LSCM along with data from literature [37–39] and the DSC measurements of **Paper I**. The measured values are compared with published assessments [25–27] and the optimization in **Paper II**. [173]

Finally, *in-situ* HT-XRD experiments were carried out to quantitatively determine the phase fractions of austenite and ferrite by Rietveld refinement at elevated temperatures of 1050 °C, 1100 °C and 1150 °C; again, the sample containing 0.394 %P was investigated. The results were compared with recalculated phase fractions obtained by Lorenz et al. [38] using the thermo-magnetic balance. Excellent agreement between both experimental datasets is evident from **Figure 31**. Further, thermodynamic calculations of phase fractions over temperature were performed with references [25–27] and the assessment in **Paper II**. In general, the HT-XRD data indicate less stability of austenite than predicted by the models. This fact can be directly assigned to the optimized phase boundaries in **Figure 30**: The γ -loop in all modelling studies is slightly shifted to higher concentrations of P. As a consequence, the stability of austenite is increased and applying the Lever-Rule will give higher values for the austenite fractions. It can be seen in the phase diagram of **Figure 30**, that within the modelling work of **Paper II**, the maximum solubility of P, as proposed by Fischer et al. [39], was considered as most reliable. The reduced stability of austenite assumed in the γ -loop of **Paper II** results in the best agreement with the quantitative phase fractions from the HT-XRD experiments. The

calculations are nearly within the experimental error and qualitatively represent the course of the present phase fractions most accurately.

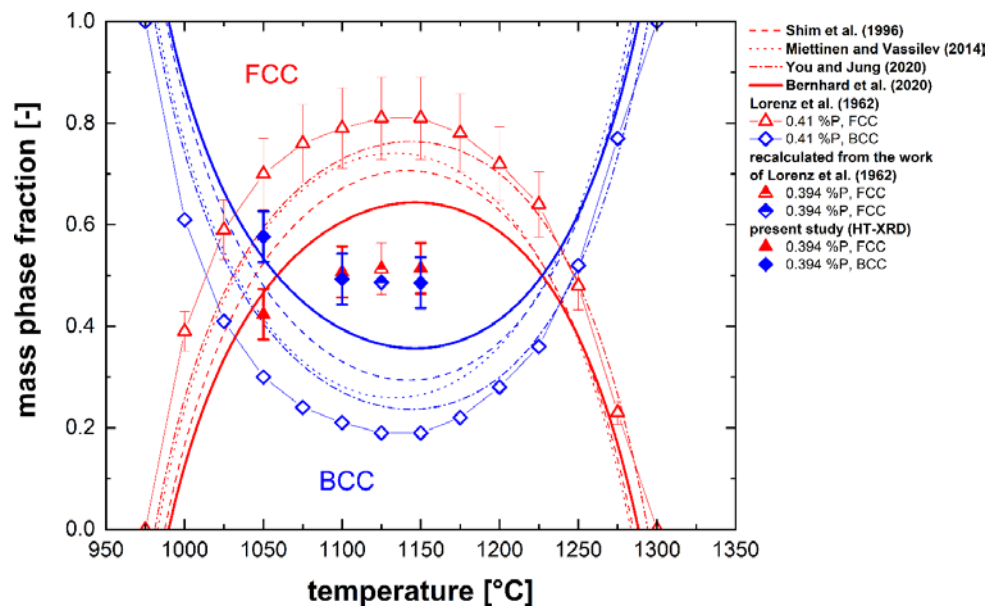


Figure 31: Quantitative phase fractions of austenite and ferrite obtained by Rietveld refinement using HT-XRD at 1050 °C, 1100 °C and 1150 °C and the comparison with experimental data from literature [38]. The phase fractions were calculated with references [25–27] and **Paper II.** [173]

4.4 Development of a microsegregation model for the continuous casting process with special focus on rephosphorized steels (Paper IV-V)

The topic on microsegregation in continuous casting and the relevance for determining the real solidus temperature under non-equilibrium solidification conditions was extensively discussed in **Chapter 2.1.3**. The development of an in-house solution for microsegregation modelling was started by the present author in the master thesis [174] with focus on calculating solidification of low carbon steel grades. Within the PhD thesis, this model was extended to a general approach covering the whole peritectic range in the multicomponent Fe-based system. Though the algorithm is partly explained in **Paper V** [175], the calculation scheme is described in detail in this chapter, as several updates have been performed in the PhD work, since publication of **Paper V** due to recently available thermodynamic data, particularly with respect to phosphorus.

4.4.1 General model description

All input and out parameters of the microsegregation model are schematically represented in **Figure 32**:

Initial data: The general calculation starts by inserting the chemical composition of the steel grade and the definition of the local cooling rate T' . In the current version, 15 elements can be considered in the calculation; including C, Si, Mn, P, S, Al, Cu, Cr, Ni, Mo, V, Nb, Ti, B and N. The algorithm itself is based on the semi-integrated Ohnaka equation according to You et al. [84]. In contrast to the original form of the Ohnaka model in **Equation 4 (Chapter 2.1.3.2)**, the semi-integrated form in **Equation 19** enables to take into account local partition coefficients [84] by respecting the mass balance. Δf_s is the pre-defined increment of the solidification progress and increases from 0 to 1; Δf_s is currently set to 0.005.

$$C_L^{f_s+\Delta f_s} = C_L^{f_s} \left[\frac{1-\Gamma f_s}{1-\Gamma(f_s+\Delta f_s)} \right]^{\frac{1-k}{\Gamma}} \quad (19)$$

Morphology: In the model, dendritic-columnar growth is assumed with $\Gamma = 1-4\alpha k/(1+4\alpha k)$ according to **Equation 5 (Chapter 2.1.3.2)**. The coarsening of the dendrites during solidification is described by a semi-empirical relation between the local solidification time (t_f , s) and the secondary dendrite arm spacing (λ_2 , μm); given in **Equation 20** [176], depending on the initial carbon concentration C_0 in mass percent.

$$\lambda_2 = (23.7 - 13.1C_0^{1/3})t_f^{1/3} \quad (20)$$

Diffusion: Together with the diffusion coefficients of the elements in the solid state (D_s), using the Arrhenius approach (**Equation 21**), the λ_2 - t_f relation is inserted into the Fourier-Number α , given in **Equation 3 (Chapter 2.1.3.2)**. In the Arrhenius equation, D_0 is a pre-exponential coefficient in cm^2/s , Q is the activation energy in J/mol , R is the gas constant with 8.314 J/mol.K and T is the temperature in Kelvin.

$$D_s = D_0 \exp(-Q/RT) \quad (21)$$

Partition coefficients: The partition coefficients of each alloying element are required for the ferrite phase and the austenite phase (see **Chapter 2.1.3.2**) for calculating the enrichment in the interdendritic liquid. The partition coefficients of C, Si, Mn, P, S, Al, Cr, Ni, Mo and Cu were partly assessed in a publication [177] of the present author and within previous project work. In the PhD project work, data of micro-alloying elements (V, Nb, Ti), nitrogen and the strongly segregating element boron were implemented by FactSage [28] calculations, using the most recently available thermodynamic database FSSStel2019. For P, the newly obtained data in **Paper I and II** were used to improve the partition coefficient input data, see **Chapter 4.4.2**.

Temperature calculation: Empirical liquidus equations are applied to obtain the relation between f_s and the solidification temperatures. Analytical expressions for T_L are typically used to adjust the superheat of a specific steel grade in the continuous casting process, but can also be applied in conjunction with microsegregation models. In the latter case, the interdendritic liquid can be seen as a melt with very high amount of enriched elements. Inserting the actual chemical composition, calculated by **Equation 19** at each step of f_s will give the characteristic function of T depending on the solid fraction. The final solidus temperature is therefore defined as T_L of the melt with calculated enrichments of C_L at $f_s = 1$. In the model, the liquidus formula as suggested by Howe and Miettinen [178] is used. The expression of the liquidus equation is given in **Equation 22** [178], where T_L is separately calculated for austenite and ferrite.

$$T_L = T_L^0 + \sum_{i=1}^n A_i \%X_i + \sum_{j=1}^n B_j \%X_j \%C \quad (22)$$

T_L^0 is the melting point of pure iron (1538 °C for δ -Fe and 1528 °C for γ -Fe [178]). The coefficients A_i describe the decreasing effect of the alloying element X_i in mass pct. on T_L of Fe according to the phase diagram; whereas B_i represents the interaction of X_i with carbon (%C). The parameters A_i and B_i for C, Si, Mn and P were evaluated in **Paper IV**, where the coefficient of P was slightly modified; according to the results of **Paper I**. The original values of A_i and B_i [178] were taken for S, Cr, Ni and Mo. Similarly to the calculations of the partition coefficients, simulations with FactSage [28] and FSStel2019 were performed to extend the liquidus equation for Cu, V, Nb, Ti, N and B by fitting the results to the approach of Miettinen and Howe [178] in **Equation 22** within internal research work.

MnS formation: During solidification, the high enrichment of Mn and S may lead to the formation of MnS. Based on the interdendritic concentration and the current temperature, the MnS product is calculated at each step of f_s . If the solubility product is exceeded, MnS will form and the concentration of Mn and S is reduced to the equilibrium value given by the T-dependent **Equation 23** [179].

$$\log K_{MnS} = \frac{-8750}{T[K]} + 4.63 \quad (23)$$

Output: The main output data of the model are (i) the relation between f_s and T , (ii) enrichment concentrations of alloying elements and (iii) the phase transformation temperatures and phase fraction prediction of austenite, ferrite and the liquid phase during solidification. The latter data can be determined by incorporating the peritectic reaction into the model; the procedure is described in the next **chapter 4.4.2**. Based on the results, the thermo-physical properties [180] (i) heat capacity, (ii) latent heats, (iii) thermal conductivity and (iv) density can be calculated for further use in solidification modelling. The current parameter settings of the

microsegregation models for $D_S^{y,\delta}$, $k^{y,\delta}$ and the liquidus equation are summarized in **Table 8** and **Table 9**.

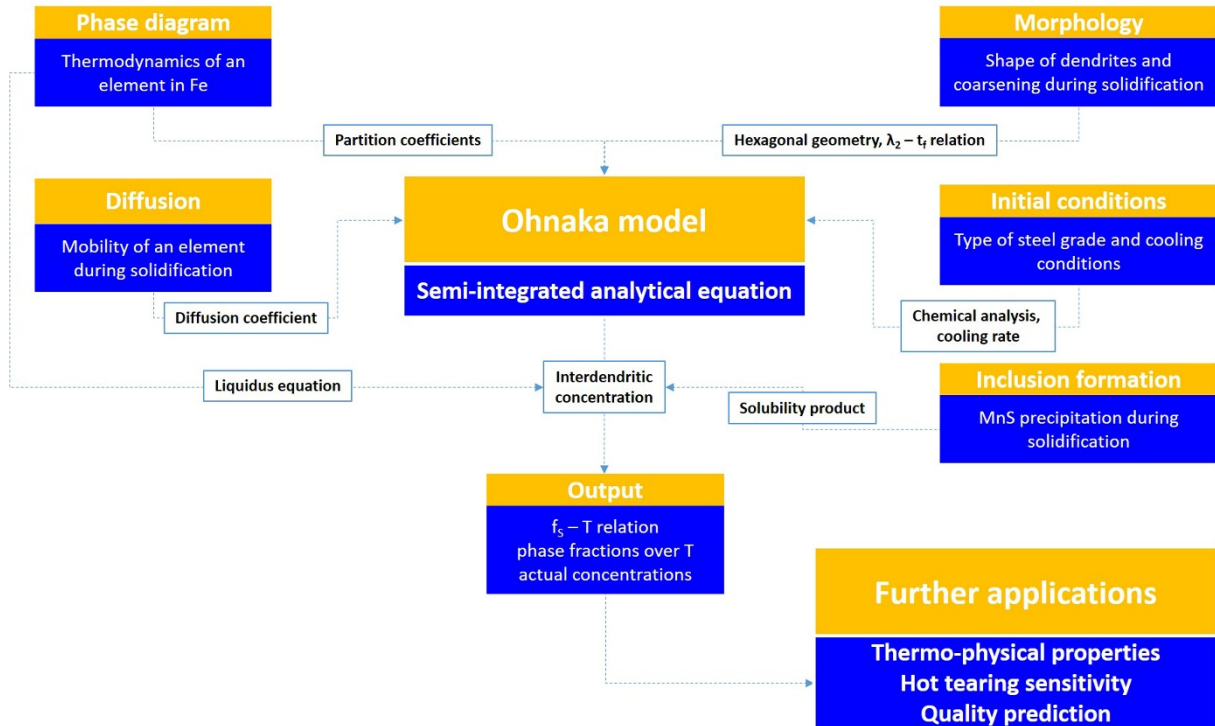


Figure 32: Schematic illustration of the microsegregation model with input and output data.

Table 8: Input parameters for the microsegregation model, partly referenced to [79,177,178,181] and internal research work at Chair of Ferrous Metallurgy (Montanuniversitaet Leoben).

	C	Si	Mn	P	S	Al
k^δ [-]	0.17	0.72	0.70	0.17	0.04	1.1
k^y [-]	$0.29+0.057\%C-5.47 \times 10^{-3}\%C^2$	0.70	0.70	0.12	0.02	1.1
D_0^δ [cm ² /s]	0.0127	8	0.76	2.9	4.56	5.9
Q^δ [J/mol]	-81379	-248948	-224430	-230120	-214639	-241186
D_0^y [cm ² /s]	0.0761	0.3	0.055	0.01	2.4	5.1
Q^y [J/mol]	-134429	-251218	-249128	-182666	-212232	-245800
A^δ [°C/wt%]	-76.24	-11.66	-5.62	-35.23	-32.81	0
B^δ [°C/wt% ²]	-10.3542	-4.3512	-0.223	-11.2	-17.7234	0
A^y [°C/wt%]	-60.09	-11.49	-4.26	-30.92	-33.19	0
B^y [°C/wt% ²]	-6.1399	-5.6055	0.453	-5.3494	-10.09	0

Table 9: Input parameters for the microsegregation model, partly referenced to [79,181] and internal research work at Chair of Ferrous Metallurgy (Montanuniversitaet Leoben).

	Cr	Ni	Mo	Cu	V	Nb	Ti	B	N
k^δ [-]	0.90	0.81	0.65	1	0.73	0.26	0.28	0.025	0.30
k^γ [-]	0.83	0.89	0.47	1	0.50	0.15	0.15	0.020	0.60
D_0^δ [cm ² /s]	2.4	1.6	3.47	2.6	4.8	50	3.15	0.008	0.008
Q^δ [J/mol]	-239785	-239994	-241375	-239994	-239994	-251960	-247693	-87900	-79078
D_0^γ [cm ² /s]	0.0012	0.34	0.068	0.7	0.284	0.83	0.15	0.002	0.91
Q^γ [J/mol]	-218991	-282378	-246856	-285976	-258990	-266479	-250956	-87900	-168490
A^δ [°C/wt%]	-1.95	-3.58	-2.2	0.17	-3.97	-6.61	-16.123	-101.06	-58.4
B^δ [°C/wt% ²]	-0.0329	-0.8364	-0.8451	0.22	2.871	1	9	-20.48	-10.4
A^γ [°C/wt%]	-2.47	-1.97	-4.36	0.36	-7.425	-8.43	-16.05	-95.77	-48.29
B^γ [°C/wt% ²]	1.3303	-0.5886	0.0701	1.3	4.7	2.5	7.49	-9.41	-0.92

4.4.2 Determination of the partition coefficients $k_P^{\delta,\gamma}$ from Paper I and II

The experimentally reconstructed liquidus and solidus phase boundaries from **Paper I** were used to determine the partition coefficient k_P^δ over temperature; the results are graphically compared with data of previous publications [45,69] in **Figure 33**. The melting temperature of pure Fe (1538 °C) represents the dilute solution, whereas the lower limit of 1100 °C is already close to the eutectic temperature in the binary Fe-P phase diagram (see **Figure 1**). In order to guarantee a better comparability with the data of Battle and Pehlke [69], the values of Morita and Tanaka [45] and those obtained within the present work were converted from mass percent-related to mole fraction-related; according to references [182,183]. The lines are plotted separately in **Figure 33**. However, k_P^δ (mole fraction) and k_P^δ (mass percent) are identical at infinite dilution and only a minor difference is observed at lower temperatures ($\Delta k_P^\delta \sim 0.01$ at 1150 °C). Since in fact, the solidus and liquidus line in the Fe-P phase diagram do not decrease perfectly linear, all plotted partition coefficients are clearly dependent on temperature. The temperature dependence of k_P^δ is mostly pronounced in the work of Battle and Pehlke [69]; k_P^δ increases from a very low value of 0.02 at the melting point of pure Fe (1538 °C) to 0.27 at 1130 °C. The strong curvature of k_P^δ can be explained by the shape of the solidus line in the phase diagram of Spencer and Kubaschewski [72]. Further, $k_P^\delta = 0.02$ at infinite dilution seems not to be reliable, because this value significantly disagrees with other

data reported in literature ranging from $k_P^\delta = 0.136 - 0.27$ [45,65–67,71]. In general, the results of the present study correlate well with the data of Morita and Tanaka [45], see **Figure 33**. The value of $k_P^\delta = 0.17$ at infinite dilution is slightly higher; below 1350 °C both datasets become very similar. Setting the value of $k_P^\delta = 0.17$ in the microsegregation model as constant is in agreement with the data of Fischer et al. [66,67].

As the value of k_P^γ in binary Fe-P alloys can not be derived from the phase diagram data of **Paper I** (see **Chapter 2.1.3.2**), the partition coefficient was estimated by thermodynamic optimizations [25–27] and **Paper II** in **Figure 34** taking the example of an Fe-0.10%P alloy. In order to check the reliability of the calculations, k_P^δ was firstly calculated in **Figure 34 (a)** and **(b)**. It can be seen that the dependence on temperature is less pronounced using **Paper II** than in other assessments. The calculated value of $k_P^\delta = 0.17-0.18$ is in excellent correlation with data of **Paper I** in **Figure 33** at infinite dilution. Within the calculations of k_P^γ , the ferrite phase was suppressed. The final partition coefficient of P between liquid and austenite is 0.12 and lower than predicted by other assessments, but correlates with the work of Nakamura and Esaka [71]. The presently obtained values for $k_P^{\delta,\gamma}$ were implemented into the current version of the microsegregation model.

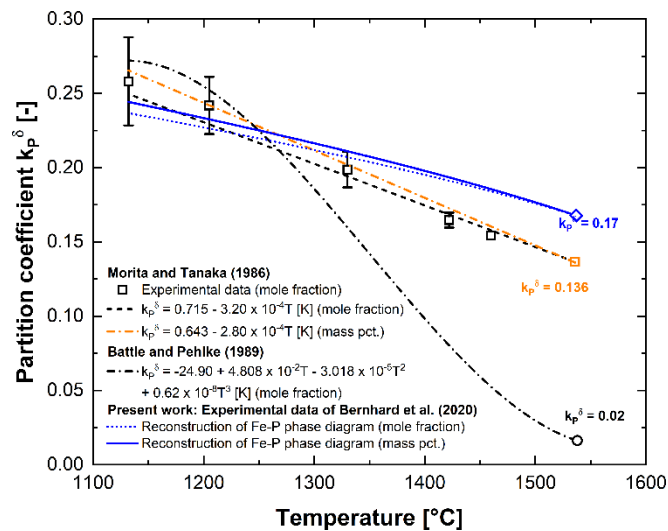


Figure 33: Partition coefficient of phosphorus between δ -Fe and liquid, depending on temperature reported in literature [45,69] along with the present analysis based on **Paper I**.

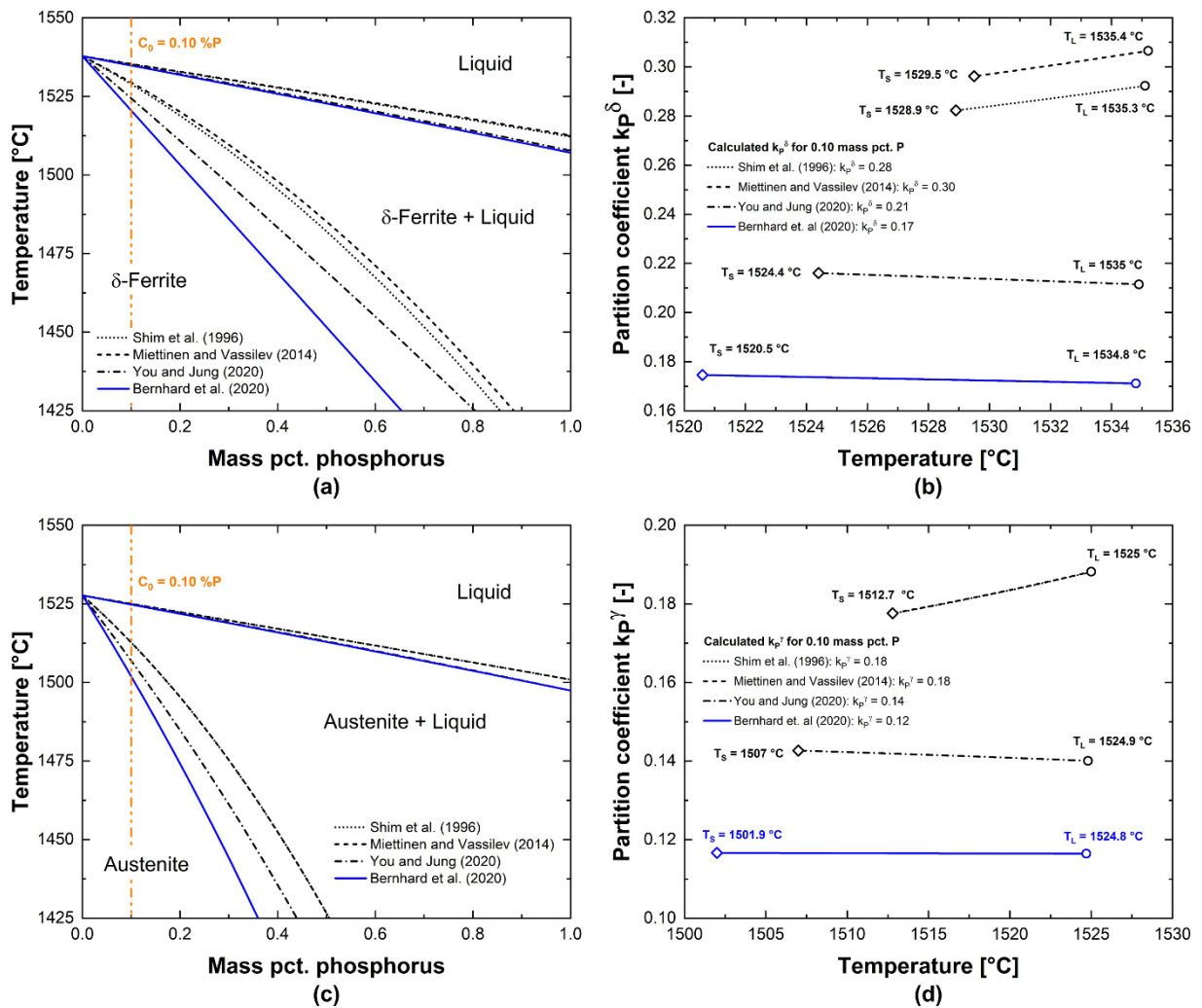


Figure 34: Calculated values of $k_P^{\delta, \gamma}$ for a Fe-0.10%P alloy using thermodynamic optimizations [25–27] and **Paper II**.

4.4.3 Assessment of analytical liquidus equations for steel and incorporating the start of the peritectic reaction into the model

The relevance of liquidus equations for use in microsegregation models was explained in **Chapter 4.4.1**. As evident from **Chapter 2.1.1**, the most important alloying elements in rephosphorized steels are C, Si, Mn, Al and P. For the Fe-C-Si-Mn-Al-P system, various analytical liquidus equations were therefore evaluated in **Paper IV**, using thermal analysis techniques. Data for Si, Mn and Al were considered from previous research work at the Chair of Ferrous Metallurgy. The measured liquidus temperatures in the Fe-P and Fe-C-P systems from **Paper I** were considered along with additional measurements in the Fe-Al-P, Fe-Si-P, Fe-C-Mn-P and Fe-C-Si-Mn-Al-P systems, which were performed within the PhD project to check the predictions of T_L in highly P-alloyed samples. In total, results of 180 alloys were analyzed

with the selected equations, where the expression of Howe and Miettinen [178] showed the best agreement with the data. The total error of the equations is 2.1 ± 1.6 °C and is close to the typical experimental error of ± 2 °C using DSC and differential thermal analysis (DTA). [166] By slightly modifying the parameters of phosphorus, the predictions of T_L could be improved particularly for P-alloyed steels. The results are summarized in **Figure 35** and show the correlation between the calculated value of T_L and the experimentally determined temperature. As described in the previous **Chapter 4.4** the implemented parameters for calculating T_L according to the approach of Miettinen and Howe [178] are given in **Table 8** and **Table 9**.

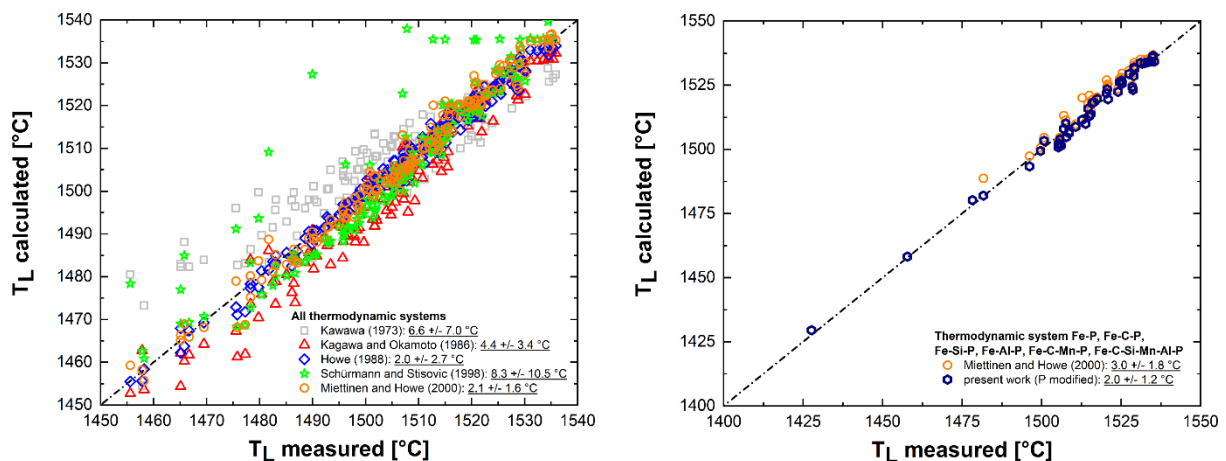


Figure 35: Comparison between calculated liquidus temperatures using analytical equations from literature and the comprehensive dataset of 180 measurements in the Fe-C-Si-Mn-Al-P system (a) and specific improvement of the expression of Miettinen and Howe [178] for P-alloyed samples by optimizing the P parameter (b) according to **Paper IV** [184].

A major difference between the expressions is the availability of a single equation or separated formulas of T_L for ferrite and austenite. If two equations are used, a thermodynamically consistent description of the peritectic start temperature during solidification of Fe-C multicomponent system can be provided. In previous microsegregation models, this temperature was modelled e.g. by regression analysis [79,86]. The calculation procedure implemented in the microsegregation model is shown in **Figure 34** on the example of an hypoperitectic Fe-0.296%C-0.11%P alloy investigated by DSC in **Paper I**. In order to compare the model with the equilibrium data, the Fourier-Number was set to infinity. In the Miettinen-Howe equation [178], the primary stable phase at the liquidus temperature is always the phase showing the higher value of T_L , depending on the actual chemical composition. In the present microsegregation model, the calculated enrichment with **Equation 19** is inserted to both equations at each solidification step and if at a specific phase fraction, T_L of austenite exceeds the value for ferrite, the peritectic transformation starts. In **Figure 34**, the calculated start of the

peritectic reaction is 1491 °C at $f_s = 0.46$ and is in excellent agreement with the measured temperature of 1488.3 °C. The consideration of the peritectic reaction is of major importance for the enrichment calculations as the solidification is then controlled by the austenite phase and the partition coefficients and the diffusion coefficients are changing. As demonstrated in **Chapter 2.1.3.2** the change in the solidification sequence result generally in a much more strongly pronounced enrichment of the alloying elements. In contrast to the start, the end of the peritectic reaction is only possible by using a numerical approach to solve the solute redistribution during solidification. The implementation of the algorithm, solving the diffusion profile in the solid state, will be part of future research work. Applications of the microsegregation model for enrichment calculations and predicting the hot tear sensitivity of P-alloyed steels were demonstrated in the state of the art section (**chapter 2**).

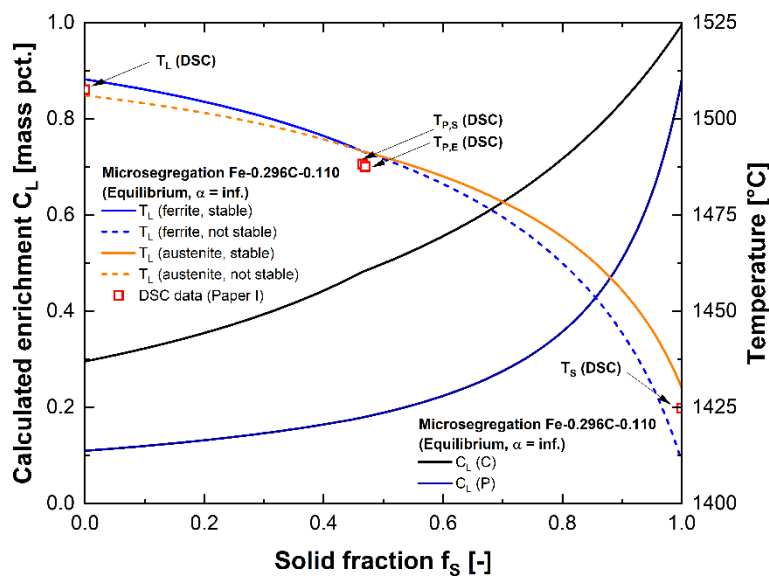


Figure 36: Calculated enrichments of C and P under equilibrium conditions ($\alpha \rightarrow \infty$) and temperature evolution predicted for an Fe-0.296%C-0.110%P alloy (hypo-peritectic) with the present model along with experimental data obtained by DSC in **Paper I**.

The present **Chapter 4** demonstrates a systematic approach of transferring experimental data obtained close to equilibrium conditions into kinetic solidification models, in order to consider localized cooling in the continuous casting process. New accurate phase diagram data are the basis for further development of solidification models and can be converted from experimental and modelling work into relevant input parameters for microsegregation calculations. In this chapter, the methodology was demonstrated for rephosphorized steels with phosphorus as important alloying element. Future research work will focus on the implementation of improved thermodynamics (experimental data and modelling studies) of other strongly segregating elements, as boron and sulphur, into the microsegregation model.

5 Summary and conclusion

Within this thesis, the effect of phosphorus on solidification and high-temperature phase transformations in steel was extensively studied. In the experimental part, the *in-situ* methods of differential scanning calorimetry (DSC), high-temperature laser scanning confocal microscopy (HT-LSCM), high-temperature X-ray diffraction (HT-XRD) and dilatometry were applied to investigate phase equilibria in 40 high-purity alloys of the Fe-P and Fe-C-P key-systems. Based on the experimental results, a complete CALPHAD-type (Calculation of Phase Diagrams) thermodynamic modelling study was carried out. Finally, the new results were implemented into a microsegregation model for calculating solidification of steel under continuous casting conditions.

In the binary Fe-P system, the DSC trials indicated a significantly lower solidus temperature (T_S) than predicted by most recently published thermodynamic assessments. Special focus was placed on composition range of $P < 1$ mass pct. as a lack of experimental data was identified in literature. In this region, the deviation between the measured values of T_S and the calculations exceeded 50 °C; with increasing amount of phosphorus ($P = 1.5 - 2$ %) a better correlation of T_S was obtained. Similar to the calculation results in the binary Fe-P system, the stability of the liquid phase was underestimated in the vertical sections Fe-C-0.10%P and Fe-0.20%C-P. In a third ternary section with mass percent of P to C equals two, the analysis of the DSC signals was supported by HT-LSCM observations. In those alloys, containing high amounts of C and P, the calculated phase stabilities of ferrite (δ -Fe) and austenite (γ -Fe), using previous thermodynamic assessments of the Fe-C-P system, significantly disagreed with the new experimental data.

In the CALPHAD-type thermodynamic modelling of the Fe-P and Fe-C-P system, the use of the modified quasichemical model (MQM) for the liquid phase resolved the discrepancies in the solidus temperature without introducing a ternary excess Gibbs energy parameter. By improving the thermodynamic description of the binary Fe-P phase diagram, the measured phase equilibria in the Fe-C-P could be predicted more accurately. The consideration of *ab-initio* calculations of enthalpies of formation for the austenite and ferrite phase enhanced the calculations in various ternary isothermal sections between 800 - 1100 °C. Finally, the predicted phase stabilities of δ -Fe and γ -Fe phases in the vertical section with high carbon and phosphorus concentrations are in excellent agreement with the experimental data.

A novel approach of coupling DSC analysis and HT-LSCM observations for characterizing the phase boundaries in the Fe-P γ -loop was successfully evaluated with the well established in-situ methods of HT-XRD and dilatometry. The obtained phase transformation temperatures correlate with the most recently published data from literature. Further, quantitative phase fraction analysis of ferrite and austenite were carried out by Rietveld refinement using HT-XRD at elevated temperatures of 1050 °C, 1100 °C and 1150 °C. The measured phase fractions are in reasonable agreement with calculations of the thermodynamic reassessment, performed in the present study.

Finally, the obtained experimental data and thermodynamic calculations were used to improve a microsegregation model with particular focus on rephosphorized steel grades. Therefore, analytical liquidus equations from literature were evaluated and the partition coefficients $k_{P^{\gamma,\delta}}$ were calculated with the current optimization of the Fe-P system. The thermodynamically consistent implementation of the peritectic start temperature was compared with DSC results of the Fe-C-0.10%P system by setting the model to the equilibrium mode.

Bibliography

- [1] worldsteel association, <https://www.worldsteel.org/media-centre/press-releases/2021/world-steel-in-figures-2021.html>, Accessed: 28.06.2021
- [2] R.A. Mulford, C.J. McMahon, D.P. Pope and H.C. Feng, Temper embrittlement of Ni-Cr Steels by phosphorus. *Metallurgical and Materials Transactions A* 7 (1976), 8, pp. 1183–1195. doi:10.1007/BF02656602
- [3] I. Olefjord, Temper embrittlement. *International Metals Reviews* 23 (1978), 1, pp. 149–163. doi:10.1179/imtr.1978.23.1.149
- [4] R. Viswanathan, Temper embrittlement in a Ni-Cr steel containing phosphorus as impurity. *Metallurgical and Materials Transactions B* 2 (1971), 3, pp. 809–815. doi:10.1007/BF02662740
- [5] D.B.V.d. Castro, J.M. Ventura, C.O.F.T. Ruckert, D. Spinelli and W.W. Bose Filho, Influence of phosphorus content and quenching/tempering temperatures on fracture toughness and fatigue life of SAE 5160 steel. *Materials Research* 13 (2010), 4, pp. 445–455. doi:10.1590/S1516-14392010000400005
- [6] X.-M. Chen, S.-H. Song, L.-Q. Weng, S.-J. Liu and K. Wang, Relation of ductile-to-brittle transition temperature to phosphorus grain boundary segregation for a Ti-stabilized interstitial free steel. *Materials Science and Engineering: A* 528 (2011), 28, pp. 8299–8304. doi:10.1016/j.msea.2011.08.002
- [7] J.S. Rege, M. Hua, C.I. Garcia and A.J. Deardo, The Segregation Behavior of Phosphorus in Ti and Ti+Nb Stabilized Interstitial-Free Steels. *ISIJ International* 40 (2000), 2, pp. 191–199. doi:10.2355/isijinternational.40.191

- [8] W.-m. Guo, Z.-c. Wang, Y.-d. Li, N. Xu and J.-b. Shi, Effect of Phosphorus Content on Properties of Warm-Rolled Interstitial-Free Steel Sheets. *Metallography, Microstructure, and Analysis* 2 (2013), 4, pp. 249–256. doi:10.1007/s13632-013-0086-4
- [9] X.-l. Zhang, H.-f. Hou, T. Liu, Q. Zhou, H.-j. Liu, Y.-l. Zhang, H.-x. Cui and Z. Lv, Effect of annealing time and phosphorus addition on bake hardening behavior of ultra-low carbon bake hardening steel. *Journal of Iron and Steel Research International* 25 (2018), 12, pp. 1287–1295. doi:10.1007/s42243-018-0189-x
- [10] D. Krizan, TRIP steels: Advanced High-Strength Multiphase Steels for Automotive Applications. 14th International Scientific Conference CO-MAT-TECH, pp. 1-10, Trnava, Slovak Republic (2006).
- [11] E. Jimenez-Melero, N.H. van Dijk, L. Zhao, J. Sietsma, S.E. Offerman, J.P. Wright and S. van der Zwaag, The effect of aluminium and phosphorus on the stability of individual austenite grains in TRIP steels. *Acta Materialia* 57 (2009), 2, pp. 533–543. doi:10.1016/j.actamat.2008.09.040
- [12] L. Barbé, K. Verbeken and E. Weytjck, Effect of the Addition of P on the Mechanical Properties of Low Alloyed TRIP Steels. *ISIJ International* 46 (2006), 8, pp. 1251–1257. doi:10.2355/isijinternational.46.1251
- [13] G. Sahoo, A. Deva, B. Singh and A. Sexena, Corrosion Behaviour of High Phosphorus Containing Cu-Cr Weather Resistant Steel. *Journal of Metals, Materials and Minerals* 24 (2014), 2, pp. 1–7. doi:10.14456/jmmm.2014.9
- [14] M. Yamashita, H. Nagano, T. Misawa and H.E. Townsend, Structure of Protective Rust Layers Formed on Weathering Steels by Long-term Exposure in the Industrial Atmospheres of Japan and North America. *ISIJ International* 38 (1998), 3, pp. 285–290. doi:10.2355/isijinternational.38.285
- [15] M. Yamashita, H. Miyuki, Y. Matsuda, H. Nagano and T. Misawa, The long term growth of the protective rust layer formed on weathering steel by atmospheric corrosion during a quarter of a century. *Corrosion Science* 36 (1994), 2, pp. 283–299. doi:10.1016/0010-938X(94)90158-9
- [16] S. Lee and B.C.D. Cooman, Effect of Phosphorus on the Magnetic Losses of Non-oriented 2% Si Steel. *ISIJ International* 52 (2012), 6, pp. 1162–1170. doi:10.2355/isijinternational.52.1162

- [17] I. Tanaka and H. Yashiki, Magnetic properties and recrystallization texture of phosphorus-added non-oriented electrical steel sheets. *Journal of Magnetism and Magnetic Materials* 304 (2006), 2, e611-e613. doi:10.1016/j.jmmm.2006.02.155
- [18] H. Okamoto, The Fe-P (iron-phosphorus) system. *Bulletin of Alloy Phase Diagrams* 11 (1990), 4, pp. 404–412. doi:10.1007/BF02843320
- [19] P. Perrot, Carbon – Iron – Phosphorus. Berlin Heidelberg (2008), Springer.
- [20] W. Franke, K. Meisel, R. Juza and W. Biltz, Beiträge zur systematischen Verwandtschaftslehre. 60. Über die Verwandtschaft von Phosphor zu Eisen. *Zeitschrift für anorganische und allgemeine Chemie* 218 (1934), 4, pp. 346–359. doi:10.1002/zaac.19342180403
- [21] K. Meisel, Über die Kristallstruktur des FeP₂. *Zeitschrift für anorganische und allgemeine Chemie* 218 (1934), 4, pp. 360–364. doi:10.1002/zaac.19342180404
- [22] M. Heimbrecht and W. Biltz, Zur Frage des Bestehens eines höheren Eisenphosphids. *Zeitschrift für anorganische und allgemeine Chemie* 242 (1939), 3, pp. 233–236. doi:10.1002/zaac.19392420303
- [23] W. Jeitschko and D.J. Braun, Synthesis and crystal structure of the iron polyphosphide FeP₄. *Acta Crystallographica Section B: Structural Crystallography and Crystal Chemistry* 34 (1978), 11, pp. 3196–3201. doi:10.1107/S056774087801047X
- [24] H. Ohtani, N. Hanaya, M. Hasebe, S.-i. Teraoka and M. Abe, Thermodynamic analysis of the Fe–Ti–P ternary system by incorporating first-principles calculations into the CALPHAD approach. *Calphad* 30 (2006), 2, pp. 147–158. doi:10.1016/J.CALPHAD.2005.09.006
- [25] J.H. Shim, C.S. Oh and D.N. Lee, Thermodynamic Properties and Calculation of Phase Diagram of the Fe-P System. *Journal of the Korean Institute of Metals and Materials* 34 (1996), 11, pp. 1385–1393.
- [26] J. Miettinen and G. Vassilev, Thermodynamic Description of Ternary Fe-X-P Systems. Part 1: Fe-Cr-P. *Journal of Phase Equilibria and Diffusion* 35 (2014), 4, pp. 458–468. doi:10.1007/s11669-014-0314-x
- [27] Z. You and I.-H. Jung, Critical Evaluation and Thermodynamic Optimization of the Fe-P System. *Metallurgical and Materials Transactions B* 51 (2020), 6, pp. 3108–3129. doi:10.1007/s11663-020-01939-0
- [28] C.W. Bale, E. Bélisle, P. Chartrand, S.A. Deckerov, G. Eriksson, A.E. Gheribi, K. Hack, I.-H. Jung, Y.-B. Kang, J. Melançon, A.D. Pelton, S. Petersen, C. Robelin, J. Sangster, P.

Spencer and M.-A. van Ende, FactSage thermochemical software and databases, 2010–2016. *Calphad* 54 (2016), pp. 35–53.

[29] P. Gustafson, Study of the Thermodynamic Properties of the C-Cu-Fe-P, Fe-Mo-P and Fe-Ni-P Systems. Report IM-2549, Swedish Institute for Metals Research, Stockholm, Sweden, 1990

[30] J.H. Shim, D.N. Lee and C.S. Oh, Thermodynamic assessment of the Fe-C-P system. *Zeitschrift für Metallkunde* 91 (2000), pp. 114–120.

[31] V. Raghavan, C-Fe-P (Carbon-Iron-Phosphorus). *Journal of Phase Equilibria and Diffusion* 25 (2004), 6, pp. 541–542. doi:10.1007/s11669-004-0070-4

[32] J.E. Stead, Iron and Phosphorus. *Journal of the Iron and Steel Institute* 58 (1900), pp. 60–155.

[33] E. Gercke, Experimental Thermal and Metallographic Investigation on the System Iron Phosphorus. *Metallurgie* 5 (1908), 20, pp. 604–609.

[34] B. Saklatwalla, Constitution of the Iron and Phosphorous Compounds. *Journal of the Iron and Steel Institute* 77 (1908), pp. 92–103.

[35] N. Konstantinow, Phosphide of Iron. *Zeitschrift für anorganische und allgemeine Chemie* 66 (1910), pp. 209–227.

[36] J.L. Haughton, Alloys of Iron Research. Part VIII. The Constitution of Alloys of Iron and Phosphorus. *Journal of the Iron and Steel Institute* 115 (1927), pp. 417–433.

[37] P. Roquet and G. Jegaden, Contribution à l'étude du diagramme fer-phosphore. *Revue de Métallurgie* 48 (1951), 9, pp. 712–721. doi:10.1051/metal/195148090712

[38] K. Lorenz and H. Fabritius, Anwendung der magnetischen Waage zur Aufstellung von Zustandsschaubildern im Bereich des festen Zustandes eisenreicher Systeme Untersuchung am System Eisen-Phosphor. *Archiv für das Eisenhüttenwesen* 33 (1962), 4, pp. 269–275. doi:10.1002/srin.196203329

[39] W.A. Fischer, K. Lorenz, H. Fabritius, A. Hoffmann and G. Kalwa, Untersuchung von Phasenumwandlungen in reinen Eisenlegierungen mit der magnetischen Waage. *Archiv für das Eisenhüttenwesen* 37 (1966), 1, pp. 79–86. doi:10.1002/srin.196602736

[40] E. Wachtel, G. Urbain and E. Übelacker, Étude du Diagramme Fer-Phosphore par Analyse Magnétique et Thermique. *Comptes Rendus* 257 (1963), pp. 2470–2472.

- [41] H. Kaneko, T. Nishizawa, K. Tamaki and A. Tanifuji, Solubility of Phosphorus in alpha and gamma-Iron. *Journal of the Japan Institute of Metals* 29 (1965), 2, pp. 166–170. doi:10.2320/jinstmet1952.29.2_166
- [42] A.S. Doan and J.I. Goldstein, The ternary phase diagram, Fe-Ni-P. *Metallurgical and Materials Transactions B* 1 (1970), 6, pp. 1759–1767. doi:10.1007/BF02642026
- [43] M. Ko and T. Nishizawa, Effect of Magnetic Transition on the Solubility of Alloying Elements in Alpha Iron. *Journal of the Japan Institute of Metals* 43 (1979), 2, pp. 118–126. doi:10.2320/jinstmet1952.43.2_118
- [44] E. Schürmann and H.-P. Kaiser, Beitrag zu den Schmelzgleichgewichten der Eisen-Aluminium- und Eisen-Phosphor-Legierungen. *Archiv für das Eisenhüttenwesen* 51 (1980), 8, pp. 325–327. doi:10.1002/srin.198004848
- [45] Z. Morita and T. Tanaka, Equilibrium distribution coefficient of phosphorus in iron alloys. *ISIJ International* 26 (1986), 2, pp. 114–120. doi:10.2355/isijinternational1966.26.114
- [46] H.-P. Hofmann, K. Löhberg and W. Reif, Über die Löslichkeit des Phosphors in Eisen und Eisen-Kohlenstoff-Legierungen unterhalb 1000°C. *Archiv für das Eisenhüttenwesen* 41 (1970), 10, pp. 975–982. doi:10.1002/srin.197001687
- [47] E. Schürmann, U. Hensgen and J. Schweinichen, Schmelzgleichgewichte der ternären Systeme Eisen-Kohlenstoff-Silicium und Eisen-Kohlenstoff-Phosphor: Untersuchungen zur Festlegung der Liquidusflächen und der Linien doppelter Sättigung auf der eisenreichen Seite der stabilen und metastabilen Systeme Eisen-Kohlenstoff-Silicium und Eisen-Kohlenstoff-Phosphor. *Giessereiforschung* 36 (1984), 4, pp. 121–129.
- [48] Foundry Technologies & Engineering GmbH (FT&E), <https://www.giessereilexikon.com/>, Accessed: 16.06.2021
- [49] P. Görens and W. Döbelstein, The Fe-P-C Ternary System. *Metallurgie* 5 (1908), pp. 561–566.
- [50] F. Wüst, Influence of Phosphorus on Iron-Carbon (in German). *Metallurgie* 5 (1908), pp. 73–87.
- [51] J.E. Stead, Iron, Carbon, Phosphorus. *Journal of the Iron and Steel Institute* 97 (1918), pp. 389–415.
- [52] R. Vogel, Ueber das System Eisen-Phosphor-Kohlenstoff. *Archiv für das Eisenhüttenwesen* 3 (1929), 5, pp. 369–381.

- [53] T. Ohide and G. Ohira, The solidification structures of iron-carbon-phosphorus ternary Alloys. *British Foundryman* 68 (1975), pp. 106–115.
- [54] G. Langenscheid, H.A. Mathesius and F.K. Naumann, Anwendung des quantitativen Fernsehmikroskopes und der Elektronenstrahlmikrosonde für die Untersuchung des Systems Eisen-Kohlenstoff-Phosphor bei 900 bis 1000°C. *Archiv für das Eisenhüttenwesen* 41 (1970), 8, pp. 817–824. doi:10.1002/srin.197001663
- [55] T. Nishizawa, unpublished work, cited by Gustafson (1990) and Shim et al. (2000).
- [56] P. Presoly, R. Pierer and C. Bernhard, Identification of Defect Prone Peritectic Steel Grades by Analyzing High-Temperature Phase Transformations. *Metallurgical and Materials Transactions A* 44 (2013), 12, pp. 5377–5388. doi:10.1007/s11661-013-1671-5
- [57] P. Presoly, G. Xia, P. Reisinger and C. Bernhard, Continuous Casting of Hypo-peritectic Steels: Mould Thermal Monitoring and DSC-analysis. *Berg- und Hüttenmännische Monatshefte* 159 (2014), 11, pp. 430–437. doi:10.1007/s00501-014-0306-5
- [58] G. Azizi, B.G. Thomas and M. Asle Zaeem, Review of Peritectic Solidification Mechanisms and Effects in Steel Casting. *Metallurgical and Materials Transactions B* 51 (2020), 5, pp. 1875–1903. doi:10.1007/s11663-020-01942-5
- [59] R. Vertnik and B. Šarler, Solution of a continuous casting of steel benchmark test by a meshless method. *Engineering Analysis with Boundary Elements* 45 (2014), pp. 45–61. doi:10.1016/j.enganabound.2014.01.017
- [60] B.G. Thomas, J.K. Brimacombe and I.V. Samarasekera, The Formation of Panel Cracks in Steel Ingots: A State-of-the-Art Review. *ISS Transactions* 7 (1986), pp. 7–20.
- [61] J.K. Brimacombe, The challenge of quality in continuous casting processes. *Metallurgical and Materials Transactions B* 30 (1999), 4, pp. 553–566. doi:10.1007/s11663-999-0016-7
- [62] J.K. Brimacombe and K. Sorimachi, Crack formation in the continuous casting of steel. *Metallurgical and Materials Transactions B* 8 (1977), 2, pp. 489–505. doi:10.1007/BF02696937
- [63] R. Kroboth, C. Bernhard, S. Ilie, J. Six, S. Hahn and P. Pennerstorfer, The Role of Grain Boundary Oxidation on Surface Crack Formation under Continuous Casting Conditions. *Berg- und Hüttenmännische Monatshefte* 164 (2019), 11, pp. 461–465. doi:10.1007/s00501-019-00902-0
- [64] Z. Morita and T. Tanaka, Thermodynamics of solute distributions between solid and liquid phases in iron-base ternary alloys. *ISIJ International* 23 (1983), 10, pp. 824–833. doi:10.2355/isijinternational1966.23.824

- [65] R.L. Smith and J.L. Rutherford, Zone purification of reactive metals. *Journal of Metals* 9 (1957), 4, pp. 478–484. doi:10.1007/BF03397903
- [66] W.A. Fischer, H. Spitzer and M. Hishinuma, Das Zonenschmelzen von Eisen und die Ermittlung der Verteilungskoeffizienten für Kohlenstoff, Phosphor, Schwefel und Sauerstoff. *Archiv für das Eisenhüttenwesen* 31 (1960), 6, pp. 365–371. doi:10.1002/srin.196002871
- [67] W.A. Fischer and H. Frye, Das Zonenschmelzen von weichmagnetischen Stählen und sein Einfluß auf den Konzentrationsverlauf der Begleitelemente in Stäben bis 60 mm Durchmesser. *Archiv für das Eisenhüttenwesen* 41 (1970), 3, pp. 293–302. doi:10.1002/srin.197001604
- [68] F. Oeters, K. Rüttiger, A. Diener and G. Zahs, Zur Theorie der metallurgischen Vorgänge bei der Erstarrung von Stahl. *Archiv für das Eisenhüttenwesen* 40 (1969), 8, pp. 603–613. doi:10.1002/srin.196904363
- [69] T.P. Battle and R.D. Pehlke, Equilibrium partition coefficients in iron-based alloys. *Metallurgical and Materials Transactions B* 20 (1989), 2, pp. 149–160. doi:10.1007/BF02825596
- [70] W.G. Pfann, Principles of Zone-Melting. *Journal of Metals* 4 (1952), 7, pp. 747–753. doi:10.1007/BF03398137
- [71] Y. Nakamura and H. Esaka, Measurement of the equilibrium partition coefficient of phosphorus in carbon steel. *Tetsu-to-Hagane* 67 (1981), S140 - S141.
- [72] P. Spencer and O. Kubaschewski, A thermodynamic assessment of the iron-phosphorus system. *Archiv für das Eisenhüttenwesen* 49 (1978), 5, pp. 225–228. doi:10.1002/srin.197804616
- [73] N. Yoshida, O. Umezawa and K. Nagai, Influence of Phosphorus on Solidification Structure in Continuously Cast 0.1 mass% Carbon Steel. *ISIJ International* 43 (2003), 3, pp. 348–357. doi:10.2355/isijinternational.43.348
- [74] G.H. Gulliver, *Metallic Alloys* (1922), Griffin.
- [75] E. Scheil, Bemerkungen zur Schichtkristallbildung. *Zeitschrift für Metallkunde* 34 (1942), pp. 70–72.
- [76] H.D. Brody and M.C. Flemings, Solute Redistribution in Dendritic Solidification. *Transactions of the Metallurgical Society of AIME* 236 (1966), pp. 615–623.

- [77] T.W. Clyne and W. Kurz, Solute redistribution during solidification with rapid solid state diffusion. *Metallurgical and Materials Transactions A* 12 (1981), 6, pp. 965–971. doi:10.1007/BF02643477
- [78] I. Ohnaka, Mathematical analysis of solute redistribution during solidification with diffusion in solid phase. *ISIJ International* 26 (1986), 12, pp. 1045–1051. doi:10.2355/isijinternational1966.26.1045
- [79] Y. Ueshima, S. Mizoguchi, T. Matsumiya and H. Kajioka, Analysis of solute distribution in dendrites of carbon steel with δ/γ transformation during solidification. *Metallurgical and Materials Transactions B* 17 (1986), 4, pp. 845–859. doi:10.1007/BF02657148
- [80] S. Kobayashi, Solute redistribution during solidification with diffusion in solid phase: A theoretical analysis. *Journal of Crystal Growth* 88 (1988), 1, pp. 87–96. doi:10.1016/S0022-0248(98)90010-0
- [81] E. Kozeschnik, A Scheil-gulliver model with back-diffusion applied to the microsegregation of chromium in Fe-Cr-C alloys. *Metallurgical and Materials Transactions A* 31 (2000), 6, pp. 1682–1684. doi:10.1007/s11661-000-0179-y
- [82] E. Kozeschnik, W. Rindler and B. Buchmayr, Scheil–Gulliver simulation with partial redistribution of fast diffusers and simultaneous solid–solid phase transformations. *International Journal of Materials Research* 98 (2007), 9, pp. 826–831. doi:10.3139/146.101535
- [83] Q. Chen and B. Sundman, Computation of Partial Equilibrium Solidification with Complete Interstitial and Negligible Substitutional Solute Back Diffusion. *Materials Transactions* 43 (2002), 3, pp. 551–559. doi:10.2320/matertrans.43.551
- [84] D. You, C. Bernhard, G. Wieser and S. Michelic, Microsegregation Model with Local Equilibrium Partition Coefficients During Solidification of Steels. *steel research international* 87 (2016), 7, pp. 840–849. doi:10.1002/srin.201500216
- [85] M. Wolf and W. Kurz, The effect of carbon content on solidification of steel in the continuous casting mold. *Metallurgical and Materials Transactions B* 12 (1981), 1, pp. 85–93. doi:10.1007/BF02674761
- [86] Y.-M. Won and B.G. Thomas, Simple model of microsegregation during solidification of steels. *Metallurgical and Materials Transactions A* 32 (2001), 7, pp. 1755–1767. doi:10.1007/s11661-001-0152-4
- [87] C. Bernhard, Anforderungen an prozessorientierte Heißrissbildungsmodelle. *Berg- und Hüttenmännische Monatshefte* 149 (2004), 3, pp. 90–95.

- [88] R. Pierer, Formulation of a Hot Tearing Criterion for the Continuous Casting Process. PhD thesis, Leoben, Austria (2007).
- [89] W.S. Pellini, Strain Theory of Hot Tearing. *Foundry* 80 (1952), pp. 125–199.
- [90] J. Reiter, R. Pierer, C. Bernhard and S. Ilie, The role of tramp elements in hot tearing of steels in the continuous casting process. *European Congress on Advanced Materials and Processes*, Nürnberg, Germany (2007).
- [91] J. Reiter, R. Pierer, S. Ilie, H. Preßlinger, J. Fluch and C. Bernhard, Über die Bildung von Heißrisseigerungen in Stahl: Vergleichende Untersuchungen an Stranggussbrammen und Laborversuchsproben. *Berg- und Hüttenmännische Monatshefte* 155 (2010), 3, pp. 129–135. doi:10.1007/s00501-010-0549-8
- [92] T.W. Clyne, M. Wolf and W. Kurz, The effect of melt composition on solidification cracking of steel, with particular reference to continuous casting. *Metallurgical and Materials Transactions B* 13 (1982), 2, pp. 259–266. doi:10.1007/BF02664583
- [93] M. Wintz, M. Bobadilla and J.M. Jolivet, Fragilité à la solidification des aciers influence du carbone, du soufre et du phosphore. *Revue de Métallurgie* 91 (1994), 1, pp. 105–114. doi:10.1051/metal/199491010105
- [94] L. Kaufmann and H. Bernstein, Computer calculation of phase diagrams with special reference to refractory metals. New York (1970), Academic Press.
- [95] J. Allison, D. Backman and L. Christodoulou, Integrated computational materials engineering: A new paradigm for the global materials profession. *JOM (The Journal of The Minerals, Metals & Materials Society)* 58 (2006), 11, pp. 25–27. doi:10.1007/s11837-006-0223-5
- [96] National Research Council, *Integrated Computational Materials Engineering: A Transformational Discipline for Improved Competitiveness and National Security*. Washington, DC (2008), The National Academies Press.
- [97] W. Yi Wang, J. Li, W. Liu and Z.-K. Liu, Integrated computational materials engineering for advanced materials: A brief review. *Computational Materials Science* 158 (2019), pp. 42–48. doi:10.1016/j.commatsci.2018.11.001
- [98] R. Schmid-Fetzer and J. Gröbner, Focused Development of Magnesium Alloys Using the Calphad Approach. *Advanced Engineering Materials* 3 (2001), 12, pp. 947–961.
- [99] E. Kozeschnik and B. Buchmayer, Matcalc—a simulation tool for multicomponent thermodynamics, diffusion and phase transformation kinetics. in *Mathematical modelling of weld phenomena* (2001), pp. 349–361.

-
- [100] R.H. Davies, A.T. Dinsdale, J.A. Gisby, J.A.J. Robinson and S.M. Martin, MTDATA - thermodynamic and phase equilibrium software from the national physical laboratory. *Calphad* 26 (2002), 2, pp. 229–271. doi:10.1016/S0364-5916(02)00036-6
- [101] W. Cao, S.-L. Chen, F. Zhang, K. Wu, Y. Yang, Y.A. Chang, R. Schmid-Fetzer and W.A. Oates, PANDAT software with PanEngine, PanOptimizer and PanPrecipitation for multi-component phase diagram calculation and materials property simulation. *Calphad* 33 (2009), 2, pp. 328–342. doi:10.1016/j.calphad.2008.08.004
- [102] J.-O. Andersson, T. Helander, L. Höglund, P. Shi and B. Sundman, Thermo-Calc & DICTRA, computational tools for materials science. *Calphad* 26 (2002), 2, pp. 273–312.
- [103] B. Sundman, U.R. Kattner, M. Palumbo and S.G. Fries, OpenCalphad - a free thermodynamic software. *Integrating Materials and Manufacturing Innovation* 4 (2015), 1, pp. 1–15. doi:10.1186/s40192-014-0029-1
- [104] R. Otis and Z.-K. Liu, pycalphad: CALPHAD-based Computational Thermodynamics in Python. *Journal of Open Research Software* 5 (2017), 2, pp. 273. doi:10.5334/jors.140
- [105] H.L. Lukas, S.G. Fries and B. Sundman, *Computational thermodynamics*. Cambridge (2007), Cambridge University Press.
- [106] National Institute of Standards and Technology, *Thermodynamic & Kinetic Data for Sustainable Energy*. <https://www.nist.gov/programs-projects/thermodynamic-kinetic-data-sustainable-energy>, Accessed: 24.05.2021
- [107] Scientific Group Thermodata Europe, *Thermochemistry methods*. <https://www.sgte.net/en/thermochemistry-methods>, Accessed: 24.05.2021
- [108] A. Kroupa, Modelling of phase diagrams and thermodynamic properties using Calphad method – Development of thermodynamic databases. *Computational Materials Science* 66 (2013), May, pp. 3–13. doi:10.1016/j.commatsci.2012.02.003
- [109] A.T. Dinsdale, SGTE data for pure elements. *Calphad* 15 (1991), 4, pp. 317–425. doi:10.1016/0364-5916(91)90030-N
- [110] U.R. Kattner, The Calphad Method and its Role in Material and Process Development. *Tecnologia em metalurgia, materiais e mineracao* 13 (2016), 1, pp. 3–15.
- [111] R. Schmid-Fetzer, D. Andersson, P.Y. Chevalier, L. Eleno, O. Fabrichnaya, U.R. Kattner, B. Sundman, C. Wang, A. Watson, L. Zabdyr and M. Zinkevich, Assessment techniques, database design and software facilities for thermodynamics and diffusion. *Calphad* 31 (2007), 1, pp. 38–52. doi:10.1016/j.calphad.2006.02.007

- [112] U.R. Kattner, The need for reliable data in computational thermodynamics. *High Temperatures-High Pressures* 49 (2020), 1-2, pp. 31–47. doi:10.32908/hthp.v49.853
- [113] U.R. Kattner, The Art of Data Evaluation. *Journal of Phase Equilibria and Diffusion* 32 (2011), 2, pp. 85. doi:10.1007/s11669-011-9850-9
- [114] Y. Wang, S. Curtarolo, C. Jiang, R. Arroyave, T. Wang, G. Ceder, L.-Q. Chen and Z.-K. Liu, Ab initio lattice stability in comparison with CALPHAD lattice stability. *Calphad* 28 (2004), 1, pp. 79–90. doi:10.1016/j.calphad.2004.05.002
- [115] P.E.A. Turchi, I.A. Abrikosov, B. Burton, S.G. Fries, G. Grimvall, L. Kaufman, P. Korzhavyi, V. Rao Manga, M. Ohno, A. Pisch, A. Scott and W. Zhang, Interface between quantum-mechanical-based approaches, experiments, and CALPHAD methodology. *Calphad* 31 (2007), 1, pp. 4–27. doi:10.1016/j.calphad.2006.02.009
- [116] Z.-K. Liu, First-Principles Calculations and CALPHAD Modeling of Thermodynamics. *Journal of Phase Equilibria and Diffusion* 30 (2009), 5, pp. 517–534. doi:10.1007/s11669-009-9570-6
- [117] H.L. Lukas, E.T. Henig and B. Zimmermann, Optimization of phase diagrams by a least squares method using simultaneously different types of data. *Calphad* 1 (1977), 3, pp. 225–236. doi:10.1016/0364-5916(77)90002-5
- [118] D.W. Marquardt, An Algorithm for Least-Squares Estimation of Nonlinear Parameters. *Journal of the Society for Industrial and Applied Mathematics* 11 (1963), 2, pp. 431–441. doi:10.1137/0111030
- [119] E. Königsberger, Improvement of excess parameters from thermodynamic and phase diagram data by a sequential Bayes algorithm. *Calphad* 15 (1991), 1, pp. 69–78. doi:10.1016/0364-5916(91)90027-H
- [120] H.L. Lukas and S.G. Fries, Demonstration of the use of “BINGSS” with the Mg-Zn system as example. *Journal of Phase Equilibria* 13 (1992), 5, pp. 532–542. doi:10.1007/BF02665766
- [121] B. Bocklund, R. Otis, A. Egorov, A. Obaied, I. Roslyakova and Z.-K. Liu, ESPEI for efficient thermodynamic database development, modification, and uncertainty quantification: application to Cu–Mg. *MRS Communications* 9 (2019), 2, pp. 618–627. doi:10.1557/mrc.2019.59
- [122] F. Tang and B. Hallstedt, Using the PARROT module of Thermo-Calc with the Cr–Ni system as example. *Calphad* 55 (2016), 5, pp. 260–269. doi:10.1016/j.calphad.2016.10.003

-
- [123] I.-H. Jung and M.-A. van Ende, Computational Thermodynamic Calculations: FactSage from CALPHAD Thermodynamic Database to Virtual Process Simulation. *Metallurgical and Materials Transactions B* 51 (2020), 5, pp. 1851–1874.
- [124] M. Pudar, S. Zamberger, K. Spiradek-Hahn, R. Radis and E. Kozeschnik, Computational Analysis of Precipitation during Continuous Casting of Microalloyed Steel. *steel research international* 81 (2010), 5, pp. 372–380. doi:10.1002/srin.201000021
- [125] S. Zamberger, M. Pudar, K. Spiradek-Hahn, M. Reischl and E. Kozeschnik, Numerical simulation of the evolution of primary and secondary Nb(CN), Ti(CN) and AlN in Nb-microalloyed steel during continuous casting. *International Journal of Materials Research* 103 (2012), 6, pp. 680–687. doi:10.3139/146.110688
- [126] M. Lückl, O. Caliskanoglu, S. Ilie, J. Six and E. Kozeschnik, Impact of Surface Structure Control Cooling During Continuous Casting on Hot Ductility of Microalloyed Steel. *steel research international* 87 (2016), 7, pp. 871–879. doi:10.1002/srin.201500248
- [127] B. Sundman, Q. Chen and Y. Du, A Review of Calphad Modeling of Ordered Phases. *Journal of Phase Equilibria and Diffusion* 39 (2018), 5, pp. 678–693. doi:10.1007/s11669-018-0671-y
- [128] A.D. Pelton, *Phase Diagrams and Thermodynamic Modeling of Solutions* (2019), Elsevier.
- [129] A.I. Zaitsev, Z.V. Dobrokhotova, A.D. Litvina and B.M. Mogutnov, Thermodynamic properties and phase equilibria in the Fe–P system. *Journal of the Chemical Society, Faraday Transactions* 91 (1995), 4, pp. 703–712. doi:10.1039/FT9959100703
- [130] O. Redlich and A.T. Kister, Algebraic Representation of Thermodynamic Properties and the Classification of Solutions. *Industrial & Engineering Chemistry* 40 (1948), 2, pp. 345–348. doi:10.1021/ie50458a036
- [131] M. Hillert, Empirical methods of predicting and representing thermodynamic properties of ternary solution phases. *Calphad* 4 (1980), 1, pp. 1–12. doi:10.1016/0364-5916(80)90016-4
- [132] M. Hillert, The compound energy formalism. *Journal of Alloys and Compounds* 320 (2001), 2, pp. 161–176. doi:10.1016/S0925-8388(00)01481-X
- [133] R.-Z. Zhang and M.J. Reece, High-Entropy Ceramics, in: *Reference Module in Materials Science and Materials Engineering*. 119 (2021), Elsevier.
- [134] A.D. Pelton and Y.-B. Kang, Modeling short-range ordering in solutions. *International Journal of Materials Research* 98 (2007), 10, pp. 907–917. doi:10.3139/146.101554

- [135] A.D. Pelton, S.A. Degterov, G. Eriksson, C. Robelin and Y. Dessureault, The modified quasichemical model I—Binary solutions. *Metallurgical and Materials Transactions B* 31 (2000), 4, pp. 651–659. doi:10.1007/s11663-000-0103-2
- [136] A.D. Pelton and P. Chartrand, The modified quasi-chemical model: Part II. Multicomponent solutions. *Metallurgical and Materials Transactions A* 32 (2001), 6, pp. 1355–1360. doi:10.1007/s11661-001-0226-3
- [137] S. Cui and I.-H. Jung, Critical reassessment of the Fe-Si system. *Calphad* 56 (2017), 584, pp. 108–125. doi:10.1016/j.calphad.2016.11.003
- [138] M.-A. van Ende and I.-H. Jung, Critical thermodynamic evaluation and optimization of the Fe–B, Fe–Nd, B–Nd and Nd–Fe–B systems. *Journal of Alloys and Compounds* 548 (2013), pp. 133–154. doi:10.1016/j.jallcom.2012.08.127
- [139] M.-S. Kim and Y.-B. Kang, Thermodynamic Modeling of the Fe-Mn-C and the Fe-Mn-Al Systems Using the Modified Quasichemical Model for Liquid Phase. *Journal of Phase Equilibria and Diffusion* 36 (2015), 5, pp. 453–470. doi:10.1007/s11669-015-0401-7
- [140] K. Shubhank and Y.-B. Kang, Critical evaluation and thermodynamic optimization of Fe–Cu, Cu–C, Fe–C binary systems and Fe–Cu–C ternary system. *Calphad* 45 (2014), pp. 127–137. doi:10.1016/j.calphad.2013.12.002
- [141] P. Walder and A.D. Pelton, Thermodynamic modeling of the Fe-S system. *Journal of Phase Equilibria and Diffusion* 26 (2005), 1, pp. 23–38. doi:10.1007/s11669-005-0055-y
- [142] Y.-B. Kang, Critical evaluations and thermodynamic optimizations of the Mn–S and the Fe–Mn–S systems. *Calphad* 34 (2010), 2, pp. 232–244. doi:10.1016/j.calphad.2010.03.005
- [143] F. Tafwidli and Y.-B. Kang, Thermodynamic Modeling of Fe–C–S Ternary System. *ISIJ International* 57 (2017), 5, pp. 782–790. doi:10.2355/isijinternational.ISIJINT-2016-672
- [144] P. Waldner and A.D. Pelton, Thermodynamic modeling of the Ni–S system. *Zeitschrift für Metallkunde* 95 (2004), 8, pp. 672–681. doi:10.3139/146.018005
- [145] P. Waldner and A.D. Pelton, Critical thermodynamic assessment and modeling of the Fe-Ni-S system. *Metallurgical and Materials Transactions B* 35 (2004), 5, pp. 897–907. doi:10.1007/s11663-004-0084-7
- [146] M.-K. Paek, J.-J. Pak and Y.-B. Kang, Phase equilibria and thermodynamics of Mn–C, Mn–Si, Si–C binary systems and Mn–Si–C ternary system by critical evaluation, combined with experiment and thermodynamic modeling. *Calphad* 46 (2014), S415, pp. 92–102. doi:10.1016/j.calphad.2014.02.007

- [147] B. Hallmans, P. Wollants and J.R. Roos, Thermodynamic Reassessment and Calculation of the Fe-B Phase Diagram. *International Journal of Materials Research* 85 (1994), 10, pp. 676–682. doi:10.1515/ijmr-1994-851002
- [148] D. Djurovic, B. Hallstedt, J. von Appen and R. Dronskowski, Thermodynamic assessment of the Mn–C system. *Calphad* 34 (2010), 3, pp. 279–285. doi:10.1016/j.calphad.2010.05.002
- [149] Y.O. Esin, V.M. Baev, M.S. Petrushevskii and P.V. Gel'd, Enthalpies of formation of liquid binary alloys of cobalt and iron with boron (in Russian). *Izvestija Akademii Nauk SSSR* 3 (1975), pp. 82–86.
- [150] V.T. Witusiewicz, A.K. Biletski and V.S. Shumikin, Thermodynamic properties of liquid Mn-C alloys. *Metally* 6 (1988), pp. 26–29.
- [151] Y.-M. Muggianu, M. Gambino and J.-P. Bros, Enthalpies de formation des alliages liquides bismuth-étain-gallium à 723 k. Choix d'une représentation analytique des grandeurs d'excès intégrales et partielles de mélange. *Journal de Chimie Physique* 72 (1975), pp. 83–88. doi:10.1051/jcp/1975720083
- [152] F. Kohler, Zur Berechnung der thermodynamischen Daten eines ternen Systems aus den zugehörigen binären Systemen. *Monatshefte für Chemie* 91 (1960), 4, pp. 738–740. doi:10.1007/BF00899814
- [153] G.W. Toop, Predicting ternary activities using binary data. *Transactions of the Metallurgical Society of AIME* 233 (1965), 5, pp. 850–855.
- [154] Z.-M. Cao, K.-P. Wang, Z.-Y. Qiao and G.-W. Du, Thermodynamic Reoptimization of the Fe-P System. *Acta Physico-Chimica Sinica* 28 (2012), 01, pp. 37–43. doi:10.3866/PKU.WHXB201111172
- [155] J. Miettinen, S. Louhenkilpi, H. Kytönen and J. Laine, IDS: Thermodynamic–kinetic–empirical tool for modelling of solidification, microstructure and material properties. *Mathematics and Computers in Simulation* 80 (2010), 7, pp. 1536–1550. doi:10.1016/j.matcom.2009.11.002
- [156] J. Miettinen, S. Louhenkilpi, V.-V. Visuri and T. Fabritius, Advances in Modeling of Steel Solidification with IDS. *IOP Conference Series: Materials Science and Engineering* 529 (2019), pp. 12063. doi:10.1088/1757-899X/529/1/012063
- [157] S. Louhenkilpi, M. Mäkinen, S. Vapalahti, T. Räisänen and J. Laine, 3D steady state and transient simulation tools for heat transfer and solidification in continuous casting. *Materials Science and Engineering: A* 413–414 (2005), pp. 135–138. doi:10.1016/j.msea.2005.08.153

- [158] S. Louhenkilpi, J. Miettinen, J. Laine, R. Vesänen, I. Rentola, J. Moilanen, V.-V. Visuri, E.-P. Heikkinen and A. Jokilaakso, Online Modelling of Heat Transfer, Solidification and Microstructure in Continuous Casting of Steel. IOP Conference Series: Materials Science and Engineering 529 (2019), pp. 12051. doi:10.1088/1757-899X/529/1/012051
- [159] S. Louhenkilpi, J. Miettinen, V.-V. Visuri, M.C. Somani, S. Koskenniska and T. Fabritius, New phenomenological quality criteria for continuous casting of steel based on solidification and microstructure tool IDS. Ironmaking & Steelmaking 48 (2021), 2, pp. 170–179. doi:10.1080/03019233.2020.1758994
- [160] S. Saleem, M. Vynnycky and H. Fredriksson, The Influence of Peritectic Reaction/Transformation on Crack Susceptibility in the Continuous Casting of Steels. Metallurgical and Materials Transactions B 48 (2017), 3, pp. 1625–1635. doi:10.1007/s11663-017-0926-8
- [161] E. Moukhina and E. Kaisersberger, Temperature dependence of the time constants for deconvolution of heat flow curves. Thermochimica Acta 492 (2009), 1-2, pp. 101–109. doi:10.1016/j.tca.2008.12.022
- [162] Software: NETZSCH Tau-Calibration 8.0.1 from Netzsch Gerätebau GmbH, Selb, Germany, 2019.
- [163] W.J. Boettinger, U.R. Kattner, K.W. Moon and J. Perepezko, NIST Recommended Practice Guide: DTA and Heat-Flux DSC Measurements of Alloy Melting and Freezing. Special Publication 960-15 (2006)
- [164] L.A. Chapman, Application of high temperature DSC technique to nickel based superalloys. Journal of Materials Science 39 (2004), 24, pp. 7229–7236. doi:10.1023/B:JMSC.0000048736.86794.12
- [165] M. Bernhard, P. Presoly, N. Fuchs, C. Bernhard and Y.-B. Kang, Experimental Study of High Temperature Phase Equilibria in the Iron-Rich Part of the Fe-P and Fe-C-P Systems. Metallurgical and Materials Transactions A 51 (2020), 10, pp. 5351–5364. doi:10.1007/s11661-020-05912-z
- [166] M. Bernhard, Y.-B. Kang, P. Presoly, A.E. Gheribi and C. Bernhard, Critical evaluation and thermodynamic modeling of the Fe–P and Fe–C–P system. Calphad 70 (2020), 1, pp. 101795. doi:10.1016/j.calphad.2020.101795
- [167] E.T. Turkdogan and L.E. Leake, Thermodynamics of carbon dissolved in iron alloys. Part I: Solubility of carbon in iron-phosphorus, iron-silicon, and iron-manganese melts. Journal of the Iron and Steel Institute 179 (1955), pp. 39–43.

- [168] H. Schenck, E. Steinmetz and R. Gohlke, Beitrag zur chemischen Aktivität der Elemente Phosphor, Schwefel, Silizium, Kupfer und Chrom in flüssigen kohlenstoffgesättigten Eisenlösungen. *Archiv für das Eisenhüttenwesen* 37 (1966), 12, pp. 919–924. doi:10.1002/srin.196604304
- [169] E. Schürmann and D. Kramer, Untersuchungen über den Einfluss der Temperatur und über die äquivalente Wirkung der Legierungselemente auf die Kohlenstofflöslichkeit in eisenreichen, kohlenstoffgesättigten Drei- und Mehrstoffschmelzen. *Giessereiforschung* 21 (1969), 1, pp. 29–42.
- [170] H.G. Hadrys, M.G. Froberg and J.F. Elliott, Activities in the liquid Fe-Cr-C(sat), Fe-P-C(sat) and Fe-Cr-P systems at 1600 °C. *Metallurgical Transactions* 1 (1970), 7, pp. 1867–1874.
- [171] Y.D. Yang, Interaction coefficients in Fe-C-P ternary and Fe-Cr-C-P quaternary solutions at 1400 °C. *Scandinavian Journal of Metallurgy* 21 (1992), pp. 194–201.
- [172] P. Gustafson, A thermodynamic evaluation of the Fe-C system. *Scandinavian Journal of Metallurgy* 14 (1985), 5, pp. 259–267.
- [173] M. Bernhard, N. Fuchs, P. Presoly, P. Angerer, B. Friessnegger and C. Bernhard, Characterization of the γ -loop in the Fe-P system by coupling DSC and HT-LSCM with complementary in-situ experimental techniques. *Materials Characterization* 174 (2021), 11, pp. 111030. doi:10.1016/j.matchar.2021.111030
- [174] M. Bernhard, Adjustment of microsegregation models by means of hot tearing investigations on solidifying steel. Masterthesis, Leoben, Austria (2016).
- [175] M. Bernhard, P. Presoly, C. Bernhard, J. Six and S. Ilie, On the Relevance of Microsegregation Models for Process Control in Continuous Casting of Steel. *Proceedings of the 26th International Conference on Metallurgy and Materials*, Brno, Czech Republic (2017).
- [176] R. Pierer and C. Bernhard, On the influence of carbon on secondary dendrite arm spacing in steel. *Journal of Materials Science* 43 (2008), 21, pp. 6938–6943. doi:10.1007/s10853-008-2985-3
- [177] M. Bernhard, C. Bernhard, P. Presoly and D. You, An alternative approach for the experimental verification of microsegregation models using an in-situ hot tensile test during solidification of steel. *Proceedings of the 7th International Conference on Solidification and Gravity*, Miskolc-Lillafüred, Hungary (2018).

- [178] J. Miettinen and A.A. Howe, Estimation of liquidus temperatures for steels using thermodynamic approach. *Ironmaking & Steelmaking* 27 (2000), 3, pp. 212–227. doi:10.1179/030192300677516
- [179] G. Xia, Kokillenmetallurgie des konventionellen Brammenstranggießens von Stahl. Habilitation thesis, Leoben, Austria (2001).
- [180] J. Miettinen, Thermodynamic–kinetic simulation of solidification and phase transformations in steels. Report TKK-MK-78, Helsinki University of Technology Publications in Materials Science and Metallurgy, TKK, Espoo, 1999
- [181] S.K. Choudhary and A. Ghosh, Mathematical Model for Prediction of Composition of Inclusions Formed during Solidification of Liquid Steel. *ISIJ International* 49 (2009), 12, pp. 1819–1827. doi:10.2355/isijinternational.49.1819
- [182] A. Kagawa, S. Moriyama and T. Okamoto, Partition of solute elements during solidification of iron-carbon-chromium alloys. *Journal of Materials Science* 17 (1982), 1, pp. 135–144. doi:10.1007/BF00809045
- [183] A. Kagawa and T. Okamoto, Coefficients for equilibrium partition of a third element between solid and liquid in iron-carbon base ternary alloys and their relation to graphitization during iron-carbon eutectic solidification. *Journal of Materials Science* 19 (1984), 7, pp. 2306–2318. doi:10.1007/BF01058107
- [184] M. Bernhard, P. Presoly, C. Bernhard, S. Hahn and S. Ilie, An assessment of analytical liquidus equations for Fe-C-Si-Mn-Al-P alloyed steels using DSC/DTA techniques. *Metallurgical and Materials Transactions B* (2021). doi:10.1007/s11663-021-02251-1

Appendix: Publications

Paper I

Experimental Study of High Temperature Phase Equilibria in the Iron-Rich Part of the Fe-P and Fe-C-P Systems

M. Bernhard, P. Presoly, N. Fuchs, C. Bernhard and Y.-B. Kang

Metallurgical and Materials Transactions A, 2020, vol. 51, pp. 5351-5364.

Abstract: During the solidification of steel, phosphorus strongly segregates in the interdendritic liquid phase. In the continuous casting process, even low levels of P may have a detrimental effect on the final product quality. However, phosphorus is partly added up to 0.10 wt pct to improve the mechanical properties of advanced steel grades nowadays, e.g., High-Strength Interstitial-Free (HSIF). To provide new experimental data for the development of thermodynamic databases and solidification models for P alloyed steel grades, phase equilibria in the Fe-P and Fe-C-P key systems were studied up to 1550 °C using differential scanning calorimetry (DSC) and high temperature laser scanning confocal microscopy (HT-LSCM). Special focus was placed on solid/liquid equilibrium temperatures in the Fe-rich part of the binary Fe-P system between 0.025 and 9 wt pct P. In the ternary system, three isoplethal sections with 0.10 mass pct. P, 0.20 mass pct. C and constant mass percent ratio P/C of 2 were investigated. In the latter section, HT-LSCM observations were linked with DSC signals to optically identify present phase stabilities. Particularly at [pct P] < 1, significant differences between performed measurements and calculated phase equilibrium temperatures using thermodynamic assessments from the literature were identified. In all ternary sections, the experiments indicate less influence of P on the hypo-peritectic range compared to the thermodynamic calculations.

Used and reprinted under the Creative Commons Attribution 4.0 International License

Experimental Study of High Temperature Phase Equilibria in the Iron-Rich Part of the Fe-P and Fe-C-P Systems



MICHAEL BERNHARD, PETER PRESOLY, NORA FUCHS,
CHRISTIAN BERNHARD, and YOUN-BAE KANG

During the solidification of steel, phosphorus strongly segregates in the interdendritic liquid phase. In the continuous casting process, even low levels of P may have a detrimental effect on the final product quality. However, phosphorus is partly added up to 0.10 wt pct to improve the mechanical properties of advanced steel grades nowadays, *e.g.*, High-Strength Interstitial-Free (HSIF). To provide new experimental data for the development of thermodynamic databases and solidification models for P alloyed steel grades, phase equilibria in the Fe-P and Fe-C-P key systems were studied up to 1550 °C using differential scanning calorimetry (DSC) and high temperature laser scanning confocal microscopy (HT-LSCM). Special focus was placed on solid/liquid equilibrium temperatures in the Fe-rich part of the binary Fe-P system between 0.025 and 9 wt pct P. In the ternary system, three isoplethal sections with 0.10 mass pct. P, 0.20 mass pct. C and constant mass percent ratio P/C of 2 were investigated. In the latter section, HT-LSCM observations were linked with DSC signals to optically identify present phase stabilities. Particularly at [pct P] < 1, significant differences between performed measurements and calculated phase equilibrium temperatures using thermodynamic assessments from the literature were identified. In all ternary sections, the experiments indicate less influence of P on the hypo-peritectic range compared to the thermodynamic calculations.

<https://doi.org/10.1007/s11661-020-05912-z>
© The Author(s) 2020

I. INTRODUCTION

PHOSPHORUS is generally known as a harmful element in steel. In the continuous casting process, the strong segregation of P during solidification may lead to internal quality problems, *e.g.* hot tear formation. Increasing amounts of carbon and other alloying elements lower the solidification temperatures and possibly change the phase transformation path in the peritectic range. As a consequence, the limited diffusivity of P along the dendritic microstructure at decreased temperatures and the low solubility of P in austenite favor the interdendritic enrichment and cause an even higher risk of crack formation in the casting process.^[1-4] However, despite the detrimental effects on the product quality, phosphorus is partly added in steelmaking

nowadays to improve various performance characteristics of steel: (i) P acts as the most effective solution-hardening element in the steel matrix. This strengthening mechanism is particularly used in the production of High-Strength Interstitial-Free (HSIF) steels.^[5] (ii) P is added up to 0.10 mass pct. to structural steels in order to improve the atmospheric resistance.^[6,7] (iii) In transformation induced plasticity (TRIP) steels, P stabilizes the retained austenite; amounts up to 0.10 wt pct are considered to show beneficial influence on the TRIP effect.^[8]

Reliable phase diagram data in the high-temperature range of the ternary Fe-C-P system are essential for developing a comprehensive understanding of solidification phenomena in P alloyed steels. In the present study, high-temperature phase transformations of 37 model alloys in the Fe-P and Fe-C-P systems were investigated using differential scanning calorimetry (DSC) and high-temperature laser scanning confocal microscopy (HT-LSCM). The DSC method has already been used in previous works^[9,10] to characterize the influence of alloying elements on the peritectic range and determine melting equilibrium temperatures in Fe-C-X isoplethal sections. Linking the DSC method with HT-LSCM observations is a supportive and powerful

MICHAEL BERNHARD, PETER PRESOLY, NORA FUCHS, and CHRISTIAN BERNHARD are with the Chair of Ferrous Metallurgy, Montanuniversitaet Leoben, Franz-Josef-Strasse 18, 8700 Leoben, Austria Contact e-mail: michael.bernhard@unileoben.ac.at YOUN-BAE KANG is with the Graduate Institute of Ferrous Technology, Pohang University of Science and Technology, Kyungbuk 37673, Pohang, Republic of Korea.

Manuscript submitted February 27, 2020.

Article published online July 23, 2020

tool to gain additional information on present phase stabilities in the peritectic region and confirm the interpretation of the DSC signal.^[9]

The first part of this work deals with the reinvestigation of phase equilibria in the binary Fe-P subsystem in the range 0.025 to 9 mass percent P. Due to the lack of experimental literature data at low P compositions, special focus was placed on compositions < 1 mass percent P. In the second part, three isoplethal sections in the Fe-C-P system were investigated. Model alloys with Fe-C-0.10 wt pct P and Fe-0.20 wt pct C-P were produced according to the initial phosphorus composition of P alloyed steel grades, whereas the additional section with constant P/C mass percent ratio of 2 corresponds to typical enrichments of C and P during solidification. In the latter section, selected DSC measurements were linked with HT-LSCM observations to visually identify phase stabilities and estimate transformation temperatures. The purpose of the present work is to provide new experimental data for the further improvement of thermodynamic databases and solidification models for P alloyed steels.

II. LITERATURE REVIEW

A. Binary Fe-P System

As generally accepted from Okamoto,^[11] the binary Fe-P system consists of three solution phases - liquid, fcc (γ) and bcc (α , δ)—and three stoichiometric compounds (Fe_3P , Fe_2P and FeP). Although the existence of higher order phosphides (FeP_2 and FeP_4) was reported in previous works^[12–15] the phase diagram on the P-rich side is still unknown.^[11] A large amount of experimental phase diagram data was summarized in Okamoto's work.^[11] However, depending on the reported experimental technique and the trace element level in the investigated alloys, the published measurements significantly differ. Particularly, for bcc/liquid equilibria in the Fe-rich part, high deviations were identified in the available data sets.^[16–22] Solid phase equilibria in the fcc/bcc gamma loop region were studied in References 23 through 25; the maximum solubility of P in fcc was found to be 0.31 wt pct^[24] or 0.265 wt pct^[25] at 1150 °C. Alloys with phosphorus content higher than 0.69 wt pct^[24] or 0.59 wt pct,^[25] respectively, do not show a bcc/fcc phase transformation in solid state. The solubility of P in bcc between 550 °C and 1200 °C was reported in References 26 through 29; a maximum value of 2.8 mass pct. at the temperature 1048°C is generally accepted.^[11] The eutectic composition in the Fe-P system is 10.2 mass pct. P.^[11] From literature, various thermodynamic assessments of the binary Fe-P system are available.^[30–36] However, for the present work only assessments of the Fe-P systems that are being used in a consistent description of the ternary Fe-C-P system are of particular interest. Hence, the work of Shim *et al.*^[32] was considered for the discussion of the present experimental data. The calculated binary Fe-P phase diagram along with experimental data from the References 16 through 29 is shown in Figure 1.

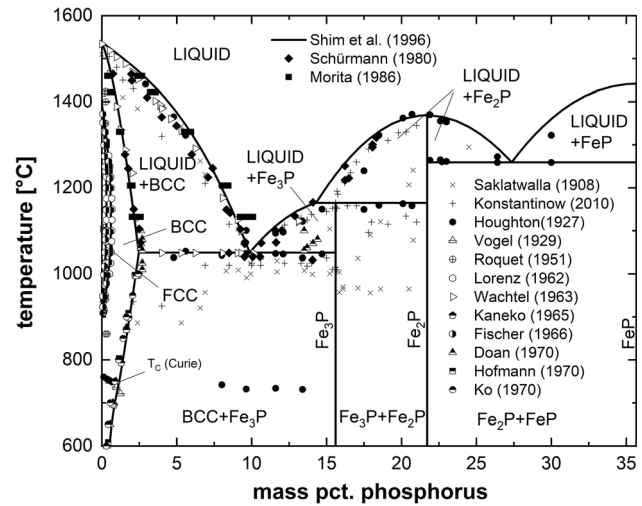


Fig. 1—Calculated binary Fe-P phase diagram according to Shim *et al.*^[32] up to composition of FeP along with experimental data from References 16 through 29.

B. Ternary Fe-C-P System

An extensive literature review of phase equilibria, thermodynamic properties and crystallographic data in the Fe-C-P system was presented by Perrot.^[37] However, since literature data on low amounts of phosphorus is limited, only melting equilibria of Schürmann *et al.*^[38] was taken to critically evaluate the present results in the [pct P]/[pct C] = 2 section. From literature, two consistent thermodynamic descriptions of the ternary Fe-C-P system are available.^[31,39] In both studies, the authors considered their own optimization of the Fe-P binary subsystems^[31,32] and the most widely used Fe-C thermodynamic description of Gustafson.^[40] Shim *et al.*^[39] already reported higher correlation with experimental data than that found in Gustafson's study.^[31] Therefore, the assessments of Shim *et al.*^[32,39] were adopted to discuss the present results in the Fe-P binary and Fe-C-P ternary system. All stable phases in the ternary Fe-C-P system and their crystallographic data are summarized in Table I.

III. EXPERIMENTAL TECHNIQUES

A. Sample Preparation and Chemical Analysis

All samples investigated by DSC and HT-LSCM were produced in a high-frequency remelting (HFR) furnace "Lifumat-Met-3.3-Vac" from Linn High Therm GmbH. Pure technical iron cylinders (99.9 mass pct. Fe), high purity red phosphorus powder (98.9 pct, Alfa Aesar, LOT# U01C005), high purity aluminum wire (for deoxidation) and a previously prepared Fe-4.4 pct C alloy were used as the starting materials. The eutectic Fe-4.4 pct C alloy was melted in a 20 kg induction furnace using synthetic desulfurized graphite powder (Alfa Aesar, LOT# BCBB5882). In order to guarantee controlled melting in the HFR process, a hole was drilled in the 50 g iron cylinders and filled with the amount of alloying elements according to the defined

Table I. Crystallographic Data of Stable Phases Found in the Fe-C-P System^[11,37]

Phase	Pearson Symbol	Space Group	Strukturbericht	Prototype	Denoted in Text
Liquid	—	—	—	—	liquid
(γ)Fe	cF4	Fm $\bar{3}$ m	A1	Cu	fcc
(α)Fe, (δ)Fe	cI2	Im $\bar{3}$ m	A2	W	bcc
Fe ₃ P	tI32	I $\bar{4}$	D0 _c	Ni ₃ P	—
Fe ₂ P	hP9	P $\bar{6}$ 2m	C22	Fe ₂ P	—
FeP	oP8	Pna2 ₁	—	MnP	—
FeP ₂	oP6	Pnnm	C18	FeS ₂ (marcasite)	—
FeP ₄	mP30	P2 ₁ /c	—	FeP ₄	—
(P) white	c**	—	—	(P) white	P
Fe ₃ C	oP16	Pnma	D0 ₁₁	Fe ₃ C	Fe ₃ C
C (gr.)	hP4	P6 ₃ /mmc	A9	C (gr.)	C

chemical composition. As powder-based red phosphorus may show high surface affinity to oxygen, samples with a higher P amount ([pct P] > 0.1) were deoxidized with 0.03 mass pct. Al. The melting process was carried out in alumina crucibles under argon 5.0 over-pressure atmosphere. After two minutes of homogenization by inductive bath movement, the melt was centrifugally casted into a copper mold. The final chemical analysis of each sample was determined by (i) optical emission spectroscopy (OES) for alloys with [pct P] ≤ 0.1. The OES of type OBLF QSG 750 was calibrated with internal standards up to 0.35 pct P. (ii) In case of [pct P] > 0.1, the samples were analyzed with an X-ray fluorescence (XRF) spectrometer Thermo Fisher XRF ARL 9900. The XRF spectrometer was calibrated up to 4 mass pct. P with results of inductively coupled plasma (ICP) - OES. (iii) For alloys with P ≥ 6 mass pct. the chemical analysis was determined by ICP-OES. For detailed chemical analysis and trace element levels of all investigated samples, the authors refer to the electronic supplementary material (ESM).

B. Differential Scanning Calorimetry (DSC)

Differential scanning calorimetry is a proven method to record phase transitions associated with an exothermic or endothermic enthalpy change. Detailed information on the DSC technique and its application to the characterization of high temperature phase transformations in Fe-C-X (X = Si, Mn, Al, ...) systems can be found in the References 9, 10, 41, 42. Measurements for the present study were performed in a NETZSCH DSC 404F1 Pegasus with an Rh furnace ($T_{\max} = 1.650$ °C) and a platinum DSC sensor with type S thermocouples. Al₂O₃ crucibles (85 μ l) and lids were used for all experiments; in each measurement the reference was an empty crucible. The protective tube of the Rh furnace was purged permanently with Ar 5.0 (purity 99.999 pct). In order to minimize oxygen levels at temperatures higher than 350 °C, a thermally active zirconium getter was placed directly below the DSC sensor. The experimental setup was calibrated by measuring the melting points of NETZSCH's standards of pure metals In, Bi, Al, Ag, Au, Ni and Co.

The DSC signal depends strongly on (i) the sample mass, (ii) the amount of heat change during the phase transformation and (iii) the heating rate (HR) applied in the scanning mode.^[42] For all experiments, a relatively low sample mass of 50 mg was selected to guarantee near-equilibrium conditions without any temperature gradients inside the sample. Moreover, measurements with small samples result in a sharp peak separation in the DSC signal. Particularly during strong exothermic or endothermic phase transformations, *e.g.* solid-liquid equilibria, the transformation peaks have to be corrected from the scanning mode signal to obtain the equilibrium value. Within the classical method,^[43] the peak temperatures are determined at various heating rates using new samples for each measurement. Finally, the HR-dependent peak temperature is extrapolated to an HR of zero °C/min, which corresponds to the equilibrium value. However, this method is very time consuming and a large number of samples have to be prepared. NETZSCH's Tau-R software^[44,45] provides a very effective way to exclude the setup influence on the DSC signal in order to calculate the equilibrium data from a single measurement. In the present study, the validity of the Tau-R method was critically evaluated by taking the example of a hypo-peritectic Fe-0.136 pct C-0.105 pct P alloy. For detailed information on the interpretation of DSC signals to determine phase transformation temperatures in alloys (*e.g.* definition of "onset" and "peak" temperatures) the authors like to refer to the NIST Recommended Practice Guide.^[42] The "onset" temperature represents the first deviation from the stable base line and is associated with the beginning of a phase transformation. A "peak" temperature is defined as a local maximum of the DSC signal and generally represents the end of the respective phase transformation. In a first step, the classic HR variation with 5, 7.5, 10, 15 and 20 °C/min was applied to determine the equilibrium temperatures. The results of the HR variation are presented in Figure 2. From Figure 2(a) it can be seen that increasing heating rates result in a stronger intensity of the DSC signal but shift the liquidus temperature (T_L) and the end of the peritectic reaction ($T_{P,E}$) to higher temperatures. The numerical values of all phase transformation

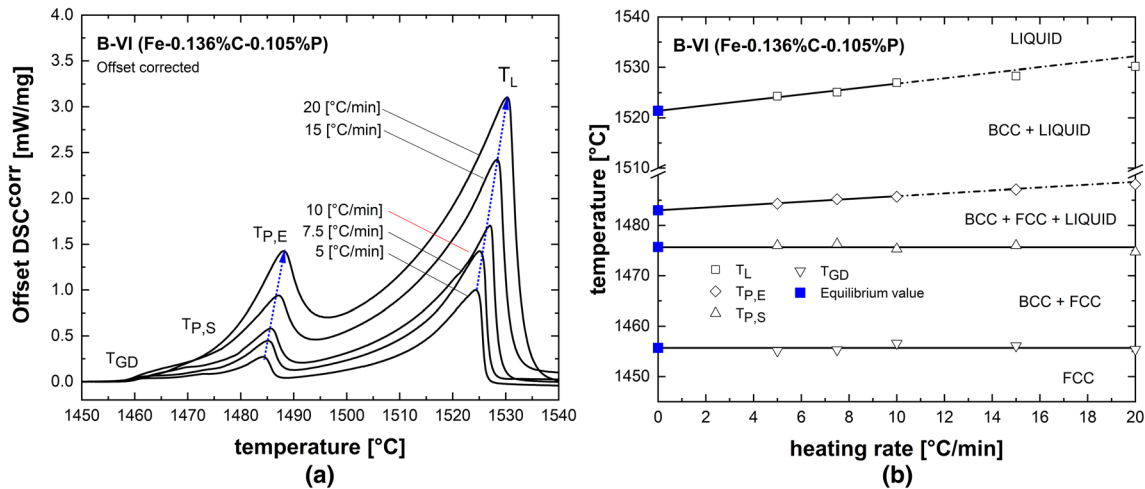


Fig. 2—DSC signal of the alloy B-VI (Fe-0.136 pct C-0.105 pct P) corrected to the baseline 0.0 mW/mg using different heating rates of 5, 7.5, 10, 15 and 20 °C (a) and analysis of the numerical results depending on the heating rate to determine the equilibrium temperatures at 0 °C/min (b).

temperatures are plotted against the HR in Figure 2(b). As expected, no influence of the HR was observed for “onset” temperatures (fcc/bcc transformation start temperature T_{GD} and peritectic start temperature $T_{P,S}$). Hence, the final values of $T_{GD} = 1455.7$ °C and $T_{P,S} = 1475.7$ °C are given as average temperatures. In case of $T_{P,E}$ and T_L , a clear dependence on the heating rate is evident from Figure 2(b). In the present DSC set-up, a linear correlation exists only from 0 to 10 °C/min, whereas at higher HR of 15 and 20 °C/min, the DSC system responds with a delay and the results of T_L and $T_{P,E}$ show a parabolic function. In terms of accuracy and reliability of the results, the HR variation for the DSC set-up used is only valid in the range of 0 to 10 °C/min and the linear extrapolation to 0 °C/min gives $T_L = 1521.4$ °C and $T_{P,E} = 1483$ °C.

Since the Tau-R calibration is only valid for a defined heating rate, a suitable HR has to be selected for the entire experimental study. Based on the results of the HR variation, the authors applied 10 °C/min within all measurements: (i) between 0 and 10 °C/min the peak temperatures show a linear correlation with the HR, (ii) a short residence time in the high temperature range (> 1450 °C) reduces aging of the Pt/Rh thermocouples of the DSC sensor, (iii) the measurement time is minimized by guaranteeing a sufficient intensity of the DSC signal at the same time and (iv) a heating rate of 10 °C/min accords with suggestions from Reference 43. For the Tau-R calibration, a comprehensive evaluation of the calibration measurements (In to Co) was performed to determine the temperature-dependent time constant (Tau) and the thermal resistances (R) of the DSC set-up. The performed Tau-R calculation of the 10 °C/min measurement and the actual DSC signal are plotted for comparisons in Figure 3. It can be seen that the equilibrium peak temperatures of the Tau-R method show a significant difference from the results in the scanning mode ($\Delta T_L = 6$ °C and $\Delta T_{P,E} = 3$ °C), whereas the onset temperatures T_{GD} and $T_{P,S}$ are not affected by the Tau-R correction. Finally, the numerical results of

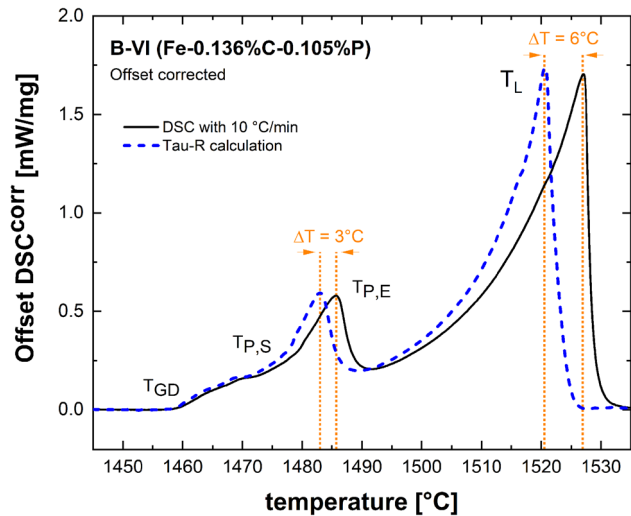


Fig. 3—Comparison of the scanning mode signal and the Tau-R calculation of alloy B-VI (Fe-0.136 pct C-0.105 pct P) for the 10 °C/min measurement.

the HR variation and the Tau-R method are summarized in Table II. The equilibrium values $T_{GD} = 1455.7$ °C and $T_{P,S} = 1475.7$ °C from the heating rate variation are in excellent agreement with the Tau-R calculation ($T_{GD} = 1455.6$ °C and $T_{P,S} = 1474.1$ °C). The peak temperature $T_{P,E} = 1483$ °C is exactly reproduced and the deviation of T_L is within ± 1 °C, which is below the typical errors of ± 1.5 °C in DSC measurements.^[9] The really good correlation between both methods confirms the application of the Tau-R software in the present study.

The detailed time-temperature-gas programs for the DSC analysis are visualized in Figure 4. For each alloy, a “slow” temperature cycle was defined for the first measurements and a “rapid” program for the second ones. Both DSC programs start with three evacuations and purging cycles followed by 45 minutes of intensive purging with 150 ml/min Ar at 25 °C. In order to

Table II. Numerical Results of the Heating Rate Variation and the Tau-R Calculation for Alloy B-VI(Fe-0.136 Pct C-0.105 Pct P)

Temperature	Phase Equilibrium	Heating Rate Variation in the DSC					Equilibrium Temperatures		
		5 [°C/ min]	7.5 [°C/ min]	10 [°C/ min]	15 [°C/ min]	20 [°C/ min]	Regression 0 [°C/min]	R^2	Tau-R [°C]
Onset: T_{GD}	(fcc → fcc + bcc)	1455.1	1455.3	1456.6	1456.1	1455.4	1455.7 ^a	—	1455.6
Onset: $T_{P,S}$	(fcc + bcc → fcc + liquid + bcc)	1476.0	1476.3	1475.3	1476.0	1474.7	1475.7 ^a	—	1474.1
Peak: $T_{P,E}$	(fcc + liquid + bcc → liquid + bcc)	1484.3	1485.2	1485.7	1487.1	1488.1	1483.0 ^b	0.97	1483.0
Peak: T_L	(bcc + liquid → liquid)	1524.3	1525.1	1527.0	1528.3	1530.2	1521.4 ^b	0.95	1520.7

^aOnset temperature shows only a minor dependency on the heating rate; the equilibrium value is averaged from 5 to 20 °C/min measurements.
^bPeak temperature is dependent on heating rate; the equilibrium value is linearly extrapolated to a heating rate of 0 °C/min.

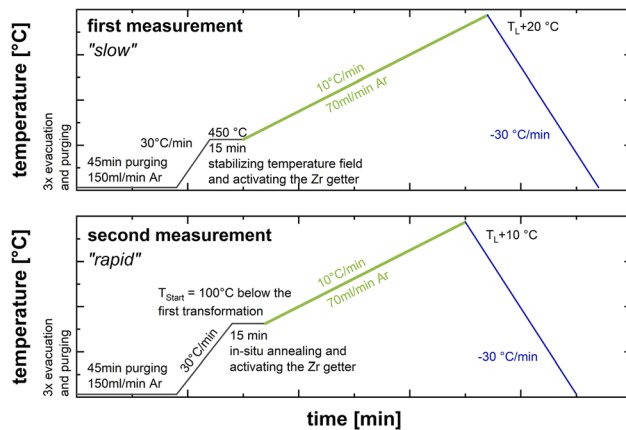


Fig. 4—Time–Temperature–Gas program of the DSC measurements.

activate the Zr getter, the first heating is carried out quickly (30 °C/min) to reach temperatures above 350 °C. The “slow” measurement starts at 450 °C with an isothermal segment for 15 minutes to activate the Zr getter and stabilize the temperature field in the DSC. Then, the actual measurement starts with a constant heating rate of 10 °C/min and an argon flow rate of 70 ml/min up to 20°C above the expected liquidus temperature. Based on the analysis of the “slow” temperature cycle, the “rapid” program starts at 100 °C below the first detected phase transformation using a new sample. The typical start temperature is between 600 and 700 °C. In comparison with the “slow” measurement, the starting segment is carried out at a significantly higher temperature. During the 15 min isothermal segment, the Zr getter is activated and the sample is annealed in-situ in order to favor diffusion equalization of alloying elements in the sample matrix. Again, the actual measurement is performed with an HR of 10 °C/min and 10 °C superheating above T_L . During cooling from T_L to room temperature (–30 °C/min) under pure atmosphere, strong nucleation phenomena may result in remarkable supercooling of the phase transformation, particularly in the case of small sample masses.^[43,46] Since the results were not reproducible, the cooling cycle was not considered in the evaluation of the DSC signal. To compensate aging of the Pt/Rh thermocouples of the

DSC sensor, recalibration of the DSC was carried out after every ten measurements with Ag and Co.

It has to be noted that the experimental methodology presented focuses particularly on a highly accurate determination of the phase transformation temperatures, but not on measurements of the $C_p(T)$ values. Hence, increased deviations of more than 10 pct have to be considered in the change of heat. Standard deviations of the evaluated phase transformation temperature from at least two independent measurements can be found in the ESM. In general, the authors suggest typical errors of ± 5 °C for solid-solid transitions with only minor change in heat and ± 2 °C for solid-liquid phase transformations. The error bars are similar to the previous investigations in Reference 9.

C. In Situ Observations of Phase Transformations Using HT-LSCM

To successfully determine the peritectic range of isoplethal Fe-C-X sections by means of the DSC method, a number of samples with varying carbon content are required to reconstruct the high temperature phase diagram. However, within measurements of individual alloys and particularly at carbon compositions between 0.12 and 0.18 mass pct., difficulties may arise in assigning the peritectic peak detected in the DSC signal to a hypo-peritectic phase transformation path, where fcc + bcc ↔ fcc + bcc + liquid, or a hyper-peritectic behavior, where fcc + liquid ↔ fcc + bcc + liquid. In such cases, high temperature laser scanning confocal microscopy (HT-LSCM) can be a valuable tool to define the phase stabilities within the observed temperature range.^[9] HT-LSCM enables real time monitoring of microstructure changes by combining laser scanning confocal optics and an infrared heating furnace. Due to the special set-up, high resolution images can be recorded up to the liquid state. A detailed description of the HT-LSCM method can be found in the References 47 through 50.

Within the present work, two alloys selected from an isoplethal section were examined in an HT-LSCM type VL2000DX-SVF17SP from Lasertec to (i) investigate phase stabilities in the peritectic phase equilibrium and (ii) characterize the solidus temperature of a

hyper-peritectic alloy. Therefore, small samples of $5 \times 5 \times 1.5$ mm were cut, ground and polished using the same basic material used for the DSC analysis. For the experiments, the samples were placed on the sample holder in the gold coated, elliptical HT furnace followed by an evacuation of the furnace chamber and flushing with high purity Ar. All samples were heated rapidly ($+100^\circ\text{C}/\text{min}$) from RT to a holding temperature of at least 50°C below the specific phase transformation start temperature determined by the DSC measurements. After annealing for 2 minutes, further heating was performed using a low-heating rate of $10^\circ\text{C}/\text{min}$ to a defined end temperature. Final cooling to RT was done using a cooling rate of $-400^\circ\text{C}/\text{min}$. Temperature control is performed using a type S thermocouple situated at the bottom of the sample holder. In order to determine the exact temperature value of the sample surface, temperature referencing must be executed before every experimental campaign using an external thermocouple welded to the test-sample surface. Throughout the experiment, a video is recorded with a maximum frame rate of 60/s, enabling detailed studies of occurring microstructure changes post experimentally.

IV. RESULTS AND DISCUSSION

All thermodynamic calculations were performed with the thermochemical software FactSage.^[51] In order to provide a better overview of the present results, tables in this chapter summarize the average phase equilibrium temperatures higher than 900°C and the determined Curie Temperature (T_C) along with the chemical compositions of the main elements C and P. For detailed

information on trace element levels in the samples, determined phase transformation temperatures below 900°C and standard deviations of measured phase transformation temperatures, the authors refer to the supplementary Table S-I, Table S-II, Table S-III and Table S-IV.

A. Phase Equilibria in the Binary Fe-P System

The results of the DSC analysis for all binary Fe-P alloys are given in Table III. Phase equilibrium temperatures denoted with “-^{a)}” were not accurately measurable due to the limited resolution of the DSC method in the solid fcc/bcc equilibrium region. Phase transformations marked by “-^{b)}” are not present in the assessment of Shim *et al.*^[32] and were not detected in the DSC signal.

The calculated iron-rich part of the Fe-P system^[32] up to 14 mass pct. P along with the DSC results and experimental data from References 16 through 29 is given in Figure 5. Within the literature research, a lack of experimental melting equilibrium data was identified at [pct P] < 1. In this composition range, the precise knowledge of the solidus temperature T_S and liquidus temperature T_L is of particular importance to characterize the influence of P on solidification phenomena in steel, *e.g.*, microsegregation. In the present study, DSC analysis of samples with 0.026 to 1.18 mass pct. P (A-I to A-XI, see Table III) shows significant lower melting equilibrium temperatures than those predicted by Shim *et al.*^[32] At 1 mass pct. P, the maximum deviations are $\Delta T_{S,\text{max}} = 50^\circ\text{C}$ and $\Delta T_{L,\text{max}} = 10^\circ\text{C}$ at the liquidus phase boundary. With an increasing amount of P (1 to 2.5 mass pct.), the measured solidus temperatures become more consistent with the calculated ones.^[32]

Table III. Chemical Composition and Determined Phase Equilibrium Transformation Temperatures of Investigated Fe-P Binary Alloys

Alloy	P [Mass Pct]	Curie T_C [°C]	$\alpha + \gamma \rightarrow \gamma$ [°C]	$\gamma \rightarrow \alpha + \gamma$ [°C]	$\alpha + \gamma \rightarrow \alpha$ [°C]	$\alpha \rightarrow \alpha + \text{Liquid}$ [°C]	$\alpha + \text{Fe}_3\text{P} \rightarrow \alpha + \text{Liquid}$ [°C]	Liquidus [°C]
A-I	0.026	765.9	924.4	1389.4	1400.3	1527.5	— ^b	1535.1
A-II	0.044	765.2	937.0	1377.7	1385.9	1523.8	— ^b	1534.9
A-III	0.102	763.8	958.2	1367.7	1380.8	1513.3	— ^b	1532.4
A-IV	0.147	767.0	999.4	1341.9	1359.0	1504.7	— ^b	1529.1
A-V	0.322	757.2	— ^b	— ^b	1320.2	1474.6	— ^b	1525.3
A-VI	0.419	758.5	— ^b	— ^b	1272.4	1454.0	— ^b	1520.5
A-VII	0.480	756.9	— ^b	— ^b	— ^a	1450.7	— ^b	1520.9
A-VIII	0.660	751.8	— ^b	— ^b	— ^a	1420.2	— ^b	1515.0
A-IX	0.700	751.6	— ^b	— ^b	— ^b	1407.6	— ^b	1512.8
A-X	0.970	742.7	— ^b	— ^b	— ^b	1348.9	— ^b	1502.6
A-XI	1.180	738.5	— ^b	— ^b	— ^b	1321.5	— ^b	1497.1
A-XII	1.980	720.1	— ^b	— ^b	— ^b	1189.5	— ^b	1468.1
A-XIII	2.300	721.5	— ^b	— ^b	— ^b	1108.3	— ^b	1452.4
A-XIV	3.700	745.9	— ^b	— ^b	— ^b	— ^b	1039.7	1405.1
A-XV	5.870	748.6	— ^b	— ^b	— ^b	— ^b	1042.1	1316.2
A-XVI	6.480	748.5	— ^b	— ^b	— ^b	— ^b	1039.1	1273.9
A-XVII	7.570	748.5	— ^b	— ^b	— ^b	— ^b	1038.8	1206.2
A-XVIII	9.080	748.6	— ^b	— ^b	— ^b	— ^b	1037.2	1134.8

^aNot accurately measurable with the DSC method.

^bNot present according to DSC and thermodynamic assessment of the Fe-P system^[32]

As evident in Figure 5, the experiments indicate that P has a stronger effect on decreasing the liquidus temperature of bcc along the whole composition range. The reconstruction of the phase boundary lines in the bcc + liquid + Fe₃P equilibrium using the present DSC data gives maximum solubility of P in bcc of 2.7 mass percent at the eutectic temperature of 1041 °C, whereas the eutectic composition is 10.26 mass pct. P. These results are in very good agreement with the generally accepted values from Okamoto.^[11] In comparison with experimental melting data from References 16 through 22, the DSC measurements show high correlation with the most recently published equilibration data of Morita and Tanaka.^[22] However, in their work, the determined amounts of P in bcc and liquid

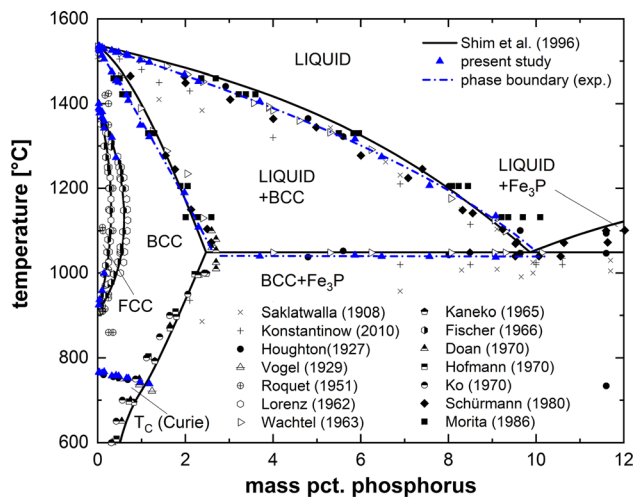
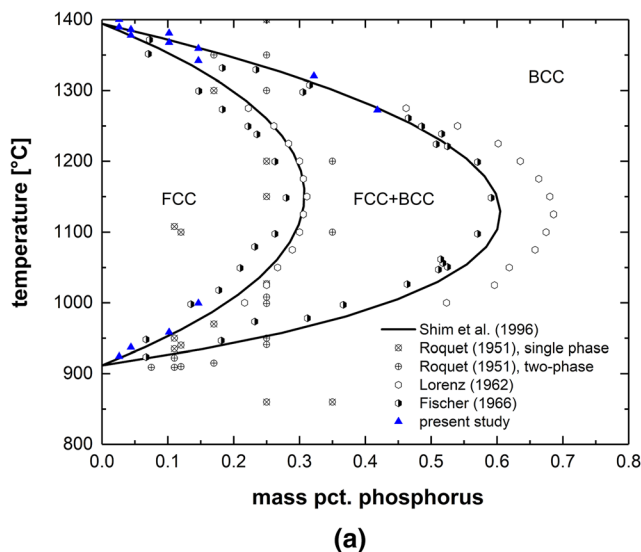


Fig. 5—Calculated iron-rich part of the Fe-P system according to the thermodynamic assessment of Shim *et al.*^[32] along with the present results. Experimental literature data are taken from Refs. 16–29.



using microprobe analysis are strongly deviating. Hence, the present results are more reliable in order to accurately model the solidus and liquidus phase boundaries in future thermodynamic modeling work regarding the Fe-P system.

The gamma loop region of the Fe-P system is shown in Figure 6(a). In general, two trends of P solubility in fcc and bcc exist according to the literature data.^[23–25] The study of Roquet and Jegadan^[23] is in agreement with the work of Lorenz *et al.*^[24], whereas the present results correlate with the measurements of Fischer *et al.*^[25]. Although Lorenz *et al.*^[24] and Fischer *et al.*^[25] used the same experimental equipment, the maximum solubility of P in fcc and bcc differ from each other. The deviation can be assigned to the trace element levels of fcc stabilizing elements (C, Mn, N) in the samples produced. Even small amounts of carbon increase the P solubility in fcc and will shift the gamma loop to higher amounts of P. As given in the supplementary Table S-I and Table S-III, alloys investigated in the present study show very low amounts of impurity elements. Similar chemical analysis was reported in the work of Fischer *et al.*^[25] (C ≤ 50 ppm, Si ≤ 50 ppm, Mn ≤ 10 ppm, S ≤ 50 ppm, N ≤ 40 ppm). Hence, these data sets^[25] are considered as the most reliable for calculating solid state equilibrium between fcc and bcc. The assessment of Shim *et al.*^[32] is in reasonable agreement with the present study, but inconsistencies in selected data from References 24, 25 were pointed out, which should be resolved in future thermodynamic assessments. The measured critical temperature T_C (Curie temperature) of the bcc solution phase as a function of the P content along with experimental data from References 18, 19 is plotted in Figure 6(b). In all studies, a decrease in the Curie temperature at higher P content was observed. Although the work of Shim *et al.*^[32] reproduces the present results satisfyingly well up to 0.50 mass pct. P, remarkable differences ($\Delta T_C = 10$ °C)

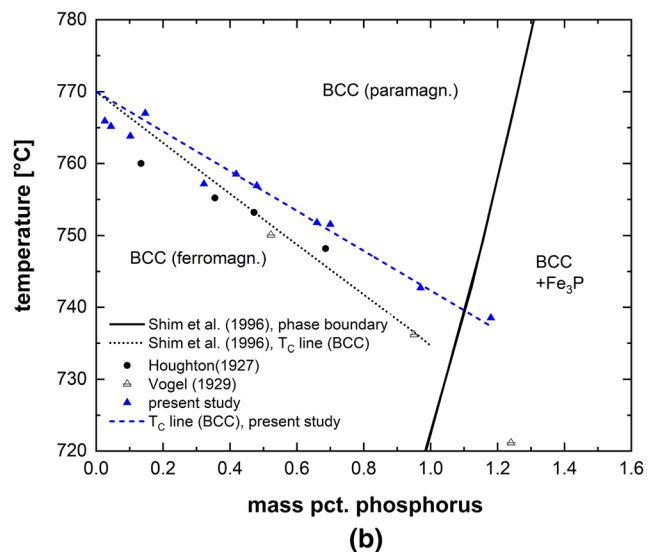


Fig. 6—Gamma loop in the Fe-P system (a) and T_C line in bcc (b) according to the thermodynamic assessment of Shim *et al.*^[32] along with the present results. Experimental literature data are taken from Refs. 18, 19, 23 through 25.

can be found at compositions close to the bcc/bcc + Fe₃P phase boundary.

B. Isolethal Sections Fe-C-0.10 pct P and Fe-0.20 Pct C-P

In general, the peritectic range of the binary Fe-C system can be divided into four different phase transformation paths according to the characteristic points c_A , c_B and c_C .^[9,10] At C content lower than $c_A = 0.09$ mass pct. C,^[40] steel solidifies/melts in bcc-Fe structure. Between c_A and $c_B = 0.17$ mass pct. C^[40] the peritectic transformation coincides with the final solidification/first melting of the alloy. From c_B to 0.53 mass pct. C ($= c_C$,^[40]) the peritectic transformation takes place in the solid/liquid two-phase region. In case of [pct C] > 0.53 mass pct., the steel melts/solidifies in fcc-Fe structure. The phase transformation paths I - IV are summarized in Table IV. In isoplethal Fe-C-X (X=Si, Mn, Al, ...) systems, the alloying element X may significantly shift the characteristic points depending on acting as bcc stabilizing element (e.g. Si, Al) or as fcc stabilizing element (e.g. Mn).^[9,10]

Numerical results of the DSC measurements in the isoplethal sections Fe-C-0.10 pct P and Fe-0.20 pct C-P are summarized in Table V and represented graphically in Figures 7(a) to (c). Depending on the carbon content, the experimentally determined phase transformations in the peritectic range of the Fe-C-P systems can be divided into four different paths, as follows^[9,10]:

- Samples B-I to B-III (0.004 to 0.059 mass pct. C) show separated solid fcc→bcc transformation and melting of the bcc phase (“Path I”) in the DSC signal. The amount of carbon is to the left of the characteristic point c_A .
- Samples B-IV to B-VI (0.096 - 0.136 mass pct. C) and B-VII to B-IX (0.203 to 0.378 mass pct. C) show a peritectic peak during melting. Between 0.096 and 0.136 mass pct. C, the measured fcc→fcc + bcc phase transformation start temperature continuously increases with increasing carbon content, whereas the peritectic start temperature (fcc + bcc→fcc + liquid + bcc) decreases. Therefore, samples B-IV to B-VI are identified as “hypo-peritectic” alloys (“Path II”) between points c_A and c_B .
- In the composition range 0.230 to 0.378 mass pct. C, the investigated samples B-VII to B-IX show a decrease in the solidus temperature (fcc→fcc + liquid) and a slight increase in the peritectic start temperature (fcc + liquid→fcc + liquid + bcc). B-VII to B-IX are “hyper-peritectic” and correspond to “Path III” between the characteristic points c_B and c_C .
- Samples B-X to B-XII (0.69 to 1.38 mass pct. C) only show a melting peak of the fcc phase, defined as “Path IV.” The carbon content is to the right of c_C .
- Based on the observations in the Fe-C-0.10 pct P section, the phase transformations of the samples investigated in the Fe-0.20 pct C-P system (C-I to C-III) can be assigned to “Path III.”

Table IV. Phase Stabilities in the Peritectic Range of the Fe-C System^[9,10]

Path	Position	Phase Stabilities	Characteristics
I	left of “ c_A ”	$L \leftrightarrow L + bcc \leftrightarrow bcc \leftrightarrow bcc + fcc \leftrightarrow fcc$	primary bcc-Fe solidification/melting
II	between c_A and c_B (hypo-peritectic)	$L \leftrightarrow L + bcc \leftrightarrow bcc + fcc \leftrightarrow fcc$	peritectic transformation coincides with the final solidification/first melting
III	between c_B and c_C (hyper-peritectic)	$L \leftrightarrow L + bcc \leftrightarrow L + fcc \leftrightarrow fcc$	peritectic transformation occurs in the solid/liquid two-phase region
IV	right of c_C	$L \leftrightarrow L + fcc \leftrightarrow fcc$	primary fcc-Fe solidification/melting

The pre-identification of hypo-peritectic steel compositions (liquid + bcc → bcc + fcc) is essential for guaranteeing a successful process control in continuous casting. Steel grades in the hypo-peritectic range show strong contraction behavior during solidification that causes non-uniform shell formation, mold-level fluctuations, a higher risk of crack formation and in the worst case, break outs.^[52–54] The experimentally determined hypo-peritectic carbon composition at 0.10 mass pct. phosphorus is between 0.084 and 0.147 mass pct. carbon. Shim *et al.*^[39] underestimated the stability of the liquid phase, which results in a hypo-peritectic range of carbon content between 0.08 to 0.185 mass pct. C. Furthermore, it is evident from Figures 7(a) through (c) that the thermodynamic assessment proposed by Shim *et al.*^[39] results in a higher solidus temperature, as found in the present experiments. At the liquid/fcc equilibrium, the difference of T_S is even more pronounced (25 °C) than at the bcc/liquid equilibrium (10 °C). As the same deviations were also identified in the binary Fe-P system, the systematic difference in the solidus temperature may be attributed to the thermodynamic description of the liquid phase in the binary system.

C. Linking the DSC Method and HT-LSCM in the Isolethal Section with Mass Percent Ratio P/C of 2

The phase equilibrium temperatures measured in the isoplethal Fe-C-P section with a ratio of [pct P]/[pct C] equals 2 are summarized in Table VI. Temperatures denoted with “(a)” were determined by the DSC method and values marked with “(b)” by HT-LSCM analysis. Since the [pct P]/[pct C] ratio in the investigated samples varies between 1.88 and 2.5, all phase diagrams^[39] in this chapter were performed for two different [pct P]/[pct C] ratios of 2 and 2.5.

Figures 8(a) and (b) show the DSC signals of samples D-I and D-II, the present results along with thermodynamic calculations^[39] and the HT-LSCM observations. The DSC offset was corrected to the baseline of 0.0 mW/mg and the DSC signal is presented considering the Tau-R calculation as described in Chapter 3.2.

During the heating of alloy D-I (0.17 pct C-0.43 pct P), first clear deviations from the DSC baseline can be found at 1359.1 °C. At 1416.9 °C the peritectic reaction starts, which is completed at 1456.6 °C. The DSC signal peak at 1507 °C corresponds to the liquidus temperature of the bcc phase. As can be seen in the phase diagram of Figure 8(a), the carbon amount of 0.17 pct C in alloy D-I is very close to the change of the transformation sequence from fcc → fcc + bcc (“hypo-peritectic”) to fcc → fcc + liquid (“hyper-peritectic”). In this case, HT-LSCM was applied to identify the correct present phase stabilities in the high temperature range. Based on the DSC results, the annealing temperature in the HT-LSCM was chosen to be 1300 °C. After 2 minutes of isothermal holding, further heating was performed with a heating rate of 10 °C/min. Within the range of constant heating, the material first shows a fully austenitic structure undergoing constant grain growth. At 1370 °C, the first liquid phase can be observed at the grain boundaries, attesting a hyper-peritectic behavior of alloy D-I; see Figure 8(a-III). The determined value of 1370 °C is in very good agreement with the results from the DSC measurements ($\Delta T \sim 10$ °C). Thermodynamic calculations using the assessment of Shim *et al.*^[39] predict a hypo-peritectic transformation path and a significantly higher phase transformation start temperature (fcc → fcc + bcc) of 1386.59 °C, as found in the DSC measurements.

In the case of alloy D-II (0.34 pct C-0.76 pct P), first noticeable deviations from the DSC baseline are observed at 1194.2 °C. At 1457.1 °C, the sharp increase

Table V. Chemical Composition and Determined High-Temperature Phase Equilibrium Transformation Temperatures of Investigated Fe-C-0.10 Pct P and Fe-0.20 Pct C-P Ternary Alloys

Alloy	C [Mass Pct]	P [Mass Pct]	$\gamma \rightarrow \gamma + \delta$ [°C]	$\gamma + \delta \rightarrow \delta$ [°C]	$\delta \rightarrow \delta + L$ [°C]	$\gamma + \delta \rightarrow \gamma + \delta + L$ [°C]	$\gamma \rightarrow \gamma + L$ [°C]	$\gamma + L \rightarrow \gamma + \delta + L$ [°C]	$\gamma + \delta + L \rightarrow \delta + L$ [°C]	Liquidus [°C]
B-I	0.004	0.107	1359.4	1373.0	1513.9	—*	—*	—*	—*	1531.1
B-II	0.033	0.106	1380.1	1421.2	1501.8	—*	—*	—*	—*	1529.3
B-III	0.059	0.108	1401.3	1452.9	1486.8	—*	—*	—*	—*	1527.5
B-IV	0.099	0.110	1429.1	—*	—*	1471.9	—*	—*	1479.0	1524.6
B-V	0.096	0.101	1425.5	—*	—*	1472.4	—*	—*	1477.9	1525.1
B-VI	0.136	0.105	1452.4	—*	—*	1475.2	—*	—*	1482.7	1520.6
B-VII	0.203	0.106	—*	—*	—*	—*	1448.3	1480.6	1485.8	1515.9
B-VIII	0.296	0.110	—*	—*	—*	—*	1424.8	1487.6	1488.3	1507.6
B-IX	0.378	0.106	—*	—*	—*	—*	1410.6	1490.0	1490.4	1500.8
B-X	0.690	0.099	—*	—*	—*	—*	1357.7	—*	—*	1478.3
B-XI	1.000	0.099	—*	—*	—*	—*	1303.1	—*	—*	1457.8
B-XII	1.380	0.101	—*	—*	—*	—*	1234.4	—*	—*	1427.7
C-I	0.206	0.057	—*	—*	—*	—*	1460.7	1486.9	1489.8	1517.5
C-II	0.199	0.103	—*	—*	—*	—*	1445.5	1480.1	1485.9	1516.3
C-III	0.203	0.158	—*	—*	—*	—*	1428.5	1472.4	1481.5	1514.6

*Phase transformation not present according to the experimental investigations of the pseudo-binary Fe-C-P system.

in the DSC signal corresponds to the start of the peritectic phase transformation. The three-phase equilibrium (bcc + fcc + liquid) is stable only in a very small temperature interval up to 1460.3 °C. Above 1481.7 °C the alloy is in the complete liquid state. It is evident from the DSC signal and the phase diagram that alloy D-II shows a two-phase equilibrium (fcc + liquid) temperature interval of more than 250 °C, resulting in only a minor change in heat when the temperature during heating reaches the solidus line. In order to confirm the determined solidus temperature in the DSC signal of Figure 8(b-I), alloy D-II was rapidly heated up to 1175 °C in the HT-LSCM, annealed for 2 minutes and subsequently heated to an end temperature of 1325°C. Similar to alloy D-I, annealing and further heating with 10 °C/min takes place in the fully austenitic region. When reaching 1210 °C, melting of the fcc phase can be observed. The material remains in the fcc/liquid

two-phase region up to the final temperature. The HT-LSCM observations again highly correlate with the DSC result of 1192.2 °C ($\Delta T \sim 15$ °C). Calculations using the assessment of Shim *et al.*^[39] give $T_S = 1255.5$ °C, which corresponds to a difference of more than 60 °C compared with the experimental results of the present work.

The results of samples D-III (0.68 pct C-1.275 pct P) and D-IV (1.36 pct C-2.96 pct P) are given in Figures 9(a) and (b), respectively. The sharp increase in the DSC signal of alloy D-III at 996.4 °C results from partial melting (fcc + Fe₃P → fcc + Fe₃P + liquid) of the sample. At 1002.7 °C, the reaction fcc + Fe₃P + liquid → fcc + liquid is completed according to the peak in the DSC signal. The liquidus temperature of fcc was obtained at 1421.7 °C. First melting of sample D-IV (1.36 pct C-2.96 pct P) was detected at 956.2 °C. This temperature corresponds to the eutectic phase

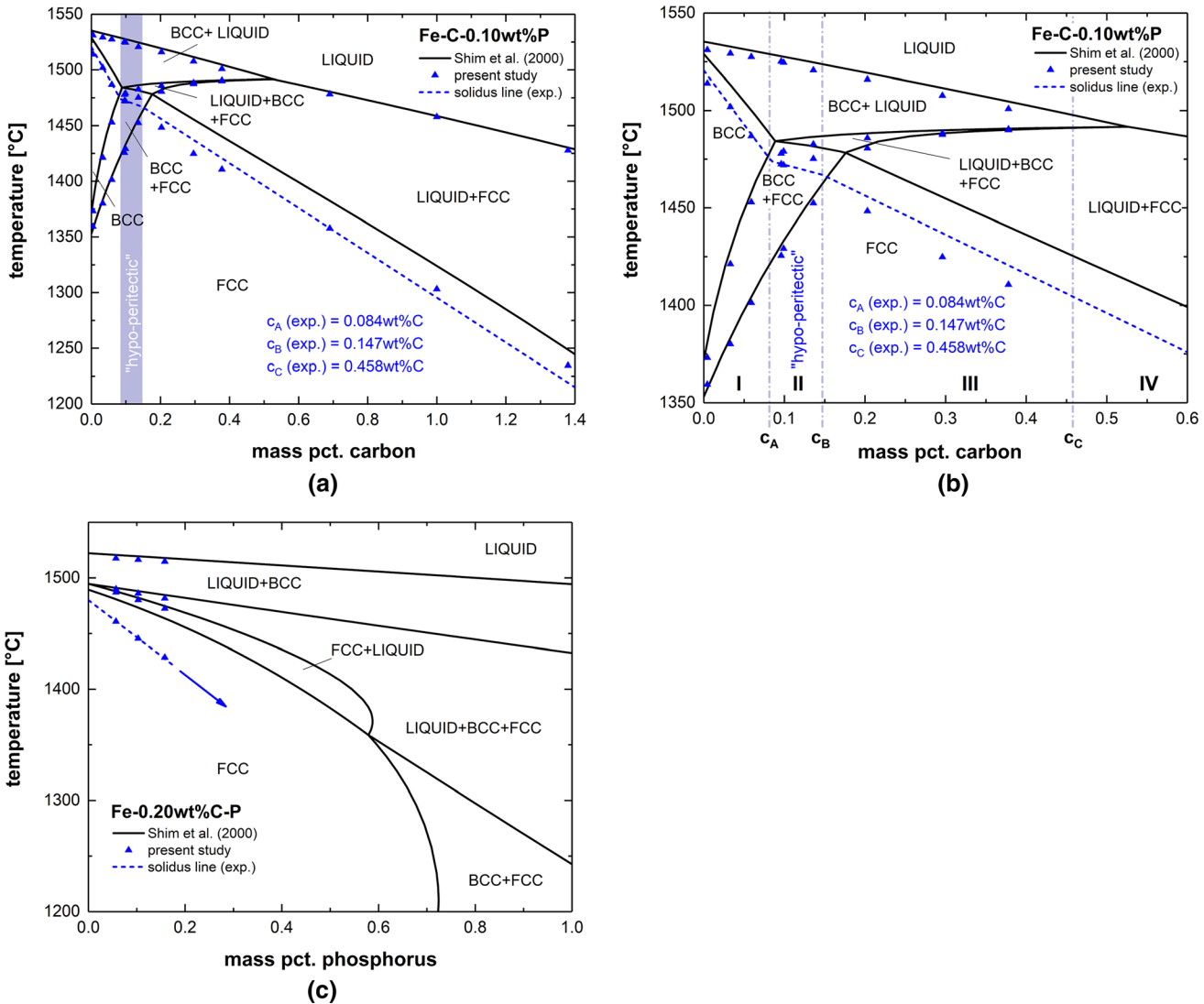


Fig. 7—Calculated vertical sections in the Fe-C-P system^[39] along with present results: Fe-C-0.10 pct P (a), peritectic range in Fe-C-0.10 pct P (b) and Fe-0.20 pct C-P (c).

Table VI. Chemical Composition and Determined High-Temperature Phase Equilibrium Transformation Temperatures in the Fe-C-P Vertical with [pct P]/[pct C] = 2

Alloy	C [Mass Pct.]	P [Mass Pct.]	P/C Ratio [—]	$\gamma + L \rightarrow \gamma + \delta + L$ [°C]	$\gamma + \delta + L \rightarrow \delta + L$ [°C]	Solidus [°C]	Liquidus [°C]
D-I	0.170	0.430	2.53	1416.9 ^a	1456.6 ^a	1359.1 ^a 1370.0 ^b	1507.0 ^a
D-II	0.340	0.760	2.24	1457.1 ^a	1460.3 ^a	1194.2 ^a 1210.0 ^b	1481.7 ^a
D-III	0.680	1.275	1.88	—	—	996.4 ^a	1421.7 ^a
D-IV	1.360	2.960	2.18	—	—	956.2 ^a	^a

^aDetermined by the DSC method.

^bDetermined by HT-LSCM.

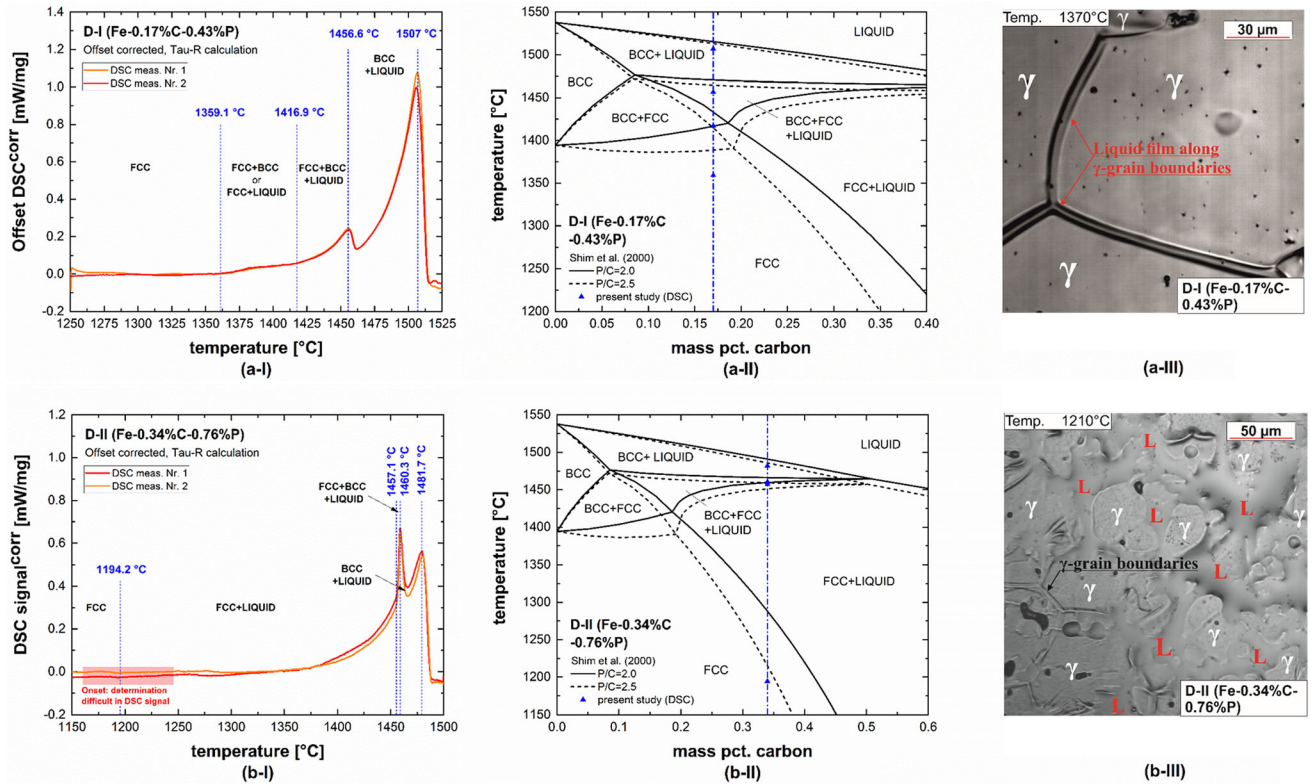


Fig. 8—Results of linking DSC and HT-LSCM for samples D-I (a) and D-II (b) showing the DSC signal (I), the calculated phase diagram along with the present experimental data (II) and the HT-LSCM observation of present phase transformations (III).

equilibrium in the ternary Fe-C-P system ($fcc + Fe_3P + Fe_3C/fcc + Fe_3P + liquid$) and highly correlates with the generally accepted values of 952 °C^[37,39] and 955 °C.^[38] Above 967.8 °C only fcc and liquid phases are stable; the liquidus temperature was found to be 1319.6 °C. In general, the phase diagrams in Figure 9 are in satisfying agreement with the DSC measurements. Particularly at temperatures lower than 1000 °C, precise prediction of phase equilibrium temperatures was achieved in the work of Shim *et al.*^[39] However, higher deviations can be found at the liquidus temperature ($\Delta T_L \sim 20^\circ C$). Finally, the results of samples D-I to D-IV are presented along with the calculated phase diagram in Figure 10.

V. CONCLUSION AND OUTLOOK

The purpose of the present work was to provide new phase diagram data for the improvement of thermodynamic databases and solidification models for P alloyed steel grades. Therefore, high temperature phase equilibria in the binary Fe-P system and three isoplethal sections in the ternary Fe-C-P system were characterized by means of differential scanning calorimetry (DSC). NETZSCH's Tau-R software^[44,45] was critically evaluated and successfully used to optimize the efficiency of the DSC measurements by guaranteeing equilibrium conditions at the same time. The binary Fe-P subsystem was reinvestigated in the range 0.025 to 9 mass percent

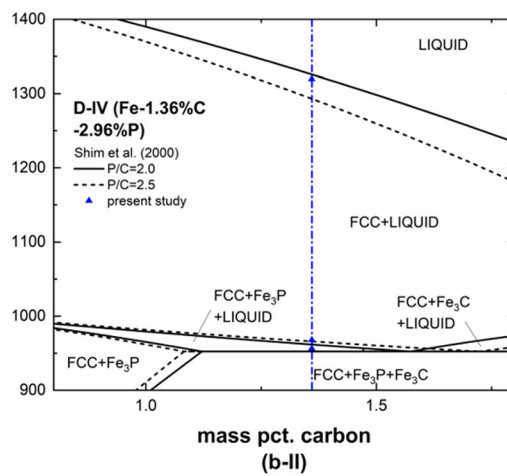
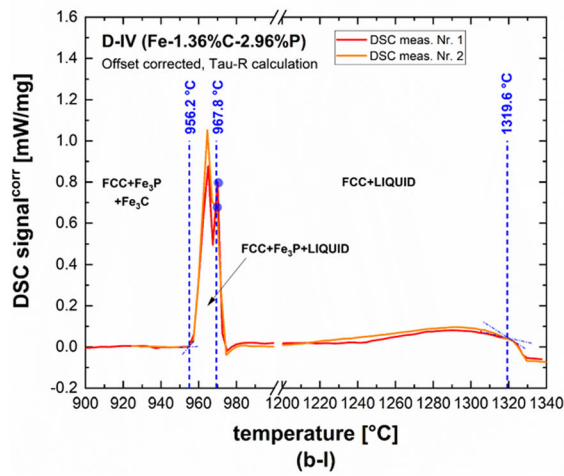
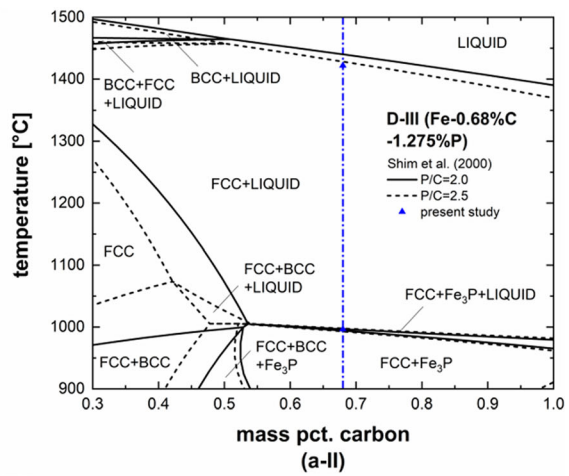
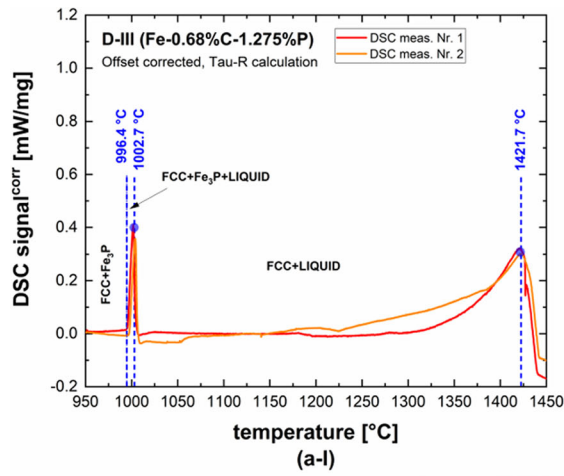


Fig. 9—Results of DSC measurements for samples D-III (a) and D-IV (b) showing the DSC signal (I) and the calculated phase diagram^[39] along with the present experimental data (II).

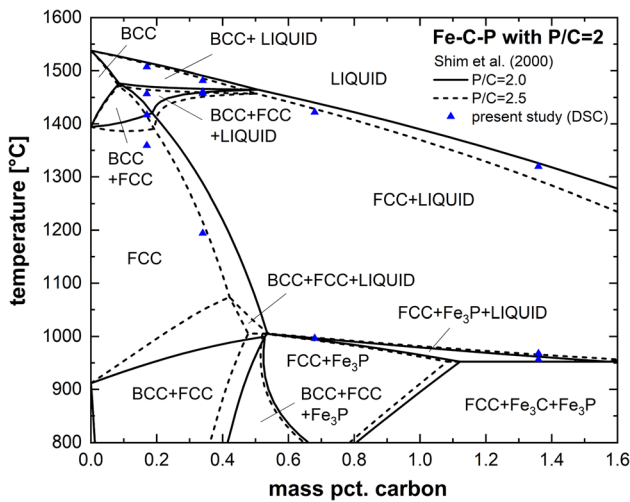


Fig. 10—Results of DSC measurements in the vertical section [pct P]/[pct C] equals 2 along with the calculated phase diagram^[39] for mass pct. P/C ratios of 2 and 2.5.

P. The two isoplethal sections Fe-C-0.10 wt pct P and Fe-0.20 wt pct C-P represent the initial phosphorus composition of P alloyed steel grades, whereas a third section with constant P/C mass percent ratio of 2 corresponds to the typical interdendritic enrichments of C and P during solidification. In the latter section, selected DSC measurements were linked with high temperature laser scanning microscopy (HT-LSCM) observations to visually identify phase stabilities in the peritectic range. In the binary Fe-P system, significant differences were found between the DSC results and the most widely accepted thermodynamic assessment of Shim *et al.*^[32] In the composition range [pct P] < 1, deviations up to 50 °C between the calculated and measured solidus temperatures were obtained. Although phase equilibria in the fcc/bcc gamma loop region are in high agreement with the most recent data of Fischer *et al.*^[25] the experiments show inconsistencies with the calculations.^[39] Similar to the binary system, experimental results in the ternary Fe-C-0.10 wt pct P and

Fe-0.20 pct C-P sections indicate higher stability of the liquid phase than that found in the optimization.^[39] The experimentally determined peritectic range in the Fe-C-0.10 wt pct P section is between 0.084-0.147 mass pct. C, whereas the calculations^[39] predict C composition 0.08-0.185. In the [pct P]/[pct C] equals 2 section, HT-LSCM was successfully applied to identify the present phase stabilities (fcc/bcc/liquid) within in the investigated temperature range and the observations highly correlate with results from the DSC measurements. The present experimental data can be used to refine previous thermodynamic modeling of the Fe-P and the Fe-C-P ternary system in a CALPHAD framework. The revised thermodynamic modeling of the two systems by the present authors is available elsewhere.^[55] This work gives much improved thermodynamic description of the two systems, which certainly yields better prediction of thermodynamic calculation for segregation behavior in these system during casting or cooling.

ACKNOWLEDGMENTS

Open access funding provided by Montanuniversität Leoben. The authors gratefully acknowledge the financial support under the scope of the COMET program within the K2 Center “Integrated Computational Material, Process and Product Engineering (ICMPPE)” (Project No 859480). This program is supported by the Austrian Federal Ministries for Transport, Innovation and Technology (BMVIT) and for Digital and Economic Affairs (BMDW), represented by the Austrian research funding association (FFG), and the federal states of Styria, Upper Austria and Tyrol.

ELECTRONIC SUPPLEMENTARY MATERIAL

The online version of this article (<https://doi.org/10.1007/s11661-020-05912-z>) contains supplementary material, which is available to authorized users.

OPEN ACCESS

This article is licensed under a Creative Commons Attribution 4.0 International License, which permits use, sharing, adaptation, distribution and reproduction in any medium or format, as long as you give appropriate credit to the original author(s) and the source, provide a link to the Creative Commons licence, and

indicate if changes were made. The images or other third party material in this article are included in the article’s Creative Commons licence, unless indicated otherwise in a credit line to the material. If material is not included in the article’s Creative Commons licence and your intended use is not permitted by statutory regulation or exceeds the permitted use, you will need to obtain permission directly from the copyright holder. To view a copy of this licence, visit <http://creativecommons.org/licenses/by/4.0/>.

REFERENCES

1. M. Wintz, M. Bobadilla, and J. Jolivet: *Rev. Metall.*, 1994, vol. 91, pp. 106–14.
2. E. Schmidtman and F. Rakoski: *Arch. Eisenhuettenwes.*, 1983, vol. 54, pp. 357–62.
3. M. Wolf and W. Kurz: *Metall. Trans. B*, 1981, vol. 12, pp. 85–93.
4. H.G. Suzuki, S. Nishimura, and Y. Nakamura: *Trans. Iron Steel Inst. Jpn.*, 1984, vol. 24, pp. 54–59.
5. X.-M. Chen, S.-H. Song, L.-Q. Weng, S.-J. Liu, and K. Wang: *Mater. Sci. Eng. A*, 2011, vol. 528, pp. 8299–04.
6. M. Yamashita, H. Miyukia, Y. Matsudaa, H. Naganoa, and T. Misawa: *Corros. Sci.*, 1994, vol. 36, pp. 283–99.
7. M. Yamashita, H. Nagano, T. Misawa, and H.E. Townsend: *ISIJ Int.*, 1998, vol. 38, pp. 285–90.
8. L. Barbé, K. Verbeken, and E. Wettinck: *ISIJ Int.*, 2006, vol. 46, pp. 1251–57.
9. P. Presoly, R. Pierer, and C. Bernhard: *Metall. Mater. Trans. A*, 2013, vol. 44A, pp. 5377–88.
10. P. Presoly, G. Xia, P. Reisinger, and C. Bernhard: *Berg- Huettenmaenn. Monatsh.*, 2014, vol. 159, pp. 430–37.
11. H. Okamoto: *Bull. Alloy Phase Diagrams*, 1990, vol. 11, pp. 404–12.
12. W. Franke, K. Meisel, and R. Juza: *Z. Anorg. Chem.*, 1934, vol. 218, pp. 346–59.
13. K. Meisel: *Z. Anorg. Chem.*, 1934, vol. 218, pp. 360–64.
14. M. Heimbrecht and W. Biltz: *Z. Anorg. Chem.*, 1939, vol. 242, pp. 233–36.
15. W. Jeitschko and D.J. Braun: *Acta Crystallogr. B*, 1978, vol. 34, pp. 3196–3201.
16. B. Saklatwalla: *J. Iron Steel Inst.*, 1908, vol. 77, pp. 92–103.
17. N. Konstantinow: *Z. Anorg. Chem.*, 1910, vol. 66, pp. 209–27.
18. J.L. Houghton: *J. Iron Steel Inst.*, 1927, vol. 115, pp. 417–33.
19. R. Vogel: *Arch. Eisenhuettenw.*, 1929, vol. 3, pp. 369–81.
20. E. Wachtel, G. Urbain, and E. Übelacker: *C.R.*, 1963, vol. 257, pp. 2470–72.
21. E. Schürmann: *Arch. Eisenhuettenw.*, 1980, vol. 51, pp. 325–27.
22. Z.I. Morita and T. Tanaka: *Trans. Iron Steel Inst. Jpn.*, 1986, vol. 26, pp. 114–20.
23. P. Roquet and G. Jegaden: *Rev. Metall.*, 1951, vol. 48, pp. 712–21.
24. K. Lorenz and H. Fabritius: *Arch. Eisenhuettenw.*, 1962, vol. 33, pp. 269–75.
25. W.A. Fischer, K. Lorenz, H. Fabritius, A. Hoffmann, and G. Kalwa: *Arch. Eisenhuettenw.*, 1966, vol. 37, pp. 79–86.
26. H. Kaneko, T. Nishizawa, K. Tamaki, and A. Tanifuji: *J. Japan. Inst. Metals*, 1965, vol. 29, pp. 166–70.
27. A.S. Doan and J.I. Goldstein: *Metall. Trans.*, 1970, vol. 1, pp. 1759–67.
28. H.P. Hofmann, K. Löhberg, and W. Reif: *Arch. Eisenhuettenw.*, 1970, vol. 41, pp. 975–82.
29. M. Ko and T. Nishizawa: *J. Jpn. Inst. Met.*, 1979, vol. 43, pp. 118–26.
30. P. Spencer and O. Kubaschewski: *Arch. Eisenhuettenwes.*, 1978, vol. 49, pp. 225–28.

31. P. Gustafson, Report IM-2549, Swedish Institute for Metals Research, Stockholm, Sweden, 1990.
32. J.H. Shim, C.S. Oh, and D.N. Lee: *J. Korean Inst. Met. Mater.*, 1996, vol. 34, pp. 1385–93.
33. H. Ohtani, N. Hanaya, M. Hasebe, S.-I. Teraoka, and M. Abe: *Calphad*, 2006, vol. 30, pp. 147–58.
34. T. Tokunaga, N. Hanaya, H. Ohtani, and M. Hasebe: *Mater. Sci. Forum*, 2007, vols. 561–565, pp. 1899–1902.
35. Z.-M. Cao, K.-P. Wang, Z.-Y. Qiao, and G.-W. Du: *Acta Phys. Chim. Sin.*, 2012, vol. 28, pp. 37–43.
36. J. Miettinen and G. Vassilev: *Phase Equilib. Diffus.*, 2014, vol. 35, pp. 458–68.
37. P. Perrot, Landolt-Börnstein—Group IV Physical Chemistry Volume 11D2: “Iron Systems, Part 2”, Springer Materials, Springer, Berlin Heidelberg, 2008. https://doi.org/10.1007/978-3-540-74196-1_11.
38. E. Schürmann, U. Hensgen, and J. Schweinichen: *Giessereiforschung*, 1984, vol. 36, pp. 121–29.
39. J.-H. Shim, C.-S. Oh, and D.N. Lee: *Z. Metallkd.*, 2000, vol. 91, pp. 114–20.
40. P. Gustafson: *Scand. J. Metall.*, 1985, vol. 14, pp. 259–67.
41. G.W. Höhne, H.W. Hemminger, and H.J. Flemmingheim: *Differential Scanning Calorimetry: An Introduction to Practitioners*, 1st ed., Springer, Berlin, 1996.
42. W. J. Boettinger, U. R. Kattner, K.-W. Moon and J. H. Perepezko, DTA and Heat-flux DSC measurements of Alloy Melting and Freezing. NIST Recommended Practice Guide, Special Publication 960-15, 2006.
43. L.A. Chapman: *J. Mater. Sci.*, 2004, vol. 39, pp. 7229–36.
44. Software: NETZSCH Tau-R Calibration 8.0.1 from Netzsch Gerätebau GmbH, Selb, Germany, 2019.
45. E. Moukhina and E. Kaisersberger: *Thermochim. Acta*, 2009, vol. 492, pp. 101–109.
46. W.J. Boettinger and U.R. Kattner: *Metall. Mater. Trans. A*, 2002, vol. 33A, pp. 1779–94.
47. M. Reid, D. Phelan, and R. Dippenaar: *ISIJ Int.*, 2004, vol. 44, pp. 565–72.
48. C. Bernhard, S. Schider, A. Sormann, G. Xia, and S. Ilie: *Berg-Huettenmaenn. Monatsh.*, 2011, vol. 156, pp. 161–67.
49. S. Griesser and R. Dippenaar: *ISIJ Int.*, 2014, vol. 54, pp. 533–35.
50. N. Fuchs, P. Krajewski, and C. Bernhard: *Berg-Huettenmaenn. Monatsh.*, 2015, vol. 160, pp. 214–20.
51. C.W. Bale, E. Bélisle, P. Chartrand, S.A. Decterov, G. Eriksson, A.E. Gheribi, K. Hack, I.-H. Jung, Y.-B. Kang, J. Melançon, A.D. Pelton, S. Petersen, C. Robelin, J. Sangster, P. Spencer, and M.-A. van Ende: *Calphad*, 2016, vol. 54, pp. 35–53.
52. A. Grill and J.K. Brimacombe: *Ironmak. Steelmak.*, 1976, vol. 3, pp. 76–79.
53. Y. Maehara, K. Yasumoto, H. Tomono, T. Nagamichi, and Y. Ohmori: *Mater. Sci. Technol.*, 1990, vol. 6, pp. 793–806.
54. G. Xia, C. Bernhard, S. Ilie and C. Fürst, Proceedings of the 6th European Conference on Continuous Casting 2008, Riccione, Italy, 2008.
55. M. Bernhard, Y.-B. Kang, P. Presoly, A.E. Gheribi, and C. Bernhard: *Calphad*, 2020, vol. 70, art. no. 101795.

Publisher’s Note Springer Nature remains neutral with regard to jurisdictional claims in published maps and institutional affiliations.

Paper II

Critical evaluation and thermodynamic modeling of the Fe–P and Fe–C–P system

M. Bernhard, Y.-B. Kang, P. Presoly, A.E. Gheribi and C. Bernhard

CALPHAD, 2020, vol. 70, art. no. 101795.

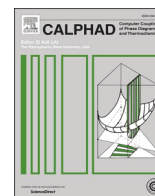
Abstract: Phosphorus is known to be a strongly segregating element in steel; even small amounts influence the solidification phenomena and product quality during casting processes. In order to provide an accurate prediction tool for process control in steelmaking, a CALPHAD-type thermodynamic optimization of the Fe–C–P system was performed including modeling of the binary Fe–P subsystem. The liquid phase was modeled using the Modified Quasichemical Model (MQM) in the pair approximation, which generally yields better results for strong short-range ordering (SRO) tendency in the solution. The solid bcc and fcc solutions were described using the Compound Energy Formalism (CEF). In addition, ab-initio calculations were performed to estimate the enthalpies of formation of the corresponding end-member for fcc and bcc, respectively. The phosphides Fe₃P, Fe₂P and FeP were treated as stoichiometric compounds. Higher order phosphides were not considered, since there is no reliable experimental information available in literature. The present model successfully reproduces most of the literature data within the experimental uncertainty in the Fe–C–P system without introducing a ternary parameter for the liquid phase. Compared with previous thermodynamic assessments, the agreement with recently published thermal analysis measurements of Fe–P and Fe–C–P alloys is significantly improved.

Used and reprinted based on author rights in Elsevier's proprietary journals



Contents lists available at ScienceDirect

Calphad

journal homepage: <http://www.elsevier.com/locate/calphad>

Critical evaluation and thermodynamic modeling of the Fe–P and Fe–C–P system

Michael Bernhard^a, Youn-Bae Kang^{b,*}, Peter Presoly^a, Aimen E. Gheribi^c, Christian Bernhard^a

^a Chair of Ferrous Metallurgy, Montanuniversitaet Leoben, Leoben, Austria

^b Graduate Institute of Ferrous Technology, Pohang University of Science and Technology, Pohang, Republic of Korea

^c Centre de Recherche en Calcul Thermochemique, École Polytechnique de Montréal, Montreal, Canada

ARTICLE INFO

Keywords:

Fe–P
Fe–P–C
CALPHAD
Modified quasichemical model (MQM)
Short-range ordering (SRO)
Thermodynamic database

ABSTRACT

Phosphorus is known to be a strongly segregating element in steel; even small amounts influence the solidification phenomena and product quality during casting processes. In order to provide an accurate prediction tool for process control in steelmaking, a CALPHAD-type thermodynamic optimization of the Fe–C–P system was performed including modeling of the binary Fe–P subsystem. The liquid phase was modeled using the Modified Quasichemical Model (MQM) in the pair approximation, which generally yields better results for strong short-range ordering (SRO) tendency in the solution. The solid bcc and fcc solutions were described using the Compound Energy Formalism (CEF). In addition, *ab-initio* calculations were performed to estimate the enthalpies of formation of the corresponding end-member for fcc and bcc, respectively. The phosphides Fe₃P, Fe₂P and FeP were treated as stoichiometric compounds. Higher order phosphides were not considered, since there is no reliable experimental information available in literature. The present model successfully reproduces most of the literature data within the experimental uncertainty in the Fe–C–P system without introducing a ternary parameter for the liquid phase. Compared with previous thermodynamic assessments, the agreement with recently published thermal analysis measurements of Fe–P and Fe–C–P alloys is significantly improved.

1. Introduction

As phosphorus is generally known as a critical element in steel, the production of low-phosphorus, high quality steel is state-of-the-art in modern steel production. Particularly in continuous casting, higher levels of phosphorus can cause serious problems in the process. During solidification, phosphorus strongly segregates in interdendritic regions and favors the formation of internal cracks. In medium carbon and high carbon steels, the segregation tendency and crack sensitivity increase due to the strong interaction with carbon and a change in the crystallization sequence [1–4]. However, in recent steel design, phosphorus has also been used as an alloying element in steel grades for automotive applications. Phosphorus is added to Interstitial-Free (IF) alloying concepts as an effective solution hardening element [5]. In Transformation-Induced-Plasticity (TRIP) steels, phosphorus partly substitutes silicon and aluminum in order to suppress the precipitation of carbides and stabilize the retained austenite [6]. Hence, reliable thermodynamic databases are required as a basis for the metallurgical process models to guarantee a successful process control for casting

phosphorus alloyed steel grades.

The binary Fe–P system has been modeled several times in the past [7–13]. Spencer and Kubaschewski [7] combined available published experimental data with estimated heat capacities and entropies of phosphides to provide a thermodynamic set of parameters for this system. In later work, Gustafson [8] assessed the system particularly in the Fe-rich side up to 50 atomic percent of P. Extensive work has been performed by Shim et al. [9] considering new thermodynamic activity data of the liquid solution and measured heat capacities of phosphides [14]. Cao et al. [12] performed a thermodynamic reoptimization of the Fe–P system over the whole composition range. Miettinen and Vassilev [13] published a description of the Fe–P system in the framework of developing a consistent Fe–P–X thermodynamic database. Shim et al.'s [9] model parameters of the liquid phase were accepted with minor modifications of the parameters for the fcc and bcc phase and change in the P reference state from red to white phosphorus. A thermodynamic model for calculating the mass action concentrations of structural units in the binary Fe–P liquid phase was developed by Yang et al. [15] based on the atom-molecule coexistence theory. Based on their own binary

* Corresponding author.

E-mail address: ybkang@postech.ac.kr (Y.-B. Kang).

<https://doi.org/10.1016/j.calphad.2020.101795>

Received 17 March 2020; Received in revised form 25 May 2020; Accepted 30 May 2020

Available online 15 June 2020

0364-5916/© 2020 Elsevier Ltd. All rights reserved.

Fe–P description and the most accepted Fe–C model [16], Gustafson [8] and later Shim et al. [17] assessed the ternary Fe–C–P system. Within their work, activity of the liquid phase, liquidus projections and several vertical and isothermal sections were considered.

Recently, four of the present authors reinvestigated the binary Fe–P system and various vertical sections of the Fe–C–P system by means of differential scanning calorimetry (DSC) [18]. Obviously, there are still discrepancies between calculated and measured phase equilibria temperatures using available thermodynamic assessments, particularly with respect to solidification. In previous assessments [8–13,17], the Bragg-Williams (BW) random mixing model was used to formulate the Gibbs energy of the liquid phase. The binary Fe–P liquid phase exhibits a strong short-range-ordering (SRO) tendency, which is difficult to take into account with the BW model. Hence, the Modified Quasichemical Model (MQM) in the pair-approximation [19,20] was applied in the present study, due to its better performance in solutions with strong SRO. The solid fcc and bcc solutions were described by the Compound Energy Formalism (CEF) [21] with two-sublattices. Fe₃P, Fe₂P and FeP phosphides were treated as stoichiometric compounds. Higher order phosphides were not considered, since there is no reliable experimental data available in literature. Model parameters of the sub-binary Fe–C system are taken from the work of Shubhank and Kang [22] and Gustafson [8]. The main purpose of the present work is to provide a set of thermodynamic parameters to reproduce the DSC data of M. Bernhard et al. [18] more accurately, in consideration of extensive experimental literature data.

2. Literature review

There is a large variety of thermodynamic and phase diagram data available in literature. A review of experimental investigations of the Fe–P system up to 1990 was given by Okamoto [23]. Perrot [24] summarized phase relations, crystallographic data and material properties in the Fe–C–P system. Another extensive literature review is not repeated in the present work, but published data with relevance to the optimization will be reported briefly.

2.1. Fe–P system

Schürmann et al. [25] indirectly derived the integral enthalpy of mixing at 1550 °C from calorimetric measurements in a high-temperature calorimeter in the composition range up to 33 at% P. Urbain [26,27] determined activities of phosphorus with respect to infinite dilution by distribution experiments between immiscible liquid iron and silver. His activity data is available in a temperature range of 1300–1600 °C and up to 33 at% P. A similar technique and experimental conditions were used in the work done by Ban-Ya and Suzuki [28]. Based on the activity measurements, Urbain [27] also provided the partial mixing enthalpy of P. Fischer et al. [29]. Performed electromotive force measurements using solid and liquid calcium-phosphate electrolytes at 1650 °C between 0.1 and 31 at% phosphorus. Vapor pressure of phosphorus in liquid Fe–P alloys was measured by Ban-Ya et al. [30] at temperatures of 1200–1500 °C and 5 to 25 at% P and by Schenck [31, 32] from 1515 to 1650 °C with maximum concentrations of 43 at% P. Zaitsev et al. [14] determined activities of phosphorus in the liquid phase from their Knudsen effusion cell data of P vapor pressure. With respect to pure liquid components, the activities are given up to 30 at% P at 1536 °C and at various fixed compositions in the temperature range from 1127 to 1527 °C. Zaitsev et al. [14] further measured heat capacities of iron phosphides using the DSC method and determined their Gibbs energies of formation from the effusion experiments. The enthalpy of formation for Fe₂P was estimated by Roth et al. [33] using combustion calorimetry. Weibke [34] measured heats of formation of Fe₃P, Fe₂P and FeP in a high-temperature calorimeter at 635 °C. Lewis and Myers [35] chose the Knudsen effusion cell to measure the heat of formation of phosphides at 627 °C. Several DFT studies have been reported in the

literature on the prediction of the enthalpy of formation of stable and metastable compounds in both Fe–P and Fe–C systems, considering the same methodology used in the present study (PAW pseudopotential and GGA exchange correlation functional) [10,11,36]. Moreover, for several stable and metastable compounds, a summary of enthalpy of formation and equilibrium lattice parameters are available in Material project [37]. For Fe–P and Fe–C, the DFT-based predictions of the enthalpy of formation compare very well with available experimental data as shown by Ohtani et al. [10] for Fe–P and, among others, by Hallstedt [38] for Fe–C. Note that for Fe–P, a significant magnetic contribution to the enthalpy of formation have been calculated. For C–P, Claeysens et al. [39] showed that P_xC_y compounds are thermodynamically unstable and defect zinc-blended structures are favored. There is no data available for P_xC_y end-member of fcc and bcc phases.

There are large discrepancies in the phase diagram data of the binary Fe–P system resulting from both the different experimental procedures and the impurity levels of the alloys used. First investigations of the Fe–P diagram were performed by Saklatwalla [40] and Konstantinow [41] evaluating cooling curves of liquid Fe–P alloys by means of the pyrometer technique. Houghton [42] applied thermal analysis and magnetic measurements to determine phase equilibrium temperatures. Phase equilibria between solid fcc and bcc solution were determined in the work of Roquet and Jegaden [43] by applying thermal treatment of samples with different P concentrations with subsequent quenching and micrographic examination. Additionally, phase boundaries in the gamma loop were measured using the dilatometer method. Lorenz et al. [44] and Fischer et al. [45] used the magnetic balance to reconstruct the fcc + bcc gamma loop up to 1400 °C. Thermal and magnetic analysis were employed by Wachtel et al. [46] to determine the solid + liquid equilibria between 0.5 and 13 mass pct. Phosphorus. Kaneko et al. [47] reported P solubility in bcc between 700 and 1000 °C. Doan and Goldstein [48] combined long-term heat treatments with electron microprobe analysis in the temperature range of 550–1100 °C to measure the compositions of coexisting stable phases. Ko and Nishizawa [49] determined the solubility of P in bcc from 600 to 1200 °C using X-ray diffraction and microprobe analysis. Schürmann [50] investigated the melting equilibria in the Fe–P system by thermal analysis and holding tests with subsequent EPMA analysis of the quenched samples. Similar holding tests were also performed in the work of Morita and Tanaka [51]. Recently, M. Bernhard et al. [18] provided new equilibrium data on phase transformations in the binary Fe–P system using the differential scanning calorimetry (DSC) method. Within this extensive work, equilibrium temperatures between 0.025 and 9 mass pct. Phosphorus were determined.

2.2. Fe–C–P system

Frohberg et al. [52] and Hadrys et al. [53] studied the influence of carbon on the activity of P using the distribution method between liquid iron and silver at 1600 °C. Schenck et al. [54] investigated the solubility of phosphorus in carbon-saturated melts at 1515 °C by means of P vapor pressure measurements. Yang [55] measured the carbon solubility depending on the P concentration with the carbon iso-activity method at 1400 °C. Carbon solubility in liquid Fe–C–P melts in the temperature ranges of 1200–1600 °C and 1300–1570 °C were determined by Turkdogan and Leake [56] and Schürmann and Kramer [57], respectively. Various vertical sections in the Fe–C–P determined by cooling curves and metallographic examinations were reported by Vogel [58]. Thermal analysis and metallographic examinations of the 2.4 mass pct. C isopleth section were performed by Ohide and Ohira [59]. The liquidus surface in the iron-rich corner was constructed by Schürmann et al. [60] using thermal analysis. Kaneko et al. [47] reported the solubility of phosphorus in fcc at 800, 900 and 1000 °C. Langenscheid et al. [61] used metallographic analysis and EPMA to determine the phase boundaries at 900, 950 and 1000 °C. Hofmann et al. [62] applied diffusion annealing experiments with subsequent EPMA analysis to determine four

Table 1
Crystallographic data of stable phases found in the Fe–C–P system [23,24].

Phase	Pearson symbol	Space group	Strukturbericht	Prototype	Model	Denoted in text
Liquid	–	–	–	–	MQM ^a	liquid
(γ Fe)	cF4	Fm $\bar{3}$ m	A1	Cu	CEF ^b	fcc
(α Fe), (δ Fe)	cI2	Im $\bar{3}$ m	A2	W	CEF	bcc
Fe ₃ P	tI32	I $\bar{4}$	D0 _e	Ni ₃ P	ST ^c	–
Fe ₂ P	hP9	P $\bar{6}$ 2m	C22	Fe ₂ P	ST	–
FeP	oP8	Pna2 ₁	–	MnP	ST	–
FeP ₂	oP6	Pnmm	C18	FeS ₂ (marcasite)	ST ^d	–
FeP ₄	mP30	P2 ₁ /c	–	FeP ₄	ST ^d	–
(P) white	c**	–	–	(P) white	ST	P
Fe ₃ C	oP16	Pnma	D0 ₁₁	Fe ₃ C	ST	Fe ₃ C
C (gr.)	hP4	P6 ₃ /mmc	A9	C (gr.)	ST	C

^a Modified Quasichemical Model.

^b Compound Energy Formalism.

^c Stoichiometric Compound.

^d Not considered in the present study.

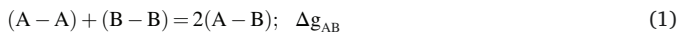
isothermal sections at 600, 700, 800 and 900 °C. The isothermal sections of Langenscheid et al. [61] are in good agreement with the unpublished ones of Nishizawa [63] reported in the assessments of Gustafson [8] and Shim et al. [17]. Three vertical section in the Fe–C–P with 0.10 mass pct. P phosphorus, 0.20 mass pct. C and constant P/C mass pct. Ratio of 2 were provided by M. Bernhard et al. [18] using the DSC method.

3. Thermodynamic models

The assessment of the Fe–C binary system by Gustafson [16] is most commonly used in thermodynamic databases. However, unreliable stabilization of the bcc phase at high temperatures was pointed out [22], due to an inverted miscibility gap of the liquid phase. This is partly due to neglecting strong SRO between Fe and C. In order to eliminate this phenomenon, Shubhank and Kang [22] re-optimized the Fe–C binary liquid phase using the MQM, keeping the Gibbs energies of solid phases unchanged, as suggested by Gustafson [16]. In the present work, the binary Fe–C description of Shubhank and Kang [22] was used. All calculations and optimizations were performed with the thermodynamic software FactSage 7.3 [64]. Gibbs energies of pure Fe, C and P are taken from Dinsdale [65]. The crystallographic data of stable phases in the Fe–C–P system are listed in Table 1. All parameters used or optimized in the present work are summarized in Table 2.

3.1. Liquid phase

In order to take into account strong SRO, the MQM in pair approximation [19,20] was applied to formulate the Gibbs energy of the liquid phase. A detailed description of this model can be found in Ref. [19,20], so the model will be described only briefly in the present study. In the pair approximation for a binary solution consisting of A and B atoms, the following pair exchange reaction on the sites of a quasi-lattice is considered:



where ($i - j$) represent the first nearest neighbor pair and Δg_{AB} is the non-configurational Gibbs free energy change forming 2 mol of ($i - j$) pairs. If n_A and n_B are the number of moles A and B, n_{ij} is the number of ($i - j$) pairs and Z_A and Z_B are the coordination numbers of A and B, then the following mass balances are considered:

$$Z_A n_A = 2n_{AA} + n_{AB} \quad (2)$$

$$Z_B n_B = 2n_{BB} + n_{AB} \quad (3)$$

The pair fractions, mole fractions and coordination-equivalent fractions are defined as:

$$X_{ij} = n_{ij} / (n_{AA} + n_{BB} + n_{AB}) \quad (4)$$

$$X_A = n_A / (n_A + n_B) = 1 - X_B \quad (5)$$

$$Y_A = Z_A n_A / (Z_A n_A + Z_B n_B) = Z_A X_A / (Z_A X_A + Z_B X_B) = 1 - Y_B \quad (6)$$

The Gibbs energy of the solution is given by:

$$G = (n_A g_A^0 + n_B g_B^0) - T \Delta S^{\text{config}} + (n_{AB} / 2) \Delta g_{AB} \quad (7)$$

where g_A^0 and g_B^0 are the molar Gibbs energies of the pure components and ΔS^{config} is the configurational entropy of mixing given by randomly distributing the (A-A), (B-B) and (A-B) pairs in the one-dimensional Ising approximation [66]:

$$\Delta S^{\text{config}} = -R(n_A \ln X_A + n_B \ln X_B) - R[n_{AA} \ln(X_{AA} / Y_A^2) + n_{BB} \ln(X_{BB} / Y_B^2) + n_{AB} \ln(X_{AB} / 2Y_A Y_B)] \quad (8)$$

The Δg_{AB} may be expanded in terms of pair fractions:

$$\Delta g_{AB} = \Delta g_{AB}^0 + \sum_{i \geq 1} g_{AB}^{i0} X_{AA}^i + \sum_{j \geq 1} g_{AB}^{0j} X_{BB}^j \quad (9)$$

where Δg_{AB}^0 , g_{AB}^{i0} and g_{AB}^{0j} are the model parameters which can be functions of temperature.

3.2. The equilibrium pair distribution is determined by setting

$$(\partial G / \partial n_{AB})_{n_A, n_B} = 0 \quad (10)$$

which leads to the equilibrium constant for the pair formation in Equation (1):

$$X_{AB}^2 / (X_{AA} X_{BB}) = 4 \exp(-\Delta g_{AB} / RT) \quad (11)$$

The composition of maximum SRO is defined by the ratio of the coordination numbers Z_B / Z_A , as given in the following equations:

$$\frac{1}{Z_A} = \frac{1}{Z_{AA}^A} \left(\frac{2n_{AA}}{2n_{AA} + n_{AB}} \right) + \frac{1}{Z_{AB}^A} \left(\frac{n_{AB}}{2n_{AA} + n_{AB}} \right) \quad (12)$$

$$\frac{1}{Z_B} = \frac{1}{Z_{BB}^B} \left(\frac{2n_{BB}}{2n_{BB} + n_{AB}} \right) + \frac{1}{Z_{BA}^B} \left(\frac{n_{AB}}{2n_{BB} + n_{AB}} \right) \quad (13)$$

where Z_{AA}^A and Z_{AB}^A are the values of Z_A when all neighbors of A are A and when all nearest neighbors of A are Bs, respectively, and where Z_{BB}^B and Z_{BA}^B are defined similarly. Z_{AB}^A and Z_{BA}^B represent the same quantity and are interchangeable. Coordination numbers of the pure components

Table 2

Model parameters for the Fe–C–P system optimized in the present study in [J/mol] or [J/mol.K].

Liquid	Model I		Model II
	MQM (Fe, P, C)		MQM (Fe, P, C)
$Z_{\text{FeFe}}^{\text{Fe}} = Z_{\text{CC}}^{\text{C}} = Z_{\text{PP}}^{\text{P}} = Z_{\text{FeC}}^{\text{C}} = 6, Z_{\text{FeC}}^{\text{Fe}} = 3$	$Z_{\text{FeP}}^{\text{Fe}} = 3, Z_{\text{FeP}}^{\text{P}} = 6$		$Z_{\text{FeP}}^{\text{Fe}} = 6, Z_{\text{FeP}}^{\text{P}} = 6$
Δg_{FeC}	–30459.5 + 3.1380T–1129.7X _{FeFe} [22]		–30459.5 + 3.1380T–1129.7X _{FeFe} [22]
Δg_{FeP}	–57655.52 + 8.2425T–(2615–1.5899T)X _{FeFe} –(3711.21 + 5.23T)X _{PP}		–44768.8 + 5.8576T–23765.12X _{FeFe} + (11296.8 + 1.8828T)X _{FeFe} ² + (5.35552T)X _{PP}
Δg_{CP}	0		0
fcc	CEF (Fe,P)1(Va,C)1		CEF (Fe,P)1(Va,C)1
$G_{\text{Fe:Va}}$	GFCCFE		GFCCFE
$G_{\text{Fe:C}}$	GFCCFE + GHSECC+77 207–15.877T [16]		GFCCFE + GHSECC+77 207–15.877T [16]
$G_{\text{P:Va}}$	GFCCPP		GFCCPP
$G_{\text{P:C}}$	GHSEPP + GHSECC+238 068		GHSEPP + GHSECC+238 068
$L_{\text{Fe:Va,C}}$	–34671 [16]		–34671 [16]
$L_{\text{Fe,P:Va}}$	–150414.8 + 12.2591T		–139745.6 + 4.10032T
$L_{\text{Fe,P:Va,C}}$	–223 844–15.2716T		–164012.8–67.7808T
$T_{\text{cFe:Va}}$	–201 [16]		–201 [16]
β_{FeVa}	–2.1 [16]		–2.1 [16]
bcc	CEF (Fe,P)1(Va,C)3		CEF (Fe,P)1(Va,C)3
$G_{\text{Fe:Va}}$	GHSEFFE		GHSEFFE
$G_{\text{Fe:C}}$	GHSEFFE + GHSECC+322 050 + 75.667T [16]		GHSEFFE + GHSECC+322 050 + 75.667T [16]
$G_{\text{P:Va}}$	GBCCP		GBCCP
$G_{\text{P:C}}$	GHSEPP+3GHSECC+783 810		GHSEPP+3GHSECC+783 810
$L_{\text{Fe:Va,C}}$	–190T [16]		–190T [16]
$L_{\text{Fe,P:Va}}$	–187 234 + 13.598T+(627.6 + 11.0876T)($y_{\text{P}}^{\text{Fe}} - y_{\text{Fe}}^{\text{P}}$) ²		–182380.56 + 8.28432T+(6485.2 + 8.1588T)($y_{\text{P}}^{\text{Fe}} - y_{\text{Fe}}^{\text{P}}$) ²
$T_{\text{cFe,P:Va}}$	1043–500 $y_{\text{P}}^{\text{Fe}}y_{\text{Fe}}^{\text{P}}$		1043–500 $y_{\text{P}}^{\text{Fe}}y_{\text{Fe}}^{\text{P}}$
$\beta_{\text{Fe:Va}}$	2.22 [16]		2.22 [16]
Stoichiometric compounds^a			
Phase	ΔH_{298}^0	S_{298}^0	Cp
Fe ₃ P (Model I)	–164 580–	114.366 122.026	100.62 + 0.02789T–700977T ^{–2}
Fe ₃ P (Model II)	155 180		
Fe ₂ P (Model I)	–165 570–	78.1863	69.95 + 0.02555T–338576T ^{–2}
Fe ₂ P (Model II)	153 870	89.1363	
FeP (Model I)	–134 000–	40.6866 45.5567	44.27 + 0.01908T–190412T ^{–2}
FeP (Model II)	139 000		

^a Reference states are bcc Fe and white P.

in the binary Fe–P ($Z_{\text{FeFe}}^{\text{Fe}}$ and Z_{PP}^{P}) were set to 6 [67]. Maximum SRO composition in the binary Fe–P liquid solution is not evident from the experimental data. For that reason, the authors decided to provide two separated thermodynamic descriptions of the binary Fe–P system, defining the maximum SRO composition as “Fe₂P” ($Z_{\text{FeP}}^{\text{Fe}} = 3, Z_{\text{FeP}}^{\text{P}} = 6$) or “FeP” ($Z_{\text{FeP}}^{\text{Fe}} = 6, Z_{\text{FeP}}^{\text{P}} = 6$), respectively. The solid solutions and stoichiometric compounds are slightly adjusted according to the liquid parameters.

After the thermodynamic optimization of the binary Fe–P liquid solution, the Gibbs energy of the ternary liquid phase is estimated by a “Toop-like” interpolation method as suggested by Pelton and Chartrand [20] using Fe as an asymmetric component. Thermodynamic properties of the ternary liquid phase can be reproduced in high agreement with available experimental data without introducing any ternary adjustable parameter.

3.3. Solid solutions and stoichiometric compounds

The fcc and bcc solid solutions were modeled using the Compound Energy Formalism (CEF) with two-sublattices [21]. Fe and P are located on the substitutional sublattice, while C and vacancy (Va) occupy the interstitial sites; the structure of both phases is given by (Fe, P)_a(C, Va)_b. a and b represent the stoichiometric coefficients, where a = b = 1 for the fcc phase and a = 1 and b = 3 for bcc, respectively. The Gibbs energy in the CEF is given by:

$$G = y_{\text{Fe}}^{\text{Fe}}y_{\text{Va}}^{\text{Fe}}G_{\text{Fe:Va}} + y_{\text{Fe}}^{\text{C}}y_{\text{C}}^{\text{Fe}}G_{\text{Fe:C}} + y_{\text{P}}^{\text{Va}}y_{\text{Va}}^{\text{P}}G_{\text{P:Va}} + y_{\text{P}}^{\text{C}}y_{\text{C}}^{\text{P}}G_{\text{P:C}} + aRT (y_{\text{Fe}}^{\text{Fe}}\ln y_{\text{Fe}}^{\text{Fe}} + y_{\text{P}}^{\text{P}}\ln y_{\text{P}}^{\text{P}}) + bRT (y_{\text{C}}^{\text{C}}\ln y_{\text{C}}^{\text{C}} + y_{\text{Va}}^{\text{Va}}\ln y_{\text{Va}}^{\text{Va}}) + \sum_{i,j,k} y_i^{\text{Fe}}y_j^{\text{Fe}}y_k^{\text{Fe}}L_{i,j,k} + \sum_{i,j,k} y_k^{\text{Fe}}y_i^{\text{Fe}}y_j^{\text{Fe}}L_{k,i,j} + \sum_{i,j,k,l} y_i^{\text{Fe}}y_j^{\text{Fe}}y_k^{\text{Fe}}y_l^{\text{Fe}}L_{i,j,k,l} + G_{\text{m}}^{\text{mo}} \quad (14)$$

where $y_i^{\text{Fe}}, y_i^{\text{P}}$ are the site fractions of component i on one sublattice, G_{ij} is the Gibbs energy of an end-member (ij for fcc or ij₃ for bcc phase), and $L_{i,j,k}$ and $L_{k,i,j}$ are the interaction energies between i and j when the other sublattice is only occupied by k. $L_{i,j,k,l}$ is the reciprocal parameter representing the interaction among i,j,k,l. G_{m}^{mo} is the contribution due to magnetic ordering. Its expression per mole of atom was suggested by Hillert and Jarl [68]:

$$G_{\text{m}}^{\text{mo}} = RT\ln(\beta_0 + 1)g(\tau) \quad (15)$$

where $\tau = T/T_{\text{C}}$ and T_{C} is the critical temperature (Néel or Curie) and β_0 is the average magnetic moment per atom, and this was used in the present study.

As no experimental data was available for the enthalpy of formation of both PC₃ and PC in the bcc and fcc structure, respectively, their enthalpy of formation was estimated ab-initio via the Density Functional Theory (DFT). The DFT calculations in periodic boundary conditions were based on plane-wave basis sets and carried out using the Vienna Ab initio Simulation Package (VASP) [69–72]. The projector augmented wave (PAW) approach was employed to represent the core electrons [73, 74]. The generalized gradient approximation (GGA) as parameterized by Perdew, Burke and Ernzerhof (PBE) [75,76] was used as the exchange–correlation functional. A plane-wave kinetic cut-off energy of

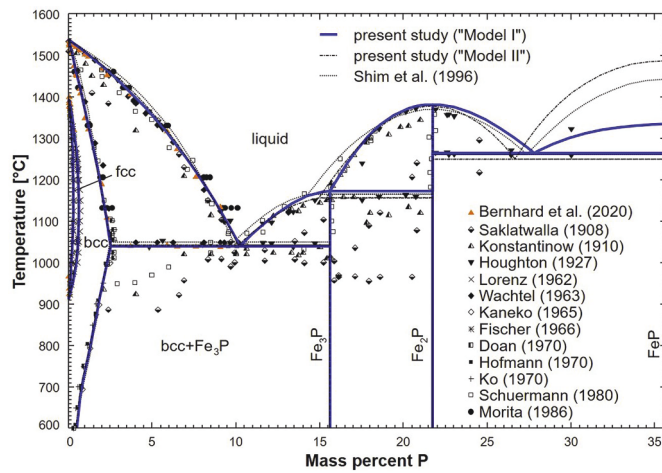


Fig. 1. Calculated binary Fe–P phase diagram up to 50 atomic percent P along with experimental data [18,40–42,44–51,62]. Solid lines refer to the present work “Model I” (maximum SRO composition at $x_p = 0.33$) and the dash-dotted ones to “Model II” (maximum SRO composition at $x_p = 0.50$). The dotted lines indicate the previous work of Shim et al. [17].

Table 3
Summary of invariant reactions in the binary Fe–P system.

Reaction type	Reaction	Temperature [°C]	Ref.		
Eutectic	liquid \leftrightarrow bcc + Fe ₃ P	1005	[40]		
		1020	[41]		
		1050	[42]		
		1048	[46]		
		1040 \pm 10	[48]		
		1039	[50]		
		1041	[18]		
		1040	Model I		
		1042	Model II		
		Peritectic	liquid + Fe ₂ P \leftrightarrow Fe ₃ P	1155	[41]
				1166	[42]
1173	[50]				
1172	Model I				
1156	Model II				
Congruent	liquid \leftrightarrow Fe ₂ P	1270	[40]		
		1350	[41]		
		1370	[42]		
		1365	[50]		
		1382	Model I		
		1376	Model II		
Eutectic	liquid \leftrightarrow Fe ₂ P + FeP	1262	[42]		
		1265	[50]		
		1265	Model I		
		1249	Model II		
Congruent	liquid \leftrightarrow FeP	1334	Model I		
		1486	Model II		

520 eV and a Monkhorst–Pack grid of suitable dimension ($15 \times 15 \times 4$ for hcp C, $7 \times 5 \times 2$ for triclinic P and $11 \times 11 \times 11$ for both bcc C₃P and fcc CP) to sample the Brillouin zone with a first-order Methfessel–Paxton smearing parameter of 0.02 eV were used to meet the force and energy convergence criteria of better than 0.02 eV/Å and 0.01 meV, respectively. The enthalpy of formation was then estimated from the difference between the calculated total energy of compound and total energy of C and P in their stable structure in standard condition of temperature and pressure according to:

$$\Delta H_{\text{form}}^{C_nP_m} = E_{\text{tot}}^{C_nP_m} - nE_{\text{tot}}^{C(\text{graphite})} - mE_{\text{tot}}^{P(\text{triclinic})} \quad (16)$$

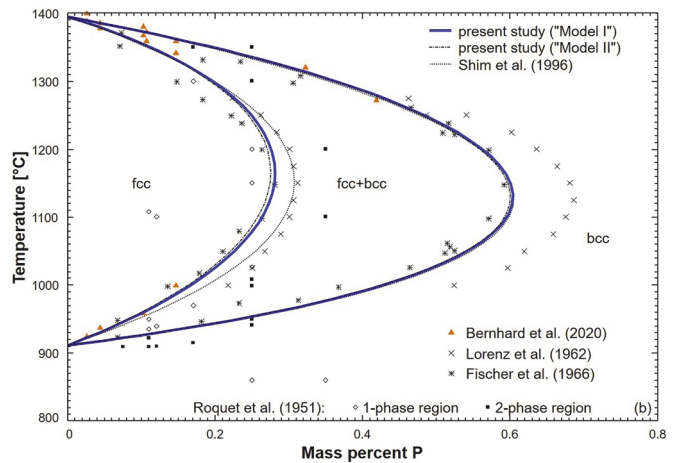
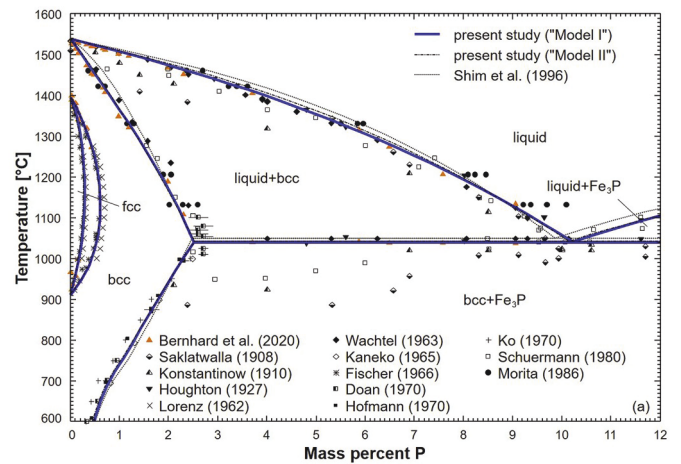


Fig. 2. Calculated Fe-rich part of the binary Fe–P system (a) and enlarged gamma loop region (b) along with experimental data [18,40–51,62]. Solid lines refer to the present work “Model I” and the dash-dotted ones to “Model II.” The dotted lines indicate the previous work of Shim et al. [17].

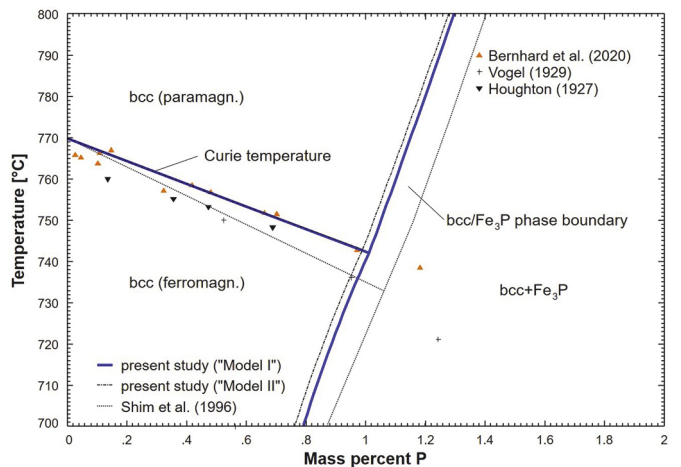


Fig. 3. Calculated Curie temperature of magnetic transition in bcc phase compared with experimental data [18,42,58]. Solid lines refer to the present work “Model I” and the dash-ones to Model II.” The dotted lines indicate the previous work of Shim et al. [17].

Three phosphides - Fe₃P, Fe₂P and FeP - were treated as stoichiometric compounds. The Gibbs energy functions are modeled as functions of temperature:

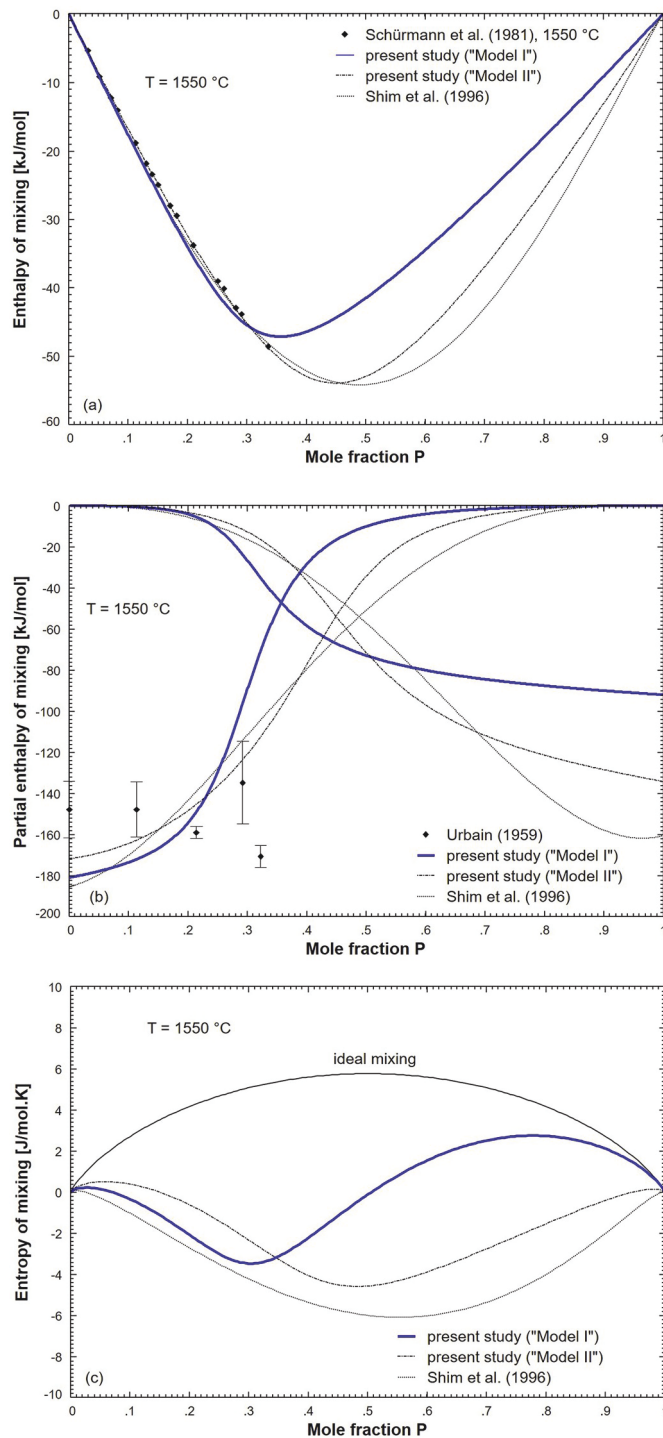


Fig. 4. Calculated enthalpy of mixing at 1550 °C (a) and partial enthalpy of mixing at 1550 °C (b) compared with available experimental data [25,27]. Calculated entropy of mixing at 1550 °C (c). Solid lines refer to the present work “Model I” and the dash-dotted ones to “Model II.” The dotted lines indicate the previous work of Shim et al. [17].

$$G = \Delta H_{298.15}^f + \int_{298.15}^T c_p dT - T \left[S_{298.15} + \int_{298.15}^T (c_p / T) dT \right] \quad (17)$$

where $\Delta H_{298.15}^f$ is the standard enthalpy of formation relative to the reference states of Fe and P (bcc and white P, respectively) and $S_{298.15}$ is the standard entropy at 25 °C. The heat capacity c_p is given as a function

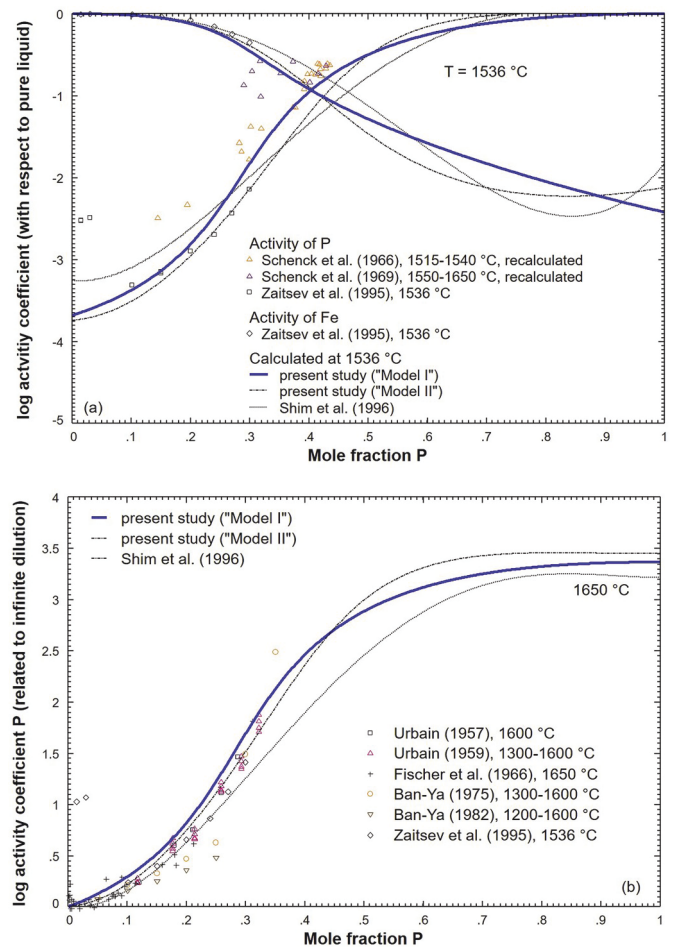


Fig. 5. Calculated activity coefficients in Fe-P melts of (a) Fe and P with respect to pure liquid phosphorus and iron and (b) with respect to infinite dilution. Experimental data is taken from Ref. [14,26–30]. Solid lines refer to the present work “Model I” and the dash-dotted ones to “Model II.” The dotted lines indicate the previous work of Shim et al. [17].

of temperature (see Table 2).

4. Results and discussions

Two sets of thermodynamic parameters were evaluated in the present study, setting the maximum SRO composition to $x_p = 0.33$ (“Model I”) and $x_p = 0.50$ (“Model II”), respectively. Based on thermodynamic data in the binary Fe-P system [14,25,31,32], the parameters for the liquid phase were optimized. According to the liquidus and solidus line [18], the Gibbs energy of the bcc solution was formulated. By reproducing the phase boundaries in the “Gamma-Loop” of [18,45], excess Gibbs energy of the fcc solution was adjusted. Experimentally determined heats of formation [34] and heat capacities [14] of phosphides were used in order to fit all phase diagram data. A ternary parameter for fcc was introduced in order to reproduce various isothermal sections. This optimization procedure was performed for both maximum SRO compositions. As will be seen in the following sections, the MQM description using Fe_2P as the maximum SRO composition leads to the most accurate prediction of the binary and ternary phase diagram; hence, the calculations in the figures presented are highlighted with solid lines.

Within the thermodynamic optimizations, particular focus was placed on reproducing the DSC data of M. Bernhard et al. [18], which is considered as superior to previous data. In their work, model alloys were produced from high purity raw materials using a high frequency

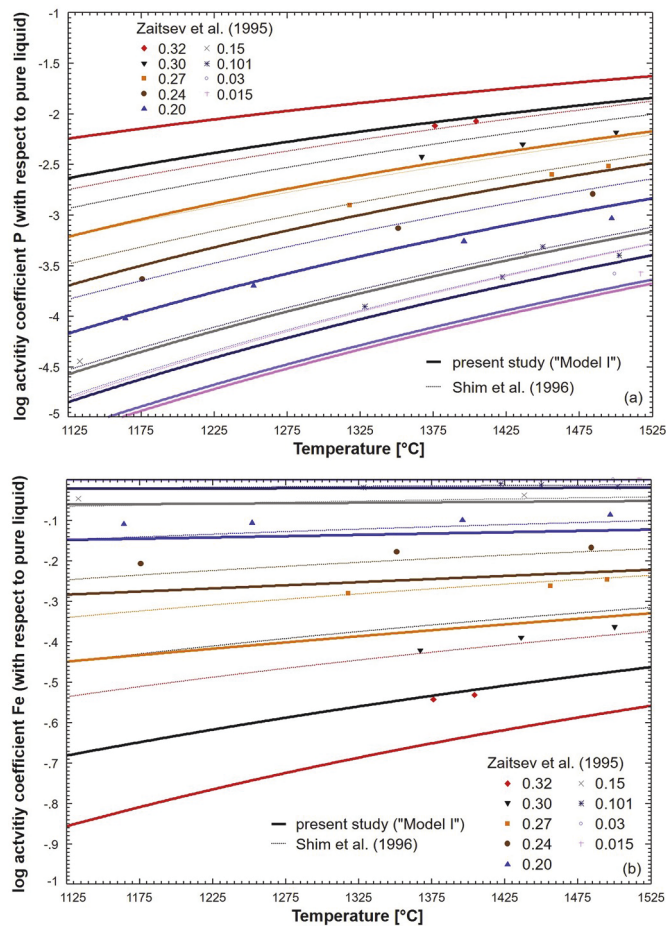


Fig. 6. Calculated temperature-dependent activity coefficients of (a) P with respect to pure liquid phosphorus and (b) Fe with respect to pure liquid iron. Experimental data is taken from Ref. [14]. Solid lines refer to the present work “Model I.” The dotted lines indicate the previous work of Shim et al. [17].

remelting furnace. The remelting process was performed under argon 5.0 atm with subsequent centrifugal casting in a copper mold. As a consequence, the final trace element level of C (70 ppm in binary Fe–P alloys), Si (30 ppm), Mn (160 ppm), S (35 ppm) and N (30 ppm) is very low. Chemical analysis was determined carefully by optical emission spectroscopy; in the case of highly alloyed samples ($P > 6$ mass pct.), the P concentration was measured by the wet chemical technique. The rapid solidification in the copper mold led to a homogeneous microstructure with extremely fine secondary dendrite arm spacing of 10 μm . Within the DSC measurements, the heating rate was fixed at 10 K/min; a special time and thermal resistance (Tau-R) correction [18] of DSC enabled the measurement of highly accurate equilibrium phase transformation temperatures.

4.1. Thermodynamic optimization of the binary Fe–P system

Fig. 1 shows the calculated binary Fe–P system up to 50 at% P using the present MQM assessments and the previous work of Shim et al. [9] together with all experimental data. It can be seen that the MQM assessment with “Model II” is in good agreement with the phase diagram, as suggested by Shim et al. [9]. The main differences between the MQM descriptions provided can be found in the shape of the phase boundary liquid/phosphides and the melting temperature of FeP. Since there is no reliable experimental data available, the calculated melting point of FeP cannot be critically evaluated. However, both optimized sets of parameters reproduce incongruent melting of Fe_3P , as generally accepted in literature [23], and the eutectic equilibrium liquid \leftrightarrow Fe_2P

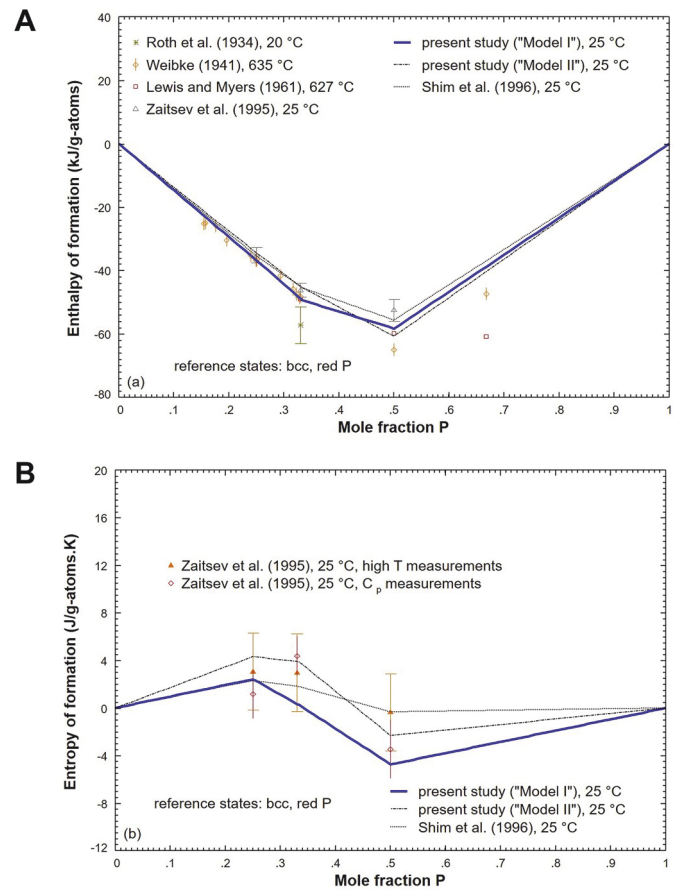


Fig. 7. Calculated enthalpy (a) and entropy of formation (b) at 25 °C compared with experimental data [14,33–35]; reference states are bcc Fe and red Phosphorus. Solid lines refer to the present work “Model I” and the dash-dotted ones to “Model II.” The dotted lines indicate the previous work of Shim et al. [17]. (For interpretation of the references to colour in this figure legend, the reader is referred to the Web version of this article.)

+ FeP satisfyingly well. Particularly in the case of “Model I,” the predicted invariant temperatures are in excellent agreement with experimental data; see Table 3.

The enlarged phase diagram in the Fe-rich region together with all experimental data is presented in Fig. 2(a). Recently published DSC measurements of M. Bernhard et al. [18] and previously determined phase equilibria of Morita and Tanaka [51] indicate significantly lower solidus temperatures (>40 °C) compared to the assessment of Shim et al. [9]. Especially at low P concentrations (<1 mass pct.), both experimental publications predict a stronger segregation tendency of P during solidification. In the present work, special focus was placed on precise modeling of the bcc/liquid phase boundary. As can be seen in Fig. 2(a), both current optimizations are in excellent agreement with the DSC data of M. Bernhard et al. [18] and reproduce additional experimental data [42,46,50,51] satisfyingly well. The temperature-dependent solubility along the bcc/ Fe_3P line is within the experimental error of available literature data and the calculated maximum P solubility of 2.5 mass pct. Is in reasonable agreement with the generally accepted value of 2.8 mass pct. given by Okamoto [23]. The gamma loop region is compared with experimental data in Fig. 2(b). Due to a higher impurity level in their samples, the solubility data of Lorenz et al. [44] and Roquet et al. [43] differ from the published values of Fischer et al. [45] and M. Bernhard et al. [18]. Particularly trace elements, e.g. carbon, manganese and nitrogen, increase the austenite stability in the gamma loop. The data of Fischer et al. [45] and M. Bernhard et al. [18] was therefore used in the present study. From Fig. 2(b) it can be seen that inconsistencies in the

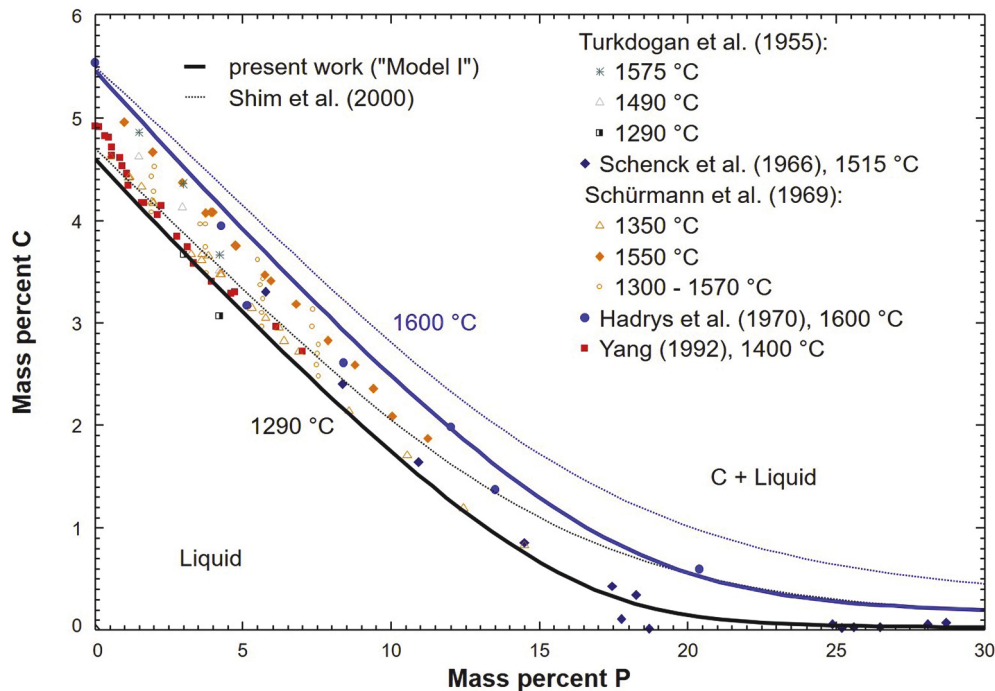


Fig. 8. Calculated C solubility in ternary Fe–C–P liquid solution at 1290 °C and 1600 °C together with experimental data [53–57]. Solid lines refer to the present work “Model I.” The dotted lines indicate the previous work of Shim et al. [17].

selected data sets in the assessment of Shim et al. [9] could be resolved. The T_c line according to M. Bernhard et al. [18] is well represented (Fig. 3).

In Fig. 4, the present thermodynamic calculations for the enthalpy/entropy of mixing at 1550 °C are compared with experimental enthalpy data of Fe–P binary liquid solution; reference states are pure liquid Fe and P. Schürmann et al. [25] derived the integral enthalpy of mixing data indirectly from high-temperature calorimetry and phase diagram calculations using a polynomial approach for the composition dependency of ΔH_{mix} , which is given by $\Delta H_{\text{mix}} = -181.065x_p + 96.234x_p^2 + 10.029x_p^3 + 74.802x_p^4$, as seen in Fig. 4(a). Since this equation shows a minimum of ΔH_{mix} close to $x_p \sim 0.58$, the previous assessment using the BW model [9] and the “Model II” inherently result in better agreement than the “Model I” with maximum SRO composition at $x_p = 0.33$. In Fig. 4(b), the partial enthalpy of mixing of P by Urbain [27] looks virtually independent on x_p up to 0.33. This is an evidence of very strong SRO [67]. As the integral enthalpy of mixing values are only available up to $x_p = 0.33$, the maximum SRO composition is not evident from the experimental enthalpy data. During the present study, it was found that “Model I” and “Model II” show equally accurate results for calculations of the enthalpy data in Fig. 4(a) and (b) and the thermodynamic data in Figs. 5 and 6, and the phase diagram in Figs. 1 and 2. However, as seen in Table 2, “Model I” could describe the Gibbs energy of the liquid Fe–P in Fe-rich side with less model parameters (without X_{Fe}^2 term). Therefore, the present authors suggest the “Model I” over the “Model II”. Calculated entropy of mixing using the model of Shim et al. [9], the “Model I”, and the “Model II” are shown in Fig. 4(c). The “Model I” shows a minimum near $x_p = 0.33$, corresponding to the maximum SRO composition.

In Fig. 5(a), the calculated activity coefficients of Fe and P in Fe–P melts at 1536 °C are presented in comparison with experimental data [14,31,32]. Reference states are pure liquid Fe and P. The P activity coefficients of Schenck et al. [31,32] were recalculated from the reaction $[P] \leftrightarrow 1/2 \{P_2\}$ using the measured vapor pressure of P_2 together with the Gibbs energies of pure liquid P ($g_{P,l}^0 = -7232.449 + 133.291873T - 26.236T \ln T$ [J/mol]) and P_2 gas ($g_{P_2,g}^0 = -161556.144 - 27.7915443T - 0.0003347378581 T^2 - 242493.487$

$T^{-1} - 8395.31409 \ln T + 1592.26513 T^{0.5} - 31.4764937 T \ln T$ [J/mol]) from literature [64,65,77]. At P concentrations $x_p < 0.20$, there seem to be large discrepancies between the P activity data of Zaitsev et al. [14] and Schenck et al. [31,32]. In this composition region, accurate reproduction of the phase diagram was only possible when the effusion method data of Zaitsev et al. [14] was used to model the Gibbs energy of the liquid phase. With increasing P content ($x_p > 0.30$), both experimental data sets become more consistent and show a sharp increase in P activity at $x_p \sim 0.30$, indicating the presence of strong SRO between Fe and P. As shown in Fig. 5(a), results of the present study are in more reasonable agreement with the activity data than the work of Shim et al. [9]. Particularly, using the MQM parameters for maximum SRO at $x_p = 0.33$ (“Model I”), the increase in P activity coefficients at $x_p \sim 0.30$ is reproduced very well. The tendency of SRO is also evident in Fig. 5(b), which shows measured activity coefficients of P with respect to the Henrian standard state [14,26–30]. Since there is no information on γ_p^0 available in those published studies [26–30], these results cannot be expressed related to pure liquid Fe and P. For comparison, P activity coefficients of Zaitsev et al. [14] were reduced to the Henrian standard state using their suggested value of $\gamma_p^0 = 2.78 \times 10^{-4}$. Noticeable deviations can be found between the current calculations and composition dependence of the P activity coefficient given in the work of Ban-Ya et al. [28,30]. However, this data shows inconsistencies with all other summarized literature values and was therefore not considered in the present study. Both MQM optimizations improve the agreement with activity data and can reproduce the composition dependence of P activity coefficients within experimental errors.

Temperature-dependent activity coefficient data of Fe and P with respect to pure liquid components is well represented in the present study and shown in Fig. 6(a) and (b). Results for both MQM optimizations are quite similar; in order to give a better overview, only calculations from “Model I” are compared with experimental data and the assessment of Shim et al. [9]. According to the already mentioned reasons in Fig. 5(a), better agreement of P activity coefficients can be found up to $x_p \sim 0.25$. Since Schenck et al.’s data [31,32] was considered at $x_p > 0.33$ to model the liquid phase, higher deviations can be found with respect to the work of Zaitsev et al. [14].

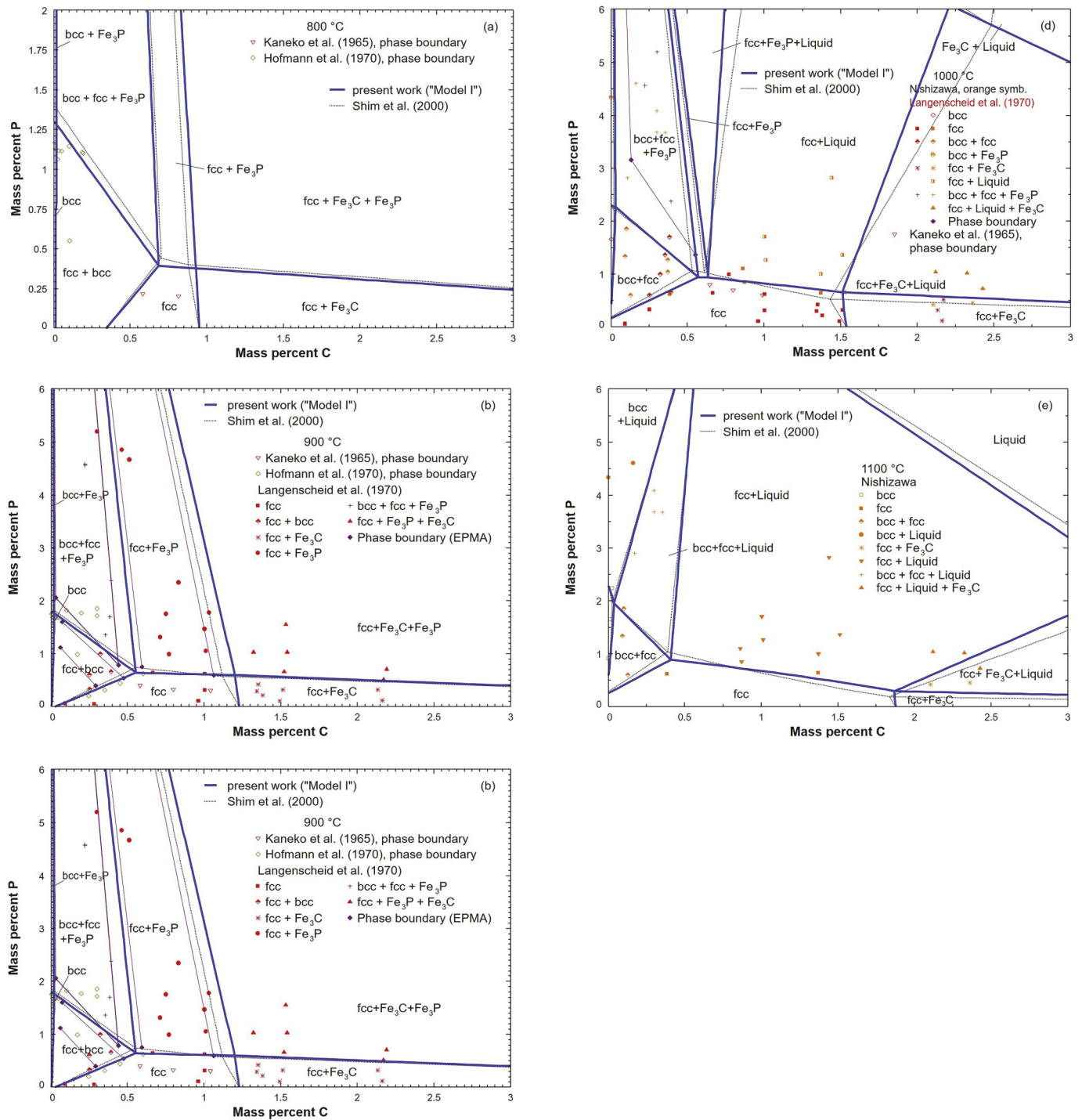


Fig. 9. Calculated isothermal sections of the Fe–C–P systems at (a) 800 °C, (b) 900 °C, (c) 950 °C, (d) 1000 °C and (e) 1100 °C along with experimental data [47, 61–63]. Solid lines refer to the present work “Model I.” The dotted lines indicate the previous work of Shim et al. [17].

The calculated enthalpy of formation at 25 °C in the binary Fe–P system is presented in Fig. 7(a). Reference states are reduced to bcc Fe and red P in order to compare the calculations with experimental data. The previous assessment of Shim et al. [9] considered the Gibbs energy measurements [14] to be the most reliable. However, in the present study, enthalpies of formation as proposed by Weibke [34] were used in the optimization process, due to higher accuracy of direct calorimetry measurements. Since higher order phosphides were not considered in the previous and present assessments, calculated ΔH_{298}° of FeP_2 show larger discrepancies. In Fig. 7(b), optimized entropies of formation at 25

°C are compared with data of Zaitsev et al. [14]. More emphasis was put on accurate calculation of the phase diagram in the Fe-rich part, but optimized entropies of formation are still within the given experimental errors [14].

4.2. Thermodynamic optimization of the ternary Fe–C–P system

In order to provide a better overview in the figures of this chapter, the authors decided to plot only the results of “Model I” in comparison with the assessment of Shim et al. [17]. Background calculations with

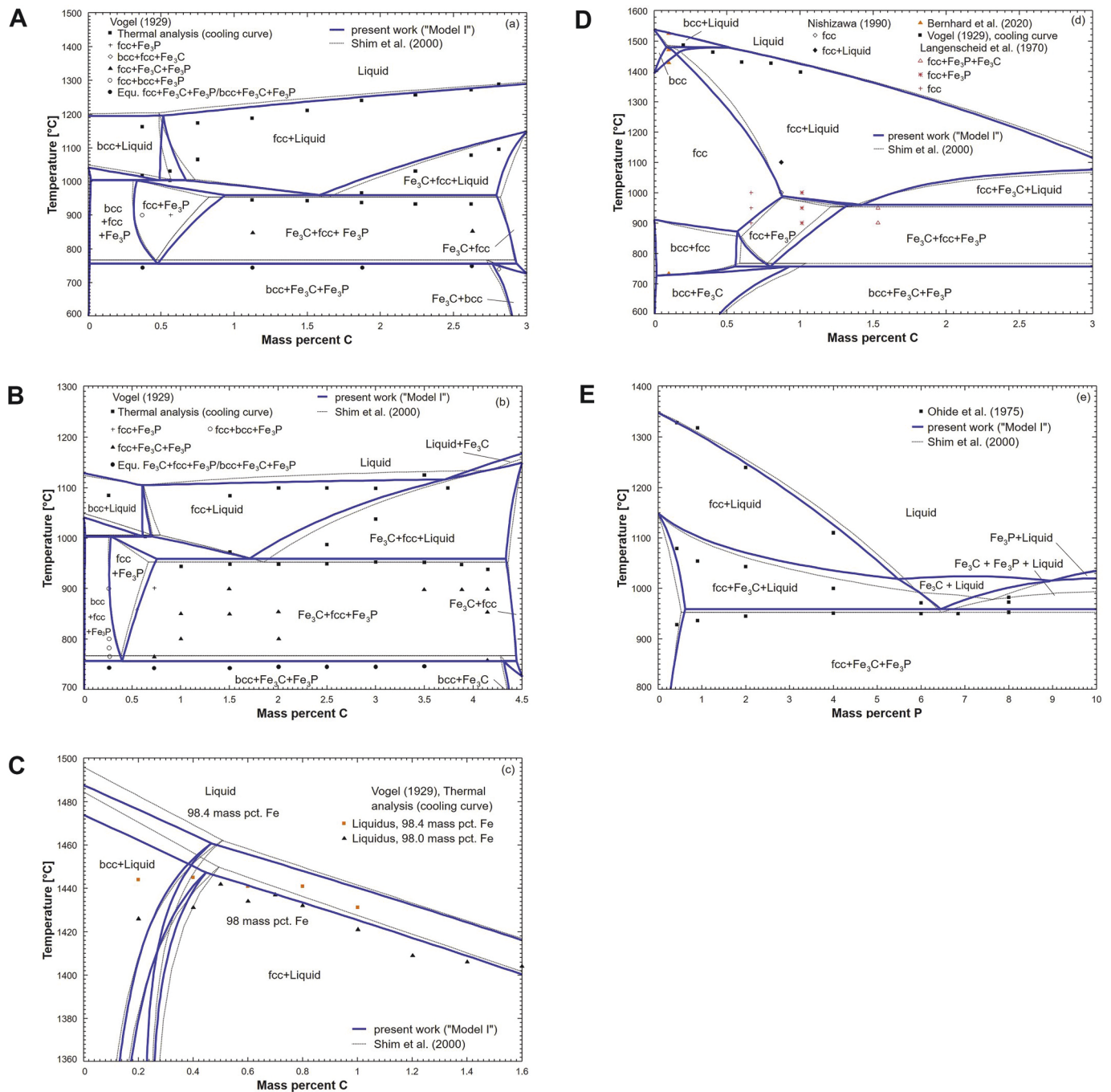


Fig. 10. Calculated vertical sections in the ternary Fe-C-P system of Fe_{0.92}P_{0.08}-Fe_{0.97}C_{0.03} (a), Fe_{0.91}P_{0.09}-Fe_{0.955}C_{0.045} (b), [%Fe] = 98.4 and 98.0 (c), Fe-Fe_{0.97}P_{0.015}C_{0.015} (d) and [%C] = 2.4 (e) along with experimental data [58,59,61,63]. Solid lines refer to the present work "Model I." The dotted lines indicate the previous work of Shim et al. [17].

"Model II" are considered in the discussion of the results. The calculated C saturation in liquid Fe-C-P solutions is presented in Fig. 8 along with experimental data [53–57] in the temperature range of 1290–1600 °C. Both MQM models are in excellent agreement with the experimentally determined data: rapid decrease of C solubility upon increasing P content. Particularly at [%P] > 20, the predicted saturation as suggested by Schenck et al. [54] is significantly improved compared with the previous assessment of Shim et al. [17].

Fig. 9(a)–(e) show calculated isothermal sections in the Fe-rich region of the ternary system at 800, 900, 950, 1000 and 1100 °C. The results of *ab-initio* calculations for G_{P,C} of fcc and bcc hypothetical end-member compositions in Table 2 mainly influence the fcc stability. The

negligible effect in bcc solution can be assigned to the low C solubility in ferrite. Introducing an additional ternary parameter $L_{Fe_3P,C,Va}$ for fcc was necessary in order to improve the accuracy of the (fcc/Fe₃C) and (fcc/fcc + Fe₃P) phase boundary with respect to the data of Langenscheid et al. [61]. As a consequence, the C solubility in ternary fcc solution is higher compared to that of Shim et al. [17]. Between both MQM optimizations presented, considerable discrepancies can be found in the 2-phase region (fcc + Fe₃P) and 3-phase region (fcc + Fe₃P + liquid) at 1000 °C. In this composition region, experimental information of Langenscheid et al. [61] and Nishizawa [63] is very limited. M. Bernhard et al. [18] reported partial melting of alloys with 0.68 wt% C and 1.23 wt % P at 996 °C, indicating the presence of a (fcc + liquid) phase

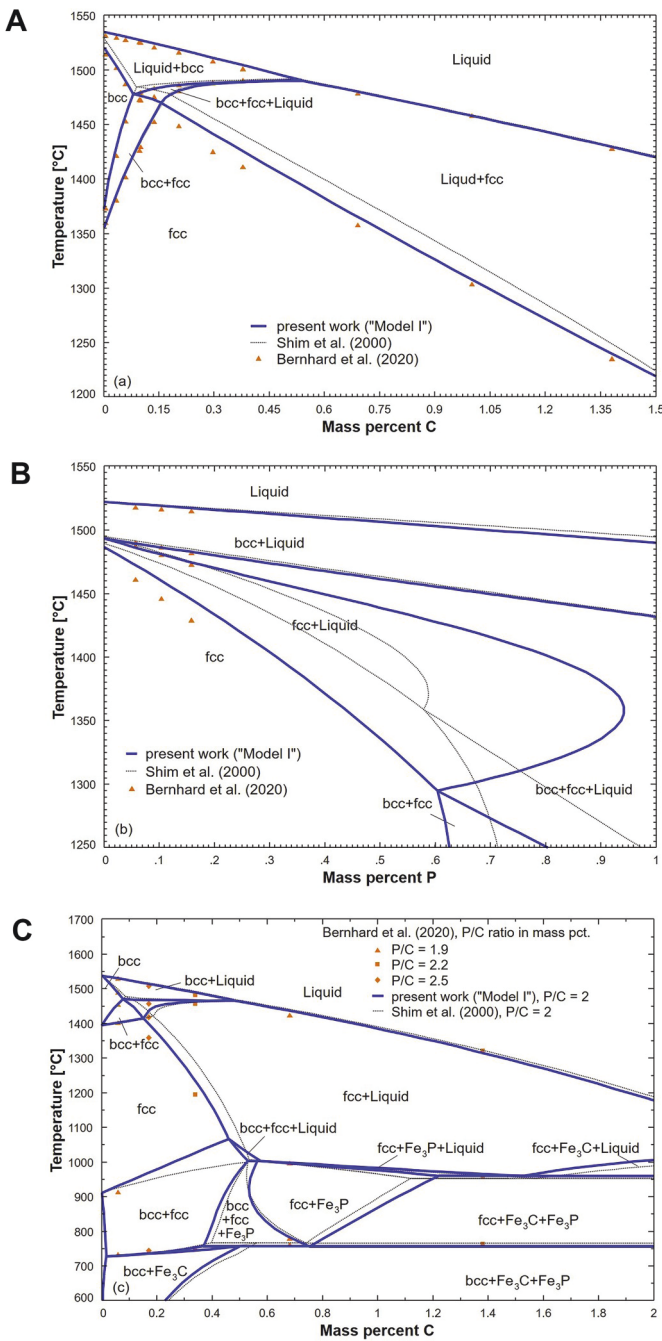


Fig. 11. Calculated vertical sections in the ternary Fe–C–P system at 0.1 mass pct. P (a), 0.2 mass pct. C (b) and Fe–Fe_{0.94}C_{0.02}P_{0.04} along with data of M. Bernhard et al. [18]. Solid lines refer to the present work “Model I.” The dotted lines indicate the previous work of Shim et al. [17].

equilibrium at 1000 °C. In consideration of that recently published data [18], the present calculation of “Model I” seems to be more reliable.

Calculated isoplethal sections from literature in Fig. 10(a)–(e) are in satisfying agreement with experimental data [58,59,61,63]. Obviously, thermal analysis data of Vogel [58] is generally lower compared with temperatures from a previous assessment [17] and the present study. As the temperatures were experimentally determined by evaluating cooling curves, the deviations can be attributed to possible supercooling of the liquid phase. More recent literature data of M. Bernhard et al. [18] in comparison with the work of Shim et al. [17] and “Model I” is shown in Fig. 11. Accuracy of transformation temperatures in the peritectic region of ternary Fe–C–P alloys with 0.1 mass pct. P and 0.2 mass pct. C are

significantly improved within the present study, as can be seen in Fig. 11 (a) and (b). Besides the precise knowledge of the solidus temperature, the identification of the “hypo-peritectic” region (liquid + bcc → bcc + fcc) is of special interest in practical casting operations [78,79]. In the work of Shim et al. [17], the underestimated influence of P on decreasing the solidus temperature results in a shift of the hypo-peritectic region to 0.08–0.185 mass pct. C. The experimentally determined hypo-peritectic range at 0.1 mass pct. P is between 0.084 and 0.147 mass pct. C [18] and corresponds well with the present thermodynamic assessments (0.079–0.155 mass pct. C). Fig. 11(c) represents the vertical section of mass pct. Ratio P/C = 2. Similar results of the present optimizations and the previous one [17] are observed in the case of phase transformation temperatures at higher C concentrations (C > 0.60 mass pct.). Considering different P/C ratios (1.9–2.5), the predicted phase stabilities and temperatures in the peritectic region are in excellent agreement with the experimental data, whereas high deviations are found in the assessment of Shim et al. [17]. In contrast to the previous work [17], the strong influence of P on the solidus temperature stabilizes the bcc + fcc + liquid 3-phase region between ~1000 and 1070 °C already at a low P/C ratio of 2.

Fig. 12 shows the liquid projection in the Fe-rich part of the ternary Fe–C–P system; the calculated invariant reactions are summarized in Table 4. The invariant compositions are in reasonable agreement with the data of Schürmann et al. [60]. However, this data is usually more difficult to determine than the corresponding invariant temperatures, which could be reproduced better setting SRO composition to $x_P = 0.33$ (“Model I”). In case of “Model II,” the temperatures show slightly higher deviation.

The present results can be summarized as follows: Both optimizations using the MQM for the liquid phase lead to a more reasonable agreement with thermodynamic properties in the binary Fe–P system. Compared with the previous assessment [17], solidus temperature and peritectic phase equilibria could be significantly improvement in the lower P region of the binary Fe–P and ternary Fe–C–P system, respectively. In consideration of all experimental data, the model parameters for SRO $Z_{FeP}^{Fe}/Z_{FeP}^P = 1/2$ (“Model I”) lead to similar results over the whole composition range as setting $Z_{FeP}^{Fe}/Z_{FeP}^P = 1$ (“Model II”). Consequently, both MQM optimizations can be used in steel databases. However, in case of “Model II” additional model parameters for the liquid phase were necessary to accurately reproduce the thermodynamic data in the Fe-rich part of the binary Fe–P system. Therefore, the authors propose the present thermodynamic modeling with maximum SRO at $x_P = 0.33$ (“Model I”).

Finally, thermodynamic calculations using “Model I” were performed to estimate the first order (ϵ_i^j , e_j^i) and second order (ρ_i^j , r_j^i) interaction parameters of P and C in liquid Fe–P(–C) alloys of Wagner’s Interaction Parameter Formalism (WIPF). The WIPF is widely used in the field of iron and steelmaking due to the simple calculation of activities of alloying in liquid solutions of Fe. The general equations for the activity coefficients of a component i and the interaction with components j are given as

$$\ln(\gamma_i) = \ln(\gamma_i^0) + \sum_{j=2}^n \epsilon_i^j x_j + \sum_{j=2}^n \rho_i^j x_j^2 \quad (18)$$

$$\log(f_i) = \sum_{j=2}^n e_i^j (\%j) + \sum_{j=2}^n \rho_i^j (\%j)^2 \quad (19)$$

where γ_i is activity coefficient of the component i used with mole fraction and f_i is used with mass percent, respectively. Binary and ternary interaction parameters of P and C in Fe as solvent are given in the work of Sigworth and Elliott [80], Froberg [52], and Lupis [81] at a temperature of 1600 °C. In the present study, calculations for γ_P and f_P were performed from 1200 °C to 1800 °C in order to provide ϵ_P^P , ρ_P^P , e_P^C , r_P^C and ϵ_P^C , ρ_P^C , e_C^P , r_C^P as a function of temperature. The composition was varied

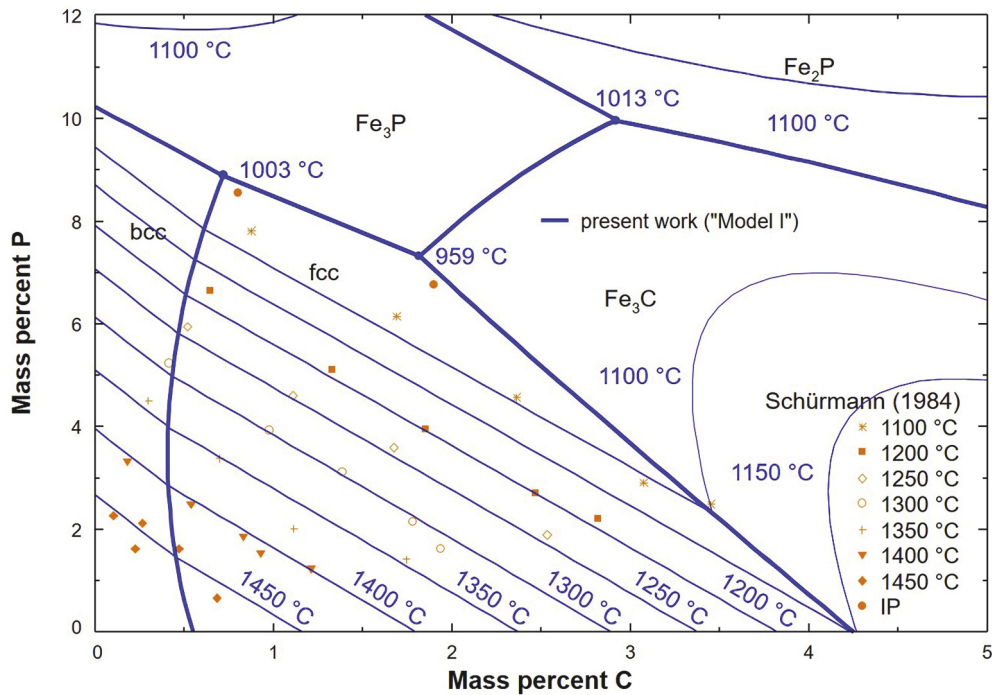


Fig. 12. Liquidus surface projection in the Fe-rich part of the ternary Fe–C–P system. Experimental data is taken from Schürmann et al. [60]. Solid lines of uni-variants and isotherms refer to the present work “Model I.”

Table 4

Comparison of calculated invariant reactions in the Fe–C–P system with experimental data [60] and assessed values [17].

Reaction	Reference	C [mass pct.]	P [mass pct.]	T [°C]
liquid + bcc \leftrightarrow fcc + Fe ₃ P	present work (“Model I”)	0.72	8.88	1003
	present work (“Model II”)	0.67	8.78	1007
	Shim et al. [17]	0.83	8.50	1006
	Schürmann et al. [60]	0.80	8.55	1004
liquid \leftrightarrow fcc + Fe ₃ P + Fe ₃ C	present work (“Model I”)	1.82	7.32	959
	present work (“Model II”)	1.75	7.19	967
	Shim et al. [17]	2.08	6.95	952
	Schürmann et al. [60]	1.90	6.75	955

from 0 to $x_p = 0.10$ (~5 wt%P) in the Fe–P system and from 0 to $x_c = 0.20$ (~5 wt%C) with $x_p = 10^{-4}$ in the Fe–C–P system. The Henrian activity coefficient of P (γ_p^0) in liquid Fe–P solution was found to be

$$\ln(\gamma_p^0) = \frac{-21746}{T[\text{K}]} + 3.548 \quad (20)$$

By fitting the activity calculations to the WIPF the following

Table 5

Binary and ternary interaction parameters of P in liquid Fe–P and Fe–C–P solution at 1600°

Reference	γ_p^0	e_p^p	ρ_p^p	e_p^c	ρ_p^c	e_p^p	r_p^p	e_p^c	r_p^c
Present study	3.15×10^{-4}	5.12	17.60	5.09	19.23	0.0367	2.2×10^{-3}	0.087	0.0146
Zaitsev et al. [14]	2.78×10^{-4}	4.19	11.50	–	–	–	–	–	–
Frohberg et al. [52]	–	8.36	–3.07	5.60	35.00	0.062	-6.5×10^{-5}	0.0975	0.0295
Sigworth and Elliott [80]	–	–	–	–	–	0.12	-1×10^{-3}	0.13	–
Lupis [81]	–	8.4	–3.1	7.0	–	0.063	-1×10^{-3}	0.13	–

interaction parameters were obtained:

$$e_p^p = \frac{5660}{T[\text{K}]} + 2.1, \quad \rho_p^p = \frac{24726}{T[\text{K}]} + 4.4, \quad e_p^c = \frac{3212}{T[\text{K}]} + 3.376, \quad \rho_p^c = \frac{49405}{T[\text{K}]} - 7.149 \quad (21)$$

(1200 °C < T < 1800 °C)

The transformation of the interaction parameters from mole fraction as composition coordinate to weight percent gives [80]:

$$e_p^p = \frac{44.38}{T[\text{K}]} + 0.013, \quad r_p^p = \frac{3.14}{T[\text{K}]} + 5.18 \times 10^{-4}, \quad e_p^c = \frac{64.94}{T[\text{K}]} + 0.0524, \quad r_p^c = \frac{44.1}{T[\text{K}]} - 8.92 \times 10^{-3} \quad (22)$$

(1200 °C < T < 1800 °C)

At 1600 °C the present results are compared with interaction parameters from literature (Table 5). In general, good agreement was found for activity coefficients of phosphorus up to 1 mass percent P in binary liquid solutions [14,52,80] and from 0 to 4 mass percent C in the Fe–C–P system [52,80,81]. At higher concentrations of P and C, the present calculations result in lower activity coefficients of phosphorus. The lower values are in agreement with the work of Zaitsev et al. [14] and Sigworth and Elliott [80].

5. Conclusion

A CALPHAD-type thermodynamic assessment of the ternary Fe–C–P system was carried out including modeling of the Fe–P binary subsystem in the experimentally investigated range up to 50 at% P. Gibbs energy of the liquid phase was formulated using the Modified Quasichemical Model (MQM) in order to take into account the strong short-range-ordering (SRO) tendency. Since maximum SRO composition was not evident from experimental information, the authors decided to provide two sets of model parameters for different maximum SRO in the binary Fe–P system. *Ab-initio* calculations were performed to estimate the enthalpy of formation of fcc and bcc endmembers in the Compound Energy Formalism (CEF). Combining the already assessed Fe–C subsystem by Shubhank and Kang [22] and the present Fe–P descriptions, solubility data of C in the Fe–C–P liquid phase could be reproduced more accurately without adding a ternary parameter for the excess Gibbs energy. Based on various isothermal and isopleth sections in the ternary Fe–C–P system, both MQM descriptions were critically evaluated. Both parameter sets are in excellent agreement with recently published phase equilibrium data of M. Bernhard et al. [18]. Regarding the solidus temperature and phase stabilities in the peritectic region, the discrepancies between the experimental data and the previous assessment of Shim et al. [17] were resolved. Although both MQM optimizations can be used particularly for steel databases, the authors suggest “Model I” (maximum SRO in the liquid near Fe₂P composition) because less model parameters were needed in order to accurately reproduce thermodynamic properties of the liquid phase in the Fe-rich part of the Fe–P system.

Data availability

The raw/processed data required to reproduce these findings are available from the authors upon a written request.

Declaration of competing interest

None.

Acknowledgments

The authors gratefully acknowledge the financial support under the scope of the COMET program within the K2 Center “Integrated Computational Material, Process and Product Engineering (IC-MPPE)” (Project No 859480). This program is supported by the Austrian Federal Ministries for Climate Action, Environment, Energy, Mobility, Innovation and Technology (BMK) and for Digital and Economic Affairs (BMDW), represented by the Austrian research funding association (FFG), and the federal states of Styria, Upper Austria and Tyrol. One of the authors (MB) appreciates the valuable discussions with Dr. Jyrki Miettinen, University of Oulu, Finland. Kind hospitality of Prof. Patrice Chartrand, Polytechnique Montreal, Canada, during the period of this work is greatly appreciated.

References

- M. Wintz, M. Bobadilla, J. Jolivet, Hot cracking during solidification of steel: effect of carbon, sulphur and phosphorus, *Rev. Metall.* 91 (1) (1994) 106–114, in French.
- E. Schmidtman, F. Rakoski, Einfluß des Kohlenstoffgehaltes von 0,015 bis 1% und der Gefügestruktur auf das Hochtemperaturfestigkeits- und zähigkeitsverhalten von Baustählen nach der Erstarrung aus der Schmelze (Influence of the carbon content of 0.015 to 1% and of the structure on the high-temperature strength and toughness behaviour of structural steels after solidification from the melt), *Arch. Eisenhuettenwes.* 54 (9) (1983) 357–362, in German.
- M. Wolf, W. Kurz, The effect of carbon content on solidification of steel in the continuous casting mold, *Metall. Trans. B* 12 (1) (1981) 85–93.
- H.G. Suzuki, S. Nishimura, Y. Nakamura, Improvement of hot ductility of continuously cast carbon steels, *Trans. Iron Steel Inst. Jpn.* 24 (1) (1984) 54–59.
- X.-M. Chen, S.-H. Song, L.-Q. Weng, S.-J. Liu, K. Wang, Relation of ductile-to-brittle transition temperature to phosphorus grain boundary segregation for a Ti-stabilized interstitial free steel, *Mater. Sci. Eng.* 528 (28) (2011) 8299–8304.
- L. Barbé, K. Verbeke, E. Wettinck, Effect of the addition of P on the mechanical properties of low alloyed TRIP steels, *ISIJ Int.* 46 (8) (2006) 1251–1257.
- P. Spencer, O. Kubaschewski, A thermodynamic assessment of the iron-phosphorus system, *Arch. Eisenhuettenwes.* 49 (5) (1978) 225–228.
- P. Gustafson, Study of the Thermodynamic Properties of the C-Cu-Fe-P, Fe-Mo-P and Fe-Ni-P Systems, Report IM-2549, Swedish Institute for Metals Research, Stockholm, Sweden, 1990.
- J.H. Shim, C.S. Oh, D.N. Lee, Thermodynamic properties and calculation of the Fe-P system, *J. Korean Inst. Met. Mater.* 34 (11) (1996) 1385–1393, in Korean.
- H. Ohtani, N. Hanaya, M. Hasebe, S.-i. Teraoka, M. Abe, Thermodynamic analysis of the Fe-Ti-P ternary system by incorporating first-principles calculations into the CALPHAD approach, *Calphad* 30 (2) (2006) 147–158.
- T. Tokunaga, N. Hanaya, H. Ohtani, M. Hasebe, Thermodynamic analysis of the Fe-Mn-P ternary phase diagram by combining the first-principles and CALPHAD methods, *Mater. Sci. Forum* 561–565 (2007) 1899–1902.
- Z.-M. Cao, K.-P. Wang, Z.-Y. Qiao, G.-W. Du, Thermodynamic reoptimization of the Fe-P system, *Acta Phys. Chim. Sin.* 28 (1) (2012) 37–43.
- J. Miettinen, G. Vassilev, Thermodynamic description of ternary Fe-X-P systems. Part 1: Fe-Cr-P, *J. Phase Equilibria Diffus.* 35 (4) (2014) 458–468.
- A.I. Zaitsev, Z.V. Dobrokhotova, A.D. Litvina, B.M. Mogutnov, Thermodynamic properties and phase equilibria in the Fe-P system, *J. Chem. Soc., Faraday Trans.* 91 (4) (1995) 703–712.
- X.-M. Yang, P.-C. Li, M. Zhang, J.-L. Zhang, J. Zhang, Representation reaction abilities of structural units and related thermodynamic properties in Fe-P binary melts based on the atom-molecule coexistence theory, *Steel Res. Int.* 85 (3) (2014) 426–460.
- P. Gustafson, A thermodynamic evaluation of the Fe-C system, *Scand. J. Metall.* 14 (5) (1985) 259–267.
- J.-H. Shim, C.-S. Oh, D.N. Lee, Thermodynamic assessment of the Fe-C-P system, *Z. Metallkd.* 91 (2) (2000) 114–120.
- M. Bernhard, P. Presoly, N. Fuchs, C. Bernhard, Y.-B. Kang, Experimental Study of High Temperature Phase Equilibria in the Iron-Rich Part of the Fe-P and Fe-C-P Systems, 2020 under revision.
- A.D. Pelton, S.A. Degterov, G. Eriksson, C. Robelin, Y. Dessureault, The modified quasichemical model I - Binary solutions, *Metall. Mater. Trans. B* 31 (4) (2000) 651–659.
- A.D. Pelton, P. Chartrand, The modified quasi-chemical model: Part II. Multicomponent solutions, *Metall. Mater. Trans.* 32 (6) (2001) 1355–1360.
- M. Hillert, The compound energy formalism, *J. Alloys Compd.* 320 (2001) 161–176.
- K. Shubhank, Y.-B. Kang, Critical evaluation and thermodynamic optimization of Fe-Cu, Cu-C, Fe-C binary systems and Fe-Cu-C ternary system, *Calphad* 45 (2014) 127–137.
- H. Okamoto, The Fe-P (Iron-Phosphorus) system, *Bull. Alloy Phase Diagrams* 11 (4) (1990) 404–412.
- P. Perrot, Carbon - Iron - Phosphorus: Datasheet from Landolt-Börnstein - Group IV Physical Chemistry, in: “Iron Systems, Part 2” in Springer Materials, ume 11D2, Springer-Verlag, Berlin Heidelberg, 2008, https://doi.org/10.1007/978-3-540-74196-1_11.
- E. Schürmann, H.P. Kaiser, U. Hensgen, Kalorimetrie und Thermodynamik des Systems Eisen-Phosphor (Calorimetry and Thermodynamics of the System Iron-Phosphorus), *Arch. Eisenhuettenwes.* 52 (2) (1981) 51–55, in German.
- G. Urbain, Activité thermodynamique du phosphore dans les alliages fer-phosphore liquides à 1600 °C, *Compt. Rend.* 244 (1957) 1036–1039, in French.
- G. Urbain, Activité du phosphore dissous dans le fer liquide, *Mem. Sci. Rev. Metall.* 56 (5) (1959) 529–544, in French.
- S. Ban-Ya, M. Suzuki, Activity of phosphorus in liquid Fe-P and Fe-P-C alloys, *Tetsu-To-Hagane* 61 (14) (1975) 2933–2942, in Japanese.
- W.A. Fischer, D. Janke, H.-J. Engell, Elektrochemische und elektrische Untersuchungen im System Eisen-Phosphor-Sauerstoff-Kalk. Teil I: die Aktivität des Phosphors in Eisen-Phosphor-Schmelzen und die Freie Enthalpie der Phosphorverschlackung (Electrochemical and Electrical Studies in the System Iron-Phosphorus-Oxygen-Lime. Part I: the Activity of Phosphorus in Iron-Phosphorus Melts and the Free Enthalpy of Phosphorus Scorification), *Arch. Eisenhuettenw.* 37 (11) (1996) 853–862, in German.
- S. Ban-Ya, N. Maruyama, S. Fujino, Vapor pressure of phosphorus in liquid Fe-P alloys, *Tetsu-To-Hagane* 68 (2) (1982) 269–276, in Japanese.
- H. Schenck, E. Steinmetz, R. Gohlke, Untersuchungen zur Phosphoraktivität im flüssigen Eisen (Investigations on the Activity of Phosphorus in Molten Iron), *Arch. Eisenhuettenw.* 37 (10) (1966) 775–778, in German.
- H. Schenck, E. Steinmetz, H. Gitzad, Die Phosphoraktivität im flüssigen Eisen und ihre Beeinflussung durch Nickel, Mangan und Chrom (The Activity of Phosphorus in Molten Iron and its Control by Nickel, Manganese and Chromium), *Arch. Eisenhuettenw.* 40 (8) (1969) 597–602, in German.
- W.A. Roth, A. Meichsner, H. Richter, Ein Näherungswert für die Bildungswärme eines Eisenphosphides [Fe₂P], *Arch. Eisenhuettenw.* 8 (6) (1934) 239–241, in German.
- F. Weibke, G. Schrag, Die Bildungswärmen der niederen Phosphide einiger Schwermetalle, *Z. Elektrochem.* 47 (3) (1941) 222–238, in German.
- G.L. Lewis, C.E. Myers, Vaporization properties of iron phosphides, *J. Phys. Chem.* 67 (6) (1963) 1289–1292.

- [36] J. Wu, X.-Y. Chong, R. Zhou, Y.-H. Jiang, J. Feng, Structure, stability, mechanical and electronic properties of Fe-P binary compounds by first-principle calculations, *RSC Adv.* 5 (2015) 81943–81956.
- [37] A. Jain, S.P. Ong, G. Hautier, W. Chen, W.D. Richards, S. Dacek, S. Cholia, D. Gunter, D. Skinner, G. Ceder, K.A. Persson, The Materials Project: a materials genome approach to accelerating materials innovation, *Apl. Mater.* 1 (1) (2013), 011002.
- [38] B. Hallstedt, D. Djurovic, J. von Appen, R. Dronskowski, A. Dick, F. Körmann, T. Hickel, J. Neugebauer, Thermodynamic properties of cementite (Fe_3C), *Calphad* 34 (1) (2010) 129–133.
- [39] F. Claeysens, J.N. Hart, N.L. Allan, J.M. Oliva, Solid phases of phosphorus carbide: an ab initio study, *Phys. Rev. B* 79 (13) (2009), 134115.
- [40] B. Saklatwalla, Constitution of the iron and phosphorus compounds, *J. Iron Steel Inst.* 77 (1908) 92–103.
- [41] N. Konstantinow, Über die Phosphide des Eisens, *Z. Anorg. Chem.* 66 (1910) 209–227, in German.
- [42] J.L. Houghton, Alloys of iron research: Part VIII.—Constitution of alloys of iron and phosphorus, *J. Iron Steel Inst.* 115 (1927) 417–433.
- [43] P. Roquet, G. Jegaden, Contribution à l'étude du diagramme fer-phosphore: etude de l'essai dit du grain de phosphore, *Rev. Métall.* 48 (9) (1951) 712–721, in French.
- [44] K. Lorenz, H. Fabritius, Anwendung der magnetischen Waage zur Aufstellung von Zustandsschaubildern im Bereich des festen Zustandes eisenreicher Systeme: untersuchung am System Eisen-Phosphor, *Arch. Eisenhuettenw.* 33 (4) (1962) 269–275, in German.
- [45] W.A. Fischer, K. Lorenz, H. Fabritius, A. Hoffmann, G. Kalwa, Untersuchung von Phasenumwandlungen in reinen Eisenlegierungen mit der magnetischen Waage (Investigation of phase transformations in pure iron alloys with a magnetic balance), *Arch. Eisenhuettenw.* 37 (1) (1966) 79–86, in German.
- [46] E. Wachtel, G. Urbain, E. Übelacker, Étude du diagramme fer-phosphore par analyse magnétique et thermique, *Compt. Rend.* 257 (1963) 2470–2472, in French.
- [47] H. Kaneko, T. Nishizawa, K. Tamaki, A. Tanifuji, Solubility of phosphorus in alpha-Fe and gamma-Fe, *Nippon Kinzoku Gakkaishi* 29 (1965) 166–170, in Japanese.
- [48] A.S. Doan, J.I. Goldstein, The ternary phase diagram, Fe-Ni-P, *Metall. Trans.* 1 (6) (1970) 1759–1767.
- [49] M. Ko, T. Nishizawa, Effect of magnetic transition on the solubility of alloying elements in alpha iron, *J. Jpn. Inst. Metals* 43 (2) (1979) 118–126.
- [50] E. Schürmann, Beitrag zu den Schmelzgleichgewichten der Eisen-Aluminium- und Eisen-Phosphor-Legierungen (On the Melting Equilibria of the Iron-Aluminium and Iron-Phosphorus Alloys), *Arch. Eisenhuettenw.* 51 (8) (1980) 325–327, in German.
- [51] Z.I. Morita, T. Tanaka, Equilibrium distribution coefficient of phosphorus in iron alloys, *Trans. Iron Steel Inst. Jpn.* 26 (1986) 114–120.
- [52] M.G. Froberg, J.F. Elliott, H.G. Hadrys, Beitrag zur Thermodynamik von Mehrstofflösungen am Beispiel homogener Eisen-Chrom-Phosphor-Kohlenstoff-Schmelzen (Contribution to the study of the thermodynamics of complex solutions shown by the example of homogeneous iron-chromium-phosphorus-carbon melts), *Arch. Eisenhuettenw.* 39 (8) (1968) 587–593, in German.
- [53] H.G. Hadrys, M.G. Froberg, J.F. Elliott, Activities in the liquid Fe-Cr-C(sat), Fe-P-C(sat) and Fe-Cr-P systems at 1600°C, *Metall. Trans.* 1 (7) (1970) 1867–1874.
- [54] H. Schenck, E. Steinmetz, R. Gohlke, Beitrag zur chemischen Aktivität der Elemente Phosphor, Schwefel, Silizium, Kupfer und Chrom in flüssigen kohlenstoffgesättigten Eisenlösungen (Contribution to the study of the chemical activity of the elements phosphorus, sulphur, silicon, copper and chromium in molten iron solutions saturated with carbon), *Arch. Eisenhuettenw.* 37 (12) (1966) 919–924, in German.
- [55] Y.-D. Yang, Interaction coefficients in Fe-C-P ternary and Fe-Cr-C-P quaternary solutions at 1400°C, *Scand. J. Metall.* 21 (1992) 194–201.
- [56] E.T. Turkdogan, L.E. Leake, Thermodynamics of carbon dissolved in iron alloys. Part I: solubility of carbon in iron-phosphorus, iron-silicon, and iron-manganese melts, *J. Iron Steel Inst.* 179 (1955) 39–43.
- [57] E. Schürmann, D. Kramer, Untersuchungen über den Einfluss der Temperatur und über die äquivalente Wirkung der Legierungselemente auf die Kohlenstofflöslichkeit in eisenreichen, kohlenstoffgesättigten Drei- und Mehrstoffschmelzen, *Giessereiforschung* 21 (1) (1969) 29–42, in German.
- [58] R. Vogel, Ueber das System Eisen-Phosphor-Kohlenstoff, *Arch. Eisenhuettenw.* 3 (5) (1929) 369–381, in German.
- [59] T. Ohide, G. Ohira, The solidification structures of iron-carbon-phosphorus ternary Alloys, *Br. Foundryman* 68 (1975) 106–115.
- [60] E. Schürmann, U. Hensgen, J. Schweinichen, Schmelzgleichgewichte der ternären Systeme Eisen-Kohlenstoff-Silizium und Eisen-Kohlenstoff-Phosphor (Melting equilibrium of the ternary systems iron-carbon-silicon and iron-carbon-phosphorus), *Giessereiforschung* 36 (4) (1984) 121–129, in German.
- [61] G. Langenscheid, H.A. Mathesius, F.K. Naumann, Anwendung des quantitativen Fernsehmikroskopes und der Elektronenstrahlmikrosonde für die Untersuchung des Systems Eisen-Kohlenstoff-Phosphor bei 900 bis 1000 °C (Use of the quantitative television microscope and of the electron beam microprobe for examining the system iron-carbon-phosphorus at 900 to 1000 °C), *Arch. Eisenhuettenw.* 41 (8) (1970) 817–824, in German.
- [62] H.P. Hofmann, K. Löhberg, W. Reif, Über die Löslichkeit des Phosphors in Eisen und Eisen-Kohlenstoff-Legierungen unterhalb 1000 °C (On the solubility of phosphorus in iron and iron-carbon alloys), *Arch. Eisenhuettenw.* 41 (10) (1970) 975–982, in German.
- [63] T. Nishizawa, unpublished work, cited in the work of Gustafson [8] and Shim et al. [17].
- [64] C.W. Bale, E. Bélisle, P. Chartrand, S.A. Decterov, G. Eriksson, A.E. Gheribi, K. Hack, I.-H. Jung, Y.-B. Kang, J. Melançon, A.D. Pelton, S. Petersen, C. Robelin, J. Sangster, P. Spencer, M.-A. van Ende, FactSage thermochemical software and databases, *Calphad* 54 (2010–2016) 35–53, 2016.
- [65] A.T. Dinsdale, SGTE Data for pure elements, *Calphad* 15 (4) (1991) 317–425.
- [66] A.D. Pelton, M. Blander, Thermodynamic analysis of ordered liquid solutions by a modified quasicheical approach - application to silicate slags, *Metall. Trans. B* 17 (4) (1986) 805–815.
- [67] A.D. Pelton, Y.-B. Kang, Modeling short-range ordering in solutions, *Int. J. Mater. Res.* 98 (10) (2007) 907–917.
- [68] M. Hillert, M. Jarl, A model for alloying effects in ferromagnetic metals, *Calphad* 2 (3) (1978) 227–238.
- [69] G. Kresse, Hafner, Ab initio molecular dynamics for liquid metals, *Phys. Rev. B* 47 (1) (1993) 558–561.
- [70] G. Kresse, Hafner, Ab initio molecular-dynamics simulation of the liquid-metal-amorphous-semiconductor transition in germanium, *Phys. Rev. B* 49 (20) (1994) 14251–14269.
- [71] G. Kresse, J. Furthmüller, Efficiency of ab-initio total energy calculations for metals and semiconductors using a plane-wave basis set, *Comput. Mater. Sci.* 6 (1) (1996) 15–50.
- [72] G. Kresse, J. Furthmüller, Efficient iterative schemes for ab initio total-energy calculations using a plane-wave basis set, *Phys. Rev. B* 54 (16) (1996) 11169–11186.
- [73] P.E. Blöchl, Projector augmented-wave method, *Phys. Rev. B* 50 (24) (1994) 17953–17979.
- [74] G. Kresse, D. Joubert, From ultrasoft pseudopotentials to the projector augmented-wave method, *Phys. Rev. B* 59 (3) (1999) 1758–1775.
- [75] J.P. Perdew, K. Burke, M. Ernzerhof, Generalized gradient approximation made simple, *Phys. Rev. Lett.* 77 (18) (1996) 3865–3868.
- [76] J.P. Perdew, K. Burke, M. Ernzerhof, Generalized gradient approximation made simple [phys. Rev. Lett. 77, 3865, *Phys. Rev. Lett.* 78 (7) (1996) 1396, 1997.
- [77] M.W. Chase, NIST-JANAF thermochemical tables, *J. Phys. Chem. Ref. Data* 9 (1998) 1–1951. Fourth Edition.
- [78] P. Presoly, R. Pierer, C. Bernhard, Identification of defect prone peritectic steel grades by analyzing high-temperature phase transformations, *Metall. Mater. Trans.* 44 (12) (2013) 5377–5388.
- [79] P. Presoly, M. Bernhard, C. Bernhard, S. Hahn, P. Pennerstorfer, S. Ilie, J. Six, High precious phase diagrams – a roadmap for a successful casting processing. Proceedings of the 4th European Steel Technology and Application Days (ESTAD), Steel Institute VDEh, Duesseldorf, Germany, 2019.
- [80] G. K. Sigworth and J. F. Elliott, The thermodynamics of liquid dilute iron alloys, *Met. Sci.*, 8, 298-310.
- [81] C.H.P. Lupis, Chemical Thermodynamics of Materials, Elsevier Science Publishing Co. Inc., New York NY, USA, 1983.

Paper III

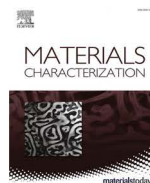
Characterization of the γ -loop in the Fe-P system by coupling DSC and HT-LSCM with complementary in-situ experimental techniques

M. Bernhard, N. Fuchs, P. Presoly, P. Angerer, B. Friessnegger and C. Bernhard

Materials Characterization, 2021, vol. 174, art. no. 111030.

Abstract: Solid-state phase transformations in the γ -loop of the binary Fe-P system were studied using differential scanning calorimetry (DSC) and high-temperature laser scanning confocal microscopy (HT-LSCM). In total, eight alloys with varying P content from 0.026 to 0.48 mass pct. P were investigated in the temperature range of 800 °C to 1450 °C. The first part of the present work deals with the critical evaluation of the approach to couple DSC experiments and HT-LSCM observations in order to characterize bcc/fcc phase equilibria in Fe-based γ -loops. The phase transformation temperatures of a selected alloy with 0.394%P were analyzed by DSC and HT-LSCM and compared with results of the well-established techniques of dilatometry and high-temperature X-ray diffraction (HT-XRD). Then, the overall phase boundaries of the γ -loop were reconstructed by HT-LSCM and DSC data and the phase diagram was compared with thermodynamic assessments from literature. Finally, the quantitative phase fractions of fcc and bcc at 0.394%P were analyzed by Rietveld refinement at temperatures of 1050 °C, 1100 °C and 1150 °C using in-situ HT-XRD. Although the phase boundaries of the γ -loop and phase transformation temperatures have been reproduced accurately by recently published thermodynamic optimizations, larger deviations between HT-XRD measurements and the calculations were identified for the phase fraction prediction. The present work clearly demonstrates that coupling DSC and HT-LSCM is a powerful tool to characterize γ -loops in steel for future research work.

Used and reprinted under the Creative Commons Attribution 4.0 International License



Characterization of the γ -loop in the Fe-P system by coupling DSC and HT-LSCM with complementary in-situ experimental techniques

Michael Bernhard^{a,*}, Nora Fuchs^a, Peter Presoly^a, Paul Angerer^b, Bernhard Friessnegger^b, Christian Bernhard^a

^a Chair of Ferrous Metallurgy, Montanuniversität Leoben, Franz-Josef-Strasse 18, 8700 Leoben, Austria

^b Materials Center Leoben Forschungs GmbH, Roseggerstrasse 12, 8700 Leoben, Austria

ARTICLE INFO

Keywords:

Fe-P
In-situ experiments
 γ -Loop
DSC
HT-LSCM
HT-XRD
Phase diagram;

ABSTRACT

Solid-state phase transformations in the γ -loop of the binary Fe-P system were studied using differential scanning calorimetry (DSC) and high-temperature laser scanning confocal microscopy (HT-LSCM). In total, eight alloys with varying P content from 0.026 to 0.48 mass pct. P were investigated in the temperature range of 800 °C to 1450 °C. The first part of the present work deals with the critical evaluation of the approach to couple DSC experiments and HT-LSCM observations in order to characterize bcc/fcc phase equilibria in Fe-based γ -loops. The phase transformation temperatures of a selected alloy with 0.394%P were analyzed by DSC and HT-LSCM and compared with results of the well-established techniques of dilatometry and high-temperature X-ray diffraction (HT-XRD). Then, the overall phase boundaries of the γ -loop were reconstructed by HT-LSCM and DSC data and the phase diagram was compared with thermodynamic assessments from literature. Finally, the quantitative phase fractions of fcc and bcc at 0.394%P were analyzed by Rietveld refinement at temperatures of 1050 °C, 1100 °C and 1150 °C using in-situ HT-XRD. Although the phase boundaries of the γ -loop and phase transformation temperatures have been reproduced accurately by recently published thermodynamic optimizations, larger deviations between HT-XRD measurements and the calculations were identified for the phase fraction prediction. The present work clearly demonstrates that coupling DSC and HT-LSCM is a powerful tool to characterize γ -loops in steel for future research work.

1. Introduction

It is well known that each alloying element in steel favors the stability of a particular phase. With respect to the body-centered cubic (bcc) ferrite phase and the face-centered cubic (fcc) austenite phase, elements in steel can generally be categorized as ferrite formers (Si, Al, P, Cr, V, Ti, Mo) and austenite formers (C, Mn, N, Co). Weven [1] formulated four different modes of typical phase equilibria between ferrite (α , δ) and austenite (γ), depending on the alloying element. This concept is graphically represented in Fig. 1 (a)–(d) [1,2]:

- Ni, Mn and Co favor the formation of the open fcc region, resulting in a large fcc single phase region, whereas the stability of bcc is very limited to a close composition range in the Fe-rich part of the system.
- C and N lead to the expanded fcc region over a large composition range with diverging phase boundaries which merge in heterogeneous phase equilibria.

- B and S strongly limit the stability of the solid solutions in the phase diagram (contracted fcc region).
- In contrast to the open fcc region, a completely closed fcc region is favored by the bcc stabilizing elements P, Si, Al, Cr, V, Ti and Mo. This type of bcc/fcc solid state equilibrium is also known as γ -loop, where the bcc single-phase region dominates over a wide composition range.

The influence of Si, Al and P on the γ -loop phase boundaries in the corresponding binary phase diagram is shown in Fig. 1 (e). In the Fe-Si system, the fcc single-phase region is stable up to 1.65 mass pct. Si. The addition of Al shifts the phase boundaries of the γ -loop to significantly lower alloying content. The maximum solubility in austenite is 0.74 mass pct. Al. Phosphorus shows a very strong bcc stabilization effect in the binary system, where the fcc single-phase region only exists up to 0.30 mass pct. P. In the Fe-C system, see Fig. 1 (f), an increasing amount of P from 0 to 0.75 mass pct. continuously stabilizes the γ -loop and the

* Corresponding author.

E-mail address: michael.bernhard@unileoben.ac.at (M. Bernhard).

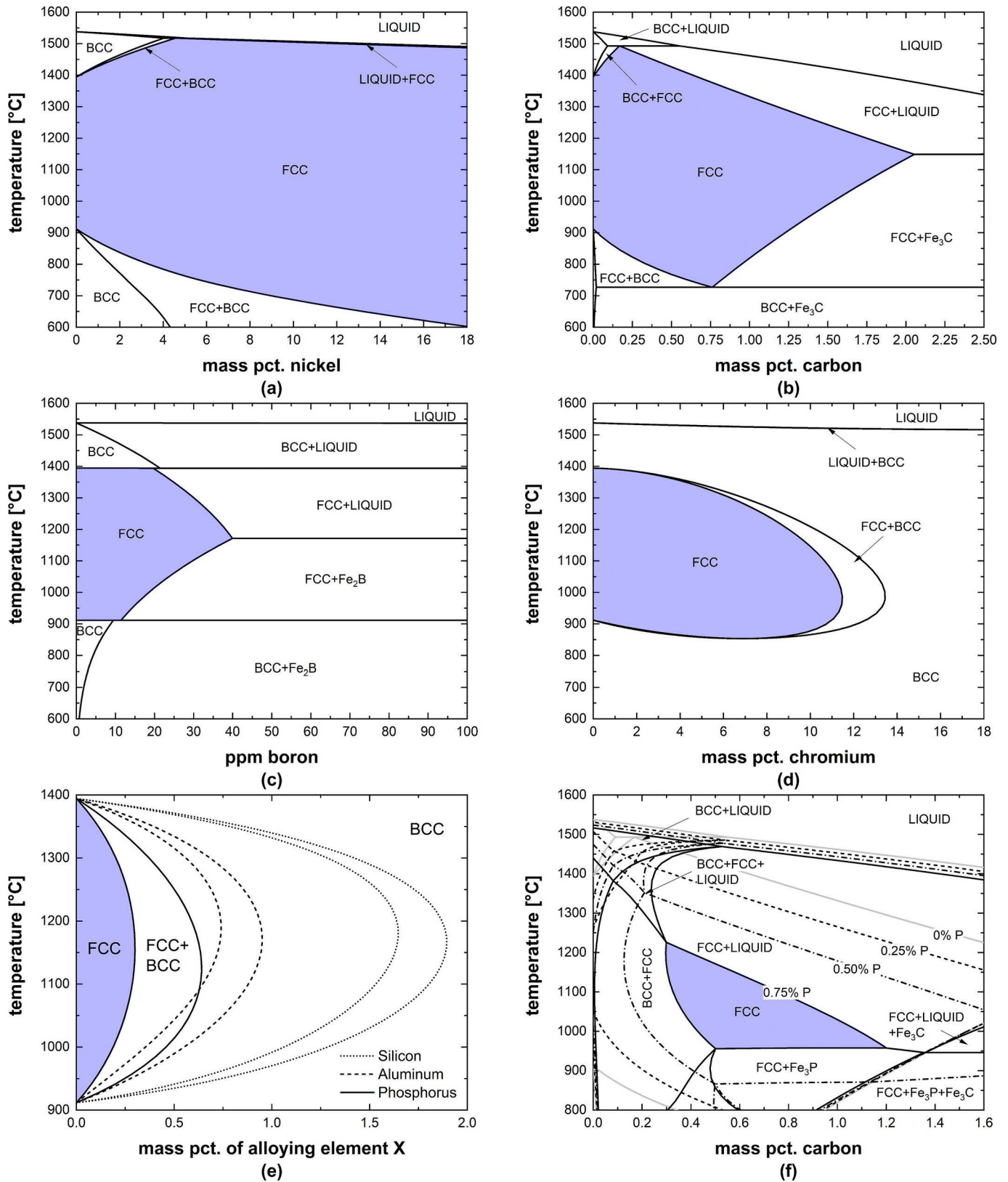


Fig. 1. Influence of alloying elements on the fcc stability in Fe-based phase diagrams according to Wever [1]; open fcc region (a) - Fe-Ni, expanded fcc region (b) - Fe-C, contracted fcc region (c) - Fe-B and closed fcc region (d) - Fe-Cr; influence of alloying elements on the binary γ -loop (e) and influence of phosphorus on the fcc stability in the Fe-C phase diagram (f). The phase diagrams were calculated using the thermochemical software FactSage 8.0 and the FSStel2019 thermodynamic database [2].

fcc single-phase region is strongly contracted. Depending on the content of P and C, the bcc + fcc two-phase region exists from solidus temperature down to room temperature, resulting in large primary ferrite grains in the final microstructure.

In recent steel design, the influence of disproportional amounts of γ -loop forming elements on phase equilibria in Fe-based multicomponent systems has been of great practical importance to optimize process conditions and guarantee the desired mechanical and physical properties of the steel grade. In Si steel sheets for electrical applications, the typical silicon content varies between 1 and 3.5 mass pct. [3]; Amounts of phosphorus up to 0.1 mass pct. improve the crystallographic texture in silicon steels [4,5] and decrease the eddy current losses by increasing the electrical resistivity [4–6]. In high strength TRIP steels for the automotive sector, Si and Al are added up to 1.5 mass pct. [7,8] in order to stabilize the retained austenite. Phosphorus is partly used to substitute Si; amounts of 0.1 mass pct. P are considered beneficial for the TRIP effect. [9]

In previous work of the authors [10], differential scanning calorimetry (DSC) was applied to reinvestigate phase equilibria in the binary Fe-P system and various isoplethal sections in the ternary Fe-C-P system. For selected alloys in the ternary system, the analysis of the DSC signal was supported by high-temperature laser scanning confocal microscopy (HT-LSCM). Although accurate melting equilibrium temperatures could be obtained with the DSC method, a complete reconstruction of the Fe-P γ -loop could not be provided. Particularly in the low temperature range of 900–1150 °C, the resolution of the DSC setup used was limited to characterize the beginning of the bcc \leftrightarrow bcc + fcc phase transformation. Consequently, it was the aim of the present study to develop a coupled DSC/HT-LSCM experimental approach as a valuable tool to reproduce the phase boundaries of binary γ -loops, including the possibility to apply the developed procedure to multicomponent steel systems.

In total, eight alloys in the Fe-P system with 0.026–0.48 mass pct. P were investigated. For a selected alloy containing 0.394 mass pct. P, the well-established methods of dilatometry (DIL) and high-temperature X-ray diffraction (HT-XRD) were utilized to critically evaluate the results of linking DSC analysis and HT-LSCM observations. Then, the overall phase boundaries of the γ -loop were reproduced by coupling HT-LSCM and DSC data and compared with recently published thermodynamic assessments of the binary Fe-P system [11–14]. Finally, thermodynamic equilibrium calculations were performed to predict the fractions of ferrite and austenite at 0.394 mass pct. P between 900 and 1350 °C and evaluated with quantitative phase fraction analysis by Rietveld refinement of fcc and bcc at 1050 °C, 1100 °C and 1150 °C using HT-XRD.

2. Literature review of experimental techniques used for γ -loop reconstructions

In general, two methodological approaches exist to investigate phase equilibria at high temperatures [15]: In the ex-situ approach, the microstructure is equilibrated at a defined temperature and the corresponding stable phases are stabilized down to room temperature by quenching the sample in water, iced water, oil or other quenching media. In this case, particular care needs to be taken in order to reach the equilibrium state in the isothermal heat treatments and retain the high-temperature structure in case of very fast phase transformations like the fcc/bcc transition in pure Fe and its dilute solutions [15]. Within in-situ experiments, e.g. HT-LSCM and HT-XRD, the microstructure and phase relations are directly characterized at elevated temperatures. Both characterization methods of γ -loops, ex-situ and in-situ, are based on the different thermophysical properties of fcc and bcc iron (magnetic susceptibility, crystal structure and density) or on the fcc/bcc phase transformation itself (enthalpy change and microstructure). Table 1 gives a summary of previously applied techniques to reconstruct γ -loops in Fe-based systems. The specific advantages, possibilities and challenges of each experiment should be discussed briefly in this chapter.

Table 1

Overview of experimental methods [10,16–22,24–29,35–40,52] to reproduce phase boundaries of γ -loops in Fe-based systems.

Method	Subcategory	Reference	System							
EQU	OM	Roquet and Jegaden [16]	Fe-P							
		Roquet et al. [17]	Fe-Al							
		Heijwegen and Rieck [18]	Fe-Mo							
		Alberry and Haworth [19]	Fe-Mo							
		Hirano and Hishinuma [20]	Fe-Al							
	Two-phase alloys	Kirchner et al. [22]	Fe-W							
		Kirchner et al. [21]	Fe-Cr							
		Kirchner et al. [22]	Fe-Mo, Fe-W							
		Crangle [24]	Fe-Si							
		Übelacker [25]	Fe-Si							
TMA		Lorenz et al. [26]	Fe-P							
		Baerlecken et al. [27]	Fe-Cr							
		Fischer et al. [28]	Fe-Si, Fe-P, Fe-Ti, Fe-C-Si							
		Fischer et al. [29]	Fe-Mo, Fe-V, Fe-W							
		Roquet and Jegaden [16]	Fe-P							
		Roquet et al. [17]	Fe-Al							
		Adcock [35]	Fe-Cr							
		Bentle and Fishel [36]	Fe-Si, Fe-Si-Ti							
		Burgardt et al. [37]	Fe-Cr							
		Wada [38]	Fe-Ti							
XRD	In-situ	Present study	Fe-P							
		Oberhoffer and Kreutzer [39]	Fe-Si, Fe-Cr							
		Present study	Fe-P							
		Speight [40]	Fe-Sn							
		Present study	Fe-P							
	TOA	HT-LSCM	Present study	Fe-P						
					TAC	DSC	M. Bernhard et al. [10]	Fe-P		
	DTA	Übelacker [25]	Fe-Si							
				TA					Adcock [35]	Fe-Cr

2.1. Equilibration experiments (EQU)

The sample is heat-treated under a given time-temperature profile. After chemical and microstructural equilibration at a defined elevated temperature, the sample is typically quenched in water to stabilize the microstructure and high-temperature phases down to room temperature. The final analysis is done by metallographic analysis of the quenched microstructure using optical microscope (OM) techniques. EQU-OM was performed by Roquet et al. [16,17] in the Fe-P and Fe-Al system. The EQU-OM method is a classic way of examining phase fractions, microstructure components, homogeneity and surface contaminations. [15] Typical limitations of EQU-OM are the magnification and the lack of possibility to identify the crystal structure.

Direct chemical analysis of fcc and bcc by electron microprobe analysis (EPMA) is similarly used in equilibration experiments, either in the concept of diffusion couples (DC) [18–20] or to analyze samples whose initial composition is already within the bcc + fcc two-phase region at respective temperature [21,22]. In a simplified outline of the EQU-DC method, two or more materials with different alloying content are in intimate contact and are equilibrated at a defined temperature. As a consequence, one material (or species) diffuses into the other, forming an interface within the diffusion zone at which the stable phases are in local equilibrium. [23] The chemical analysis of fcc and bcc close to the interface is then directly measured by EPMA and the extrapolation to the bcc/fcc interface enables the reconstruction of the phase boundaries. EQU-DC was used by Heijwegen and Rieck [18] and by Alberry and Haworth [19] to examine the Fe-Mo system. Kirchner et al. [21,22] applied EPMA for characterizations of diffusion couples and two-phase alloys in extensive γ -loop studies of the Fe-Cr, Fe-Mo and Fe-W systems. If steep

concentration gradients occur along the interface, the extrapolation to the interface may lead to major errors. [23] Other difficulties arise from the EPMA measurements (e.g. chemical composition) or from the formation of only a quasi-equilibrated diffusion zone. [23] However, the elemental analysis of the bcc/fcc phase boundary by EPMA is a time-saving method with the possibility of determining a great variety of elements over wide composition ranges and is widely accepted in the field of phase diagram research.

2.2. Thermo-magnetic analysis (TMA)

In-situ method based on the magnetic susceptibility of fcc and bcc above the Curie temperature. For this purpose, the magnetic force exerted on a sample in an inhomogeneous magnetic field is determined by a magnetic balance. This technique was applied by Crangle [24] within the examination of the Fe-Si system and used by Übelacker [25] in the Fe-Si binary system. Later, the concept of the magnetic balance was adopted by Lorenz, Fischer and Fabritius for extensive γ -loop studies of Fe-X (X = P, Cr, Si, Ti, Mo, V and W) binary systems [26–29]. The advantage of TMA is a very sharp signal due to the abrupt change in the magnetic force at the start of the phase transformation (bcc \leftrightarrow bcc + fcc or fcc \leftrightarrow fcc + bcc) and when the phase transformation is completed (bcc + fcc \leftrightarrow fcc or fcc + bcc \leftrightarrow bcc). TMA data are generally considered to be highly accurate and most reliable [14,30–32] for the development of thermodynamic databases within the CALPHAD framework [33,34].

2.3. Dilatometry (DIL)

In-situ measurement of the dilatation of a sample considering the different thermal expansion of ferrite and austenite during testing. Changes in the signal are assigned to the density/volume change during the phase transformation. This technique has been approved as a standard technique for the characterization of fcc/bcc phase transformations in steel systems. As early as the 1930s, Adcock [35] combined DIL and thermal analysis (TA) to determine the Fe-Cr phase diagram. Roquet et al. [16,17] and Bente and Fishel [36] used DIL later in their investigation of the γ -loop in the Fe-P and Fe-Al systems and in the Fe-Si and Fe-Si-Ti systems, respectively. Further DIL studies were performed by Bungardt et al. [37] in the Fe-Cr system and by Wada [38] to reconstruct the γ -loop of the Fe-Ti phase diagram. Similar to TMA, dilatometry shows a high sensitivity of the signal change during the fcc/bcc phase transformations.

2.4. X-ray diffraction (XRD)

Determination of the structural properties of a crystal by the diffraction of X-rays in a specific direction due to the different crystalline structures of fcc and bcc. Oberhoffer and Kreutzer [39] used an in-situ high-temperature XRD (HT-XRD) in a very early study to examine alloys in the Fe-Cr and Fe-Si system. Speight [40] applied XRD analysis to quenched samples after EQU treatment (ex-situ) in the Fe-Sn system. Recently, in-situ HT-XRD investigation at elevated temperatures has been presented by Wiessner et al. [41,42] to characterize fcc phase fractions and microstructure parameters, e.g. lattice constants and dislocation densities in austenitic steel samples, whereby an interesting suggestion concerning an innovative improvement to the Rietveld technique based on a Bayes approach is given in [43]. For XRD methods, the preparation of the sample is the most critical factor in order to guarantee reliable results in the XRD analysis. The ideal sample for XRD analysis shows randomly distributed grains with a crystallite size less than 10 μm in a statistically relevant amount. [15]

2.5. Thermo-optical analysis (TOA)

In-situ analysis of a sample by a microscope under a defined time-

temperature program. The aim is to optically determine the temperature-dependent change in the microstructure components. The classic thermo microscope and high-temperature laser scanning confocal microscope (HT-LSCM) are the typical experimental equipment for TOA. Particularly for steels, the HT-LSCM offers the advantage of recording phase transformations up to high temperatures since the wave length of the blue laser is not in the spectrum of the inherent radiation of the steel sample. HT-LSCM was successfully applied to observe the kinetics of the bcc/fcc phase transformations during the peritectic transformation of Fe-C based alloys [44–48] and in Fe-C-P alloys during cooling in the solid state [49]. Phase stabilities of fcc and bcc in the peritectic range of the Fe-C-Si, Fe-C-Al and Fe-C-P systems have been characterized in various previous work [10,50,51]. However, to the best of the authors' knowledge, HT-LSCM has not been specifically used for complete reconstructions of phase boundaries in γ -loops as of yet. HT-LSCM offers the possibility to observe details of the phase transformation characteristics (e.g. nucleation sites, type of ferrite) by optical evaluation of the sample surface. The experimental investigation of the phase transformation temperature is thus not based on the measurement of the change of a physical property. Limitations of the HT-LSCM method are (i) the restricted field of observation and (ii) that a sufficient contrast between the observed phases has to exist in order to optically distinguish several phases.

2.6. Thermal analysis and calorimetric methods (TAC)

Based on the enthalpy change during the investigated phase transformation. In the thermal analysis (TA), the temperature change during a phase transformation of a sample is measured by a thermocouple. In differential thermal analysis (DTA), the temperature difference between the sample and an inert reference is determined, whereas in differential scanning calorimetry (DSC), the change of heat flux between the sample and the reference is obtained. In contrast to the standard TA and DTA techniques, calorimetric measurements, e.g. DSC and adiabatic calorimetry, offer the possibility of directly determining the specific heat capacity of an alloy over temperature. A significant change in the signal can be assigned to the start or end of the phase transformation. Adiabatic calorimetry was used by Normanton [52] to obtain phase equilibria in the γ -loop of the Fe-Cr system. Recently, the authors [10] have investigated the γ -loop of the binary Fe-P system with an experimental DSC setup. A detailed discussion of challenges and opportunities of the DSC method with respect to determining phase transformation in Fe-based γ -loops can be found in Chapter 3.2.

3. Materials and methods

3.1. Sample preparation and chemical analysis

In the following chapters, the chemical composition of each alloying element is given in mass percent. In total, seven alloys (A-I to B-III in Table 2) had already been prepared and analyzed by DSC in the authors' previous work [10]. In the present study, these specimens were used for

Table 2
Chemical analysis and trace element levels of investigated samples [10].

Alloy	P [mass pct.]	C [mass pct.]	Si [mass pct.]	Mn [mass pct.]	S [mass pct.]	Al [mass pct.]	N [mass pct.]
A-I	0.026	0.008	0.002	0.014	0.0034	0.012	0.0021
A-II	0.044	0.006	0.002	0.015	0.0032	0.002	0.0028
A-III	0.102	0.008	0.002	0.013	0.0033	0.015	0.0025
A-IV	0.147	0.008	0.002	0.021	0.0036	0.037	0.0021
B-I	0.322	0.006	0.003	0.014	0.0033	0.010	0.0021
B-II	0.419	0.008	0.004	0.031	0.0034	0.032	0.0023
B-III	0.480	0.008	0.003	0.016	0.0036	0.022	0.0025
C-I	0.394	0.005	0.004	0.030	0.0029	0.027	0.0027

complementary investigation by means of HT-LSCM. According to the chemical composition and the phase diagram in Fig. 2 (a), alloys A-I to A-IV show an fcc single-phase region, while alloys B-I to B-III show a wide bcc + fcc two-phase region with stable primary ferrite over the whole temperature range. The samples of 50 g were melted in a high-frequency remelting (HFR) furnace Lifumat-Met-3.3-Vac (Linn High Therm GmbH, Germany). As the starting material, pure technical iron cylinders (99.9 mass pct. Fe), high purity red phosphorus powder (98.9%, Alfa Aesar, LOT# U01C005) and high purity aluminum wire for deoxidation were used. The melting process was carried out in alumina crucibles under argon 5.0 (purity 99.999%) atmosphere to avoid contamination of the samples with oxygen and nitrogen. Finally, the melt was centrifugally cast into a copper mold. The chemical analysis of each sample was determined either by optical emission spectroscopy (OES) for $P < 0.10$ mass pct. or by X-ray fluorescence (XRF) spectrometry, for $P > 0.10\%$. For more detailed information on the preparation of the 50 g samples, the authors refer to [10].

For the present study, an additional alloy of 400 g with a defined P amount of 0.40 mass pct. was produced in a PlatiCast PT 600 (Linn High

Therm GmbH, Germany). The increased sample mass provides sufficient testing material for the combined experiments with DSC, HT-LSCM, HT-XRD and DIL and guarantees identical chemical composition, microstructure and sample homogeneity in all in-situ examinations. The composition of 0.40%P shows a wide bcc + fcc region in the phase diagram which often makes the DSC analysis very challenging. It is therefore a suitable composition to (i) critically evaluate the potentials and limitations of the DSC method with respect to characterizing phase equilibria in γ -loops, (ii) develop a coupled experimental approach with HT-LSCM as a supportive tool for the overall reconstruction of phase boundaries in γ -loops and (iii) evaluate the results of coupling DSC/HT-LSCM with complementary in-situ techniques of HT-XRD and dilatometry. The melting procedure based on the HFR technique was very similar to that of the 50 g alloys; mainly the dimensions of the crucible, iron cylinders and copper mold differed: Pure technical iron cylinders (99.9 mass pct. Fe), iron-phosphide powder with 26.7 mass pct. P (purity 97.2%) and high purity aluminum wire for deoxidation were used as the starting materials. The sample was analyzed with an XRF spectrometer Thermo Fisher XRF ARL 9900, which was calibrated up to 4 mass pct. P with the results of inductively coupled plasma (ICP) - OES. [10] As can be seen in Table 2, the final chemical analysis of sample C-I shows very low levels of trace elements (C < 55 ppm, Si < 40 ppm, Mn < 0.03 mass pct., S < 30 ppm and N < 30 ppm), is fully deoxidized with 270 ppm Al and contains 0.394 mass pct. P.

In the case of sample C-I with 0.394 mass pct. P, the stability of primary δ -ferrite from solidification down to room temperature resulted in large ferrite grains in the final microstructure. As a small grain size with random distribution of the fcc and bcc phases is essential for reliable HT-XRD analysis [15], the cylindrical sample C-I with a diameter of 44 mm was hot-pressed at 1150 °C to a small bar measuring $12 \times 12 \times 32 \text{ mm}^3$ in order to recrystallize the microstructure. Before hot-pressing of the sample, a slice of as-cast structure with a thickness of 1 cm was cut off from the cylinder. An overview of the materials used and experiments applied is given in Fig. 2 (b). Samples A-I to B-III were previously investigated by a high-temperature DSC setup [10] and examined by HT-LSCM in the present study. Additionally, phase transformations of samples A-IV and B-II were studied in this work by heat capacity (C_p) measurements using different DSC settings at lower temperatures (LT-DSC). Sample C-I (hot-pressed) was investigated by all available experiments (DSC, HT-LSCM, HT-XRD and DIL), whereas C-I (as-cast) was only examined by DSC and HT-LSCM to identify possible differences in the phase transformation temperatures due to the different microstructures of the samples.

3.2. Differential scanning calorimetry (DSC)

Detailed information on the evaluation of DSC measurements for the characterization of phase transformations in alloys can be found in the NIST recommended practice guide [53]. In the following sections, an onset in the DSC signal corresponds to the first deviation from the baseline that can be assigned to the beginning of the phase transformation (bcc \leftrightarrow bcc + fcc; fcc \leftrightarrow fcc + bcc). A peak defines the end of the phase transformation (bcc + fcc \leftrightarrow fcc; fcc + bcc \leftrightarrow bcc).

3.2.1. Previous work [10] with high-temperature DSC setup ($T \leq 1550 \text{ }^\circ\text{C}$)

All experiments were carried out in a DSC 404F1 Pegasus (NETZSCH-Gerätebau GmbH, Germany) with an Rh furnace ($T_{\text{max}} = 1650 \text{ }^\circ\text{C}$) and a platinum DSC sensor instrumented with type S thermocouples. During the measurement, the protective tube of the Rh furnace was flushed with Ar 5.0 (purity 99.999%, 70 ml/min). A Zr getter was positioned below the DSC sensor in order to keep the oxygen level at elevated temperatures ($> 350 \text{ }^\circ\text{C}$) to a minimum. The DSC setup was calibrated by measuring the melting points and melting enthalpies of NETZSCH's standards of pure metals In, Bi, Al, Ag, Au, Ni and Co. Al_2O_3 crucibles (85 μl) and lids were used; the reference was an empty crucible. The experiments were performed with a heating rate of $10 \text{ }^\circ\text{C}/\text{min}$ using

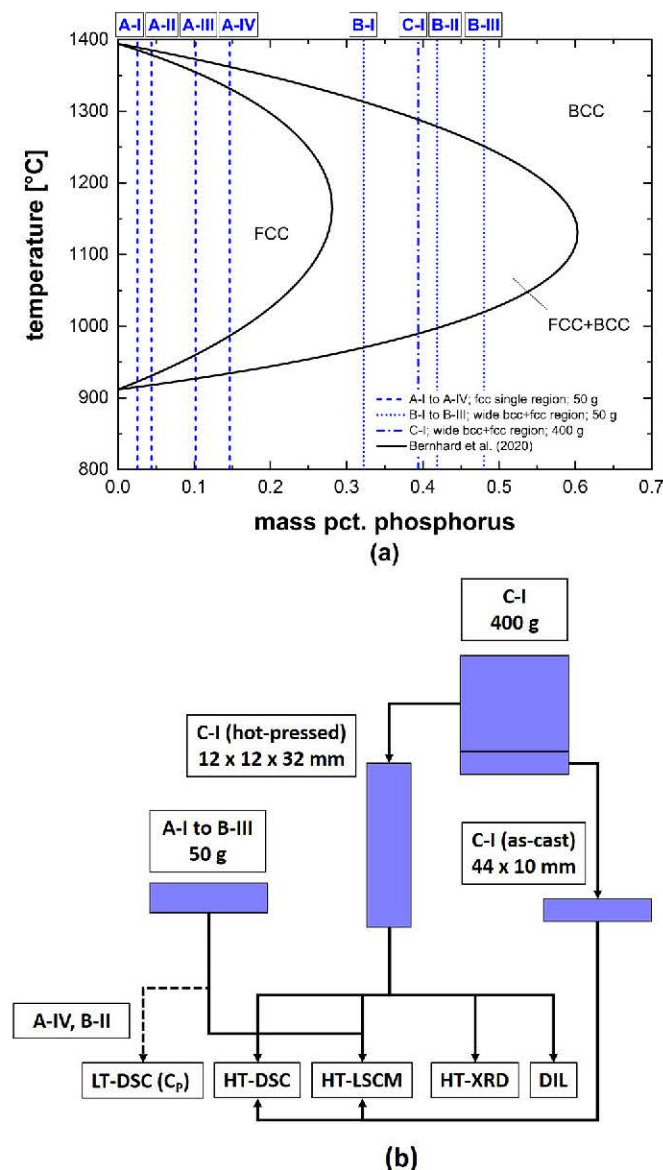


Fig. 2. Prepared samples in the present study and their chemical composition in the Fe-P γ -loop [14] (a) and sample flow with materials used and applied experimental techniques (b).

samples with a mass of 50 mg ($2.1 \times 2.1 \times 1.5 \text{ mm}^3$).

The challenges using the HT-DSC setup to obtain phase equilibria in γ -loops are discussed based on the previously published numerical results of the Fe-P system [10] together with thermodynamic calculations [2,14]. The corresponding DSC charts were corrected to the baseline of 0.0 μV and are illustrated in Fig. 3 (a-I) and (b-I). It can be seen in Fig. 3 (a-I) that at low temperatures of 850 °C to 1050 °C, no sharp onset is observable in the signal over the whole composition range investigated (0.026–0.48 mass pct. P) and an accurate determination from the first deviation of the baseline could not be detected. Hence, it was not possible to provide reliable results for the beginning of the $\text{bcc} \leftrightarrow \text{bcc} + \text{fcc}$ phase transformation. On the other hand, the peak at the end of the $\text{bcc} + \text{fcc} \leftrightarrow \text{fcc}$ transition is clearly visible in the measurements of samples A-I to A-IV. Fig. 3 (b-I) indicates that the HT-DSC setup can be used effectively to record the $\text{fcc} \leftrightarrow \text{fcc} + \text{bcc} \leftrightarrow \text{bcc}$ phase transformation temperatures between 1250 °C and 1400 °C (A-I to A-IV): The

signals show a sharp onset and the signal ends in a clearly pronounced peak when the phase transformation is completed. For samples B-I (0.322%P), B-II (0.419%P) and B-III (0.48%P), the peak when reaching the temperature of the upper phase boundary of the $\text{bcc} + \text{fcc} \leftrightarrow \text{bcc}$ is less pronounced and higher deviations have to be accepted in the DSC analysis.

It is well known that during scanning, the DSC signal is sensitive to the enthalpy-temperature relation ($\Delta H/\Delta T$) of the sample. [53] The ratio of $\Delta H/\Delta T$ is generally defined as the heat capacity C_p . Hence, the resolution of occurring onsets and peaks in Fig. 3 (a-I) and (b-I) is closely related to the magnitude of the vertical jump of C_p at the initial stage of the phase transformation and at its end, respectively. The calculated heat capacities [2,14] for each phase transformation are graphically represented in Fig. 3 (a-II) and (b-II) as a function of the fcc and bcc fraction. Note that for samples B-I to B-III the fcc phase fraction never reaches 100% as their chemical composition is within the $\text{bcc} + \text{fcc}$ two-

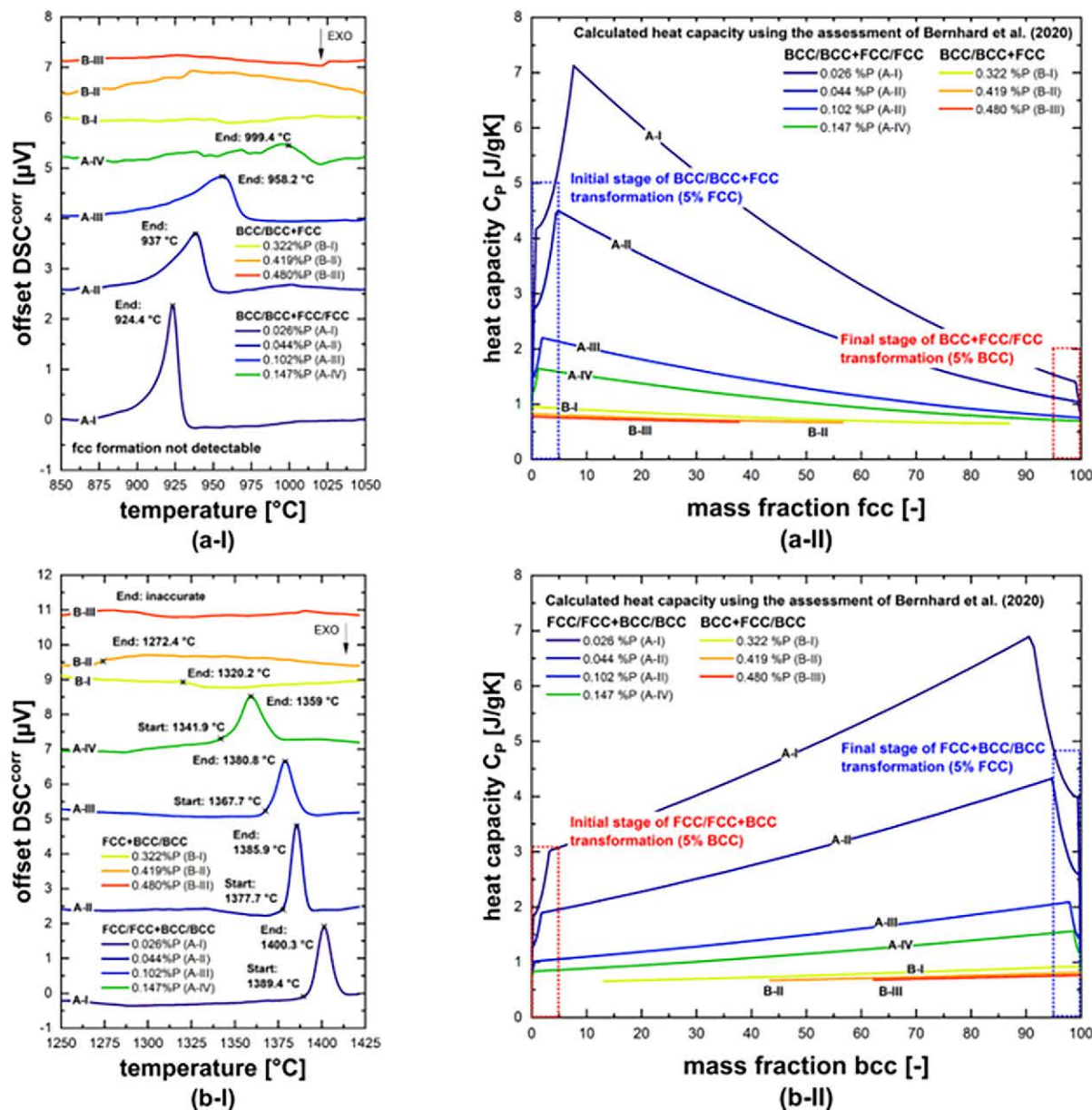


Fig. 3. DSC signals of the previously published numerical results [10] of the bcc/fcc transformations at low temperatures 850–1050 °C (a-I) and at high temperatures 1250–1450 °C (b-I); the DSC signals were corrected to the baseline of 0 μV . Calculated heat capacity during each phase transformation using FactSage 8.0 [2] and the thermodynamic assessment of Bernhard et al. [14]: Low temperature bcc/fcc phase transformations (a-II) and high temperatures bcc/fcc phase transformations (b-II).

phase field; see Fig. 2 (a). The C_p values are therefore plotted up to the maximum fcc fraction or to the minimum bcc fraction. In the following discussion it is considered that a phase transformation progress between 0 and 5% is representative for the initial stage and that a progress of 95–100% corresponds to the final stage.

In Fig. 3 (a-II) the C_p curves calculated for the compositions of samples A-I to A-IV (0.026–0.147 mass pct. P) show a steep increase at the beginning of the bcc \leftrightarrow bcc + fcc transformation. However, the vertical jump of C_p continuously decreases with increasing phosphorus content; a similar relation between C_p and the P content applies to the change of C_p close to the bcc + fcc \leftrightarrow fcc transformation. The calculation results are in reasonable agreement with the DSC signals in Fig. 3 (a-I) where the overall sensitivity of onsets and peaks is reduced at higher P content. When focusing on the C_p curve of a selected alloy, it is evident that the change of C_p close to the first fcc formation ($\sim 1\text{--}4$ J/gK) is significantly larger than during the final stage of the bcc decomposition ($\sim 0.05\text{--}1$ J/gK). This fact is somehow surprising, since more rounded shaped onsets were observed in the DSC signal in Fig. 3 (a-I) than expected from a thermodynamic point of view. Probable reasons for the weak onsets are (i) a slow progress of the fcc formation in the scanning mode resulting in a gradual change of heat and (ii) a limited resolution of the HT-DSC setup in this temperature range. The C_p curve for the fcc \leftrightarrow fcc + bcc \leftrightarrow bcc transformation in Fig. 3 (b-II) indicates quite similar values of the C_p changes at the bcc formation ($\sim 0.2\text{--}1.5$ J/gK) and at the fcc decomposition ($\sim 0.7\text{--}4$ J/gK) compared to the bcc/fcc phase transformation at $T \leq 1050$ °C. In this case, the main reasons for a sharper DSC signal are (i) a rapid phase transformation progress at elevated temperatures of 1250–1400 °C and (ii) that the HT-DSC settings (type S thermocouples, Al_2O_3 crucibles, heating rate and sample dimensions) were particularly adjusted for measuring high-temperature phase equilibria in Fe-based alloys up to $T \leq 1550$ °C [10]. The thermodynamic calculations of alloys B-I to B-III (0.322–0.48 mass pct. P), show only minor changes of C_p (0.05–0.2 J/gK) at the beginning and end of the bcc \leftrightarrow bcc + fcc \leftrightarrow bcc phase transformation; see Fig. 3 (a-II) and (b-II). Hence, the DSC analysis using the high-temperature setup was fairly challenging and only a weakly pronounced peak at the end was identified in the DSC signal in Fig. 3 (b-I).

For that reason, it was the aim of this chapter to find improved DSC settings for the general determination of the bcc \leftrightarrow bcc + fcc phase transformation (0.026–0.48 mass pct. P) as well as for the characterization of the fcc + bcc \leftrightarrow bcc phase equilibrium for alloys with a wide bcc + fcc two-phase region ($P \geq 0.322$ mass pct. P).

3.2.2. Determination of phase transformations temperatures by heat capacity measurements for alloys A-IV (0.147 mass pct. P) and B-II (0.419 mass pct. P) at $T \leq 1250$ °C

Potential adjustments of the HT-DSC setup were limited considering that the type of calorimeter, sensor and thermocouple had to be kept unchanged in the present study. When modifying the experimental parameters according to typical testing methods to determine C_p by DSC, the authors expected improved resolution for the start of the bcc \leftrightarrow bcc + fcc \leftrightarrow fcc phase transformation. Though it was not the focus of this chapter to perform quantitative heat capacity measurements, the trials were carried out similarly to those generally proposed in literature [54–57]. First, the DSC setup was recalibrated (see Chapter 3.2.1) with PtRh crucibles which were covered with a lid. The use of PtRh crucibles is recommended over Al_2O_3 crucibles because the higher thermal conductivity leads to an increased intensity of the signal. A thin-walled Al_2O_3 liner inside the PtRh crucible (PtRh/ Al_2O_3) prevents the Fe-P sample from the reacting with Pt of the crucible. The dimensions of the samples were changed to $3.5 \times 3.5 \times 1.5$ mm³ (130 mg). The shape of a flat disc guarantees a large contact between the sample, the crucible and the sensor leading to optimized heat coupling during the measurements. In all experiments the reference was an empty crucible. The temperature profile was defined as follows: After an isothermal sequence of 30 min at 30 °C the sample was constantly heated up with

20 °C/min to the final temperature of 1250 °C. Following an isothermal holding time of 20 min at 1250 °C the sample was cooled with -20 °C/min to ambient temperature. The time-temperature profile was applied (i) within the baseline run with two empty crucibles, (ii) the measurement of a NETZSCH standard sapphire ($\alpha\text{-Al}_2\text{O}_3$ single crystal) disc (6 mm diameter, 84.45 mg) with well-known values of $C_p(T)$ [58] and (iii) the analysis of samples A-IV (0.147 mass pct. P) and B-II (0.419 mass pct. P). Each trial was performed at least twice. Finally, the quantitative $C_p(T)$ curves were obtained according to ASTM E1269–11 [56].

The measured heat capacities of alloys A-IV and B-II are summarized in Fig. 4 along with the HT-DSC signal from Chapter 3.2.1. The data are given in the relevant temperature range of 500–1100 °C. It can be seen in Fig. 4 (a) that the sensitivity of the DSC signal for the bcc \leftrightarrow bcc + fcc \leftrightarrow fcc could be significantly improved in the case of alloy A-IV. A sharp onset at 935.7 °C is visible and the peak is more clearly pronounced. The slight increase in the peak temperature from 999.4 °C in the HT-DSC signal to 1008.5 °C in the $C_p(T)$ curve results from the increased sample mass and the higher heating rate in the C_p trials [53]. The same relation applies for the increase of the Curie temperature ($\Delta T \sim 6.4$ °C). On the other hand, it was still not possible to improve the resolution of the onset for alloy B-II with higher phosphorus content, see Fig. 4 (b). Hence, even specific adjustments to the presently used DSC setup do not

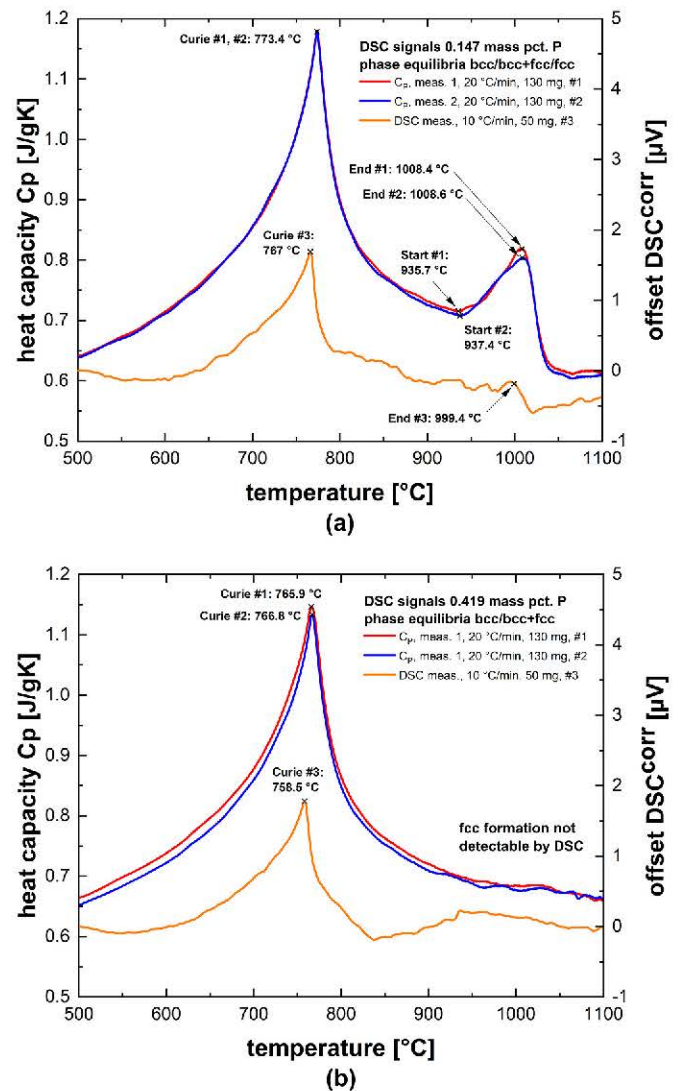


Fig. 4. Obtained heat capacity curves along with the DSC signal from Chapter 3.2.1 for alloy A-IV with 0.147 mass pct. P (a) and alloy B-II with 0.419 mass pct. P (b). The DSC signals were corrected to the baseline of 0 μ V.

guarantee the accurate characterization of the fcc formation over the whole composition range of the Fe-P γ -loop. Another limit of the current C_p method is the maximum temperature of 1250 °C. The PtRh/Al₂O₃ crucibles are generally approved up to the temperature of 1700 °C but sticking of the crucible and the sensor was observed at $T > 1250$ °C in some pre-experiments which may lead to serious damage to the sensor. Furthermore, the permanent recalibration of the DSC setup with different crucibles is not efficient in daily standard practice. The authors therefore decided to focus on optimizing the HT-DSC settings for a better resolution of the peak temperature at the bcc + fcc \leftrightarrow bcc phase boundary and propose HT-LSCM as a valuable supportive tool to characterize the fcc formation in the Fe-P γ -loop (see Chapter 3.3).

3.2.3. Modification of the HT-DSC settings for γ -loop studies

Three main factors influence the evolution of the DSC signal [53]: The sample mass, the heat change during the phase transformation and the heating rate (HR) applied during scanning. A small sample mass provides the advantage of a sharp peak separation and high sensitivity of the signal but decreases the intensity (peak height) of the heat flux. Small sample masses are highly beneficial if a large amount of heat is released/absorbed during the phase transformation (e.g. solid-liquid transformations). Increasing the HR will intensify the signal but usually shifts the peak temperature to higher values. Particularly in the case of large changes in heat (> 200 J/g), the DSC signal has to then be corrected within an HR variation in order to obtain the equilibrium value at an HR of 0 °C/min. [59] It has been pointed out in references [10, 51] that for the present DSC equipment, a heating rate of 10 °C/min and 50 mg samples are suitable parameters to determine highly accurate temperatures of melting equilibria and peritectic phase transformations in Fe-based alloy systems. As the HR of 10 °C/min is in agreement with the generally accepted values from literature [59], the authors decided to adjust the sample mass and increase it from 50 mg to 250 mg. The DSC signals for measurements with both sample masses are shown in Fig. 5 by taking the example of alloy C-I (0.394%P, as-cast). Note that as the onset in the temperature range of 850–1050 °C (bcc \leftrightarrow bcc + fcc) was still not detectable in the signal, only the evolution of the peaks is represented. The peak intensity of the signal is significantly increased with 250 mg sample mass, and a clear end of the phase transformation at 1291.6 ± 2 °C is visible. Although the determined phase transformation temperature of 1294.4 ± 2 °C with the 50 mg sample is in reasonable agreement with the value of the 250 mg samples, the evaluation of the peak is not reliable and shows poor reproducibility. The delay of the

signal due to the higher sample mass [53] is negligible since only a small change in heat is observed during the phase transformation. Furthermore, the temperature difference between the 50 mg and 250 mg samples is within the typical experimental error of ± 5 °C [10]. Based on the parameters evaluated, the DSC setting of 10 °C/min and 250 mg was applied for the measurements in the present study.

3.3. High-temperature laser scanning confocal microscopy (HT-LSCM)

High-temperature laser scanning confocal microscopy (HT-LSCM) has become an established tool to perform in-situ observations of microstructural changes by combining laser scanning confocal optics and an infrared heating furnace. The special experimental setup allows high-resolution images up to temperatures of the liquid state to be recorded. For detailed information on the HT-LSCM technique, the authors refer to the literature [60–64]. In the present study, the experiments were carried out in an HT-LSCM type VL2000DX-SVF17SP from Lasertec. Small samples of $5 \times 5 \times 1.5$ mm³ were cut from alloys listed in Table 2; the specimens were ground and polished. Within the HT-LSCM examinations, the samples were put on the sample holder in the gold coated, elliptical HT furnace. The furnace chamber was evacuated and flushed with Ar 5.0. All samples were heated at 600 °C/min to 850 °C followed by 15 min of isothermal holding, after which the phase transformations (bcc \leftrightarrow bcc + fcc \leftrightarrow fcc for samples A-I to A-IV; bcc \leftrightarrow bcc + fcc \leftrightarrow bcc for samples B-I to C-I) were investigated with a heating rate of 10 °C/min, equivalent to the DSC measurements in Chapter 3.2. The final temperature for samples A-I to A-IV was defined at 1050 °C and 1400 °C for B-I to C-I, respectively. After reaching the maximum temperature, controlled cooling to room temperature was performed with a defined cooling rate of -400 °C/min (Ar atmosphere). The temperature in the furnace chamber was controlled using a type S thermocouple located at the bottom of the sample holder. In order to obtain accurate temperatures on the sample surface, a temperature referencing procedure had to be carried out before each experimental campaign using an external thermocouple welded to the test sample surface. A video with a maximum frame rate of 60/s was recorded throughout the experiment, enabling the examination of microstructural changes and occurring phase transformations post-experimentally. Using the recorded videos, the phase transformation starting and finishing temperatures could be determined optically as all microstructural changes had become clearly visible due to the thermal etching effect [65,66].

First HT-LSCM experiments executed in this study showed that the start and further progress of the fcc formation (bcc \leftrightarrow bcc + fcc) appears slowly. Nevertheless, the proceeding fcc formation was clearly observable in the HT-LSCM, where in the DSC signal, no deviation from the baseline was detectable in this case. In order to guarantee the comparability of the results between the alloys investigated, it was essential to establish a standardized evaluation method for the HT-LSCM observations. This method should also exclude local microstructure phenomena when heating the sample (e.g. fcc formation on a single bcc phase boundary area) and in doing so, give values for the phase transformation temperature representative of the whole field of observation as well as for the bulk material. Therefore, the authors have followed a procedure that combines the optical observation received in the HT-LSCM with the generally accepted concept in examining signals of thermo-analytical techniques: To define an onset/end of a phase transformation in the course of the measured curve [53]. The approach of transferring the optical observation from the HT-LSCM systematically into a numerical value of phase fractions is presented for sample C-I (0.394%P, as-cast) in Fig. 6. For each experiment, more than five pictures were taken that represent the temperature range in which about 20% of the fcc area fraction had formed on the surface. Selected micrographs from the HT-LSCM experiment are shown in Fig. 6 a-I to c-I. The phase boundaries were then traced using image processing software, enabling a coloring of the apparent fcc and bcc phases in each HT-LSCM frame (Fig. 6 a-II to c-II). In the present paper, blue accounts for all surface areas

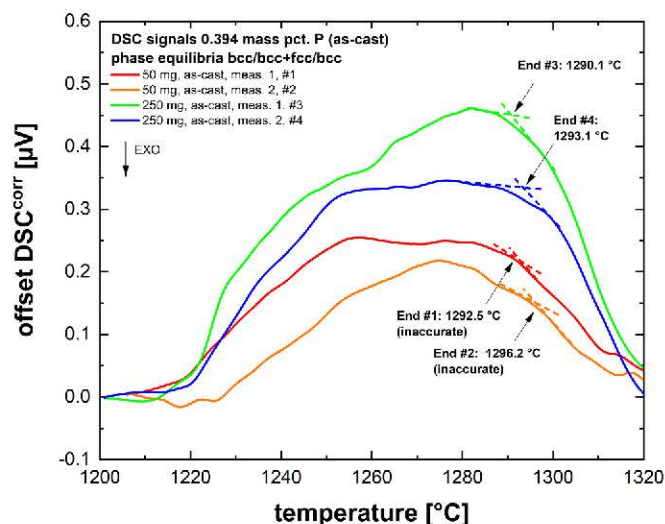


Fig. 5. Influence of the sample mass on the evolution of the DSC signal for sample C-I (0.394%P, as-cast). The signals were corrected to the baseline of 0.0 μ V.

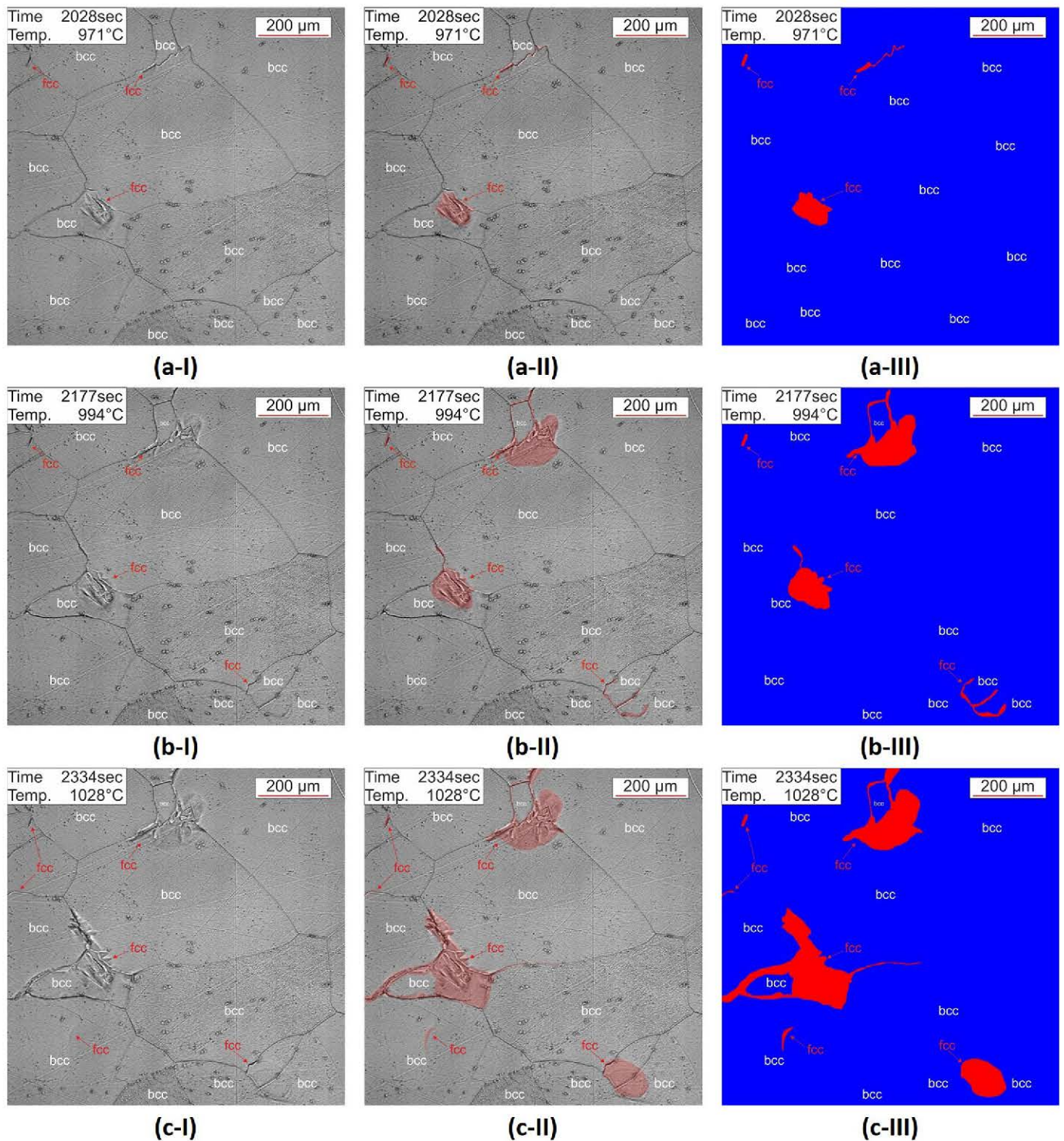


Fig. 6. HT-LSCM micrographs of $bcc \leftrightarrow bcc + fcc$ phase transformation for sample C-I (0.394%P, as-cast) at temperatures of 971 °C (a-I), 994 °C (b-I) and 1028 °C (c-I); highlighted fcc regions at temperatures of 971 °C (a-II), 994 °C (b-II) and 1028 °C (c-II); colored micrographs for the image analysis procedure with fcc (red) and bcc (blue) at temperatures of 971 °C (a-III), 994 °C (b-III) and 1028 °C (c-III); (For interpretation of the references to colour in this figure legend, the reader is referred to the web version of this article.)

representing bcc and red for fcc, respectively. The final, bicolored images as displayed in Fig. 6 a-III to c-III were transferred into the automated image analysis software Clemex Vision 7.0 PE (Clemex Technologies Inc., Canada) to evaluate the percentage of all blue bcc and red fcc areas based on a colour-threshold routine. The same procedure was done vice versa to define the end of the phase transformation

(Fig. 7).

The numerical values of fcc and bcc area fractions obtained from digital image processing can be plotted depending on temperature, as shown in Fig. 8. A first small amount of fcc (~ 1%) forms at 971 °C, whereas up to the temperature of 994 °C, only ~3% fcc are present. Above 1000 °C, the fcc area fraction increases rapidly from ~7% at

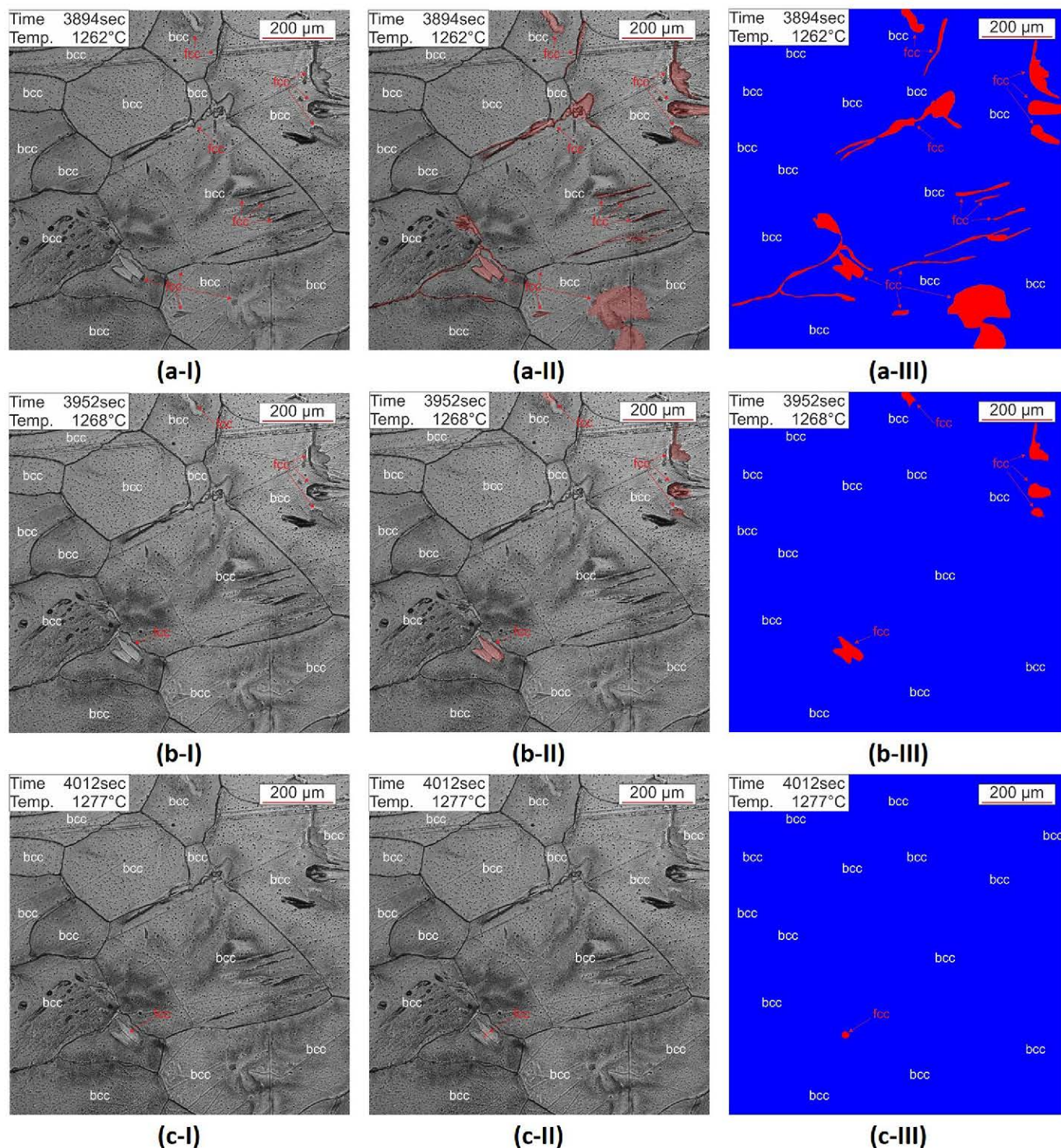


Fig. 7. HT-LSCM micrographs of $\text{bcc} + \text{fcc} \leftrightarrow \text{bcc}$ phase transformation for sample G-I (0.394%P, as-cast) at temperatures of 1262 °C (a-I), 1268 °C (b-I) and 1277 °C (c-I); highlighted fcc regions at temperatures of 1262 °C (a-II), 1268 °C (b-II) and 1277 °C (c-II); colored micrographs for the image analysis procedure with fcc (red) and bcc (blue) at temperatures of 1262 °C (a-III), 1268 °C (b-III) and 1277 °C (c-III); (For interpretation of the references to colour in this figure legend, the reader is referred to the web version of this article.)

1028 °C to 15% at 1043 °C and reaches the maximum evaluated amount of 33% fcc at 1090 °C. Based on the results, tangents were applied to determine the beginning of the phase transformation. The final result of 994 °C is in reasonable agreement with data of similar chemical composition from Lorenz and Fabritius [26] (975 °C at 0.41%P) and Fischer et al. [28] (1000 °C at 0.37%P) and indicates that the corresponding fcc amount of ~2–3% can be considered as a representative

area fraction of onset temperatures in the present HT-LSCM experiments. However, as the onset construction is generally dependent on the tangents applied and the fcc formation starts slowly (3% area fraction within 20 °C), the authors suggest a typical deviation of ± 10 °C in determining the $\text{bcc} \leftrightarrow \text{bcc} + \text{fcc}$ phase transformation temperature when employing HT-LSCM. In contrast to the start of the phase transformation, its end is very clearly pronounced in Fig. 8 due to the good

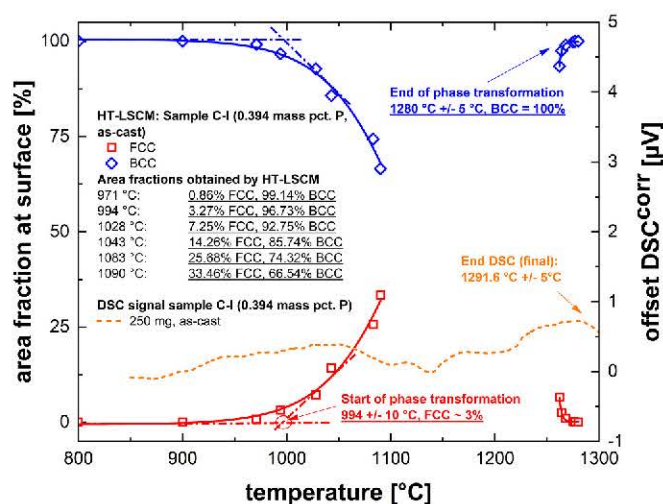


Fig. 8. Construction of onset and end of the investigated phase transformations by HT-LSCM for sample C-I (0.394%P, as-cast) along with the DSC signal of sample C-I (corrected to the baseline of 0.0 μV).

kinetics at elevated temperatures and the rapid dissolution of the fcc phase in a close temperature interval of 10 °C. Without a tangent construction, the final value of 1280 °C \pm 5 °C can be assigned to a 0% fcc area fraction. For comparison, the DSC signal of alloy C-I (Chapter 3.2.3) is plotted in Fig. 8. It is evident that by using HT-LSCM, the accuracy in determining the fcc formation could be significantly improved. Finally, the good agreement with the results of DSC analysis of the fcc decomposition (1291.6 °C) confirms the approach presented that will be applied for the overall phase boundary construction in Chapter 4.2.

3.4. High-temperature X-ray diffraction (HT-XRD)

In the present study, two kinds of experiments were carried out using sample C-I (0.394%P, hot-pressed): (i) the determination of the phase transformation temperatures (bcc \leftrightarrow bcc + fcc and bcc + fcc \leftrightarrow bcc) in the temperature range of 850–1350 °C for the evaluation of the results obtained by DSC and HT-LSCM (Chapter 4.1) and (ii) the quantitative phase fraction analysis by Rietveld refinement of fcc and bcc at 1050 °C, 1100 °C and 1150 °C (Chapter 4.3). The latter experiments also included the measurement of the bcc \leftrightarrow bcc + fcc phase transformation temperature during heating. Within all HT-XRD experiments, a heating rate of 30 °C/min was selected up to 850 °C and a subsequent isothermal holding time of 15 min was defined. Following DSC and HT-LSCM, the measurements were performed with a heating rate of 10 °C/min up to the final temperature. The layer surface after the in-situ heating investigation was inspected by conventional optical microscopy.

For the XRD experiments, various samples of polished platelets measuring $7 \times 25 \times 0.3 \text{ mm}^3$ were cut in different orientations from the original material. The aim of the preliminary XRD experiments at room temperature was a general sample screening in respect of texture (preferred crystallite orientation) and crystallite size. Pronounced texture and a large crystallite size can inhibit a precise quantitative phase analysis. This investigation was performed on a D8Discover diffractometer in parallel beam geometry (parallel polycapillary optics) with an energy-sensitive Sol-X point detector (Bruker, Germany). The experiments were conducted using MoK α radiation corresponding to a wavelength of 0.7093 Å in a diffraction angle range of 15–60°2 θ , a step size of 0.05° and a counting time of 9 s/step. Each sample was measured at two different azimuthal angles ($\varphi = 0^\circ, 90^\circ$). If the diffraction intensities differed strongly between these measurements, the sample was rejected for further in-situ investigation.

The subsequent in-situ HT-XRD experiments for the phase analysis at various temperatures were carried out in a D8Advance diffractometer

(Bruker, Germany) using the focusing Bragg-Brentano diffraction geometry. This instrument was equipped with primary and secondary soller slits. A molybdenum anode X-ray tube at 40 kV and 40 mA (also MoK α radiation, linear focus) was used as a radiation source. For the suppression of the Mo K β radiation, a Zr filter was inserted. The detection of the diffraction intensity was performed by a 1D position-sensitive detector (LynxEye also by Bruker, Germany) based on silicon strip technology (192 strips with a width of 0.075 mm). Considering a goniometer radius of 250 mm, the detector length is equal to a diffraction angle range of 3.3° in total in the setting used.

Each measured in-situ diffractogram used for the full Rietveld refinement included 1788 measurement steps altogether. They were recorded in the range of 17.5–60°2 θ with a step size of 0.024° and a counting time of 2 s/step corresponding to an integrated exposure time for each detector strip of 384 s. For the in-situ measurements, a high-temperature reaction stage HTK 2000 MSW (manufactured by Anton Paar, Austria) was attached to the diffractometer. All experiments described were performed under vacuum with a pressure of 0.001 to 0.0001 Pa (10^{-5} to 10^{-6} mbar). A rectangular molybdenum strip (10 mm width, 100 mm length) was used as a sample holder, the strip being only 8 mm wide in the center to obtain the highest electrical resistance corresponding to the highest temperature caused by Joule heating in the precise sample position. The corresponding low sample height error of the device at elevated temperature was between 40 and 60 μm . However, this parameter was refined during the Rietveld procedure. The temperature measurements were conducted with thermocouples type S (Pt/Pt-Rh10) and type D (WRe3/W-Re25). For the Rietveld refinements of the cell parameters, the TOPAS 5 software (Bruker AXS, Germany, 1999–2014) was used. For the phase transformation recording, a smaller diffraction angle range (17.5–23°2 θ) was selected to achieve a shorter scan time. The corresponding phase content was determined by the individual diffraction peak intensity.

3.5. Dilatometry (DIL)

The thermal expansion behavior of the sample C-I (0.394 mass pct. P) was investigated by means of a push-rod (corundum) dilatometer (type DIL805L/A quenching dilatometer manufactured by Bähr, Germany). The experiments were performed under vacuum with a corresponding pressure lower than 0.035 Pa (3.5×10^{-4} mbar). The sample was heated up to 850 °C with a heating rate of 30 °C/min followed by isothermal treatment for 15 min. The phase transformations were examined applying a heating rate of 3 °C/min. The dilatation behavior of the octagonal sample with 6 mm circumference diameter and 14 mm length was measured up to a temperature of 1380 °C.

4. Results and discussion

All phase diagram calculations in the present chapter were performed with the thermochemical software FactSage 8.0 [2]. The thermodynamic assessments of Shim et al. [11], Miettinen and Vassilev [12], You and Jung [13] and M. Bernhard et al. [14] were used for the comparison with the experimental results.

4.1. Determination of phase transformation temperatures for alloy C-I (0.394%P, hot-pressed) using DSC and HT-LSCM and the comparison with in-situ HT-XRD and DIL

Similar to the DSC analysis of sample C-I in the as-cast structure (Chapter 3.2.3), it was not possible to detect the beginning of the bcc \leftrightarrow bcc + fcc transformation by increasing the sample mass from 50 mg to 250 mg. However, the end of the phase transformation (bcc + fcc \leftrightarrow bcc) is clearly visible and the average value of two independent measurements is given as 1292.6 ± 2 °C. In the HT-LSCM, the first fcc formation was obtained at 974 °C; close to 1000 °C, the fcc area fraction significantly increased and the amount of fcc exceeded 10% at 1028 °C. The

onset construction results in a $\text{bcc} \leftrightarrow \text{bcc} + \text{fcc}$ phase transformation temperature of 1000 °C, corresponding to an fcc area fraction of ~2%, representative of the field observation (see Chapter 3.3). The $\text{bcc} + \text{fcc} \leftrightarrow \text{bcc}$ transformation is completed at 1285 °C. By comparing the phase transformation temperatures obtained for C-I in as-cast state (DSC 1291.6 °C, HT-LSCM 994 °C and 1280 °C) and C-I with hot-pressed recrystallized microstructure (DSC 1292.6 °C, °C, HT-LSCM 1000 °C and 1285 °C), excellent agreement between both samples is shown. Hence, the influence of the microstructure on the determined equilibrium phase transformation temperatures can be excluded.

The results of the in-situ HT-XRD measurements are graphically represented in Fig. 9 (a) - (c). The contour plot in Fig. 9 (a) shows the recorded diffraction intensity in the range between 17.5 and 23°2 θ for the temperature range of 850–1350 °C. The diffraction maximum 100 of the α -phase (bcc) at 19.9° as well as the diffraction peaks 111 at 19.4° and 200 at 22.5°2 θ of the γ -phase (fcc) can be clearly identified. The general shift of all diffraction peaks observed towards smaller diffraction angles, or larger lattice spacings, corresponds to the thermal expansion of the crystal lattice. The striking bimodal maximum observed at all peaks is obviously caused by the MoK α 1 α 2 (designation according to the Siegbahn notation) splitting of the X-ray emission lines. In this plot, the γ -phase formation ($\text{bcc} \leftrightarrow \text{bcc} + \text{fcc}$ transformation) can be roughly localized to the range of 950°–1000 °C. The γ -phase disappears near

1260 °C ($\text{bcc} + \text{fcc} \leftrightarrow \text{bcc}$). Above 1275 °C, an intermediate restructuration and subsequent disintegration reaction of the α -phase is observed. This restructuration is most likely related to an enhanced grain growth and an induction of internal residual stresses in the grains. In Fig. 9 (b), the integrated areas of the diffraction maxima 111 and 200 of the γ -phase correspond to a quantification of the diffraction intensity, and the plot of the diffraction intensities as a function of temperature enables the onset/endset temperatures to be constructed similarly to the HT-LSCM analysis in Chapter 3.3. The $\text{bcc} \leftrightarrow \text{bcc} + \text{fcc}$ transformation temperatures of 977 °C and 976 °C are in reasonable agreement with the first observation of fcc formation in the HT-LSCM (974–1000 °C). The difference between the HT-XRD results and the finally determined HT-LSCM value of 1000 °C is acceptable for the onset: As for the optical evaluation of the fcc area fraction by HT-LSCM, the increase in the diffraction intensity also appears slowly in the HT-XRD experiment. In the case of the $\text{bcc} + \text{fcc} \leftrightarrow \text{bcc}$ transformation, the values of 1258 °C and 1262 °C obtained by HT-XRD are shifted towards lower temperatures (ΔT DSC ~ 30 °C, ΔT HT-LSCM ~ 25 °C). In this case, minor restructuration processes in the material can occur without a clear relation to a strictly coherent crystal lattice change. In Fig. 9 (c), the same experimental data of sample C-I are displayed in a conventional stacked plot for selected temperatures to give a more detailed view of the diffraction peak width and peak shape.

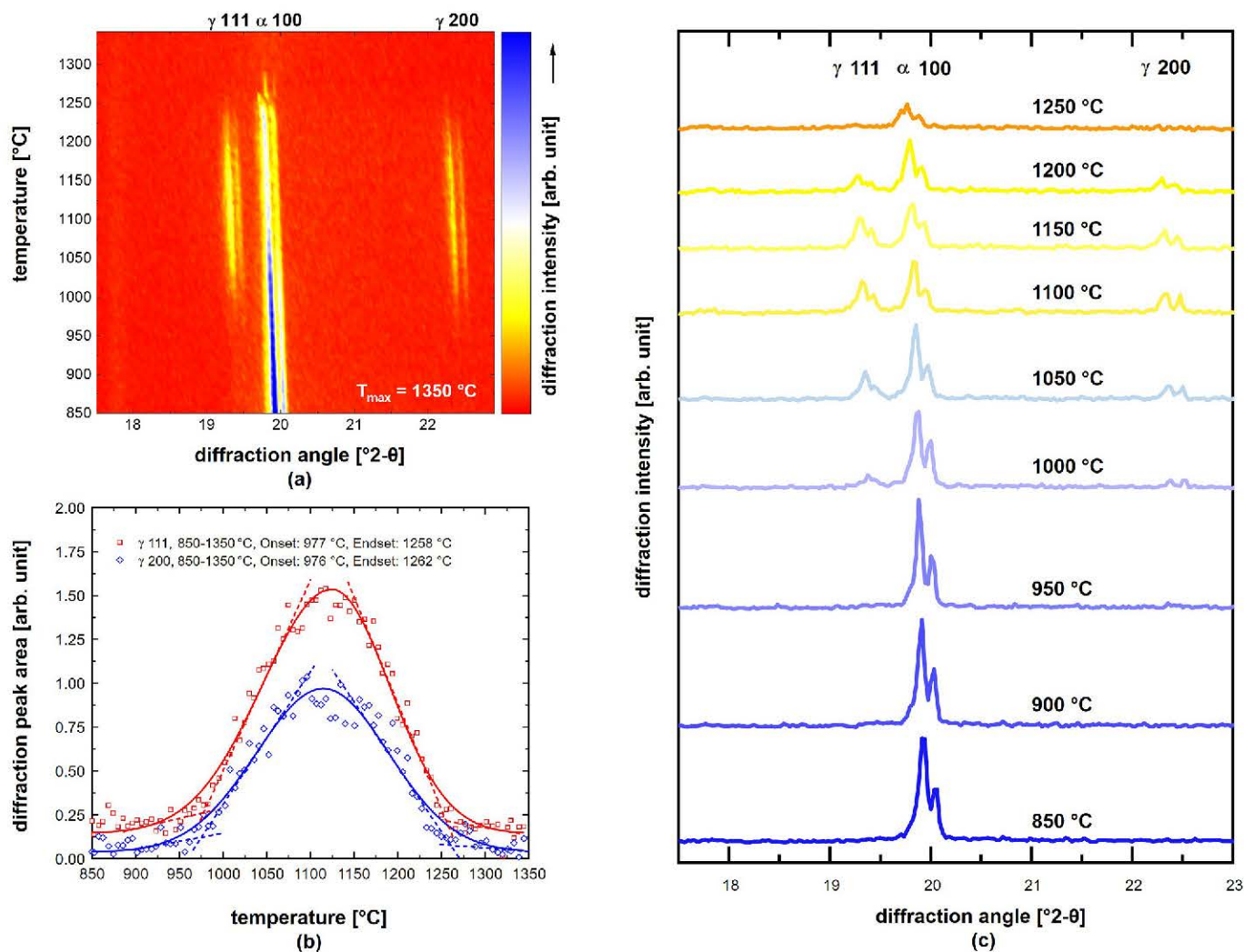


Fig. 9. In-situ HT-XRD analysis of sample C-I (0.394%P, hot-pressed) in the temperature range of 850–1350 °C; 2D contour plot of diffraction intensities over temperature and diffraction angle (a), integrated diffraction peak areas of γ 111 and γ 200 depending on temperature (b) and diffractograms at selected temperatures (c).

In Fig. 10, the dilatation during the dilatometer heating experiment is plotted as a function of the temperature. Several deviations from the linear behavior are observed. The abrupt increase at 850 °C can be assigned to the isothermal holding time of 15 min defined in the temperature program. The first deviation from the adapted tangent at 976 °C indicates the fcc formation; the temperature agrees excellently with the HT-XRD results. However, the enlarged section between 960 and 1010 °C in Fig. 10 indicates that for the dilatometer experiments, the accurate identification of the phase transformation temperature is also quite challenging. A clear deviation from the tangent is visible above 990 °C, which is in reasonable agreement with the temperatures observed by HT-LSCM (1000 °C). Similar to the beginning of the phase transformation, its end at 1260 °C is also hardly measurable in the dilatometer experiment in this case.

The comparative results of all in-situ techniques for alloy C-I (0.394%P) are summarized in Table 3. In all methods used, the exact determination of the first fcc formation in the Fe-P γ -loop is quite challenging. Regardless of the physical properties the in-situ experiments are based on, an increased error range has to be accepted. HT-LSCM observations indicate that this fact is not only a consequence of the experimental resolution related to the thermo-physical properties of fcc and bcc investigated during the phase transformation but also due to the slow increase in the fcc phase fraction itself. The highest resolution of the fcc formation was obtained by HT-LSCM and HT-XRD with a suggested error range of ± 10 °C whereas slightly larger errors are proposed for the present DIL study (± 20 °C). As expected from Chapter 3.2, the DSC technique used did not provide any information on the start of the bcc \leftrightarrow bcc + fcc phase transformation. DSC and HT-LSCM lead to the most reliable data (± 5 °C) for the fcc decomposition between 1250 and 1300 °C. The suggested error range of the HT-XRD experiments is similar to the measurement of the fcc formation. Within the DIL studies the end of the phase transformation was only weakly pronounced (± 20 °C). However, the DSC and HT-LSCM data are in very reasonable agreement with the HT-XRD and DIL studies. The differences in the phase transformation temperatures measured are in the range of ± 25 °C and are acceptable by taking into account the challenging analysis of each instrumental signal. The good agreement with the established methods of HT-XRD and dilatometry validates the present approach of using DSC and HT-LSCM to reconstruct the Fe-P γ -loop over the whole composition range.

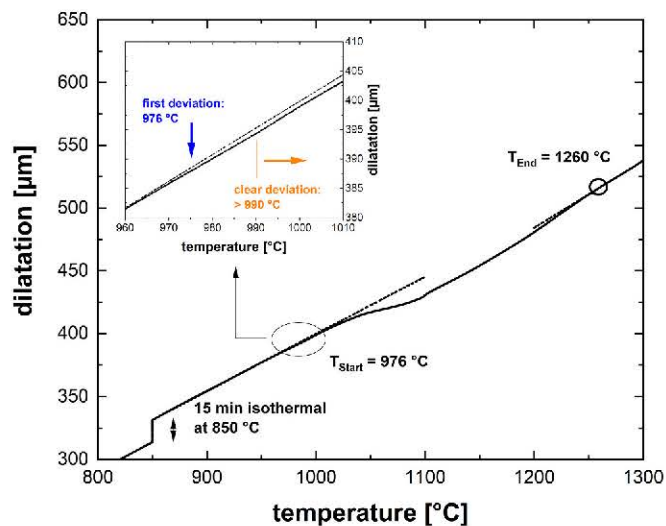


Fig. 10. Dilatometry results of sample C-I (0.394%P, hot-pressed) in the range of 800–1300 °C and enlarged part of the fcc formation between 960 and 1010 °C.

Table 3

Phase transformation temperatures of alloy C-I (0.394 mass pct. P, hot-pressed) determined in the present study along with suggested errors for each used in-situ method.

Phase boundary	DSC	HT-LSCM	HT-XRD	DIL
bcc \leftrightarrow bcc + fcc	–	1000 \pm 10 °C	976.5 \pm 10 °C	976 \pm 20 °C
fcc + bcc \leftrightarrow bcc	1292.6 \pm 5 °C	1285 \pm 5 °C	1260 \pm 10 °C	1260 \pm 20 °C

4.2. Reconstruction of the γ -loop phase boundaries by coupling HT-LSCM and DSC

The results of the phase transformation temperatures investigated by means of HT-LSCM and DSC are given in Table 4: ^{a)} denotes the temperature determined by DSC in this study (*) and the previous work of the authors [10]; values marked with ^{b)} were obtained by HT-LSCM; “n. m.” was not measurable by DSC; phase transformations marked “n.i.” were not investigated in this work by HT-LSCM; “–” indicates that the phase transformation does not exist in the phase diagram.

The calculated γ -loop [11–14] is shown in Fig. 11 along with the results of DSC and HT-LSCM and experimental data from literature [16,26,28]. It is evident that the thermo-magnetic analysis of Lorenz and Fabritius [26] correlates with the DIL and EQU-OM experiments conducted by Roquet and Jegaden [16]. In both studies, the stability of fcc is increased in comparison with the data of Fischer et al. [28]. The difference in the phase stability regions can be mainly attributed to the trace element level of the investigated alloys since even small amounts of fcc stabilizing elements (C, Mn, N) strongly affect the accuracy of the phase boundaries. The amounts of C, Mn and N reported by Fischer et al. [28] (C \leq 50 ppm, Mn \leq 10 ppm, N \leq 40 ppm) are significantly lower than those in the studies of Lorenz and Fabritius [26] (C \leq 130 ppm, Mn

Table 4

Phase transformation temperatures in the γ -loop of the binary Fe-P systems observed in the present study and previous work [10] using DSC and HT-LSCM.

Alloy	P [mass pct.]	bcc \leftrightarrow bcc + fcc [°C]	bcc + fcc \leftrightarrow fcc [°C]	fcc \leftrightarrow fcc + bcc [°C]	fcc + bcc \leftrightarrow bcc [°C]
A-I	0.026	n.m.	924.4 ^{a)} [10]	1389.4 ^{a)} [10]	1400.3 ^{a)} [10]
A-II	0.044	893 ^{b)} n.m.	948 ^{b)} 937.0 ^{a)} [10]	n.i. 1377.7 ^{a)} [10]	n.i. 1385.9 ^{a)} [10]
A-III	0.102	907 ^{b)} n.m.	958 ^{b)} 958.2 ^{a)} [10]	n.i. 1367.7 ^{a)} [10]	n.i. 1380.8 ^{a)} [10]
A-IV	0.147	892 ^{b)} n.m.	965 ^{b)} 999.4 ^{a)} [10]	n.i. 1341.9 ^{a)} [10]	n.i. 1359.0 ^{a)} [10]
B-I	0.322	944 ^{b)} n.m.	1000 ^{b)} –	n.i. –	n.i. 1320.2 ^{a)} [10]
B-II	0.419	977 ^{b)} n.m.	–	–	1306 ^{b)} 1272.4 ^{a)} [10]
B-III	0.480	984 ^{b)} n.m.	–	–	1298 ^{b)} 1290.2 ^{a)} 1280 ^{b)} [10]
C-I (as-cast)	0.394	n.m.	–	–	1291.6 ^{a)} 1280 ^{b)} [10]
C-I (hot-pressed)	0.394	n.m.	1000 ^{b)} –	–	1292.6 ^{a)} 1285 ^{b)} [10]

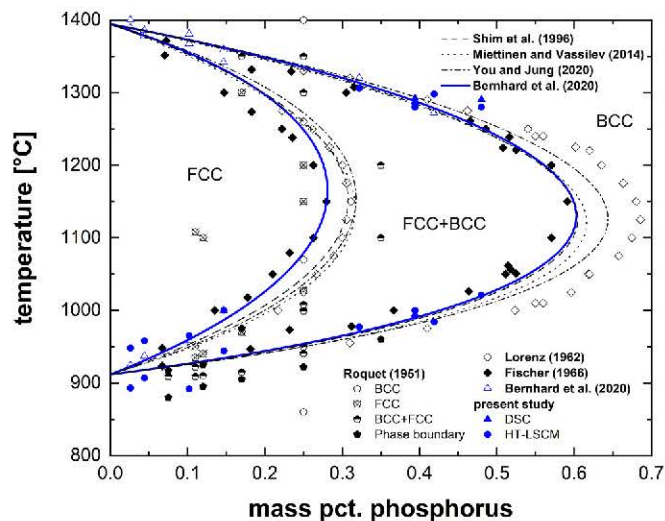


Fig. 11. Calculated γ -loop [11–14] along with results of DSC and HT-LSCM and experimental data from literature [16,26,28].

≤ 160 ppm, N ≤ 140 ppm) and Roquet and Jegaden [16] (C ≤ 250 ppm and Mn $\leq 0.40\%$). Hence, Fischer et al.'s [28] measurements are considered to be the most reliable for the critical evaluation of the present results.

In general, the phase transformation temperatures obtained by DSC and HT-LSCM are in reasonable agreement and the results can be summarized as follows:

- the phase boundary of the bcc \leftrightarrow bcc + fcc transformation is successfully reproduced by HT-LSCM, whereas it is not possible to provide reliable data using the present DSC technique. Excellent agreement with the data of Fischer et al. [28] is given for alloys B-IV to C-I containing P $\geq 0.147\%$. At low amounts of P, higher deviations in comparison with data from literature are identified. For samples A-I to A-III (0.026–0.102%P), the transformation temperatures obtained by HT-LSCM are 20 °C lower than the generally accepted value of pure iron (912 °C [67]). However, as demonstrated in Chapter 3.3, the constructed onset of the bcc \leftrightarrow bcc + fcc phase transformation shows a very slow increase in the fcc fraction at temperatures slightly above the phase boundary. Therefore, an increased error of ± 10 °C has to be accepted within the HT-LSCM measurements.
- the characterization of the bcc + fcc \leftrightarrow fcc phase boundary is possible by DSC and HT-LSCM. For samples A-III (0.102%P) and A-IV (0.147%P), both methods show similar results and are consistent with the work of Fischer et al. [28]. In the case of samples A-I (0.026%P) and A-II (0.044%P), the narrow temperature range of the bcc + fcc two-phase region leads to an overheating effect using HT-LSCM. Even at the low applied heating rate of 10 °C/min, the temperatures observed in the HT-LSCM are 25 °C higher than the values measured by DSC. It can be seen in Fig. 11 that the results of Fischer et al. [28] confirm the better resolution of the DSC technique for the accurate determination of the bcc + fcc \leftrightarrow fcc phase boundary.
- the fcc \leftrightarrow fcc + bcc \leftrightarrow bcc phase transformation was not investigated in the present study since it has already been demonstrated by M. Bernhard et al. [10] and Presoly et al. [51] that DSC and HT-LSCM are both excellent tools to identify the equilibrium temperatures in this case.
- the fcc + bcc \leftrightarrow bcc transformation (P $\geq 0.322\%$) was investigated employing both methods. The increased sample mass of 250 mg for DSC analysis enabled the identification of the phase transformation temperatures. Similar to the DSC method, the HT-LSCM observation also led to reliable results. Typical deviations between the DSC and

HT-LSCM results are ± 10 °C. Only for alloys B-II (0.419%P) was an increased deviation of 25 °C identified. However, both results agree well with the thermodynamic assessments [11–14] and the experimental data of Fischer et al. [28]. For sample B-III (0.48%P), DSC and HT-LSCM led to the same results, but the numerical value of the phase transformation temperature should be considered as critical since it does not correlate with the trend line of other results obtained in the present study. In addition, the temperatures determined are 25 °C higher compared with the experimental data from literature [26,28].

Based on the results, the authors suggest (i) the determination of the bcc \leftrightarrow bcc + fcc phase transformation using HT-LSCM, where a typical deviation of ± 10 °C has to be accepted; (ii) the higher resolution of the DSC method in characterizing the bcc + fcc \leftrightarrow fcc leads to more accurate results and is preferred over HT-LSCM; (iii) it has been shown in previous studies [10,51] that both methods are excellent tools to determine the fcc \leftrightarrow fcc + bcc \leftrightarrow bcc phase transformation temperatures. (iv) HT-LSCM accurately reproduces the bcc + fcc \leftrightarrow bcc phase boundary over the whole composition range. In the DSC analysis, a larger sample mass of 250 mg intensifies the measurement signal and similar results compared with those from using HT-LSCM were obtained. (v) with respect to thermodynamic calculations, all CALPHAD optimizations [11–14] lead to very reasonable results; the assessment of M. Bernhard et al. [14] excellently reproduces the Fe-P γ -loop measured by coupling DSC and HT-LSCM;

4.3. Quantitative phase fraction analysis of fcc and bcc by HT-XRD for alloy C-I (0.394%P, hot-pressed)

During heating, the beginning of the bcc \leftrightarrow bcc + fcc was measured according to the experimental procedure in Chapter 4.1. The temperature is given by the average value of three independent measurements as 981 ± 10 °C, which is in reasonable agreement with the single measurement in Chapter 4.1 (976 ± 10 °C). The fcc and bcc phase fractions measured by HT-XRD are summarized in Fig. 12 along with the calculated phase fractions using thermodynamic assessments from literature [11–14]. All modelling studies show a maximum fcc fraction close to 1150 °C, but the numerical values differ in the magnitude of 10% phase fraction. Compared to the work of M. Bernhard et al. [14] (64% fcc at 1146 °C), references [11–13] predict higher fcc fractions of 70–76% between 1133 °C and 1144 °C due to the increased stability of the fcc single-phase range in Fig. 11.

For comparison, data of Lorenz et al. [26] with a very similar chemical composition (0.41 mass pct. P) are plotted in Fig. 12. These data were indirectly derived from the experimental phase boundaries using the lever rule. A relative error of 10% in determining the fcc fraction was proposed [26]. Additionally, the authors addressed the fact that the higher impurity levels of fcc stabilizing elements in their samples (see also Section 4.2) shift the γ -loop to a higher P content. As a consequence, the proposed fcc fraction [26] is generally larger over the whole composition range compared to the present HT-XRD data and available thermodynamic assessments [11–14]. However, considering the relative error of 10% the data are in very reasonable agreement with the calculation results from references [11–13]. A rough estimation of the phase boundaries obtained was provided by Lorentz et al. [26] for a selected temperature. At 1125 °C, the original compositions of bcc (0.685 mass pct. P) and fcc (0.306 mass pct. P) were corrected by simple calculations to 0.557 mass pct. P (bcc) and 0.222 mass pct. P (fcc) for “pure” Fe-P alloys. In the present study, the corrected data at 1125 °C [26] were used to recalculate the fcc and bcc phase fraction for 0.394 mass pct. P, applying the lever rule. The results (51.34% fcc and 48.65% bcc) in Fig. 12 are in excellent agreement with the HT-XRD measurements in the temperature range of 1050–1150 °C (42.36% at 1050 °C, 50.71% at 1100 °C and 51.43% at 1150 °C). It can be seen in Fig. 12 that generally,

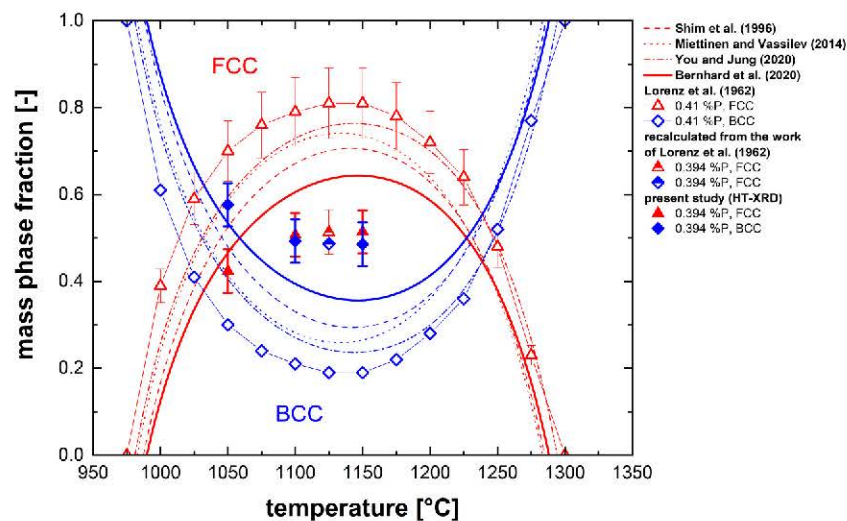


Fig. 12. Quantitative phase fraction analysis of fcc and bcc at 1050 °C, 1100 °C and 1150 °C for sample G-I (0.394 mass pct. P, hot-pressed) using HT-XRD along with experimental data from literature [26] and calculations with available thermodynamic assessments [11–14].

the HT-XRD data are lower than predicted by all calculations. Firstly, the phase fraction calculations are extremely sensitive to the individual optimization [11–14] of the fcc/bcc + fcc phase boundary in the Fe-P γ -loop. Moreover, it must be noted that the precision of the present quantitative in-situ HT-XRD evaluation by means of the Rietveld technique can be severely reduced by the anisotropic distribution of the crystallite orientation (i.e. texture). For specific diffraction maxima, the diffraction intensity discrepancy can reach factors up to one order of magnitude for a very pronounced texture. Besides, an enhanced crystallite growth can influence the correct phase content if the number of diffracting crystallites is not sufficiently large and single larger grains in diffracting orientation contribute to the peak intensity above average. However, as only a moderately pronounced texture was found in the preliminary XRD experiments (Chapter 3.4) and an averaging effect in analyzing more than one peak can be considered, a measurement error of 5% mass phase fraction is quite realistic. Taking into account the sensitivity of the calculation results and the experimental errors the HT-XRD data show good correlation with the assessment of M. Bernhard et al. [14].

5. Conclusion

The purpose of this study was the development of an experimental approach to reconstruct the phase boundaries in Fe-based γ -loops by coupling differential scanning calorimetry (DSC) and high-temperature laser scanning confocal microscopy (HT-LSCM). Eight alloys in the binary Fe-P system with varying P content from 0.026–0.48 mass pct. P were investigated in the temperature range of 850–1400 °C. Based on previous work of the authors [10], the experimental settings for the DSC setup used were adjusted in order to improve the accuracy of the DSC signal with respect to measuring bcc/fcc phase equilibrium temperatures. Using HT-LSCM, a standardized method for the characterization of solid-state transformations in the γ -loop is presented by transferring the optical observation from the HT-LSCM systematically into a numerical value of phase fractions over temperature. The results of the DSC and HT-LSCM experiments for a selected alloy (0.394%P) were critically evaluated with measurements using well-established dilatometry and HT-XRD techniques. A reasonable agreement between the phase transformation temperatures obtained in all kinds of in-situ experiments was demonstrated ($\Delta T_{\max} \sim 25$ °C). Based on the Fe-P γ -loop, a possible strategy to couple DSC and HT-LSCM in future applications for steel is illustrated in Fig. 13: Both methods provide an efficient way to determine the fcc \leftrightarrow fcc + bcc \leftrightarrow bcc phase transformation temperatures from

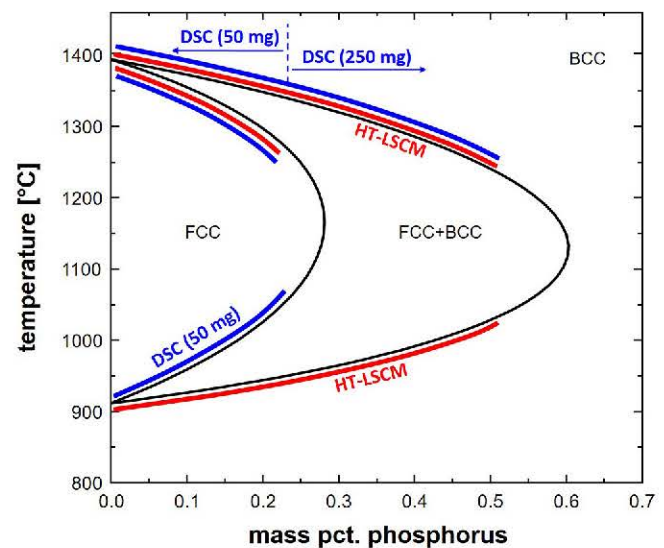


Fig. 13. Coupling DSC and HT-LSCM techniques to reproduce phase boundaries in the Fe-P γ -loop according to the present study.

1250 to 1450 °C and $P < 0.30\%$. [10,51]. If a bcc + fcc two-phase region exists over a wide temperature range ($P > 0.30\%$), increasing the sample mass from 50 mg to 250 mg intensifies the DSC signal and improves the accuracy for the determination of the bcc + fcc \leftrightarrow bcc phase transformation. In this case, HT-LSCM produces very similar results ($\Delta T = 5$ –20 °C). Unfortunately, it was not possible to determine the start of the bcc \leftrightarrow bcc + fcc phase transformation by DSC for any composition. HT-LSCM is a valuable tool for reconstructing this phase boundary considering a typical experimental error of ± 10 °C. For the investigation of the bcc + fcc \leftrightarrow fcc transformation between 900 and 1050 °C, the DSC method shows a high resolution in the signal measured and is favored over HT-LSCM.

Data availability

The raw/processed data required to reproduce these findings cannot be shared at this time due to technical or time limitations.

Declaration of Competing Interest

The authors declare that they have no known competing financial interests or personal relationships that could have appeared to influence the work reported in this paper.

Acknowledgment

The authors gratefully acknowledge the financial support under the scope of the COMET program within the K2 Center Integrated Computational Material, Process and Product Engineering (IC-MPPE) (Project No. 859480). This program is supported by the Austrian Federal Ministries for Climate Action, Environment, Energy, Mobility, Innovation and Technology (BMK) and for Digital and Economic Affairs (BMDW), represented by the Austrian research funding association (FFG), and the federal states of Styria, Upper Austria and Tyrol.

References

- [1] F. Wever, Ueber den Einfluß der Elemente auf den Polymorphismus des Eisens, *Arch. Eisenhuettenwes.* 2 (11) (1929) 739–748 (in German).
- [2] C. Bale, E. Béiste, P. Chartrand, S. Deckerov, G. Eriksson, A. Gheribi, K. Hack, I.-H. Jung, Y.-B. Kang, J. Melançon, A. Pelton, S. Petersen, C. Robelin, J. Sangster, P. Spencer, M.-A. van Ende, FactSage thermochemical software and databases (2010–2016), *Calphad* 54 (2016) 35–53.
- [3] P. Ghosh, R. Chromik, A. Knight, S. Wakade, Effect of metallurgical factors on the bulk magnetic properties of non-oriented electrical steels, *J. Magn. Magn. Mater.* 356 (2014) 42–51.
- [4] S. Lee, B. De Cooman, Effect of phosphorus on the magnetic losses of non-oriented 2% Si steel, *ISIJ Int.* 52 (6) (2012) 1162–1170.
- [5] I. Tanaka, H. Yashiki, Magnetic properties and recrystallization texture of phosphorus-added non-oriented electrical steel sheets, *J. Magn. Magn. Mater.* 304 (2006) e611–e613.
- [6] A. Moses, Electrical steels: past, present and future developments, in: *IEE Proceedings A (Physical Science, Measurement and Instrumentation, Management and Education)* vol. 137, 1990, pp. 233–245, no. 5.
- [7] M. Gomez, C. Garcia, D. Haezebrouck, A. Dardo, Design of Composition in (Al/Si)-alloyed TRIP steels, *ISIJ Int.* 49 (2) (2009) 302–311.
- [8] C. Bernhard, B. Linzer, P. Presoly, I. Watzinger, J. Watzinger, Evaluation of AHSS concepts with a focus on the product properties and appropriate casting characteristics of Arvedi ESP thin slab casters, *IOP Conf. Series: Mater. Sci. Eng.* 529 (2019) art. no. 012071.
- [9] L. Barbé, K. Verbeke, E. Wettinck, Effect of the addition of P on the mechanical properties of low alloyed TRIP steels, *ISIJ Int.* 46 (8) (2006) 1251–1257.
- [10] M. Bernhard, P. Presoly, N. Fuchs, C. Bernhard, Y.-B. Kang, Experimental study of high temperature phase Equilibria in the Iron-rich part of the Fe-P and Fe-C-P systems, *Metall. Mater. Trans. A* 51 (2020) 5351–5364.
- [11] J.-H. Shim, C.-S. Oh, D.-N. Lee, Thermodynamic properties and calculation of phase diagram of the Fe-P system, *J. Korean Inst. Metall. Mater.* 34 (11) (1996) 1385–1393.
- [12] J. Miettinen, G. Vassilev, Thermodynamic description of ternary Fe-X-P systems. Part 1: Fe-Cr-P, *J. Phase Equilib. Diffus.* 35 (2014) 458–468.
- [13] Z.M. You, I.-H. Jung, Critical evaluation and thermodynamic optimization of the Fe-P system, *Metall. Mater. Trans. B* 51 (2020) 3108–3129.
- [14] M. Bernhard, Y.-B. Kang, P. Presoly, A. Gheribi, C. Bernhard, Critical evaluation and thermodynamic modeling of the Fe-P and Fe-C-P system, *Calphad* 70 (2020) art. no. 101795.
- [15] Y. Zhan, Y. Du, Y. Zhuang, Determination of phase diagrams using equilibrated alloys, in: J. Zhao (Ed.), *Methods for Phase Diagram Determination*, Elsevier, Amsterdam, Netherlands, 2007, pp. 108–150.
- [16] P. Roquet, G. Jegaden, Contribution à l'étude du diagramme fer-phosphore: étude de l'essai dit du grain de phosphore, *Revue de Métallurgie* 48 (9) (1951) 712–721 (in French).
- [17] P. Roquet, G. Jegaden, J. Petit, The gamma loop in the Fe-Al system, *J. Iron Steel Inst.* 205 (4) (1967) 437–441.
- [18] C. Heijwegen, G. Rieck, Determination of the phase diagram of the Mo-Fe system using diffusion couples, *J. Less-Common Metals* 37 (1974) 115–121.
- [19] P. Alberry, C. Haworth, The solubility of Mo in gamma-iron, *Metal Sci.* 9 (1975) 140–149.
- [20] K.-I. Hirano, A. Hishinuma, Interdiffusion in α -solid solution of the Fe-Al system, *J. Jpn. Inst. Metals* 32 (6) (1968) 516–521.
- [21] G. Kirchner, T. Nishizawa, B. Uhrenius, The distribution of chromium between ferrite and austenite and the thermodynamics of the α/γ equilibrium in the Fe-Cr and Fe-Mn systems, *Metall. Mater. Trans. A* 4 (1973) 167–174.
- [22] G. Kirchner, H. Harvig, B. Uhrenius, Experimental and thermodynamic study of the equilibria between ferrite, austenite and intermediate phases in the Fe-Mo, Fe-W, and Fe-Mo-W systems, *Metal. Trans. A* 4 (1973) 1059–1067.
- [23] A. Kodentsov, G. Bastin, F. van Loo, Application of diffusion couples in phase diagram determination, in: J. Zhao (Ed.), *Methods for Phase Diagram Determination*, Elsevier, Amsterdam, Netherlands, 2007, pp. 222–245.
- [24] J. Crangle, Magnetic method for the determination of γ -loops in binary iron alloys and its application to the iron-silicon system, *Br. J. Appl. Phys.* 5 (4) (1954) 151–154.
- [25] E. Übelacker, Étude de la susceptibilité magnétique du fer pur et d'alliages fer-silicium avec détermination du diagramme de phases Fe-Si entre 0 et 10% at. de silicium, *Comptes Rendus* 261 (1965) 976–979.
- [26] K. Lorenz, H. Fabritius, Anwendung der magnetischen Waage zur Aufstellung von Zustandschaubildern im Bereich des festen Zustandes eisenreicher Systeme: Untersuchung am System Eisen-Phosphor, *Arch. Eisenhuettenw.* 33 (4) (1962) 269–275.
- [27] E. Baedeecken, W. Fischer, K. Lorenz, Untersuchungen über das Umwandlungsverhalten, die Kerbschlagzähigkeit und die Neigung zur interkristallinen Korrosion von Eisen-Chrom-Legierungen mit Chromgehalten bis 30%, *Stahl und Eisen* 81 (12) (1961) 768–778.
- [28] W. Fischer, K. Lorenz, H. Fabritius, A. Hoffmann, G. Kalwa, Untersuchung von Phasenumwandlungen in reinen Eisenlegierungen mit der magnetischen Waage, *Arch. Eisenhuettenw.* 37 (1) (1966) 79–86.
- [29] W. Fischer, K. Lorenz, H. Fabritius, D. Schlegel, Untersuchung der α/γ -Umwandlung in hochreinen Zweistofflegierungen des Eisens mit Molybdän, Vanadin, Wolfram, Niob, Tantal, Zirkon und Kobalt, *Arch. Eisenhuettenw.* 41 (5) (1970) 489–498.
- [30] S. Cui, I.-H. Jung, Critical reassessment of the Fe-Si system, *Calphad* 56 (2017) 108–125.
- [31] W. Xiong, An improved thermodynamic modeling of the Fe-Cr system down to zero kelvin coupled with key experiments, *Calphad* 35 (3) (2011) 355–366.
- [32] V. Witusiewicz, A. Bondar, U. Hecht, A. Theofilatos, N. Tsyganenko, S. Utkin, I. Tikhonova, Experimental study and thermodynamic re-modelling of the constitutive binaries and ternary B-Fe-Ti system, *J. Alloys Compd.* 800 (2019) 419–449.
- [33] The CALPHAD method, in: H. Ohtani, H. Cizichos, T. Saito, L. Smith (Eds.), *Springer Handbook of Materials Measurement Methods*, Springer, Berlin, 2006, pp. 1001–1030.
- [34] P. Spencer, A brief history of CALPHAD, *Calphad* 32 (1) (2008) 1–8.
- [35] F. Adecock, Alloys of iron research, part X. - the chromium-iron constitutional diagram, *J. Iron Steel Inst.* 124 (1931) 99–149.
- [36] G. Bente, W. Fishel, Gamma loop studies in the Iron-silicon and iron-silicon-titanium systems, *J. Metals* 8 (1956) 1345–1348.
- [37] K. Bungardt, E. Kunze, E. Horn, Untersuchungen über den Aufbau des Systems Eisen-Chrom-Kohlenstoff, *Arch. Eisenhuettenw.* 29 (3) (1958) 193–203.
- [38] T. Wada, Austenite loop in Iron-titanium system, *J. Jpn. Inst. Metals* 27 (3) (1963) 119–121.
- [39] P. Oberhoffer, C. Kreuzer, Contributions to the systems iron-silicon, iron-chromium and iron-phosphorus, *Arch. Eisenhuettenw.* 2 (7) (1929) 449–456.
- [40] E. Speight, The gamma loop in the iron-tin system, *Metal Sci. J.* 6 (1972) 57–60.
- [41] M. Wiessner, P. Angerer, P. Prevedel, K. Skalnik, S. Marsoner, R. Ebner, Advanced X-ray diffraction techniques for quantitative phase content and lattice defect characterization during heat treatment of high speed steels, *Berg-Huettenmann. Monatsh.* 159 (2014) 390–393.
- [42] M. Wiessner, E. Gamsjäger, S. van der Zwaag, P. Angerer, Effect of reverted austenite on tensile and impact strength in a martensitic stainless steel - in-situ X-ray diffraction study, *Mater. Sci. Eng. A* 682 (2017) 117–125.
- [43] M. Wiessner, P. Angerer, Bayesian approach applied to the Rietveld method, *J. Appl. Crystallogr.* 47 (2014) 1819–1825.
- [44] D. Phelan, M. Reid, R. Dippenaar, Kinetics of the peritectic phase transformation: in-situ measurements and phase field modeling, *Metall. Mater. Trans. A* 37 (2006) 985–994.
- [45] S. Griesser, C. Bernhard, R. Dippenaar, Effect of nucleation undercooling on the kinetics and mechanism of the peritectic phase transition in steel, *Acta Mater.* 81 (2014) 111–120.
- [46] S. Griesser, C. Bernhard, R. Dippenaar, Mechanism of the peritectic phase transition in Fe-C and Fe-Ni alloys under conditions close to chemical and thermal equilibrium, *ISIJ Int.* 54 (2) (2014) 466–473.
- [47] S. Griesser, M. Reid, C. Bernhard, R. Dippenaar, Diffusional constrained crystal nucleation during peritectic phase transitions, *Acta Mater.* 67 (2014) 335–341.
- [48] K. Hechu, C. Slater, B. Santillana, S. Clark, S. Sridhar, A novel approach for interpreting the solidification behaviour of peritectic steels by combining CSLM and DSC, *Mater. Charact.* 133 (2017) 25–32.
- [49] Z. Liu, Y. Kobayashi, J. Yang, K. Nagai, M. Kuwabara, In-situ observation of the δ/γ -phase transformation on the surface of low carbon steel containing phosphorus at various cooling rates, *ISIJ Int.* 46 (6) (2006) 847–853.
- [50] P. Presoly, R. Pierer, C. Bernhard, Linking up of HT-LSCM and DSC measurements to characterize phase diagrams of steels, *IOP Conf. Series (MCWASP XIII) - Mater. Sci. Eng.* 33 (2012) art. no. 012064.
- [51] P. Presoly, R. Pierer, C. Bernhard, Identification of defect prone Peritectic steel grades by analyzing high-temperature phase transformations, *Metall. Mater. Trans. A* 44 (2013) 5377–5388.
- [52] A. Normanton, Calorimetric study of the γ -loop region of the iron-chromium system, *Faraday Symp. Chem. Soc.* 8 (1973) 52–55.
- [53] W. Boettinger, U. Kattner, K.-W. Moon, J. Perepezko, DTA and heat-flux DSC measurements of alloy melting and freezing, in: *NIST Recommended Practice Guide 960-15, Special Publication*, 2006.
- [54] G.P. Krielaart, C.M. Brakman, S. Van der Zwaag, Analysis of phase transformation in Fe-C alloys using differential scanning calorimetry, *J. Mater. Sci.* 31 (1996) 1501–1508.

- [55] V.T. Witusiewicz, F. Sommer, E.J. Mittemeijer, Enthalpy of formation and heat capacity of Fe-Mn alloys, *Metall. Mater. Trans. B Process Metall. Mater. Process. Sci.* 34 (2003) 209–223.
- [56] ASTM E1269–11, Standard Test Method for Determining Specific Heat Capacity by Differential Scanning Calorimetry, ASTM International, West Conshohocken, PA, 2011, <https://doi.org/10.1520/E1269-11>.
- [57] B. Wlthan, Uncertainty budget for high temperature heat flux DSCs, *J. Therm. Anal. Calorim.* 118 (2014) 603–611.
- [58] D.A. Ditmars, S. Ishihara, S.S. Chang, G. Bernstein, Enthalpy and heat-capacity standard reference material: synthetic sapphire (α -Al₂O₃) from 10 to 2250 K, *J. Res. Natl. Bur. Stand.* 87 (2) (1982) 159–163.
- [59] L. Chapman, Application of high temperature DSC technique to nickel based superalloys, *J. Mater. Sci.* 39 (2004) 7229–7236.
- [60] M. Reid, D. Phelan, R. Dippenaar, Concentric solidification for high temperature laser scanning confocal microscopy, *ISIJ Int.* 44 (3) (2004) 565–572.
- [61] C. Bernhard, S. Schider, A. Sormann, G. Xia, S. Ilie, First results of the high-temperature laser scanning confocal microscope at the montanuniversitaet leoben, *Berg-Huettenmaenn. Monatsh.* 156 (2011) 161–167.
- [62] S. Griesser, R. Dippenaar, Enhanced concentric solidification technique for high-temperature laser-scanning confocal microscopy, *ISIJ Int.* 54 (3) (2014) 533–535.
- [63] N. Fuchs, P. Krajewski, C. Bernhard, In-situ observation of austenite grain growth in plain carbon steels by means of high-temperature laser scanning confocal microscopy, *Berg-Huettenmaenn. Monatsh.* 160 (2015) 214–220.
- [64] N. Fuchs, C. Bernhard, S. Michelic, R. Dippenaar, HT-LSCM as a tool for indirect determination of precipitates by real-time grain growth observations, in: TMS 2020 149th Annual Meeting & Exhibition Supplemental Proceedings, 2020, pp. 47–55.
- [65] E. Rabkin, L. Klinger, The fascination of grain boundary grooves, *Mater. Sci. Technol.* 7 (17) (2001) 772–776.
- [66] C. Garcia de Andrés, F. Caballero, C. Capdevila, D. San Martín, Revealing austenite grain boundaries by thermal etching: advantages and disadvantages, *Mater. Charact.* 49 (9) (2002) 121–127.
- [67] American Society for Metals, *Metals Handbook, Volume 2 Properties and Selection: Nonferrous Alloys and Pure Metals*, 9th edition, Metals Park, Ohio, United States, 1979.

Paper IV

An assessment of analytical liquidus equations for Fe-C-Si-Mn-Al-P alloyed steels using DSC/DTA techniques

M. Bernhard, P. Presoly, C. Bernhard, S. Hahn and S. Ilie

Metallurgical and Materials Transactions B, 2021.

Abstract: Analytical liquidus equations were evaluated using differential scanning calorimetry (DSC) and differential thermal analysis (DTA). Results of 180 measurements in the Fe-C-Si-Mn-Al-P subsystems were considered, where the experimental methodology was demonstrated for four alloys in the Fe-Si-Mn-Al system. Excellent agreement between the DSC/DTA dataset and the most recently published equation was found (error 2.1 ± 1.6 °C). For this equation, suggested modifications of phosphorus parameters will help to improve calculations for P-alloyed steels.

Used and reprinted under the Creative Commons Attribution 4.0 International License

An Assessment of Analytical Liquidus Equations for Fe-C-Si-Mn-Al-P-Alloyed Steels Using DSC/DTA Techniques



MICHAEL BERNHARD, PETER PRESOLY, CHRISTIAN BERNHARD,
SUSANNE HAHN, and SERGIU ILIE

Analytical liquidus equations were evaluated using differential scanning calorimetry (DSC) and differential thermal analysis (DTA). Results of 180 measurements in the Fe-C-Si-Mn-Al-P subsystems were considered, where the experimental methodology was demonstrated for four alloys in the Fe-Si-Mn-Al system. Excellent agreement between the DSC/DTA dataset and the most recently published equation was found (error 2.1 ± 1.6 °C). For this equation, suggested modifications of phosphorus parameters will help to improve calculations for P-alloyed steels.

<https://doi.org/10.1007/s11663-021-02251-1>
© The Author(s) 2021

I. INTRODUCTION

PRECISE knowledge of the liquidus temperature T_L is essential to adjust the superheat in the continuous casting of steel and optimize the casting operations. In order to predict the solidification progress in the casting machine, it is required to extend the estimation of T_L down to solidus temperature with respect to microsegregation modeling. The actual temperature of the interdendritic melt corresponds to the liquidus temperature of its changing chemical composition due to the enrichment of alloying elements in the liquid phase during solidification.^[1,2] Microsegregation models can be used to calculate the non-equilibrium solidus temperature depending on the solidification kinetics or to characterize the hot tear sensitivity of a steel grade close to the final solidification stage.^[3]

In general, two methods are available to estimate T_L based on the chemical composition of a steel grade: Within (i) the CALculation of PHase Diagram (CALPHAD) framework,^[4,5] the phase equilibrium temperature is obtained by minimizing the Gibbs energy of the system. For this purpose, various commercial software packages with comprehensive thermodynamic databases are available, *e.g.*, FactSage,^[6]

ThermoCalc,^[7] Pandat,^[8] and IDS.^[9] The great advantage of self-consistent CALPHAD databases is their accurate extrapolation to high concentration and the possibility to perform phase equilibrium calculations over the whole composition range of multicomponent alloys. In practical steelmaking, a simplified way of calculating T_L is (ii) the application of empirically derived equations that are more or less linear regressions fitted to experimental data. Based on regression analysis and phase diagram calculations, several equations have been proposed in the past.^[10–14] Empirical equations enable fast calculations of T_L within defined alloying limits, can be used without thermodynamic databases and numerical solvers and are, therefore, cost-saving alternatives for a successful casting process control in steelmaking plants. Nevertheless, the published equations are only valid in the investigated composition range and may lead to significant errors in the case of higher concentrations and stronger interaction of the alloying elements in the liquid phase.

Analytical liquidus equations are expressed in the form of

$$T_L = T_L^0 + \sum_i f([\%X_i]), \quad [1]$$

where T_L^0 is the melting temperature of pure iron handled as a constant^[10,12] or, more specifically, separated into T_L^0 of δ -iron (1534 °C,^[11] 1536 °C,^[13] and 1538 °C^[14]) and γ -iron (1491 °C,^[11] 1526 °C,^[13] and 1528 °C^[14]). Note that, if separated equations for δ -Fe and γ -Fe are proposed,^[11,13,14] (Table I and II) then the phase with the higher value of T_L is the primary phase at the liquidus temperature. The parameter $f([\text{pct } X_i])$ describes the influence of the element X on the melting temperature of Fe depending on the concentration of

MICHAEL BERNHARD, PETER PRESOLY, CHRISTIAN BERNHARD are with the Chair of Ferrous Metallurgy, Montanuniversitaet Leoben, Franz-Josef-Strasse 18, 8700 Leoben, Austria. Contact E-mail: michael.bernhard@unileoben.ac.at. SUSANNE HAHN is with the Primetals Technologies Austria GmbH, Turmstrasse 44, 4031 Linz, Austria. SERGIU ILIE is with the voestalpine Stahl GmbH, voestalpine-Strasse 3, 4020 Linz, Austria.

Manuscript submitted on January 10, 2021; accepted June 5, 2021.

X in mass percent. The individual functions $f([\text{pct } X_i])$ of analytical equations from literature^[10–12,14] with relevance for Fe-C-Si-Mn-Al-P alloys are given in Table I. Typically, these are linear^[10–12,14] and parabolic functions^[11,12] representing the slope of the liquidus line in binary Fe-X systems. As carbon is in general the most dominating alloying element in steel, additional cross products $[\text{pct } X] \times [\text{pct } C]$ were introduced by Miettinen and Howe^[14] in order to describe the interaction of the alloying element X with C. A slightly different approach was proposed in the work of Schürmann and Stisovic,^[13] assigning the decrease of T_L caused by an alloying element to an equivalent factor of carbon. The equation is given by

$$T_L = T_L^0 + A_{\delta,\gamma} \left\{ [\%C] + \sum_i \left([\%X_i] \left(1 + a_{\delta,\gamma}^i + b_{\delta,\gamma}^i [\%X_i] \right) \right) \right\} + B_{\delta,\gamma} \left\{ [\%C] + \sum_i \left([\%X_i] \left(1 + a_{\delta,\gamma}^i + b_{\delta,\gamma}^i [\%X_i] \right) \right) \right\}^2 \quad [2]$$

where $A_\delta = -76.77$, $A_\gamma = -58.74$, $B_\delta = -6.89$ and $B_\gamma = -4.64$. The values for $a_{\delta,\gamma}^i$ and $b_{\delta,\gamma}^i$ are summarized in Table II.

Miettinen and Howe^[14] evaluated various liquidus equations^[10–15] based on extensive experimental data from literature and pointed out the following difficulties in comparing each of the equations and possible reasons for differences in the calculations:

- the equations relate closely to the alloys studied, and the corresponding composition of the alloys is only roughly reported (low-alloyed or stainless steels),
- the number of investigated alloys is too small or the alloys studied show only minor variation in their chemical composition,
- the focus was placed on the selection of specific alloys or some solutes are only found in a few alloys, and
- often, the change in the solidifying phase (austenite or ferrite) was not taken into account.

It was, therefore, not the aim of this work to introduce another empirical equation but to critically evaluate the available expressions from the literature^[10–14] and check the valid composition range of the calculations based on a comprehensive experimental dataset obtained from thermal analysis techniques.

All equations^[10–14] were derived for specific applications. Kawawa^[10] tested his proposed description of T_L against thermal analysis results of carbon steels and reported an average error of ± 4 °C. Kagawa and Okamoto^[11] not only focused on the influence of small amounts of alloying elements (typically < 3 mass pct.) on the peritectic phase transformation but also gave a liquidus equation for the dilute solutions of Fe. Howe's studies^[12] and later, those of Miettinen and Howe,^[14] are general in nature and provide the possibility to estimate T_L for low-alloyed and stainless steels. In the calculation scheme, Howe,^[12] therefore, lists various different parameters for C, Si, Ni, and V depending on the

Table I. Selected Parameters of Presently Evaluated Empirical Liquidus Equations^[10–12,14] With Relevance for the Fe-C-Si-Mn-Al-P System

Phases	Kawawa ^[10]		Kagawa and Okamoto ^[11]		Howe ^[12]		Miettinen and Howe ^[14]	
	T_L^0 (°C)	$f([\text{Percent } X_i])$ [°C]	ferrite (δ)	austenite (γ)	ferrite (δ)	austenite (γ)	ferrite (δ)	austenite (γ)
C	1536	- 78 [pct C]	1534 - 48.24 [pct C] - 63.04 [pct C] ²	1491 + 36.33[pct C] - 61.90 [pct C] ²	1537 [pct C] < 0.471: - 87 [pct C] [pct C] < 1: - 70 [pct C] - 8 1 < [pct C]: - 76[pct C] - 2	1528 - 76.24 [pct C] - 10.3542 [pct C] ²	1538 - 76.24 [pct C] - 10.3542 [pct C] ²	
Si	- 7.6 [pct Si]		- 14.39 [pct Si]	- 17.10 [pct Si]	[pct Si] < 1: - 9 [pct Si] 1 < [pct Si]: - [pct Si] ² - 9[pct Si] + 1 - 5[pct Mn]	- 11.66 [pct Si] - 4.3512[pct C][pct Si] - 5.62[pct Mn]	- 11.66 [pct Si] - 4.3512[pct C][pct Si] - 5.62[pct Mn]	
Mn	- 4.90[pct Mn]		- 4.88[pct Mn]	- 3.32[pct Mn]		- 0.223[pct C][pct Mn]	- 0.223[pct C][pct Mn]	
Al	- 3.60[pct Al]				0[pct Al]			
P	- 34.40[pct P]		- 31.83[pct P]	- 27.07[pct P]	- 34[pct P]	- 24.78[pct P] - 12.9409[pct C][pct P]	- 30.92[pct P] - 5.3494[pct C][pct P]	

Table II. Parameters Derived by Schürmann and Stisovic^[13] for Fe-C-Si-Mn-Al-P Alloys (Note That P is Not Considered In This Equation)

	T_L^0 [°C]	Si	Mn	Al
Ferrite (δ)	1536	$a = -0.8384$ $b = 3.544E^{-3}$	$a = -0.9433$ $b = -2.6E^{-4}$	$a = -1.0011$ $b = -2.8154E^{-5}$
Austenite (γ)	1526	$a = -0.6931$ $b = -0.0459$	$a = -0.9323$ $b = -4.1584E^{-4}$	$a = -0.9169$ $b = -0.3084$

Table III. Composition Range of the Samples Investigated Using DSC/DTA Techniques

Constituent Systems	C [Mass Percent]	Si [Mass Percent]	Mn [Mass Percent]	Al [Mass Percent]	P [Mass Percent]	No. of Alloys
Fe-C-Si	0.007 to 1.56	0.49 to 4.39	—	—	—	46
Fe-C-Mn	0.054 to 0.30	—	1.02 to 5.39	—	—	10
Fe-C-Al	0.035 to 0.59	—	—	0.37 to 1.97	—	28
Fe-P, Fe-C-P	0.004 to 1.38	—	—	—	0.026 to 0.76	26
Fe-Si-P, Fe-Al-P	< 0.006	< 2.96	—	< 1.66	0.092 to 0.096	8
Fe-Si-Mn, Fe-C-Si-Mn, Fe-Si-Mn-Al	0.005 to 0.32	0.54 to 4.12	0.03 to 6.05	< 0.87	—	49
Fe-C-Mn-P, Fe-C-Si-Mn-Al-P	0.012 to 0.24	< 0.44	1.58 to 2.01	< 0.74	0.005 to 0.33	12
All Data	0.007 to 1.56	< 4.39	< 6.05	< 1.97	< 0.76	179

chemical composition range, but suggests for high-alloyed Cr-Ni steels that the T_L^0 temperature should be relevant to the ternary Fe-Cr-Ni system and that Cr and Ni have to then be excluded from the summation. On the other hand, Miettinen and Howe^[14] derived two separated sets of equations (ferrite and austenite) for both low-alloyed and stainless steels by performing a large number of thermodynamic calculations using the IDS database.^[9] Schürmann and Stisovic^[13] evaluated their equation with the experimental data documented by Howe^[12] and additional thermal analysis measurements from different steel plants ([pct C] < 1, [pct Si] < 4, [pct Mn] < 10, and [pct Cr] < 1.6) but the exact chemical analysis of the commercial steel grades was not documented in the study. In this work,^[13] the parameter for phosphorus was not derived by the authors. Phosphorus strongly decreases the melting point of steel by ~ 25 to 35 °C per mass pct. (see Table I). If P is only considered as trace element in steel (P < 0.025 mass pct.), the equation will give accurate liquidus predictions but in rephosphorized grades with typical concentration of 0.10 [pct P],^[16–18] the resulting error of about 3 to 4 °C is significant in optimizing the superheat in the continuous casting process.

In total, liquidus temperatures of 180 alloys in the Fe-C-Si-Mn-Al-P system were determined using differential thermal analysis (DTA) and differential scanning calorimetry (DSC). The alloys studied cover a wide composition range (see Table III) with great practical relevance for the continuous slab casting of flat products as various recently developed advanced steel grades are based on constituent thermodynamic systems:

- high-strength interstitial free (HSIF) with 0.30 pct Mn and P < 0.10 pct^[16]
- transformation-induced plasticity (TRIP) steels with classic alloying concepts of 0.175 to 0.25 pct C, 1.5 to 2 pct Mn, 2 pct (Al+Si), and P up to 0.1 pct,^[17]
- electrical steel sheets with 1 to 3.5 pct Si,^[18] P < 0.1 pct, 0.5 pct Mn, and 0.5 pct Al,
- low carbon (C < 0.10 pct) medium Mn steels with manganese content ranging from 3 to 10 mass percent,^[19] and
- dual-phase (DP) steels with a typical composition of 0.06 to 0.15 pct C, 1.5 to 3 pct Mn,^[20] and 0.5 to 1 pct Si.

A part of the DSC/DTA dataset has already been published in previous work of the authors^[21–26] and further liquidus data in the Fe-C-Al and Fe-Si-Mn-Al key-systems are provided in the present study, see Table IV. Additional background results of ternary (Fe-C-Si, Fe-C-Mn, Fe-Si-P, Fe-Al-P), quaternary (Fe-C-Si-Mn, Fe-C-Mn-P), and multicomponent (Fe-C-Si-Mn-Al-P) alloys within the composition range of Table III are considered in the discussion.

The typical experimental methodology is demonstrated by examining four alloys in the Fe-Si-Mn-Al quaternary system using DSC. The specimens for the DSC measurements were prepared in a 25 kg induction furnace by taking lollipop steel samples without any deoxidizing agents (Al or Zr). The bath level was protected by argon flushing in order to minimize the contact between the atmosphere and the liquid steel. The chemical analysis was determined using an optical emission spectrometer (OES), type Spectromax Version F (SPECTRO Analytical Instruments & Co.KG,

Table IV. Selected Experimental Data of Previous Work^[21-26] and the Present Work (Fe-C-Al and Fe-Si-Mn-Al) Along With Calculations Using Analytical Equations From Literature.^[10-14]

Sample	References	C [Mass Percent]	Si [Mass Percent]	Mn [Mass Percent]	Al [Mass Percent]	P [Mass Percent]	T_L (DSC/DTA)	$\Delta T_L^{[10]}$	$\Delta T_L^{[11]}$	$\Delta T_L^{[12]}$	$\Delta T_L^{[13]}$	$\Delta T_L^{[14]}$	ΔT_L (PW)
Fe-C-Si_1	21	0.0461	1.026	—	—	—	1521.6	3.0	-4.7	2.1	-2.5	0.7	0.7
Fe-C-Si_2		0.0839	0.993	—	—	—	1519.3	2.6	-4.1	1.5	-2.8	0.3	0.3
Fe-C-Si_3		0.1423	0.980	—	—	—	1512.3	5.2	-0.5	3.5	-0.3	2.6	2.6
Fe-C-Al_1	25	0.2244	—	—	1.996	—	1521.7	-10.4	-1.7	-4.2	50.3	-1.3	-1.3
Fe-Si-Mn_1		0.0071	2.900	0.033	—	—	1501.7	11.5	-9.9	1.0	-6.4	1.7	1.7
Fe-Si-Mn_2		0.0073	3.070	1.050	—	—	1495.7	11.3	-11.4	-0.6	-5.8	-0.1	-0.1
Fe-Si-Mn_3		0.0140	3.090	3.060	—	—	1486.7	9.7	-12.8	-2.6	-5.9	-3.2	-3.2
Fe-Si-Mn_4		0.0155	2.925	5.996	—	—	1477.3	5.9	-15.4	-5.5	-8.7	-8.5	-8.5
Fe-Si-Mn_5	0.016	2.950	6.050	—	—	1475.8	6.9	-14.6	-4.7	-7.5	-7.6	-7.6	
Fe-C-Al_2	22	0.2244	—	—	0.394	—	1520.6	-3.5	-0.6	-3.1	-2.1	-0.2	-0.2
Fe-C-Al_3		0.2286	—	—	1.475	—	1520.0	-7.1	-0.3	-2.9	24.3	0.0	0.0
Fe-C-Si-Mn_1	23	0.1140	1.001	1.996	—	—	1508.4	1.3	-4.9	-0.3	-3.5	-2.7	-2.7
Fe-C-Si-Mn_2		0.1430	1.031	2.053	—	—	1504.2	2.8	-3.2	0.8	-2.4	-1.6	-1.6
Fe-C-Si-Mn_3		0.1850	1.031	2.051	—	—	1501.7	2.0	-3.6	-0.4	-3.4	-2.6	-2.6
Fe-C-Si-Mn_4	24	0.2640	1.034	2.027	—	—	1495.0	2.6	-2.9	-0.5	-3.2	-2.6	-2.6
Fe-C-Si-Mn_5		0.2995	1.034	2.027	—	—	1492.2	2.6	-3.1	-0.8	-3.4	-2.9	-2.9
Fe-C-Si-Mn_6		0.0270	2.040	2.080	—	—	1502.2	6.0	-9.1	0.5	-5.3	-2.0	-2.0
Fe-C-Si-Mn_7		0.1270	2.050	2.060	—	—	1492.8	7.6	-5.5	1.2	-4.4	-1.3	-1.3
Fe-C-Si-Mn_8		0.1660	2.040	2.070	—	—	1490.8	6.6	-6.0	-0.1	-5.6	-2.7	-2.7
Fe-C-Si-Mn_9	26	0.2250	2.040	2.060	—	—	1485.1	7.8	-4.6	0.5	-4.9	-2.2	-2.2
Fe-C-Si-Mn_10		0.3070	2.060	2.050	—	—	1478.3	8.1	-4.7	0.0	-5.5	-3.1	-3.1
Fe-P_1		—	—	—	—	—	1535.1	0.0	-1.9	1.0	0.9	2.3	1.9
Fe-P_2		—	—	—	—	—	1534.9	-0.4	-2.3	0.6	1.1	2.0	1.5
Fe-P_3		—	—	—	—	—	1532.4	0.1	-1.6	1.1	3.6	3.1	1.8
Fe-P_4	—	—	—	—	—	1529.1	1.8	0.2	2.9	6.9	5.3	3.4	
Fe-P_5	—	—	—	—	—	1525.3	-0.4	-1.5	0.8	10.7	4.7	0.8	
Fe-P_6	—	—	—	—	—	1520.5	1.1	0.2	2.3	15.5	7.1	2.0	
Fe-P_7	—	—	—	—	—	1520.9	-1.4	-2.2	-0.2	-0.2	15.1	5.2	-0.7
Fe-P_8	—	—	—	—	—	1515.0	-1.7	-2.0	-0.4	21.0	6.6	-1.5	
Fe-P_9	—	—	—	—	—	1512.8	-0.9	-1.1	0.4	23.2	7.9	-0.8	
Fe-C-P_1	0.0040	—	—	—	—	1531.1	0.9	-0.7	1.9	4.6	3.9	2.6	
Fe-C-P_2	0.0330	—	—	—	—	1529.3	0.5	-0.3	1.2	4.2	3.5	2.2	
Fe-C-P_3	0.0590	—	—	—	—	1527.5	0.2	0.0	0.7	3.9	3.2	1.9	
Fe-C-P_4	0.0990	—	—	—	—	1524.6	-0.1	0.5	0.0	3.7	2.9	1.5	
Fe-C-P_5	0.0960	—	—	—	—	1525.1	-0.1	0.5	0.1	3.5	2.9	1.6	
Fe-C-P_6	0.1360	—	—	—	—	1520.6	1.2	2.3	1.0	4.8	4.1	2.8	
Fe-C-P_7	0.2030	—	—	—	—	1515.9	0.6	2.3	-0.2	4.2	3.3	2.0	
Fe-C-P_8	0.2960	—	—	—	—	1507.6	1.5	3.1	-0.1	5.1	3.8	2.5	
Fe-C-P_9	0.3780	—	—	—	—	1500.8	2.1	2.6	-0.3	5.2	3.8	2.5	
Fe-C-P_10	0.6900	—	—	—	—	1478.3	0.5	5.6	-1.0	5.0	1.9	1.9	
Fe-C-P_11	1.0000	—	—	—	—	1457.8	-3.2	5.0	-2.2	4.8	0.4	0.4	

Table IV. Continued

Sample	References	C [Mass Percent]	Si [Mass Percent]	Mn [Mass Percent]	Al [Mass Percent]	P [Mass Percent]	T_L (DSC/DTA)	$\Delta T_L^{[10]}$	$\Delta T_L^{[11]}$	$\Delta T_L^{[12]}$	$\Delta T_L^{[13]}$	$\Delta T_L^{[14]}$	ΔT_L (PW)
Fe-C-P ₁₂	1.3800	—	—	—	0.101	1427.7	-2.8	-7.2	-1.0	8.4	1.8	1.8	0.7
Fe-C-P ₁₃	0.2060	—	—	—	0.057	1517.5	0.5	2.1	-0.4	2.4	2.8	2.1	0.6
Fe-C-P ₁₄	0.1990	—	—	—	0.103	1516.3	0.6	2.3	-0.1	4.1	3.3	2.1	0.6
Fe-C-P ₁₅	0.2030	—	—	—	0.158	1514.6	0.1	2.0	-0.6	5.5	3.2	1.3	0.6
Fe-C-P ₁₆	0.1700	—	—	—	0.430	1507.0	0.9	3.3	0.6	15.7	6.1	1.0	0.6
Fe-C-P ₁₇	0.3400	—	—	—	0.760	1481.7	1.6	4.4	-0.1	27.4	7.0	0.3	0.6
Fe-C-Al ₄	present work	0.2130	—	—	0.390	—	1520.6	-2.6	0.3	-2.1	-1.2	0.7	0.7
Fe-C-Al ₅	—	0.3130	—	—	0.370	—	1512.5	-2.2	0.2	-2.7	-1.2	0.6	0.6
Fe-C-Al ₆	—	0.0350	—	—	1.671	—	1535.9	-8.6	-3.7	-1.9	28.3	-0.6	-0.6
Fe-C-Al ₇	—	0.1370	—	—	1.654	—	1527.6	-8.2	-1.4	-2.5	30.3	-0.2	-0.2
Fe-Si-Mn-Al ₁	—	0.0048	0.539	0.698	0.125	—	1530.1	-2.4	-7.5	-1.9	-4.4	-2.7	-2.7
Fe-Si-Mn-Al ₂	—	0.0056	1.150	0.688	0.342	—	1521.9	0.3	-8.1	0.5	-4.3	-1.6	-1.6
Fe-Si-Mn-Al ₃	—	0.0053	2.270	0.683	0.579	—	1509.3	3.6	-11.6	-0.8	-7.5	-2.1	-2.1
Fe-Si-Mn-Al ₄	—	0.0048	2.440	0.718	0.868	—	1508.0	2.4	-12.8	-1.9	-4.3	-2.9	-2.9

Note, that the present work (PW) differs from Miettinen and Howe's formula^[14] only in the modified P coefficient of ferrite. T_L in references^[21,25] were measured by DTA (NETZSCH STA409PG Luxx); in references^[22-24,26] and in the present work a NETZSCH DSC404F1 Pegasus was used. $\Delta T_L = T_L$ (calculated) - T_L (DSC/DTA).

Germany). The final compositions of alloys FeSiMnAl-I to FeSiMnAl-IV are listed in Table IV; the trace element levels are given as C ≤ 55 ppm, P ≤ 46 ppm, S ≤ 22 ppm, and N ≤ 44 ppm.

The DSC analysis was carried out in a DSC 404F1 Pegasus (NETZSCH Gerätebau GmbH, Germany) with an Rh furnace and a Pt DSC sensor instrumented with type S thermocouples. Al₂O₃ crucibles with a volume of 85 μl and lids were used for all experiments; in each trial, the reference was an empty crucible. The protective tube of the Rh furnace was purged permanently with Ar 5.0 (purity 99.999 pct), and a thermally active Zr getter was placed below the DSC sensor to avoid oxidation of the sample at temperatures above 350 °C. The experimental setup was calibrated by measuring the melting points and melting enthalpies of NETZSCH's standards of pure metals In, Bi, Al, Ag, Au, Ni, and Co. In all DSC experiments, a heating rate (HR) of 10 °C/min was applied and samples of 50 mg were used.^[26] In the following section an "onset" in the DSC signal represents the first deviation from the baseline and corresponds to the solidus temperature T_S . A "peak" indicates the end of the phase transformation and is defined as T_L . Detailed information on the analysis of DSC and DTA signals can be found in the NIST-recommended practice guide.^[27]

Melting of Fe-based alloys takes place under a large change in heat ($\Delta H > 200$ J/g). Within the DSC analysis of strongly endothermic phase transformations, special care has to be taken in order to accurately determine the equilibrium peak temperature. While the onset (T_S) in the DSC signal is less affected by the heating rate, the peak (T_L) is shifted to higher temperatures with increasing HR.^[27] The generally accepted approach^[28] requires measuring the liquidus peak with several heating rates (e.g. 5 to 20 °C/min) using new samples in each trial, and the extrapolation of the HR-dependent peak to zero °C/min gives the equilibrium liquidus temperature. In daily DSC practice, the variation of heating rates represents a work-intensive procedure. A more effective way to exclude the experimental setup influences on the DSC signal is provided by NETZSCH's Tau-R software.^[29,30] The Tau-R method enables the determination of the equilibrium data from only a single DSC experiment. At this point, the authors refer to their previous work^[26] regarding more detailed information on the Tau-R method and its successful application to characterize melting equilibria in steel using DSC.

The DSC signals of samples FeSiMnAl-I to FeSiMnAl-IV obtained from heating with 10 °C/min and the corresponding Tau-R calculations are shown in Figures 1(a) and (b), respectively. All signals were corrected to the base line of 0.0 mW/mg and the given solidus and liquidus temperatures are the average values of at least two independent DSC runs. The typical experimental error in measuring solid-liquid phase transformations with the present setup is suggested to be ± 2 °C.^[26] As expected, the onset temperature (T_S) is not dependent on the heating rate: T_S measured with 10 °C/min and the equilibrium data calculated using the Tau-R software are identical. In measuring the peak temperature (T_L), the scanning

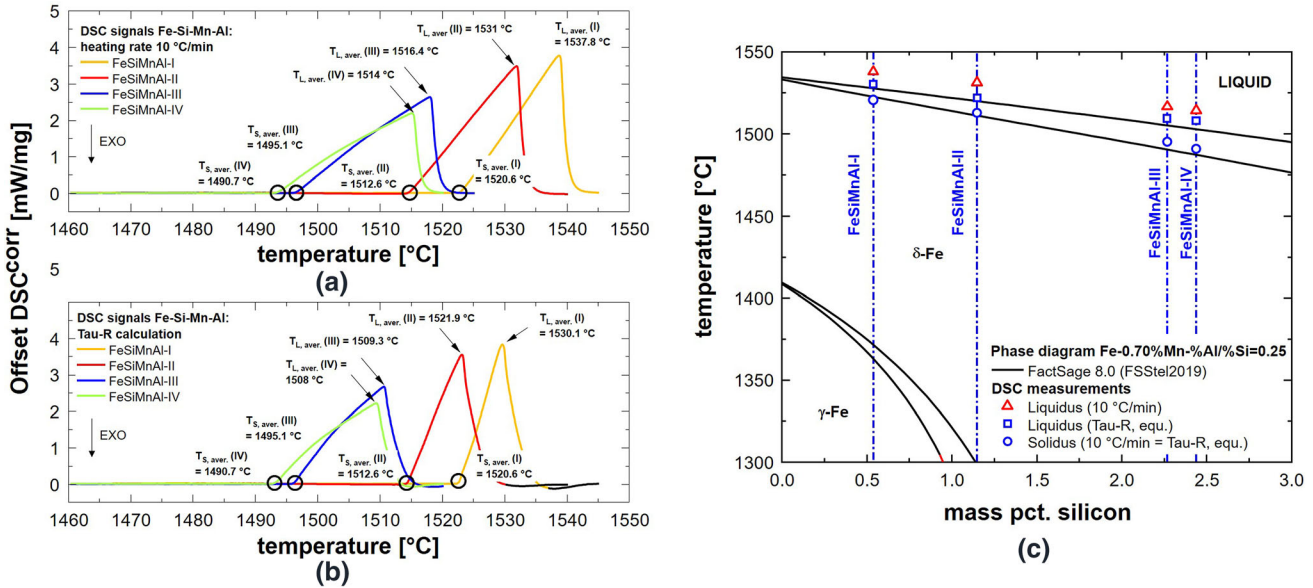


Fig. 1—DSC signals of the Fe-Si-Mn-Al alloys corrected to the baseline of 0.0 mW/mg using a heating rate of 10 °C/min (a) and Tau-R calculations of the original DSC signals (b). All experimental temperatures given are the average values of at least two independent measurements. Calculated phase diagram for the Fe-Si-Mn-Al alloys using FactSage 8.0 and FStel2019 database^[6] along with the experimental results (c).

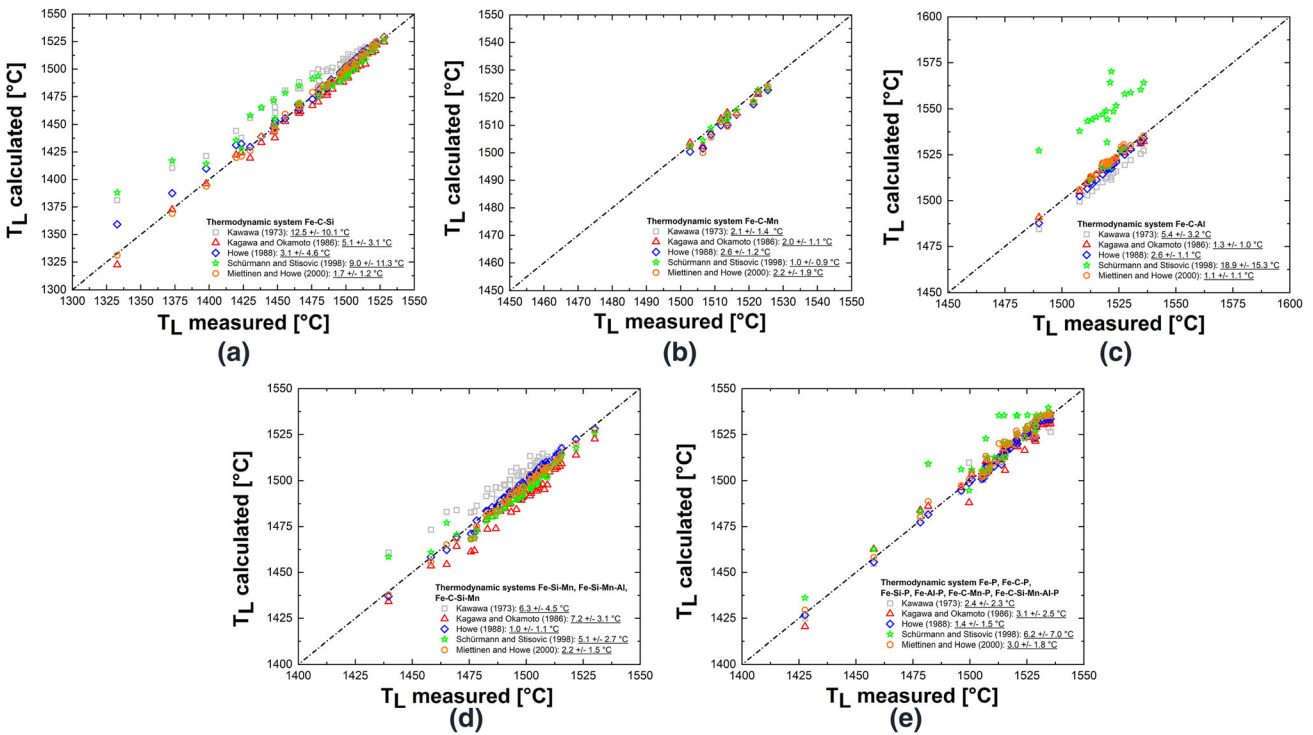


Fig. 2—Comparison between calculated liquidus temperatures^[10–14] and experimentally determined values in the Fe-C-Si system (a), Fe-C-Mn system (b), Fe-C-Al system (c), Fe-Si-Mn/Fe-Si-Mn-Al/Fe-C-Si-Mn systems (d), and highly P-alloyed systems (e).

mode leads to significant superheating above the actual liquidus temperature; the deviation of 7 to 10 °C clearly demonstrates the necessary correction of the DSC signal to get the real value of T_L . With respect to the primary phase (δ , γ) stable at T_L , the DSC signals

indicate a single melting peak of the δ -ferrite phase which is in reasonable agreement with the phase diagram calculated in Figure 1(c).^[6] The thermodynamic calculations of the vertical phase diagram section were performed with a defined composition of

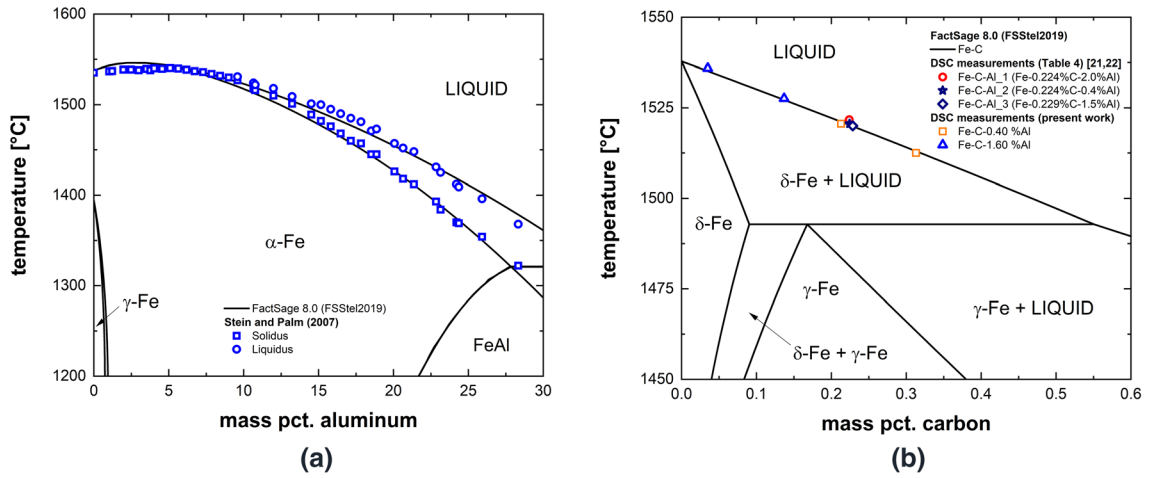


Fig. 3—Binary Fe-Al system^[6] along with experimental data of Stein and Palm^[31] (a) and calculated Fe-C diagram^[6] compared with liquidus temperatures published in previous work^[21, 22] and ternary Fe-C-0.40 pct Al and Fe-C-1.60 pct Al alloys (b) (see also Table IV).

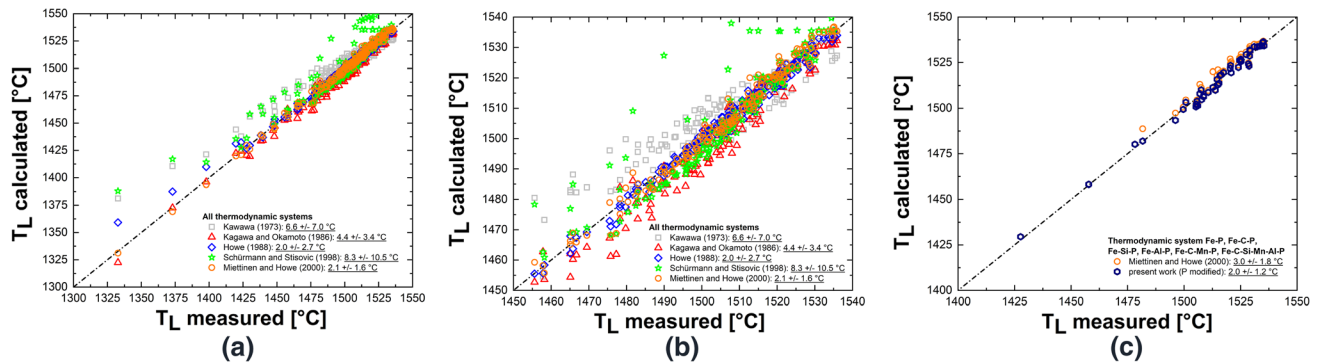


Fig. 4—Comparison between calculated liquidus temperature^[10–14] and experimentally determined values in all thermodynamic systems (a) and the corresponding enlarged section between 1450 °C and 1540 °C (b). Improved calculations in the P-alloyed system by modifying the P coefficients of δ -Fe in Miettinen and Howe’s equation^[14] (c).

Table V. Originally Documented Limits of Howe and Miettinen’s^[14] Equation Based on the Defined Composition Range in Their Thermodynamic Calculations Using IDS^[9] and Validated Composition Range of Their Work by Experimental DSC/DTA Data in the Present Work (PW)

Reference	C [Mass Percent]	Si [Mass Percent]	Mn [Mass Percent]	Al [Mass Percent]	P [Mass Percent]
[14]	0 to 1.20	0 to 2	0 to 2	—	0 to 0.03
PW	0 to 1.56	0 to 4.5	0 to 5	0 to 2	0 to 0.10

For calculations up to 0.10 [pct P] the proposed modifications of the P coefficients for δ -Fe are suggested.

Fe-0.70 pct Mn and a constant [pctAl]/[pctSi] ratio of 0.25. Due to induction melting practice, the [pct Al]/[pct Si] ratio in the samples varies in the range of 0.23 to 0.36 (see Table IV). Hence, minor differences of ~ 5 °C between the calculated and measured temperatures have to be considered in Figure 1(c).

The final equilibrium liquidus temperatures T_L (Tau-R) in the system Fe-Si-Mn-Al are summarized in Table IV. In a first comparison with the analytical equations,^[10–14] the best agreement was found for the studies of Kawawa^[10] (error 2.2 ± 1.2 °C), Howe^[12] (error 1.3 ± 0.6 °C) and Miettinen and Howe^[14] (2.3 ± 0.5 °C). The deviations are close to or below the typical

experimental error. However, for C-free Fe-Si-Mn-Al alloys, only the liquidus slopes of the binary system are of relevance, as the interaction parameters with carbon^[14] cannot be evaluated.

The comparison between the DSC/DTA dataset (Table III) and the calculations using the analytical liquidus equations^[10–14] is summarized graphically in Figures 2(a) through (e) and discussed in the following subsystems:

- Fe-C-Si: The binary coefficients of the Fe-Si system significantly differ in the equations. The liquidus slope of -7.6 °C/[pct Si] as proposed by Kawawa^[10] systematically predicts too high values of T_L compared

to the measurements, while Kagawa and Okamoto's equation^[11] ($-14.39\text{ °C}/[\text{pct Si}]$) results in slightly lower calculated liquidus temperatures. The equation of Schürmann and Stisovic^[13] gives good correlation up to 3 mass pct. Si; the error is typically smaller than 8 °C, which is in agreement with the evaluation of high-Si commercial steels in their work^[13] (error $\pm 10\text{ °C}$). Deviations of more than 40 °C were found in the case of high amounts of Si ($\sim 4\text{ pct}$) and C ($> 1\text{ pct}$). Excellent results were obtained using Miettinen and Howe's equations.^[14] The small averaged error of $1.7 \pm 1.2\text{ °C}$ indicates that the most suitable Fe-Si factor for ferrite and austenite corresponds to about $-12\text{ °C}/[\text{pct Si}]$. Even for the high-alloyed samples, the consideration of the Si-C interaction^[14] provides an accurate description of T_L .

- Fe-C-Mn: As the liquidus slopes of each equation are consistent, all liquidus formulas give very similar results (error $< \pm 2.5\text{ °C}$). However, at $[\text{pct Mn}] > 5$, the calculations of T_L with equations^[10–12,14] lead to higher deviations from the DSC results ($\Delta T = 4\text{ to }6\text{ °C}$). In this system, the equation of Schürmann and Stisovic^[13] provides reliable predictions of T_L up to the maximum alloying content of 5.3 mass pct. Mn (error $1 \pm 1.1\text{ °C}$).
- Fe-C-Al: Most recently published experimental data of Stein and Palm^[31] showed that the addition of aluminum increases the melting point of Fe in the binary Fe-Al system by $+1\text{ °C}/[\text{pct Al}]$. A local maximum was reported at 1540 °C and $\sim 5\text{ mass pct. Al}$ ^[31] before T_L continuously decreases with increasing Al content, see Figure 3(a).^[6, 31] It is therefore evident that at high Al content, CALPHAD based thermodynamic optimizations are essential to accurately model the liquidus phase boundary. In this case, analytical equations for T_L have to include numerous fitting parameters to reproduce the curvature of the liquidus line for alloys with $[\text{pct Al}] > 2.5$. Hence, the authors decided to consider only alloys with Al content below the composition of the Fe-Al inflection point covering the typical composition range typical AHSS ($[\text{pct Al}] < 2$).^[17, 18] However, the effect of Al on T_L is hardly measureable in ternary Fe-C-Al vertical sections with 0.40, [pct Al], 1.60 [pct Al] and 2 [pct Al], see Figure 3(b). In this alloying range the minor change of T_L is within the experimental error of $\pm 2\text{ °C}$ ^[26] and a clear influence of Al on the melting point in the Fe-C diagram^[6] cannot be observed. In analytical equations for T_L the effect of Al is considered in the expressions of Kawawa^[10] ($-3.6\text{ °C}/[\text{pct Al}]$) and Howe^[12] ($0\text{ °C}/[\text{pct Al}]$). It can be seen in Figure 2(c) and Table IV that the negative coefficient in Kawawa's equation^[10] results in too low values of T_L . In agreement with Howe's study,^[12] setting the Fe-Al coefficient specifically to $0\text{ °C}/[\text{pct Al}]$, Miettinen and Howe's equation^[14] results in the lowest deviation from the DSC data ($\Delta T_L \sim \pm 1\text{ °C}$). In the case of the Schürmann and Stisovic^[13] equation, the measurements are most presumably outside of the valid composition range for Al. This results in an unreliable stabilization effect of austenite and a very high liquidus temperature.

- Fe-Si-Mn and Fe-C-Si-Mn: In general, all liquidus equations evaluated provide sufficiently accurate predictions of T_L , including calculations for alloys containing Si and Mn up to 4 pct. Again the work of Howe^[12] (error $1.0 \pm 1.1\text{ °C}$) and Miettinen and Howe^[14] (error $2.2 \pm 1.5\text{ °C}$) result in lowest deviation from the DSC/DTA data.
- P-alloyed systems: Excellent predictions of T_L in highly P-alloyed systems could be performed using the equation of Howe^[12], showing a deviation from the experimental results of only $1.4 \pm 1.5\text{ °C}$. Miettinen and Howe's^[14] coefficients underestimate the decrease of T_L induced by alloying P, resulting in systematically higher values of T_L in the Fe-P and Fe-C-P systems. As all other ternary subsystems (Fe-C-Si, Fe-C-Al and Fe-C-Mn) are well described by their work, the deviation may result from a factor too large for phosphorus. Compared to other work,^[10–12] the parameter of P is considered to be generally lower than $-30\text{ °C}/[\text{pct P}]$, whereas Miettinen and Howe^[14] suggest a value of $-24.78\text{ °C}/[\text{pct P}]$ for ferrite and $-30.92\text{ °C}/[\text{pct P}]$ for austenite. It has to be noted, that the P content of most alloys investigated by DSC/DTA exceeds the defined valid composition range of their derived equations (0.03 mass pct.^[14]). The increased error of the Schürmann and Stisovic^[13] equation is a consequence of the missing factor of P. For that reason, the results will not be discussed at this point.

By evaluating all 180 DSC/DTA measurements in Figures 4(a) and (b), highly accurate liquidus temperatures for steel were predicted using the equations of Howe^[12] (error $2.0 \pm 2.7\text{ °C}$) and Miettinen and Howe^[14] (error $2.1 \pm 1.6\text{ °C}$). Although both equations yield very similar calculation results, the work of Miettinen and Howe^[14] offers the significant advantage of providing two separated equations for ferrite and austenite. It is, therefore, possible (i) to identify the most stable phase at the liquidus temperature based on the initial chemical composition and (ii) to estimate the start of the peritectic reaction during solidification in conjunction with microsegregation models. For this equation, the authors suggest specifically setting the parameter of aluminum to $0\text{ °C}/[\text{pct Al}]$ for the best correlation in Al-alloyed systems up to 2 pct. Based on the present experimental DSC/DTA data, the results show clearly that Miettinen and Howe's^[14] liquidus formula may be used without hesitation for liquidus calculations of steels even at elevated alloying content of C ($< 1.56\text{ pct}$), Si ($< 4.5\text{ pct}$), Mn ($< 5\text{ pct}$), and Al ($< 2\text{ pct}$) outside the originally documented valid composition limits^[14] in Table V.

However, for the strongly segregating element phosphorus, there is still some room to improve the liquidus slope in the expressions of Miettinen and Howe.^[14] By fitting the binary coefficient and the cross product parameter in their equations to the recently published data^[26] of Fe-P and Fe-C-P alloys in Table IV, values of $-35.23\text{ °C}/[\text{pct P}]$ and $-11.2\text{ °C}/([\text{pct P}] \times [\text{pct C}])$ for δ -Fe were obtained. The binary Fe-P coefficient for ferrite is in reasonable agreement with the literature

values^[10–12] (see Table I) and the interaction parameter with carbon is not changed significantly. As only a few liquidus data for austenite were available and the correlation between the calculations and the measurements is very accurate (1.4 ± 0.7 °C), the γ -Fe parameter set^[14] (Table I) was kept unchanged. By using the optimized factors for phosphorus, the error in the P-alloyed systems could be reduced from 3.0 ± 1.8 °C to 2.0 ± 1.2 °C, and the overall error is then decreased below the value of 2 °C (1.9 ± 1.4 °C). Further, by introducing the modified phosphorus coefficient, the concentration limit of Miettinen and Howe's equation could be extended up to 0.10 mass pct. P (Table V). The improved calculations for highly P-alloyed samples are graphically represented in Figure 4(c).

In summary, various analytical liquidus equations^[10–14] for steel were evaluated based on a comprehensive DTA/DSC dataset of 180 alloys in the Fe-C-Si-Mn-Al-P thermodynamic subsystems. Excellent agreement was obtained with the most recently published expressions by Miettinen and Howe.^[14] The average error of 2.1 ± 1.6 °C is close to the typical experimental error of ± 2 °C in determining solid–liquid phase equilibria with the present DSC/DTA setups.^[26] For this equation, the slight adjustments for the Fe-P and Fe-C-P liquidus slope suggested here may help to improve calculations for steel with higher P content.

The present work demonstrates a systematic methodology to evaluate liquidus equations using DSC and DTA. Future research will focus on measurements of the high-carbon austenite melting equilibria for systems already examined in the past (Fe-C-Al, Fe-C-P, Fe-C-Mn, Fe-C-Si-Mn, etc.) and further thermodynamic systems (e.g., Fe-C-Si-Mn-P, Fe-C-Si-Mn-Al, etc.) will be investigated.

ACKNOWLEDGMENT

The authors gratefully acknowledge the financial support under the scope of the COMET program within the K2 Center “Integrated Computational Material. Process and Product Engineering (IC-MPPE)” (Project No 859480). This program is supported by the Austrian Federal Ministries for Climate Action, Environment, Energy, Mobility, Innovation, and Technology (BMK) and for Digital and Economic Affairs (BMDW), represented by the Austrian research funding association (FFG), and the federal states of Styria, Upper Austria and Tyrol.

FUNDING

Open access funding provided by Montanuniversität Leoben.

OPEN ACCESS

This article is licensed under a Creative Commons Attribution 4.0 International License, which permits use, sharing, adaptation, distribution and reproduction

in any medium or format, as long as you give appropriate credit to the original author(s) and the source, provide a link to the Creative Commons licence, and indicate if changes were made. The images or other third party material in this article are included in the article's Creative Commons licence, unless indicated otherwise in a credit line to the material. If material is not included in the article's Creative Commons licence and your intended use is not permitted by statutory regulation or exceeds the permitted use, you will need to obtain permission directly from the copyright holder. To view a copy of this licence, visit <http://creativecommons.org/licenses/by/4.0/>.

REFERENCES

1. Y. Ueshima, S. Mizoguchi, T. Matsumiya, and H. Kajioka: *Metall. Trans. B*, 1986, vol. 17, pp. 845–59.
2. A. Howe: *Appl. Sci. Res.*, 1987, vol. 44, pp. 51–59.
3. R. Pierer, C. Bernhard, and C. Chimani: *Rev. Met. (Paris)*, 2007, vol. 104, pp. 72–83.
4. P. Spencer: *Calphad*, 2008, vol. 31, pp. 1–8.
5. H. Lukas, S. Fries, and B. Sundman: *Computational Thermodynamics: The Calphad Method*, Cambridge University Press, New York, 2007.
6. C. Bale, E. Bêlisle, P. Chartrand, S. Decterov, G. Eriksson, A. Gheribi, K. Hack, I.-H. Jung, Y.-B. Kang, J. Melançon, A. Pelton, S. Petersen, C. Robelin, J. Sangster, P. Spencer, and M.-A. van Ende: *Calphad*, 2016, vol. 54, pp. 35–53.
7. J. Andersson, T. Helander, L. Höglund, P. Shi, and B. Sundman: *Calphad*, 2002, vol. 26, pp. 73–312.
8. W. Cao, S.-L. Chen, F. Zhang, K. Wu, Y. Yang, Y. Chang, R. Schmid-Fetzer and W. Oates: *Calphad*, 2009, vol. 33, pp. 328–342.
9. J. Miettinen, S. Louhenkilpi, H. Kytönen, and J. Laine: *Math. Comput. Simul.*, 2010, vol. 80, pp. 1536–50.
10. T. Kawawa: *Report of 6th Meeting on Solidification of Steel*, No. 6-III-9, Japan, 1973.
11. A. Kagawa and T. Okamoto: *Mater. Sci. Technol.*, 1986, vol. 2, pp. 997–1008.
12. A. Howe: *Ironmaking Steelmaking*, 1988, vol. 15, pp. 134–42.
13. E. Schürmann and T. Stisovic: *Stahl Eisen*, 1998, vol. 118, pp. 97–102.
14. J. Miettinen and A. Howe: *Ironmaking Steelmaking*, 2000, vol. 27, pp. 212–27.
15. M. Wolf: *Proceedings of Concast Metallurgical Seminar*, Zurich, Switzerland, 1982.
16. X.-M. Chen, S.-H. Song, L.-Q. Weng, S.-J. Liu, and K. Wang: *Mater. Sci. Eng. A*, 2011, vol. 528, pp. 8299–04.
17. C. Bernhard, B. Linzer, P. Presoly, I. Watzinger and J. Watzinger: *IOP Conf. Ser.: Mater. Sci. Eng.*, 2019, vol. 529, art. no. 012071.
18. P. Ghosh, R. Chromik, A. Knight, and S. Wakade: *J. Magn. Mater.*, 2014, vol. 356, pp. 42–51.
19. Y.-K. Lee and J. Han: *Mater. Sci. Technol.*, 2015, vol. 31 (7), pp. 843–56.
20. C. Tasan, M. Diehl, D. Yan, M. Bechtold, F. Roters, L. Schemmann, C. Zheng, N. Peranio, D. Ponge, M. Koayama, K. Tsuzaki, and D. Raabe: *Annu. Rev. Mater. Res.*, 2015, vol. 45, pp. 391–31.
21. P. Presoly, R. Pierer, and C. Bernhard: *Metall. Mater. Trans. A*, 2013, vol. 44, pp. 5377–88.
22. P. Presoly, R. Pierer and C. Bernhard: *IOP Conf. Ser.: Mater. Sci. Eng.*, 2012, vol. 33, art. no. 012064.
23. P. Presoly, C. Bernhard, N. Fuchs, J. Miettinen, S. Louhenkilpi and J. Laine: *Proceedings of 9th ECCO European Continuous Casting Conference*, Vienna, Austria, 2017.
24. P. Presoly, C. Bernhard and J. Six: *IOP Conf. Ser.: Mater. Sci. Eng.*, 2015, vol. 119, art. no. 012013.
25. P. Presoly, M. Bernhard, and C. Bernhard: *Calphad XLVII Conference Proceedings*, Queretaro, Mexico, 2018.
26. M. Bernhard, P. Presoly, N. Fuchs, C. Bernhard, and Y.-B. Kang: *Metall. Mater. Trans. A*, 2020, vol. 51, pp. 5351–64.

27. W. J. Boettinger, U. R. Kattner, K.-W. Moon and J. H. Perepezko, *DTA and Heat-flux DSC measurements of Alloy Melting and Freezing. NIST Recommended Practice Guide*, Special Publication 960-15, 2006.
28. L. Chapman: *J. Mater. Sci.*, 2004, vol. 39, pp. 7229–36.
29. Software: NETZSCH Tau-R Calibration 8.0.1 from Netzsch Gerätebau GmbH, Selb, Germany, 2019.
30. E. Moukhina and E. Kaisersberger: *Thermochim. Acta*, 2009, vol. 492, pp. 101–109.
31. F. Stein and M. Palm: *Int. J. Mat. Res.*, 2007, vol. 98 (7), pp. 580–88.

Publisher's Note Springer Nature remains neutral with regard to jurisdictional claims in published maps and institutional affiliations.

Paper V

On the relevance of microsegregation models for process control in continuous casting of steel

M. Bernhard, P. Presoly, C. Bernhard, J. Six and S. Ilie

Proceedings of the 26th International Conference on Metallurgy and Materials, 2017, Brno, Czech Republic.

Abstract: Microsegregation in general is the consequence of the different solubility of alloying and residual elements in liquid and solid steel. The result is an enrichment of segregating elements between the dendrites due to incomplete diffusion equalization. This enrichment favours the precipitation of inclusions (e.g. MnS) during solidification as well as the formation of hot tear segregations (HTS) along primary grain boundaries. Hence, the modelling of microsegregation phenomena is an important task in order to predict the final product quality and to optimize the process parameters in continuous casting of steel. A microsegregation model based on the analytical solution proposed by Ohnaka was implemented in an in-house 1D-FV solidification simulation software. Considering equilibrium partition coefficients from FactSage (FSStel2015) non-equilibrium solidus temperatures of various steel grades were calculated. These results show very good correspondence with values determined from an in-situ hot tensile on solidifying steel. Finally, the results were applied to calculate solidification in a continuous slab casting machine and to analyse the strain in the mushy zone subsequently. For selected steel grades the probability of HTS formation was predicted and the influence of operating parameters was quantified.

Used and reprinted under the Creative Commons Attribution 4.0 International License

ON THE RELEVANCE OF MICROSEGREGATION MODELS FOR PROCESS CONTROL IN CONTINUOUS CASTING OF STEEL

BERNHARD Michael¹, PRESOLY Peter¹, BERNHARD Christian¹, SIX Jakob², ILIE Sergiu²

¹ Chair of Ferrous Metallurgy, Montanuniversitaet Leoben, Leoben, Austria, EU,
michael.bernhard@unileoben.ac.at

² voestalpine Stahl GmbH, Linz, Austria, EU

Abstract

Microsegregation in general is the consequence of the different solubility of alloying and residual elements in liquid and solid steel. The result is an enrichment of segregating elements between the dendrites due to incomplete diffusion equalization. This enrichment favours the precipitation of inclusions (e.g. MnS) during solidification as well as the formation of hot tear segregations (HTS) along primary grain boundaries. Hence, the modelling of microsegregation phenomena is an important task in order to predict the final product quality and to optimize the process parameters in continuous casting of steel.

A microsegregation model based on the analytical solution proposed by Ohnaka was implemented in an in-house 1D-FV solidification simulation software. Considering equilibrium partition coefficients from FactSage (FSStel2015) non-equilibrium solidus temperatures of various steel grades were calculated. These results show very good correspondence with values determined from an in-situ hot tensile on solidifying steel. Finally, the results were applied to calculate solidification in a continuous slab casting machine and to analyse the strain in the mushy zone subsequently. For selected steel grades the probability of HTS formation was predicted and the influence of operating parameters was quantified.

Keywords: solidification, microsegregation, continuous casting, hot tearing

1. INTRODUCTION

Elements generally show a different solubility in solid and liquid steel. In contrast to the thermodynamic equilibrium, the complete diffusion equalization of elements inside the solidifying microstructure is limited under continuous casting conditions. The consequence is an enrichment of alloying elements and tramp elements in the interdendritic melt. This phenomenon, known as microsegregation, has a decisive influence on the process quality and subsequently on the final product properties: The enrichment favours the formation of hot tear segregations (HTS) along primary grain boundaries as well as precipitation of inclusions during solidification. Further, the segregation on microscopic scale could lead to a macroscopic inhomogeneity in the center of the strand.

In the present work a microsegregation model based on Ohnaka's analytical solution [1] was implemented in an in-house 1D-FV solidification simulation software using input parameters from literature and FactSage (FSStel2015). Further, an evaluation of liquidus formulas by the comparison with results from Differential Scanning Calorimetry (DSC) measurements for a wide range of steel compositions was performed. A published formula could be slightly modified and improved. Calculated solidus temperatures are in good agreement with values determined from an in-situ hot tensile test on solidifying steel. Finally, the model was used for the solidification simulation and the prediction of hot tear formation in a continuous slab caster. Considering different steel compositions and secondary cooling strategies, the relevance of microsegregation modelling regarding quality control in the continuous casting process is shown.

2. MICROSEGREGATION MODELLING

2.1 Model description

Various models for the mathematical description of microsegregation during solidification have been developed in the past [1-7]. Ohnaka [1] presented an analytical model based on the assumption of a quadratic solute distribution profile in the solid. The solution of the model is given in **Equation 1**.

$$\frac{dc_l}{c_l} = \frac{(1-k)df_s}{1 - \left(1 - \frac{\beta k}{1+\beta}\right) f_s} \quad (1)$$

c_l is the solute concentration in the liquid, f_s is the fraction of solid, dc_l is the change of the solute concentration in the liquid corresponding to an increase of the solid fraction df_s and k is the equilibrium distribution coefficient. The backdiffusion parameter β depends on the dendrite geometry and the dimensionless Fourier-Number α ($\beta=2\alpha$ for the plate-like model and $\beta=4\alpha$ for the columnar model). In solidification processes α is generally defined by **Equation 2**, where D_s is the diffusion coefficient of elements in the solid steel, t_f is the local solidification time and λ_2 is the secondary dendrite arm spacing (SDAS).

$$\alpha = \frac{4D_s t_f}{\lambda_2^2} \quad (2)$$

Setting $\Gamma=1-\beta k/(1+\beta k)$ and assuming that the backdiffusion parameter is constant within an increase of solid fraction by Δf_s , integration of **Equation 1** from f_s to $f_s+\Delta f_s$ results in the semi-integrated **Equation 3** according to You et al. [8]. In the present work the semi-integrated form with a columnar dendrite structure ($\beta=4\alpha$) is applied for the microsegregation calculation.

$$c_l^{f_s+\Delta f_s} = c_l^{f_s} \left[\frac{1-\Gamma f_s}{1-\Gamma(f_s+\Delta f_s)} \right]^{\frac{1-k}{\Gamma}} \quad (3)$$

2.2 Input parameters

The temperature dependence of solute diffusion coefficients follows an Arrhenius approach (**Equation 4**), where the gas constant R is 8.314 J / (mol·K) and T is the temperature in Kelvin. The used values for the activation energy Q and D_0 are listed in **Table 1**.

$$D_s = D_0 e^{-\frac{Q}{RT}} \quad (4)$$

Table 1: Diffusion coefficients of solutes in ferrite (δ) and austenite (γ) [6,9]

		C	Si	Mn	P	S	Al	Cr	Ni	Mo	Cu
δ	D_0 [cm ² /s]	0.0127	8.0	0.76	2.9	4.56	5.9	2.4	1.6	3.47	2.6
	Q [10 ³ J/mol]	81.4	248.9	224.4	230.1	214.6	241.2	239.8	240	241.4	240
γ	D_0 [cm ² /s]	0.0761	0.30	0.055	0.01	2.4	5.1	0.0012	0.34	0.068	0.7
	Q [10 ³ J/mol]	134.4	251.2	249.1	182.7	212.2	245.8	219	282.4	246.9	286

Equilibrium partition coefficients are taken from FactSage (FSStel2015) [10]. SDAS is computed as a function of local solidification time and carbon content as proposed by Pierer and Bernhard [11]. Further it

was assumed, that if the enrichment of manganese and sulphur exceeds the solubility product of manganese sulphide [12], precipitation takes place until the equilibrium concentrations are reached.

2.3 Evaluation of empirical equations for the estimation of liquidus temperatures

Numerous equations for the estimation of liquidus temperatures have been published in the past [13-17]. In general these empirical equations are based on regression analysis from thermal analysis measurements or thermodynamic calculations. With respect to microsegregation modelling, regression formulas are useful for a simple prediction of the current interdendritic temperature and the solidus temperature, respectively. Therefore, selected equations were evaluated with more than 300 Difference Scanning Calorimetry (DSC) measurements [18]. The results for a wide range of steel grades are shown in **Figure 1 (a) and (b)**. The formula according to Kawawa already differs at high temperatures from the experimental results and shows the highest deviation of 7.53 ± 9.20 °C, followed by Kagawa-Okamoto (K-O) equation with an average error of 5.77 ± 6.57 °C. The Howe and Schürmann-Stisovic (S-S) formulas show approximately the same accuracy. However, best correlation between experimental data and calculated temperatures was found for the Howe and Miettinen (H-M) regression polynoms with a deviation of 2.97 ± 3.48 °C. Based on the experimental data, an increase of the liquidus temperature by 2 °C / wt% was observed for aluminum contents up to 3 wt%. Considering this coefficient in the H-M equations, a further improvement could be achieved as the error decreases to 2.61 ± 2.32 °C. Since the optimized expression enables the precise determination of liquidus temperatures even at high amounts of alloying elements, it is particularly suitable for the application in the model.

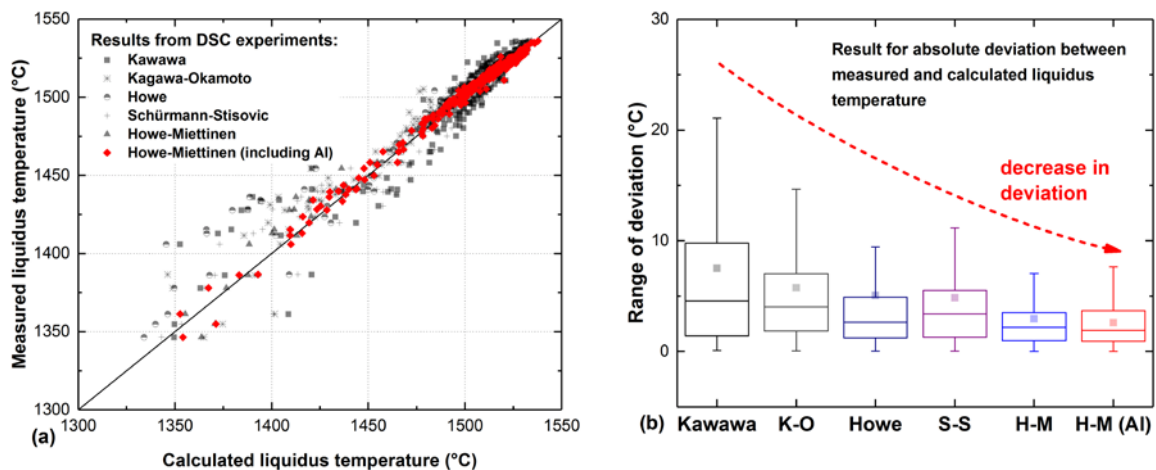


Figure 1: Comparison between measured liquidus temperatures by means of DSC measurements and using empirical equations (a) and resulting absolute deviation for selected equations (b)

3. VERIFICATION OF THE MICROSEGREGATION MODEL

At the Chair of Ferrous Metallurgy the hot tearing sensitivity of different steel grades can be investigated by the Submerged Split Chill Tensile (SSCT) -Test. The schematic representation of the SSCT-Test is shown in **Figure 2**. Within the experiment a cylindrical test body is submerged into a superheated melt. Simultaneously a thin shell solidifies on the surface of the test body and after a predefined holding time an in-situ tensile test starts during solidification. If the initiated strain exceeds a critical value, hot tears can be found in the following metallographic examination. The measured shell thickness and the detected position and number of hot tears can be used for the correlation with the numerical simulation. Finally, the evaluation of the calculated solidus temperature under non-equilibrium conditions and the prediction of critical strains for hot tear formation are possible. A detailed description of the experimental procedure and the numerical simulation of the SSCT test can be found elsewhere [19].

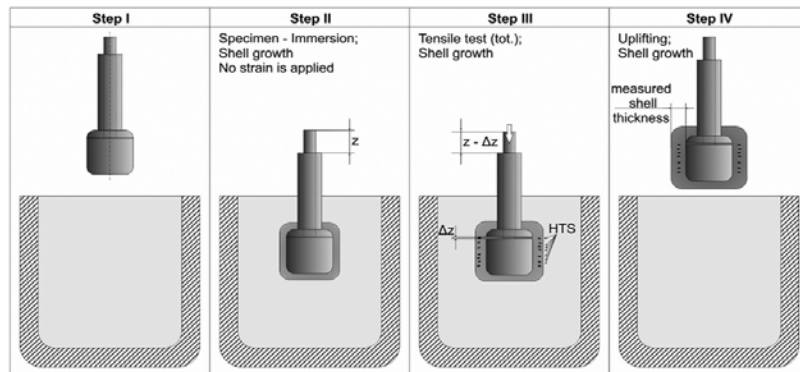


Figure 2: Schematic representation of the SSCT-Test at the Chair of Ferrous Metallurgy [20]

In a first step the present “stand-alone” microsegregation model was compared with an already evaluated model from You et al. [8] which is fully coupled with the thermodynamic database FSStel2015. On the example of medium carbon steel with an increased phosphorus content of 500ppm and assuming a cooling rate of 10 K/s, the calculated temperatures and concentrations in **Figure 3 (a)** show very good agreement. Since both models are based on Ohnaka’s assumptions and use nearly the same input parameters, the high correspondence indicates, that the algorithm was properly implemented.

Subsequently, an in-house 1D-FV solidification software involving the microsegregation model was used to analyze more than 70 already available results from SSCT-Tests on Low Carbon (LC) und Medium Carbon (MC) steels. In **Figure 3 (b)** the experimental values are plotted against the calculated solidus temperatures. Although the deviation in case of MC steels (± 10 °C) is slightly higher than for LC steels (± 5 °C), the obtained results are highly satisfying and confirm the present method of microsegregation modelling.

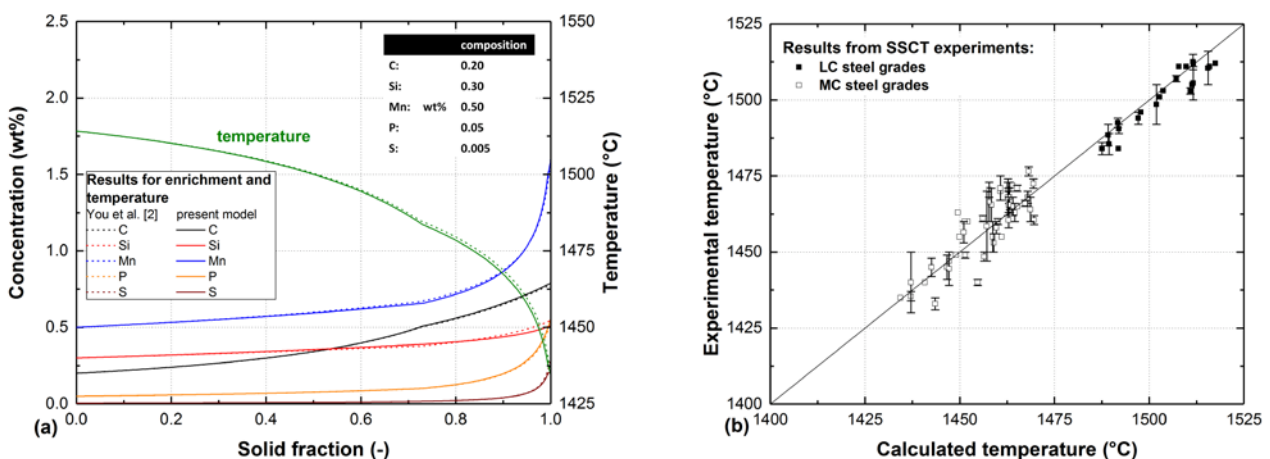


Figure 3: Comparison of the present „stand-alone“ microsegregation model and a model which is fully coupled with the database FSStel2015 (a) and the correlation with results of SSCT-Tests (b)

4. SOLIDIFICATION SIMULATION OF A CONTINUOUS SLAB CASTER

The 1D-FV software was applied for the solidification simulation and strain analysis in a 250mm continuous slab caster considering a casting speed of 1.2 m/min. Thermal boundary conditions and casting machine configuration are taken from the previous work by Arth et al. [20].

In continuous casting of slabs the internal quality regarding macrosegregation is mainly improved by the installation of a softreduction close to end of the solidification. Practically, the final solidification point is determined by the numerical simulation of the process. The precision of the simulation may decide, if the

softreduction is successful or not. In order to demonstrate the relevance of microsegregation modelling for the positioning of the softreduction, the calculated final solidification point is compared with the results obtained under assumption of equilibrium conditions (=Lever-rule). **Figure 4 (a)** shows the calculated metallurgical length for a Low Carbon (LC) and a Medium Carbon (MC) steel grade. Due to the low amount of alloying elements in the LC steel, the difference in the predicted final solidification point Δl_{MET} is negligible. Higher amounts of strongly segregating elements like carbon, phosphorus and sulphur raise Δl_{MET} significantly up to 0.2 m. Further, the influence of segregating elements on the difference in the metallurgical length is enhanced by the defined cooling program, as can be seen in **Figure 4 (b)**. Maximum values of Δl_{MET} are observed for slow cooling rates (= soft cooling strategy) and high carbon contents. The positioning of the softreduction according to the equilibrium conditions will miss the real final solidification point by 0.5 m. Deviation on this scale may lead to a downgrade of the slab, or in the worst case to a rejection.

In the second part, the microsegregation model was used for strain analysis in the casting machine with respect to the formation of hot tear segregations (HTS). In **Figure 4 (c)**, the occurring strain ϵ due to bending, straightening, bulging and reheating (= accumulated strain) is compared with the critical strain measured by the SSCT-Test. Intensive cooling results in low values of the predicted strain whereas the soft cooling favours the strain accumulation during the process. However, under the assumption of 100 % maintenance of the casting plant, the calculated strain in this case never exceeds the critical value. In **Figure 4 (d)** it can be seen, that microsegregation has decisive influence on the accumulated strain: Even at low carbon contents (0.1 wt%) the calculated strain is nearly doubled compared to equilibrium conditions. Hence, the microsegregation phenomenon has to be considered to adjust the casting parameters and to prevent hot tear formation.

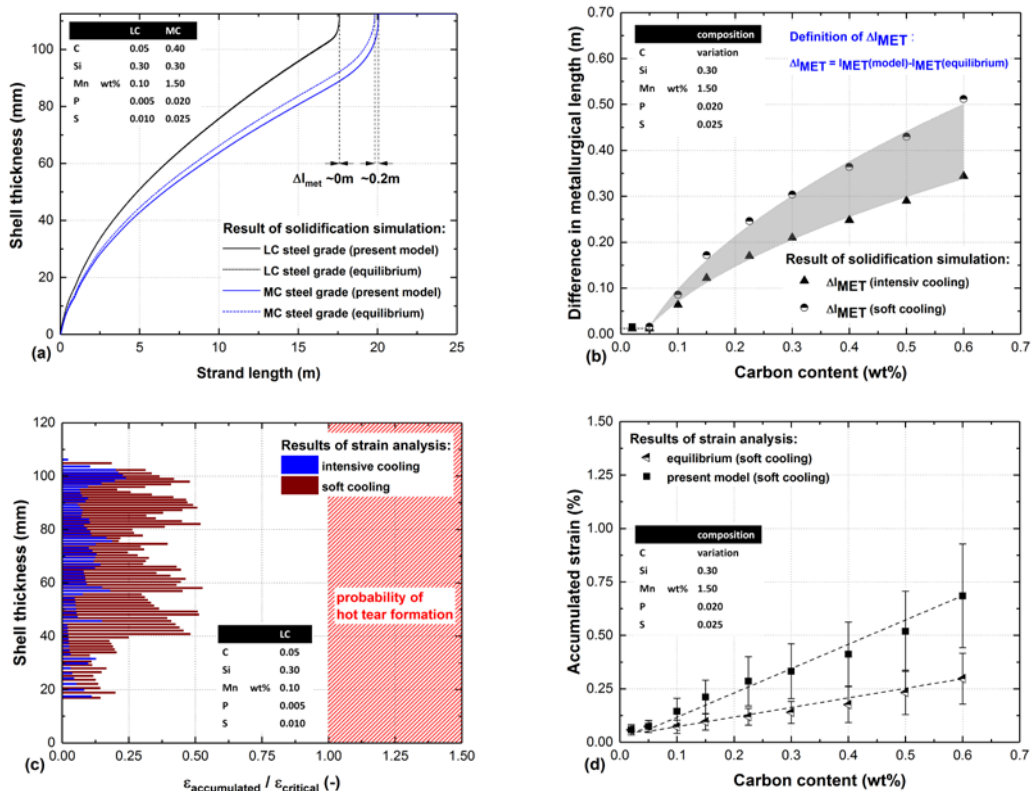


Figure 4: Difference in the metallurgical length compared to equilibrium conditions: (a) in presence of segregating elements and (b) in dependence of carbon content and cooling strategy; Calculation of accumulated strain during casting and comparison with critical values from the SSCT-Test (c); Influence of microsegregation modelling on strain accumulation compared to equilibrium conditions (d)

5. CONCLUSION

By means of Difference Scanning Calorimetry measurements the published equation for the estimation of liquidus temperature by Miettinen and Howe [17] could be slightly modified. Based on the experimental data, an increase of the liquidus temperature by 2 °C / wt% was observed for aluminum contents up to 3 wt%. The consideration of the coefficient leads to a further improvement of the equation. The optimized expression enables the accurate calculation of liquidus temperature even at higher amount of alloying elements and is thus used for determination of the current temperature in the microsegregation model. The calculated solidus temperatures and concentrations performed with the present “stand-alone” model are in very good agreement with a model from literature which is fully coupled to the thermodynamic database FSSel2015 (FactSage) [10]. Further, the model has been evaluated with more than 70 hot tensile tests on Low Carbon and Medium Carbon steels. The solidification simulations of continuous slab caster and the subsequently strain analysis regarding hot tear show the relevance of microsegregation modelling for process control in continuous casting processes.

ACKNOWLEDGEMENTS

The authors gratefully acknowledge the funding support of K1-MET GmbH, metallurgical competence center. The research program of the K1-MET competence center is supported by COMET (Competence Center for Excellent Technologies), the Austrian program for competence centers. COMET is funded by the Federal Ministry for Transport, Innovation and Technology, the Federal Ministry for Science, Research and Economy, the provinces of Upper Austria, Tyrol and Styria as well as the Styrian Business Promotion Agency (SFG). This work is also part of the ongoing K2-MPPE project A3.32 (SmartCast).

REFERENCES

- [1] OHNAKA, I. Mathematical analysis of solute redistribution during solidification with diffusion in the solid state, *Transactions ISIJ*, 1986, vol. 26, no. 12, pp. 1045-1051.
- [2] GULLIVER, G. H. *Metallic Alloys*, London: Griffin, 1922, 439 p.
- [3] SCHEIL, E. Bemerkungen zur Schichtkristallbildung, *Zeitschrift für Metallkunde*, 1942, vol. 34, pp. 70-72.
- [4] BRODY, H. D., FLEMINGS, M. C. Solute Redistribution in Dendritic Solidification, *Transactions of the Metallurgical Society of AIME*, 1966, vol. 236, pp. 615-623.
- [5] CLYNE, T. W., KURZ, W. Solute Redistribution during Solidification with Rapid Solid State Diffusion, *Metallurgical Transactions A*, 1981, vol. 12, no. 6, pp. 965-971.
- [6] UESHIMA, Y., MIZOGUCHI, S., MATSUMIYA, T., KAJIOKA, H. Analysis of solute distribution in dendrites of carbon steels with δ/γ transformation during solidification, *Metallurgical Transactions B*, 1986, vol. 17B, no. 4, pp. 845-859.
- [7] KOBAYASHI, S. Solute redistribution during solidification with diffusion in solid phase: A theoretical analysis, *Journal of Crystal Growth*, 1988, vol. 88, no. 1, pp. 87-96
- [8] YOU, D., BERNHARD, C., WIESER, G., MICHELIC, S. Microsegregation model with local equilibrium partition coefficients during solidification of steels, *steel research international*, 2016, vol. 87, no. 7, pp. 840-849.
- [9] YAMADA, W., MATSUMIYA, T., ITO, A. Development of simulation model for composition change of nonmetallic inclusions during solidification of steels. In *6th International Iron and Steel Congress*, Tokyo, 1990, pp. 618-625.
- [10] BALE, C. W., BÉLISLE, E., CHARTRAND, P., DECTEROV, S. A., ERIKSSON, G., GHERIBI, A. E., HACK, K., JUNG, I.-H., KANG, Y.-B., MELANCON, J., PELTON, A. D., PETERSON, S., ROBELIN, C., SANGSTER, J., SPENCER, P., VAN ENDE, M.-A. FactSage thermochemical software and databases, 2010–2016, *CALPHAD*, 2016, vol. 54, pp. 35-53.
- [11] PIERER, R., BERNHARD, C. On the influence of carbon on secondary dendrite arm spacing in steel, *Journal of Material Science*, 2008, vol. 43, no. 21, pp. 6938-6943.

- [12] XIA, G. Untersuchungen über das mechanische Verhalten von erstarrendem Stahl unter stranggußähnlichen Bedingungen, PhD Thesis, Chair of Ferrous Metallurgy, Montanuniversitaet Leoben, 1992.
- [13] KAWAWA, T. Estimation of liquidus temperatures of steel, *Report of 6th Meeting on Solidification of Steel*, 1973, No. 6-III-9.
- [14] KAGAWA, A., OKAMOTO, T. Influence of alloying elements on temperature and composition for peritectic reaction in plain carbon steels, *Materials Science and Technology*, 1986, vol. 2, no. 10, pp. 997-1008.
- [15] HOWE, A. Estimation of liquidus temperatures for steels, *Ironmaking and Steelmaking*, 1988, vol. 15, no. 3, pp. 134–142.
- [16] SCHÜRMAN, E., STISOVIC, T. Berechnung der Liquidustemperatur aus der chemischen Analyse legierter Stahlschmelzen, *Stahl und Eisen*, 1998, vol. 118, no. 11, pp. 97–102.
- [17] MIETTINEN, J., HOWE, A. A. Estimation of liquidus temperatures for steels using thermodynamic approach, *Ironmaking and Steelmaking*, 2000, vol. 27, no. 3, pp. 212–227.
- [18] PRESOLY, P., PIERER, R., BERNHARD, C. Identification of defect prone peritectic steel grades by analyzing high temperature phase transformations, *Metallurgical and Materials Transactions A*, 2013, vol. 44, no. 12, 5377-5388.
- [19] PIERER, R. Formulation of a new hot tearing criterion for the continuous casting process, PhD Thesis, Chair of Ferrous Metallurgy, Montanuniversitaet Leoben, 2007.
- [20] ARTH, G., BERNHARD, C., ILIE, S., SCHADEN, T., PIERER, R. Experimental und numerical investigations on hot tearing during continuous casting of steel, *Berg- und Hüttenmännische Monatshefte*, 2015, vol. 160, no. 3, pp. 103–108.